Swansea University
Prifysgol Abertawe

Multi-Scale Simulation and Validation of Hot Rolling Processes for DP800 Steel

Liam Moody

Submitted to Swansea University in fulfilment of the requirements for the Degree of Doctor of Engineering

Swansea University

2024

The EPSRC funded Prosperity Partnership led by Swansea University

Abstract

Dual-phase (DP) steels are of increased interest in the automotive sector due to their attractive blend of high strength and high formability, which helps automotive designers reduce vehicle weight, thereby driving down both manufacturing costs and vehicle emissions.

Optimising the manufacture of Advanced High Strength Steels (AHSSs) is critical to the future of steel manufacturing, and as AHSSs have complex chemistries, this makes them extremely challenging to process. This project focuses on a laboratory scale process that attempts to mimic the manufacture of DP800 hot-band material (hot rolled material, before any annealing processes) on the industrial scale. This laboratory process was investigated in depth, and it was clear that challenges with geometry and physical restrictions gave rise to inconsistencies between the industrial and laboratory process. In parallel to this, a proprietary Tata Steel simulation model of the finishing mill and run out table was also evaluated and investigated in conjunction with JMat Pro®, a commercial simulation software. It was found that changing key parameters in the Tata Steel software did not have the intended outcome as expected, and when compared to the experimental data, this also confirmed that careful consideration was required when tuning these settings. Furthermore, JMat Pro® was utilised throughout this research to compare processing routes, understand the microstructural evolution at various stages through the hot mill and understand the effect of varying product chemistries in the laboratory hot rolling setting.

The findings of this research complement the work of the Prosperity Partnership in the manufacture of novel alloys through Rapid Alloy Prototyping (RAP), in the pursuit of steel manufacturing in the laboratory setting.

Declarations and Statements

I declare that this work has not previously been accepted in substance for any degree and is not being concurrently submitted in candidature for any other degree.

Signed: ███████████

Date: _____ 27/09/2024 _____

I declare that this thesis is the result of my own investigations, except where otherwise stated and that other sources are acknowledged, where a bibliography is appended.

Signed: ███████████

Date: _____ 27/09/2024 _____

I give permission for this thesis to be available for download and photocopy and for the title and abstract to be made available outside Swansea University.

Signed: ███████████

Date: _____ 27/09/2024 _____

Swansea University's ethical procedures and code of conduct have been followed in the research within this document.

Signed: ███████████

Date: _____ 27/09/2024 _____

Acknowledgements

List of Figures

List of Tables

Introduction & Industrial Context

Dual phase steels are part of a family of steel, often referred to as AHSS (Advanced High Strength Steels). They are favoured due to their high UTS and high formability, credited to the inclusion of both a Martensite and Ferrite phase respectively[1].
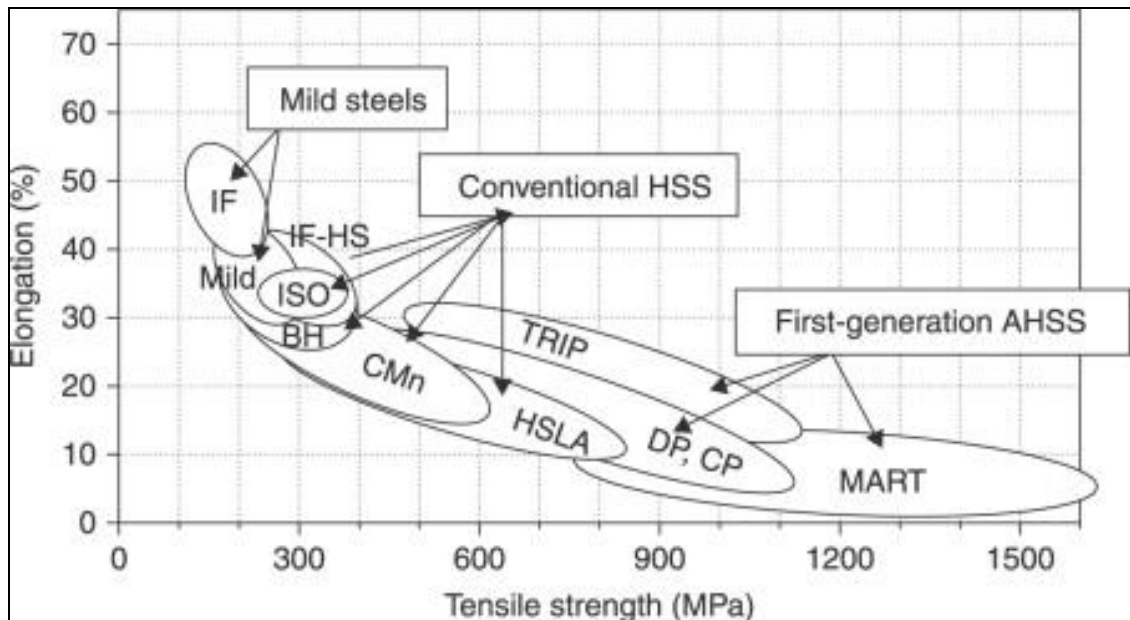
Figure 1- 'Banana Diagram' of steel grades, comparing strength and formability[2].

DP steels are now commonplace in automotive BIW (Body in White) automotive applications. They play a key role due to their relatively high strength and high formability, which allows thinner section material to be used, improving the design freedom of

automotive engineers, by allowing stiffness to be 'designed-in' to the vehicle rather than relying on bulk material properties.

At the time of writing the UK government has pledged to end the sale of passenger vehicles that are powered exclusively, or in part, by an internal combustion engine will cease by 2030[3]. Other European nations are also expected to follow suit to tackle the increasing burden of CO_2 emissions upon the environment. The most effective way of reducing emissions and overall performance in any vehicle is the reduce the total mass of the vehicle. The lower the mass of the vehicle the less energy required to propel it, therefore reducing emissions, be it directly from an internal combustion engine or secondary emissions from non-renewable electrical power generation. In addition to this a reduced material usage also correlates to a reduced energy consumption in production (where like for like materials are used) as well as reducing the TCO (Total Cost of Ownership) for the consumer. Lastly one of the largest criticisms of the electric vehicle is the limited range, this is directly linked to the weight of the vehicle, the lower the weight the longer the range, making weight reduction in such a vehicle of upmost interest. This illustrates simply why incremental weight savings in the materials used are hugely beneficial and of significant commercial interest.

The World Auto Steel programme, an international program comprised of 22 independent members including Tata Steel, conducted a three-year program regarding the steel usage likely to be used in an electric vehicle. The aim was to create a body structure with a 50-70% reduction in life cycle emissions[4]. The results yielded the design of a vehicle with over 95% usage of High-Strength and AHSS steels, with 48% of which have a yield strength over 1000MPa[5].
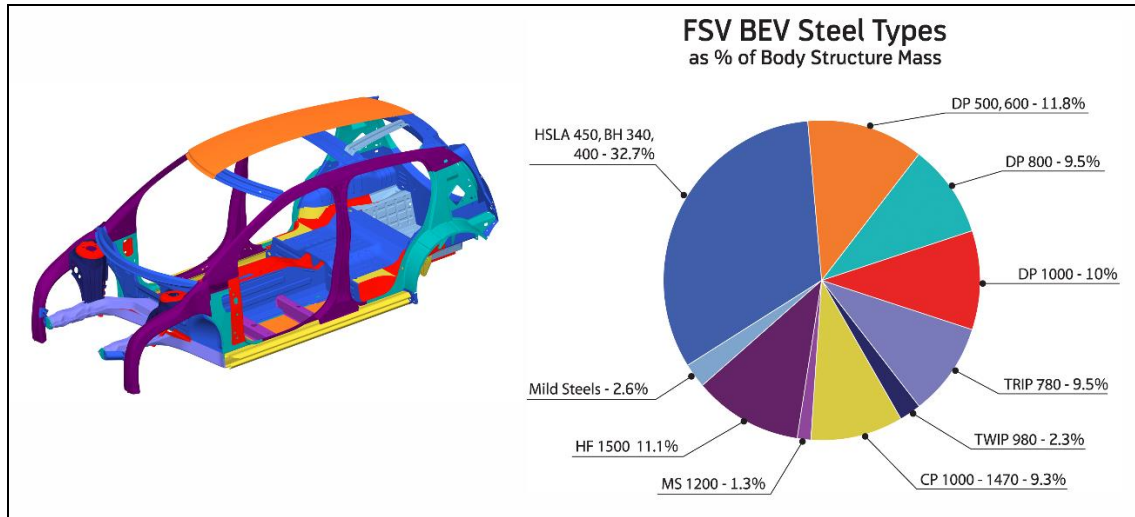
Figure 2- World Auto Steel's FSV, steel usage across a BIW application[5].

This therefore highlights the importance of research into DP (Dual Phase) steels, from a processing standpoint. In response to this demand the Prosperity Partnership's use of RAP (Rapid Alloy Prototyping), allows for the rapid generation of multiple novel alloys with varying chemistries and heat treatments to create steels with varying properties. This 'virtual factory' approach is a collaboration between EPSRC, Tata Steel, Warwick University and Swansea University[6]. The RAP approach utilises small scale samples (40g), the research outlined in this project will focus on larger 2.5kg samples and aligning this 2.5kg route with industrial hot rolling and ROT (Run Out Table) processes. The 30g route allows for rapid creation of novel material grades, but due to inherent limitations with sample geometry and size, such as small mass and large surface area to volume ratios, they cool far too quickly and are not suitable for multi-pass hot rolling.

A software tool called Titan, is also employed within this body of research. Titan is a proprietary software used by Tata to simulate a number of processes within the steel making process. Embedded within Titan is a transformation model for the Run Out Table. This transformation model is referred to as Mitron. Mitron is capable of taking the process parameters of the hot mill and ROT, combining these with product chemistry and predicting the product transformation that was achieved prior to hot band coiling. One of the goals of this EngD thesis is to evaluate the Titan model of the ROT, more specifically the Mitron transformation model and optimise it, where possible, such that it better predicts the pearlite ferrite composition of Tata Steel's DP800 chemistry. In doing so, this optimised tool can be used to make simulated process changes with the aim of increasing product yield and reducing coil waste due to industrially specific problems which will be explained fully in the this thesis.

Key definitions

Hot-Band: Material produced after hot mill finishing and run out table cooling.

Transfer Bar: Material produced after the roughing mill, prior to the finishing mill.

ROT: Run Out Table

PAGS: Prior Austenite Grain Size

CT: Coiling Temperature, the temperature of the steel after run out table cooling.

FRT: Final Rolling Temperature, also referred to as FT (Finishing Temperature), the temperature of the strip at the last roller pass of the finishing mill.

T_{NR}:   The Temperature of No Recrystallisation.

DP: Dual Phase

HSLA: High Strength Low Alloy

IF: Interstitial Free

AHSS: Advanced High Strength Steel

1. Literature Review

1.1. Steel Categories

1.1.1. HSLA

High Strength Low Alloy steels, fit within the broader category of microalloyed steels. These steels are designed to exhibit superior mechanical properties, and often corrosion resistance, over more conventional mild steels[7]. HSLAs generally have relatively low carbon contents (0.05-0.25% Wt.), providing beneficial formability characteristics, in addition to this other alloying elements may include Cr, Ni, Mo, Cu, N, V, Ti, and Zr, depending upon desired properties[7]. ASTM International classifies HSLAs into six distinct categories:

- Weathering Steels
- Microalloyed ferrite-pearlite steels
- As-rolled pearlitic steels
- Acicular ferrite (low-carbon bainite) steels
- Dual-phase steels
- Inclusion-shape-controlled steels

Conventional HSLA steels generally consist of a single-phase ferrite microstructure due to their carbon content, with the exception of C-MN steels[8], as described in the iron-carbon diagram below:
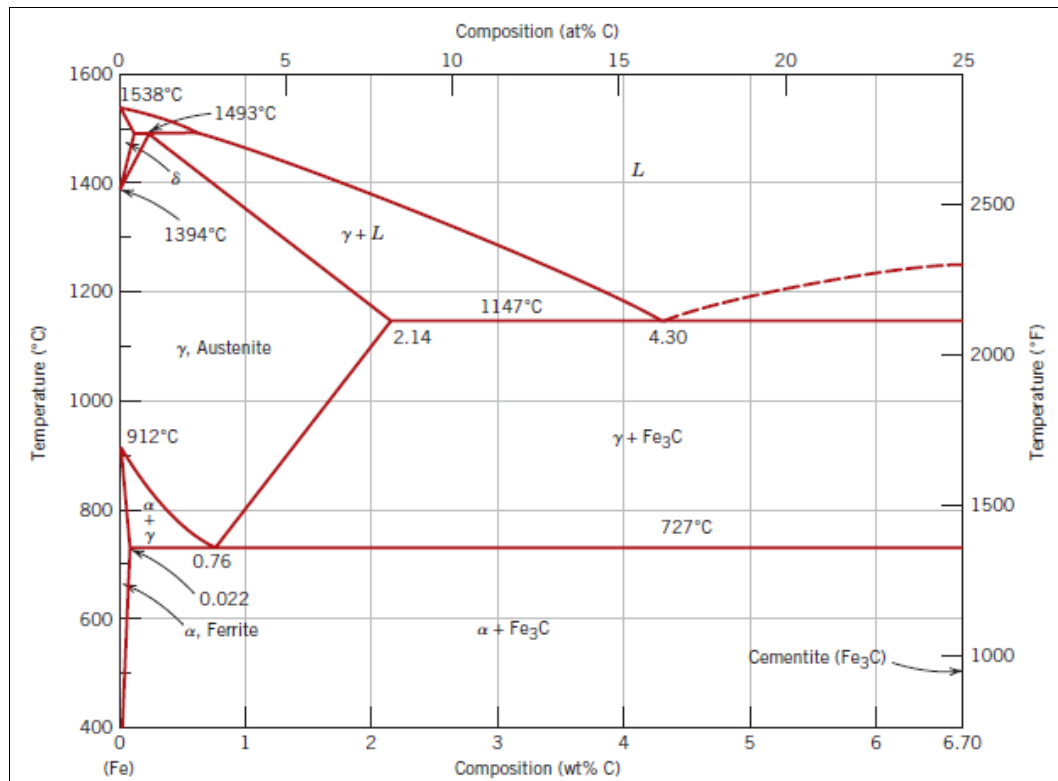
Figure 3- Iron-iron carbide phase diagram showing phases present at increasing percentage weights of carbon and varying temperatures[9].

1.1.2. AHSS

Advanced High Strength Steels are considered 'advanced' due to their containing more than one phase present, which differentiates them from HSLAs. AHSSs are used to a great degree in BIW applications due to their novel combination of high strength and formability, which can be 'tuned' to the requirement within the vehicle. This is exemplified by crash structures in which greater energy absorption is required, or alternatively A-pillars where low deformation is essential for vehicle stiffness and passenger safety. AHSSs have been described generationally due to the time period in which most of the major developments took place, although development has been ongoing in all cases, it is generally agreed AHSSs fit into the following categories:
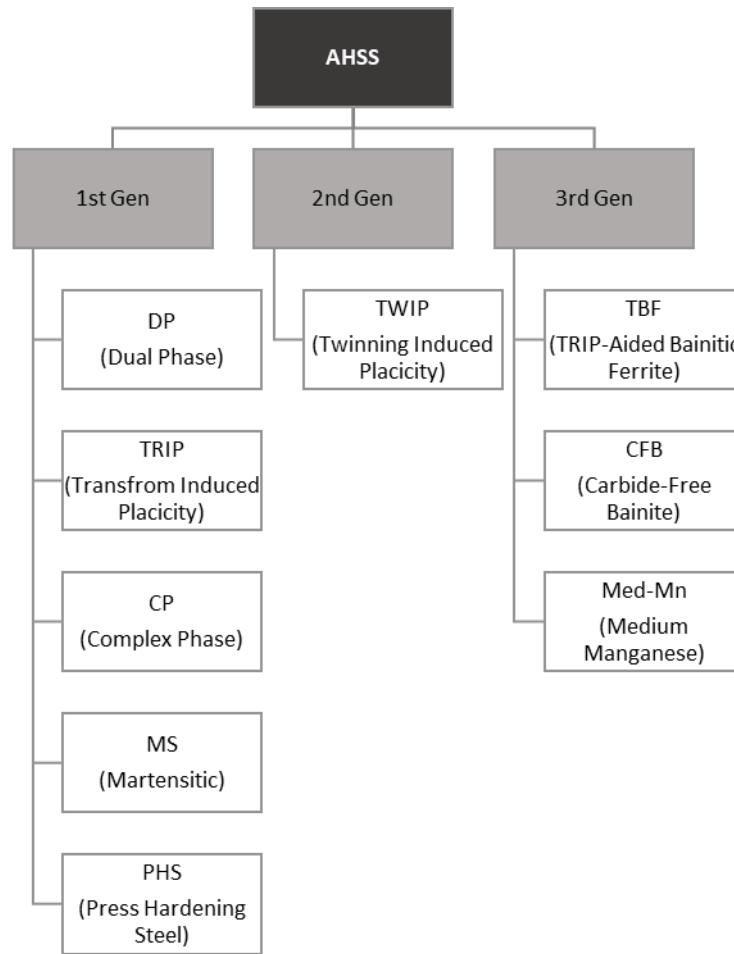
Figure 4- Hierarchy of AHSS generations, created from data provided by World Auto Steel[8].

1.1.3. DP Steels

Dual Phase steels are so called due to the presence of two phases in the finished product microstructure. They offer a combination of high formability and high tensile strength, which can range from 450 to 1200 MPa[10]. They are also popular due to their continuous yielding properties and high rates of strain hardening[11]. As described previously DP steel fits into the broad umbrella group of AHSSs (Advanced High Strength Steels). They are considered 'low alloy steels' however have a large variety of alloying elements to influence the transformation characteristics, such that the appropriate ratios of Martensite and Ferrite are present for the required mechanical properties for the intended use. In order to facilitate the formation of hard martensite 'island' within a softer ferrite matrix, manganese and silicon are frequently utilised, among other micro alloying elements[12]. Dual phase steels are capable of exhibiting a wide variety of mechanical properties, see Figure 5, and as such can be tailored for different requirements, especially in the case of automotive BIW applications within the automotive industry.
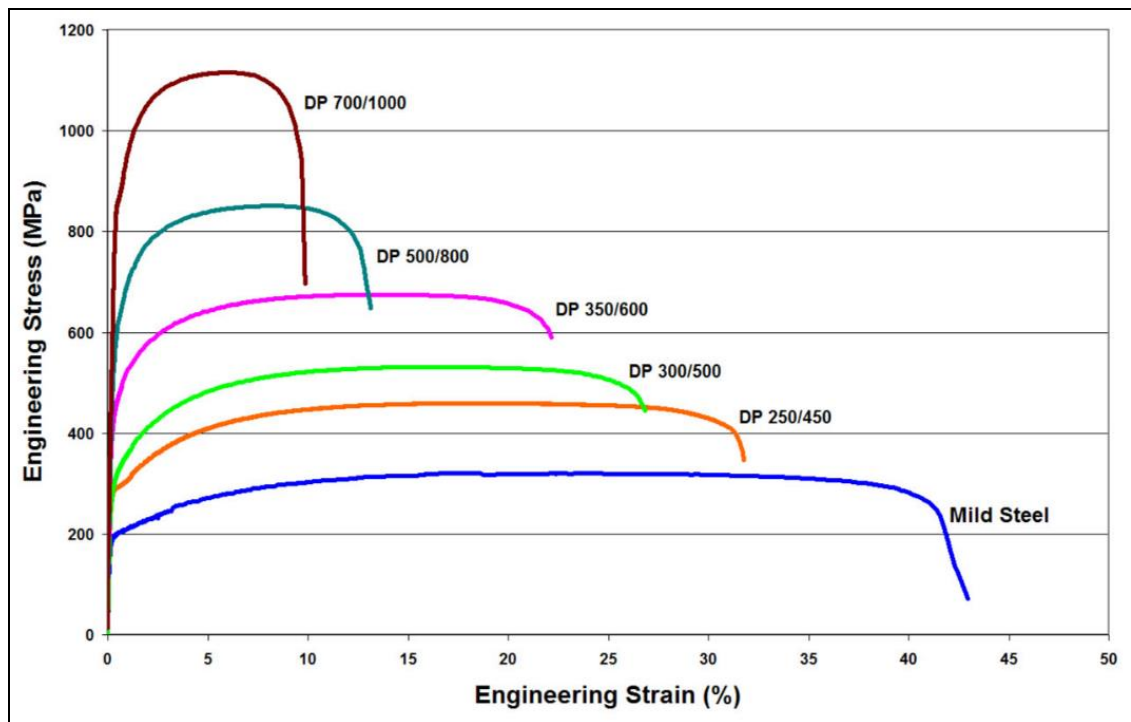
Figure 5- Stress Strain curves for a variety of different DP Grades[13].

The bulk of this work described in the following will concentrate on DP800, which is of particular commercial interest, at the time of writing, to the Tata Steel Port Talbot site.

As is the case with all steel grades, DP steels rely upon controlled thermomechanical processes in order to create the describable microstructure that is responsible for the combination of high strength and formability that the automotive market demands. As mentioned previously DP800 consists of martensite 'islands' within a ferrite matrix. This is made possible by a series of rolling processes that refine the grain structure, this creates a high density of grain boundaries and therefore sites for ferrite nucleation within the ferrite temperature region[14]. The temperatures at which these transformations occur are also affected by steel chemistry. The complete chemistry for Tata Steel's proprietary DP800 composition is not explicitly outlined due to corporate sensitivity reasons, however relevant elements are discussed throughout the thesis most often Nb and other grain refiners and precipitate formers, since these are key to the processability and final properties for the steel in question.

The research in this project will concentrate on the thermomechanical treatment of DP800 rather than modification of existing commercial chemistry. E.I. Poliak concluded that the thermomechanical parameters on the ROT of AHSSs is the most important factor in

achieving the desired microstructure, such that problems can be avoided downstream of the ROT and hot mill[14]. This highlights the importance of this research in reducing not only coil end effects (which will be addressed later in this thesis) but also product consistency. As well as replicating the hot rolling process at the laboratory scale to help to tacking such industrial problems.

1.1.4. IF Steels

Although not the main focus of this Thesis, IF (Interstitial Free) steels are another grade of steels which contrast to DP800 in their comparatively lesser strength greater formability making them suitable automotive products such as body panels. As the name suggests, IF steels have very low amounts of interstitial elements in them, eliminating the effect of precipitate strengthening mechanisms, making them highly ductile[15]. Similarly to DP800, IF steels consist of a BCC ferrite matrix, and typically have low levels of carbon and nitrogen to reduce precipitate formations, improving ductility. IF steels, like many grades, are also subject to microalloying to promote certain mechanical properties. The absence of precipitate formers, allows ductility, but also limits the mechanical strength, as such other elements such as phosphorus, silicon and manganese promote solid solution strengthening where high strength is needed[15]. Figure 6 shows the distribution of multiple steel grades for a BIW application, notable both DP and IF grades are present. The DP grades are used in the parts of the vehicle which require higher mechanical strengths, such as the floorplan and engine sub-frame (shown in blue). Whereases the IF grades (red) are used in the door frames, where deep drawability is needed.
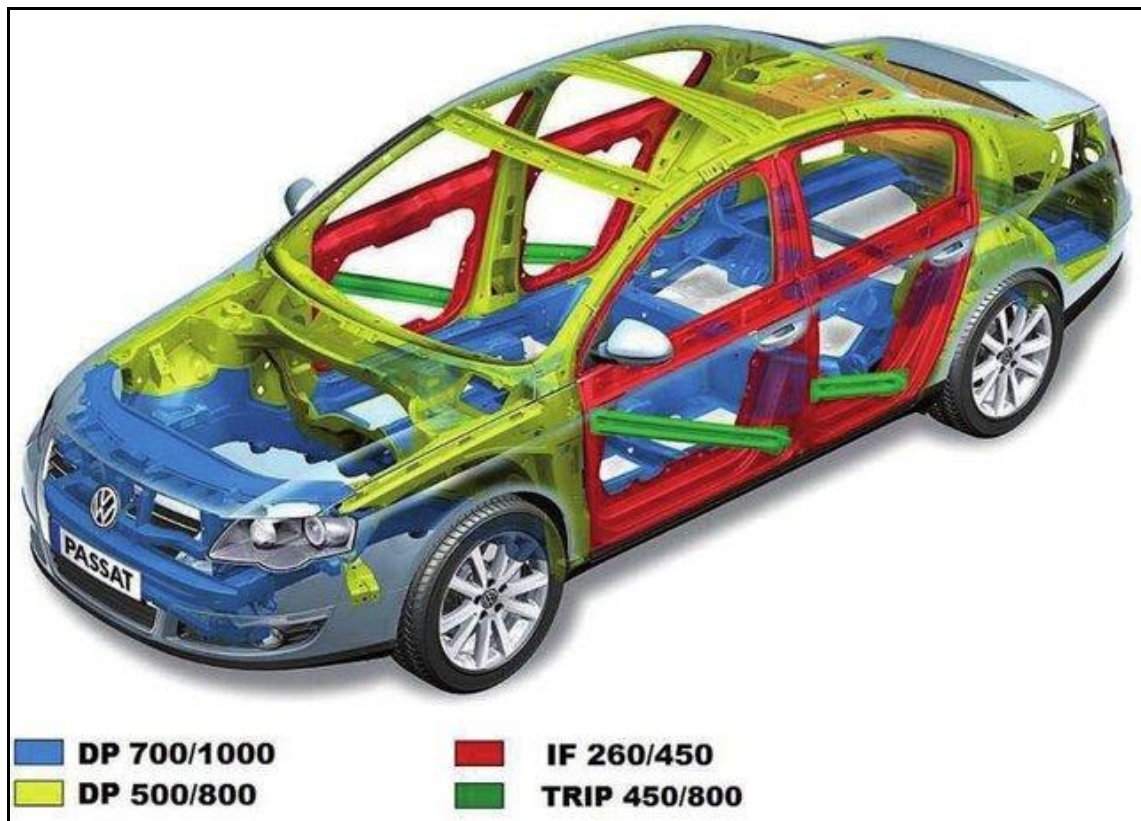
Figure 6- Use of DP, IF and TRIP steel grades in a BIW application.

With reference to Figure 1, the difference in mechanical properties is evident between DP and IF grades. Broadly DP steels exhibit a higher tensile strength, and lower ductility and IF grades are broadly the inverse of this.

1.2. Alloying Elements

1.2.1. Effect of each Element (literature)

Dual Phase Steels, as discussed previously, are often described as microalloyed steels due to the small additions of a diverse number of alloys used to promote beneficial properties, be that for increased processability or enhanced mechanical properties. This is of key significance for the metallurgist since the addition of these elements often influence the transformation characteristics during heat treatments, this is illustrated in the figure below showing the modification of the ferrite, perlite and bainite transformation start times subject to alloying additions of boron. Figure 7 illustrates this point, it shows the effect of increasing boron additions of the transformation of Ferrite and Pearlite transformation curves. In this instance increasing the additions of boron resulted in a retardation of both the Ferrite and Pearlite transformation curves.
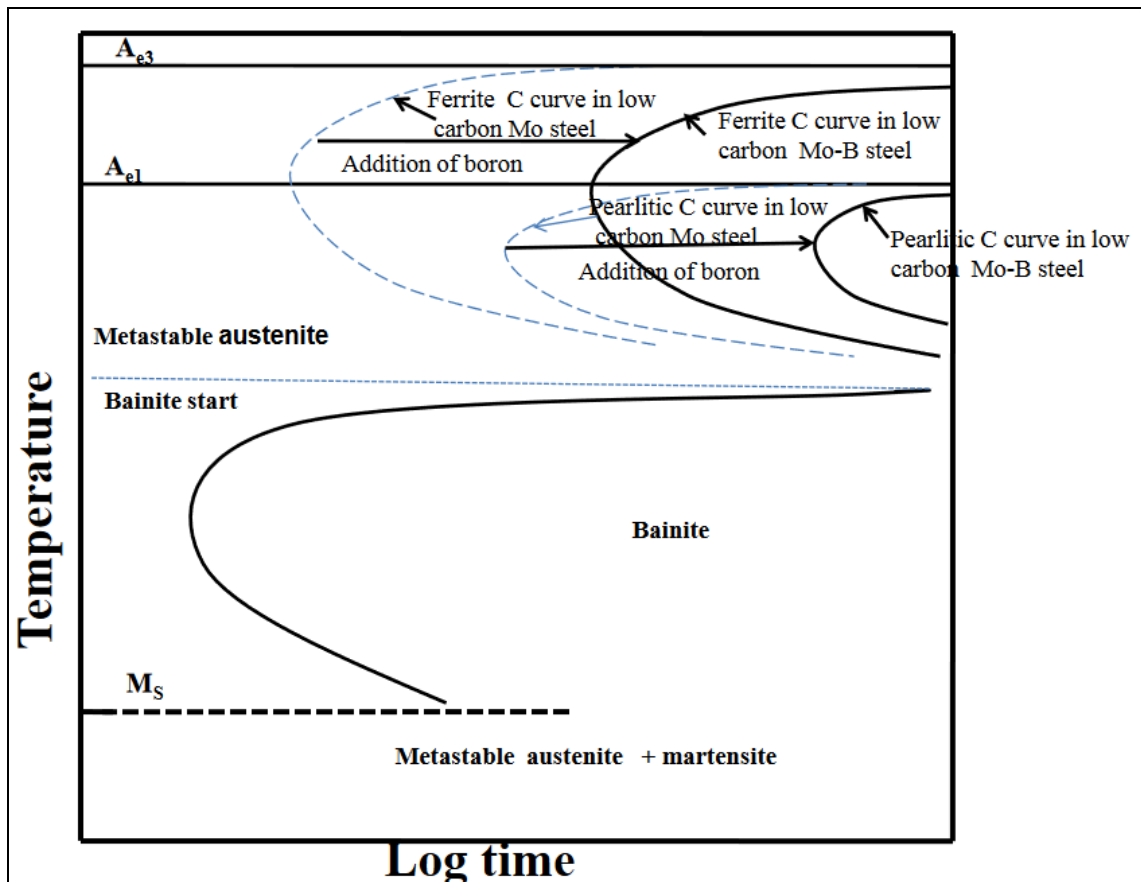
Figure 7- Influence of Boron additions on transformation characteristics of steel[16].

The following section describes some of the key alloying elements used in DP800, outlined in 1.1.3, and their role within the steel.

Manganese

Manganese is a frequently used addition in microalloyed HSLA steels, offering multiple effects to the transformation kinetics. H. Terao [17] and colleagues found that by significantly increasing the percentage weight of Mn, resulted in an increase in the strength of the steel, irrespective of heat treatment, it was also noted that the strength increased not by the usual mechanism of increased Martensite volume fraction, but instead by increasing the strength of the Ferrite grains themselves. Reductions in manganese has been reported to alter the transformation kinetics of dual phase steels, by decreasing both the Ac1 and Ac3 temperature points[18].

Silicon

Silicon is a common addition in the steel making industry, a component present in most grades. Si is a highly critical grade in the manufacture of Nb bearing microalloyed

steels[19, 20]. Si plays a particularly important role regarding the rate of precipitation formation[19]. In the case of hot rolled Ni alloyed steels, Si has been found to be an effective grain refiner, resulting in ferrite grains as small as 3µm[20]. As a result, Si additions results in an increase in the yield strength of HSLA grades predominantly via solid solution strengthening[21]. Si also is a stabiliser of the ferrite phase. Si has been found to increase the eutectoid temperature, increases the stability of ferrite over austenite, increasing the rate of ferrite transformation[22].

Aluminium

Small additions of aluminium of often added into steel to control the size of the austenite grain growth at high temperatures[23, 24]. Nitrogen has also been shown to have a similar effect experimentally[24]. At higher percentage weights (>0.08%) aluminium is capable of increasing the strength of the steel by pinning the grain boundaries however this is not the case in the alloy composition in question with reference to the low Al additions (0.052%)[24].

Chromium

Chromium is primarily a carbide former, and therefore improve the wear resistance of steels, as well as decreases in bainite start temperature with increased CR additions[25]. However compared to other microalloying elements, such as Si, Mn, Ni, Mo, V, and T, Cr is known to have the least hardening effect[26]. Increase in Cr additions (0.13% - 1.07%) in HSLA steels have been shown to decrease the PAGS (Prior Austenite Grain Size) [27]. Despite the numerous benefits of Cr in steels, especially in automotive grades, it is often used sparingly due to its relatively high cost and hence the small additions used in the case of Tata Steel's DP800 composition.

Niobium

Similarly, to Cr, Nb is also a carbine former, predominantly forming Niobium Carbide and Niobium Nitride resulting in grain refinement[26]. The mechanism by which this occurs is the formation of fine precipitates which pin grain boundaries and retard the austenite grain growth resulting in a refined grain structure. This grain refinement ultimately increasing the strength of the steel as described by the Hall-Petch relationship[28]. It has been found that when compared to elements which offer similar advantages such as Ti and V, Nb offers better improvements in strength when like for like additions are added[29]. When solidified these precipitates also enhance the strength of the steel by acting as barriers to

dislocation movement under deformation, increasing the yield strength. In the case of DP steels Nb modified the transformation kinetics such that larger volume fractions of ferrite are able to form in a constant cooling process, which would otherwise require a 'hold' to maximise ferrite formation, in the case of non Nb-bearing steels, as illustrated in Figure 8 [30].

Figure 8- Effect of Nb additions to DP steel ferrite transformation curve for hot mill continuous cooling applications[30].

A study conducted by H. Mohrbacher, and colleagues shows the benefits of Nb microalloying (0.03%wt) for DP980 grades at various stages in the steel making process. It was shown that Nb additions resulted in grain refinement during the soaking phase of the annealing cycle, improving mechanical strength and drawability of the final product, which is critical in automotive applications. However the study also highlighted the need for critical control over slab reheat condition when utilising Nb additions, since insufficient soak temperature, or time, will result in not all Nb being dissolved and therefore impeding the microstructural effects[31].

Nb also has profound effects during the hot rolling process. Nb additions increase the stored energy during deformation due the retardation of recrystallization, caused by the solute dragging as Nb atoms impede dislocation movement, whilst Nb carbides (Nb-C and Nb-N) also pin grain boundaries, as summarised by R. Adab and colleagues[32]. This shows the Nb is arguably one of the most critical microalloying elements in achieving the characteristic microstructure of DP800.

Vanadium

The primary role of V, similarly to Nb, it to retard the austenitic grain growth during heating[33]. Again, similarly to Nb, the mechanism by which the austenite grain is refined is due the presence of undissolved V(C,N) precipitates at high temperatures (800-870°C), hindering the recrystallization process, by pinning grain boundaries preventing grain growth[34]. However in the case of hot rolling it has been shown that Nb is more effective at retarding recrystallization than V[34]. During constant cooling on the ROT, when austenite transforms to ferrite and pearlite, V has been shown to refine the ferrite microstructure in microalloyed steels by pinning the ferrite grain boundary, preventing growth[35]. This is the primary reason for the use of V over Nb. Again, similarly to Nb V also increases the strength of steel via both grain refinement and solid solution strengthening.

Nickel

Nickel, in the case of microalloyed steels, offers a large advantage in terms of processability. Nickel has the ability to limit the decomposition of Austenite, so much so that with sufficient additions, austenite can be made stable at room temperature, as is the case with austenitic stainless steels[26]. However, in the case for microalloyed steels, such as DP800, it extends the stable temperature region for austenite, allowing for further grain refinement during rolling operations.

Molybdenum

Similarly, to many of the microalloying elements discussed in this section Mo is a carbide former, increasing the hardness of the steel. However much of the literature discussing the benefits of Mo additions, occur with percentage weight far higher than that included in Tata Steel's DP800 composition. Mo additions have been shown to promote the formation of bainitic structures upon cooling with percentage weights as low as 0.138%[36]. The mechanism by which this occurs is lowering the bainite start temperature, it does this by decreasing the carbon mobility delaying the formation of bainite when cooling[37]. This effect is a disadvantage in the manufacture of DP800 due to the phenomena of 'coil end effects' as discussed in section 1.4.2.6.2, hence why it is likely only present as 0.004%wt.

Titanium

Titanium is known to improve steel toughness and weldability when microalloying[38]. The mechanism for the increase in toughness is due the formation of TiO_2 during smelting, these inclusions (at lower temperatures) promote the nucleation of ferrite from austenite and thereby increasing the presence of acicular ferrite[39]. Ti, like many of the microalloying elements discussed, forms carbides which increases the strength of the steel, by pinning grain boundaries. Especially when combined with Mo additions, as is the case with DP800[38].

1.2.2. Titan Niobium Related Parameters

Within the Titan software several internal settings relate to Niobium found within microalloyed steels. These settings are designed to reflect, in some capacity, the effects Niobium has in the domain of the hot mill and ROT. The name of each setting is given, with a description of the effect. These will later play a part in the optimisation of the ROT model within Titan.

NbEffectiveMax

The maximum amount of Nb, by percentage weight, that the transformation model considers when calculating the effects of Nb. i.e., an adding more that stated value of this element will not result in any changes within the transformation model. At default settings this value is set to 0.05 (1/wt%), since at conception of the model this yielded reasonable results, rather than being a true reflection of the product chemistry, since this factor applies for a number of steel grades.

UnderCoolingNbEffect

As discussed previously Nb is a precipitate former, along with V and Ti. This setting modifies the degree to which these elements contribute to the undercooling, of the steel at it transform from austenite to ferrite, within the transformation model. At default settings this this value is set to 1000 (K/wt%).

NbSlowDown

This setting 'slows down' the effect of Nb on in the transformation model. Increasing percentage weights of Nb withing microalloyed steels has been shown to retard the bainite transformation[40]. At default settings this this value is set to 4.0 (1/wt%).

1.3.Microstructure and Transformation

1.3.1. Martensite

Martensite is the harder of the two phases present in finished product DP800 and is responsible for all DPs high tensile strength[41]. The volume fraction of Martensite in Dual Phase steels is proportional to the UTS, within limits, as shown by E.N. Birgani and colleagues in the below figure.
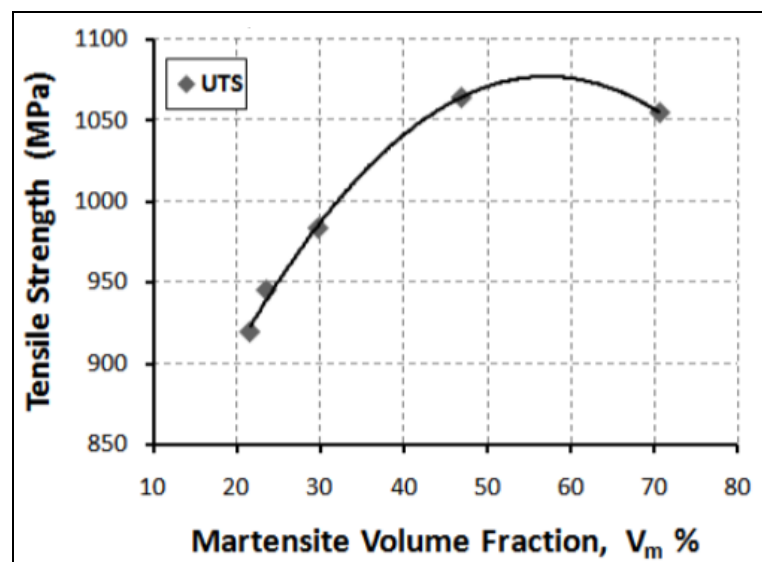
Figure 9- Effect on Martensite volume fraction on the UTS of SAE1010 sheet steel[42].

The volume fraction was plotted and the tensile strength recorded for each the steel specimens. It appears to follow a polynomial relationship in which there is now discernible benefit for UTS with volume fractions above 57%. Generally speaking in the case of automotive grades DP steel the volume fraction of martensite is in the minority compared to ferrite.

Martensite is formed when an steel, above the austenite temperature, is rapidly cooled to near ambient temperatures, during this process a diffusionless transformation of austenite

26

occurs resulting in a non-equilibrium single phase structure with a BCT atomic structure[9]. With reference to Tata Steel's industrial route, martensite is formed during the annealing cycle, where the final microstructure is dictated. Note, this thesis focusses primarily on hot rolling, "finished microstructure" in this context refers to a steel that will subsequently be sold to a customer. In the case of DP800 this would be a ferrite and martensite dual phase. Figure 10 shows the presence of hard Martensite islands within a soft Ferrite matrix for a commercial available grade of DP steel, images were obtained through optical microscopy[41].
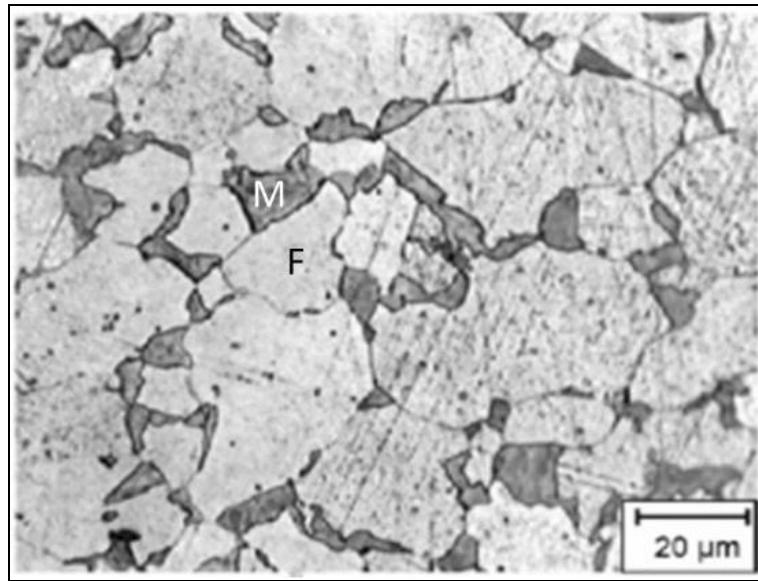
Figure 10- Martensite Islands within a Ferrite matrix of a DP steel, denoted by 'M' and 'F' respectively[41].

Tata steel produced DP800 is created on a CAPL (Continuous Annealing Processing Line). The steel is headed above the ferrite start temperature and cooled in a controlled manner such that the desired volume fractions of ferrite and martensite are formed. Martensite is formed though a diffusionless interaction where austenite is cooled too rapidly for other phases to form. The speed of the cooling prevents carbon diffusion and hence prevents other phases from forming such as ferrite or pearlite. The temperature at which martensite forms is known as the martensite start temperature.

1.3.2. Ferrite

1.3.2.1. Conventional Ferrite

Ferrite is an interstitial solid solution consisting exclusively of iron and carbon. It occurs in BCC (Body Centred Cubic) formation within the atomic lattice. Typically metals with low percentage weights of carbon, consisting of ferrite, are more ductile and exhibit low yield if it is the only phase present in the metal. Ferrite one of the two phases in present in DP

steel's final product. With reference to this body of work, Ferrite forms from Austenite as the strip cools on the ROT, since below the Ae_3 Ferrite is more stable and therefore nucleation occurs which in turn becomes a ferrite grain. As the ferrite grains form, carbon is diffused into the surrounding austenite grains. Since ferrite nucleates at the grain boundary, the PAGS (Prior Austenite Grain Size) is an important parameter in predicting final product microstructure, therefore ferrite formation and morphology is a key point of interest within this research.

1.3.2.2. Widmanstätten Ferrite

Due to the relatively coarse grain sizes exhibited in the hot rolling stage of steel, the formation of Widmanstätten ferrite can occur[43]. This is apparent is the case of DP800 [44], since steels with less than 0.3% wt. C are susceptible to the formation of Widmanstätten ferrite, in addition to their coarse grain structure [43]. As a result is an important consideration in creating a comprehensive model for hot rolled steel transformations, as outlined by Parker [45]. Widmanstätten ferrite is characterised by long acicular formations of ferrite, differentiating from a more uniform front seen in conversional ferrite formation, after nucleation at the grain boundaries, as illustrated in Figure 11.
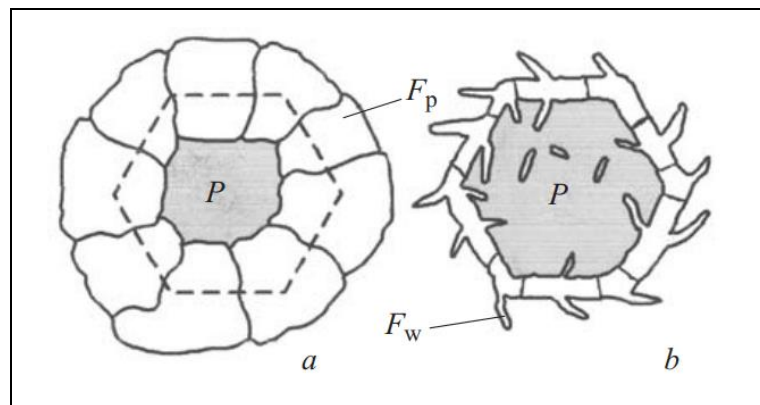
Figure 11- Diagram illustrating the comparison of conventional ferrite formation (a) and Widmanstätten ferrite (b) formation[43].

The main drivers for the formation of and Widmanstätten ferrite are the carbon content, the cooling rate, and the austenite grain size[43]. This is relevant in the production of dual phase steels since the presence of dual Widmanstätten ferrite can reduce the fracture toughness of the material[46, 47]. In order to mitigate this phenomena from occurring during the annealing process it has been suggested that higher holding temperatures and longer holding times may be beneficial[48].

1.3.2.3.   Allotriomorphic and Idiomorphic Ferrite

Allotriomorphic ferrite is a type of ferrite, that is formed the most readily below the Ae_3 temperature[49]. It also tends to nucleate at prior austenite grain boundaries, and grows fastest in the direction normal to the grain boundary, hence the shape of the ferrite grain is strongly influenced by the shape of the grain boundary[50], as shown in Figure 12.
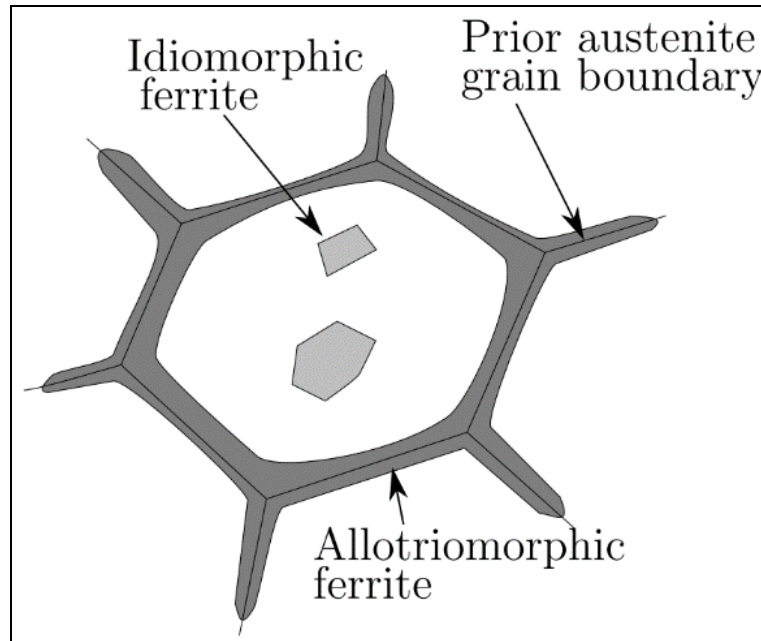
Figure 12- Diagram illustrating the growth of Idiomorphic ferrite within an Austenite Grain[51].

Due to their presence in the manufacture of hot rolled steel, and their differing growth rates and mechanisms, both are relevant in the influence over final microstructural and by extension mechanical properties. These forms of ferrite differ in the nucleation sites. allotriomorphic ferrite nucleates on grain boundaries, whereas idiomorphic ferrite nucleates on impurities in the steel.

1.3.2.4.   Strain Induced Ferrite

Strain Induced Ferrite is formed exclusively in the region between austenite and ferrite transformation temperature [52]. As is the case with conventional ferrite, in the case for DP steels SIF is found to nucleate around (PAG) Prior Austenite Grain boundaries [52-55]. This phenomena is found to occur in the case of hot rolling when particularly large percentage reductions are undertaken within this temperature range. SIF generally has a

finer grain size than conventional ferrite, with the possibility of being as low as 1μm, this has been studied with the view of intentionally reducing the grain size to improve through process mechanical properties[52]. This ultra-fine ferrite formation was initially studied by Yada and colleagues by heavy deformation, above the respective A_{r3} temperature for that particular grade, which resulted in grains measuring between 1 and 4μm[56]. This could prove to be a promising avenue in increasing the rate of transformation on the ROT, since a finer grain size would result in an increased rate of ferrite nucleation.

1.3.3.   Austenite

1.3.3.1.   PAGS

As described in section 1.3.2, PAGS (Prior Austenite Grain Size) is a key parameter in dictating the final microstructure in plant produced steels. The PAGS is also known to affect the martensite start temperature, it has been observed experimentally that a decrease in Austenite grain size results in a decrease of the martensite start temperature[57]. Therefore the downstream effects of the slab reheat temperature, and soak time will affect the kinetics of the transformation on the ROT and therefore later at an annealing stage. Therefore, the PAGS can be viewed as an input parameter that will affect the final microstructural outcomes of hot rolling operations. It has been reported that there can be some variation in soak times during the slab reheat stage, and therefore possible variations in PAGS before finishing mill applications.

1.3.4.   Pearlite

Pearlitic structures consist of alternating layers of ferrite and cementite (Fe_3C), the latter being hard and brittle. It is formed when carbon atoms move away from the ferrite, once the solubility limit is reached (0.02wt% at 727°C), through the process of diffusion. The structure begins to form in one of two ways; either the nucleation of a cementite grain or a ferrite grain from an austenite grain boundary. Once cooperation between the two phases begins the lamellar structure can propagate through the austenite. Pearlite is often present and useful in carbide formation to produce hardened ferrous products. Figure 13 shows the lamellar microstructure of pearlite. The lighter areas within the lamellar are cementite phases and the darker is the ferrite phases, and the large dark areas are proeutectoid ferrite.

Pearlite formation is key to this project since at the end of the ROT the desired microstructure is Ferrite and Pearlite, this provides the necessary mechanical properties for coiling and subsequent annealing processes.
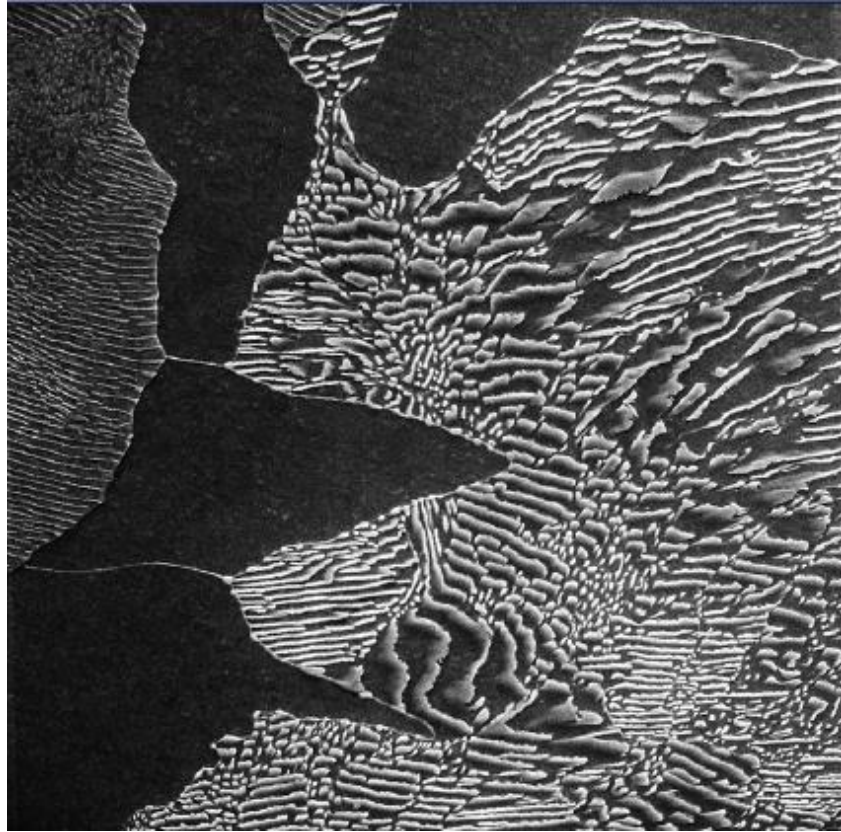
Figure 13-A SEM (Scanning Electron Micrograph) image showing areas of a lamellar microstructure within a steel sample of 0.44 wt% C[9].

1.3.5. T_{NR}

The Temperature of No Recrystallization, often referred to as T_{NR}, is a critical property in control of hot rolling operations. The term T_{NR} can be defined as "The temperature below which complete static recrystallization does not occur between consecutive rolling passes"[58]. For most steels this is in the region of 850-1000°C. It is vital to know this temperature for the DP800 composition when studying phase transformation in an experimental setting. There is little literature regarding the exact T_{NR} of Tata's DP800 grade, however TNR has been successfully measured experimentally using a Gleeble thermomechanical analyser route[59-61].

Microstructure is particularly affected by hot rolling operation below the T_{NR}. It is well documented that the degree of deformation imparted into steel either above or below the

T_{NR} will result in different microstructures[58, 62, 63]. Figure 14 illustrates the resultant evolution in microstructure when hot rolling above and below critical temperatures such and the T_{NR} and A_{r3}. Note the 'pancaking' of grains when rolled at temperatures below the T_{NR}, this in turn increases the number of Austenite grain boundaries and therefore increases the number of nucleation sites for ferrite. It is therefore imperative that when simulating hot rolling processes within a laboratory setting, the representative strain imparted into the sample must reflect that of the plant processes, especially below the T_{NR}.
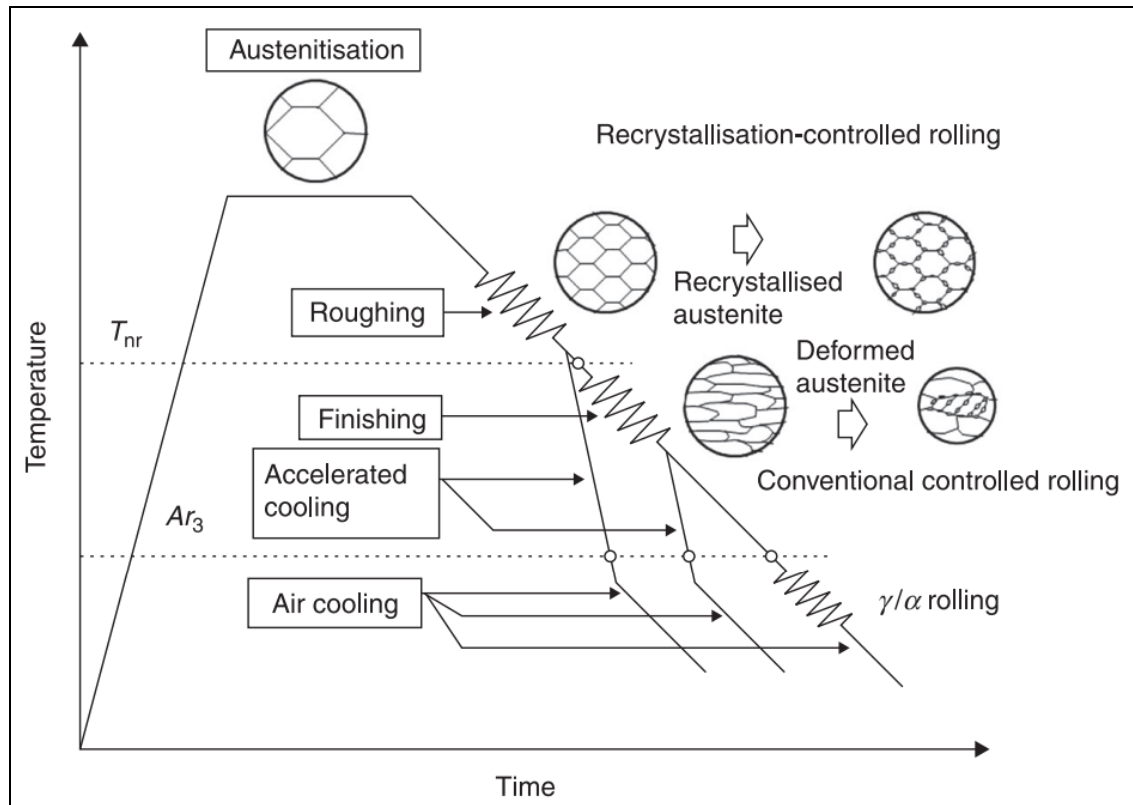
Figure 14-Illustration of effect of hot rolling above and below critical temperatures on microstructure[58].

In addition to experimental routes there are also mathematical models to approximate the T_{NR} given the percentage weight of given elements. One such example of this is the Boratto equation. The Boratto equation is well established as a method for estimating the T_{NR}[64, 65]. Other mathematical models also exist, such as that developed by Bai and colleagues, which provides a modified version of Boratto's equation[66]. A more comprehensive insight into the various equations used to predict T_{NR} is given in section 1.7.1.1.1. Data driven approaches have been taken to estimate T_{NR}, such as that by Fletcher and colleagues in which a database of multiple steels was used to formulate an equation based on the Boratto equation using stepwise regression[67]. A summary of the various models as assessments of them is helpfully provided by M.N. Akhtar and colleagues and

comparing these to Gleeble testing as an experimental validation/ comparison for Nb microalloyed steels[61].

1.3.6. MITRON Transformation Model

This section briefly outlines the transformation model used in the Titan Software; MITRON. Titan is capable of employing a variety of different transformation models, however MITRON is deemed the most up to date, and the most suitable model for modelling dual phase steels, whilst also in need of optimisation and therefore has been chosen for this research.

Fundamentally MITRON is a physical model of phase transformations on a ROT. The model accounts for Austenite grain size (at the start of the ROT), the steel chemistry (as discussed in section 1.2.2) and the cooling rate. The model also models the amount of heat generated due to transformation, and its subsequent effects. MITRON models the entire steel strip in a number of elements, along its length. Each transformation increment is calculated in a discrete time step.

The austenite grain size, for a given steel grade is approximated by the below graph:
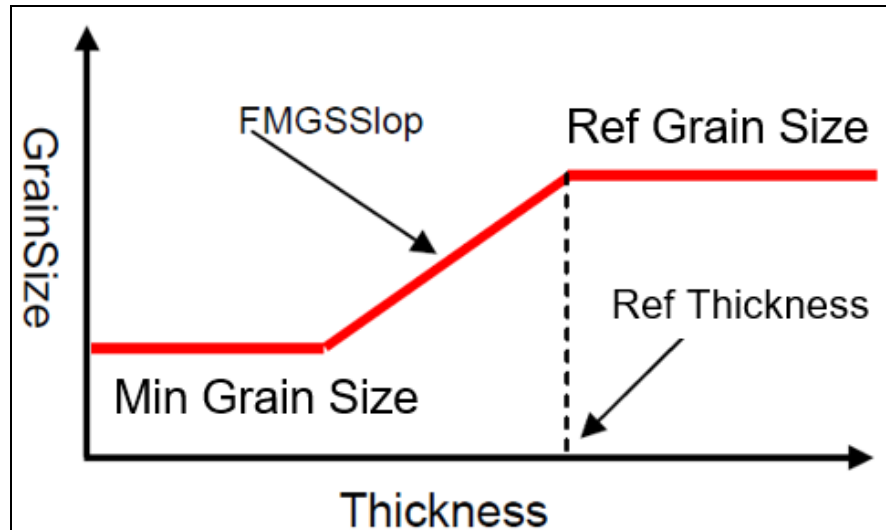
Figure 15- Austenite grain size as a function of strip thickness for MITRON input parameters[68].

Note the above graph shows the relationship between the thickness of the material and the approximated grain size that the MITRON transformation model uses. Above and below certain strip thicknesses the grain size does not change, however there is a region of thickness in which the grain size is a function of strip thickness. This is described by the "FMGSSlope" shown above.

Broadly speaking, above the MinGrainSize, the strip starting austenite grain size is proportional to the strip thickness, up to the RefGrainSize where it becomes constant independent of product thickness. The justification for this model is that when the transfer bar (post rough rolling) enters the finishing mill, it will undergo seven reductions regardless of the desired thickness. A material with a lower final thickness will undergo more strain, and therefore more grain refinement will occur in the material. This approximation is considered a short fall of the model, since it does not account for product chemistry and its effect of recrystallization and grain growth effects. This may be particularly apparent in the case of DP grades because of the effect of Nb in retarding dynamic recrystallisation due to precipitate pinning of grain boundaries[69, 70].

Once the starting grain size has been determined the model determines the critical temperature at which the different phases begin to form, in the case of DP800 ferrite and pearlite. These temperatures are calculated mathematically as a function of both grainsize and product chemistry. The rate at which the phases develop is calculated also as a function of free energy and the product chemistry, this is known as the Mobility Factor or 'M0'. As mentioned the mobility is affected by product chemistry, and predominantly by the effect of Nb and other precipitate formers. This is encapsulated by the parameter 'NbEffective'. This describes the total effect of Niobium, Vanadium and Titanium on the rate of transformation of the steel, since these elements are known precipitate formers and therefore slow the rate of transformation, however Nb has the largest bearing on this parameter compared to V and Ti. The equation to describe the total effect of these elements is shown below:

$$[71] \quad NbEffective = Nb + 0.1V + 0.1Ti \qquad \text{Equation 1}$$

As mentioned previously with each timestep the heat due to the transformation is calculated. The total energy to transformation is proportional to the volume fraction of that given phase. The calculation of heat released due to transformation of austenite to ferrite is complicated. Heat at each timestep is dependent upon a number of constants for that given material; the Ae3 temperature (for that specific steel chemistry) the Curie temperature, the Ae3 temperature of pure iron and the temperature of the steel at that given timestep. Each condition results in a different calculation. The result is different 'cases' or methods by

which the heat of transformation can be determined. Once the heat due to ferrite transformation is determined, from this the heat of Pearlite transformation is determined simple by:

$$[71] \quad Q_{Pearlite} = Q_{Ferrite} + 35000 \qquad \text{Equation 2}$$

The temperatures used in the calculations, which also determine cooling rate, modelled within the Titan software and are therefore external to the transformation model. This depends upon several external factors such as water temperature and air temperature. The temperature of the strip is approximated for the top, bottom and core of the steel. The surface temperature is calculated using simple thermodynamic models of which the inputs are; the strip velocity, the mass flow of the water, the water temperature, and the ambient temperature. The core temperature of the strip is used in MITRON transformation model.

1.4. Manufacturing Industrial Scale

1.4.1. Overview of Steel Making

When modelling industrial processes in the lab it is essential to have a comprehensive understanding of the 'real' process. As such the process is outlined this section, in the setting of the manufacture of an automotive steel product.

Blast furnace
- Raw materials (iron ore, coke and limestone) are charged into the blast furnace in carefully controlled quantities.
- As the coke combusts, oxygen supply is limited such that carbon monoxide is formed, the reduced the iron ore.
- The immense heat of the burning coke melts the iron ore until it is fully liquidus.

BOS
- In this stage the molten iron is converted into steel.
- Oxygen is blown through the molten iron to reduce the carbon content (usually less than 0.1% for automotive grades).
- Alloying elements are added in carefully controlled quantities, in the case of automotive products this usually consists of a high number of elements added in at low percentage weights, some of

these include manganese, silicon and niobium.

Secondary Steel Making	• Defined by four key processes: deoxidation, desulphurisation, degassing and decarburisation
	• Here the chemical composition is adjusted, and further alloying elements can be added.
Continuous Casting	• The molten alloy flows from the ladle, into the water-cooling copper mould called the tundish.
	• This casting is cut to length to form a slab
	• The solidified slabs measure approximately 0.25 x 2 x 9 meters
	• Here slabs are either transferred to the coil yard to awaiting re-heating, on in the case of DP grades the slab will travel directly to the reheat furnace. This is known as 'hot connect'.
Reheat Furnace	• Here the slab is prepared for hot rolling by heating to 1250°C
	• The time spent in the reheat furnace can vary from 40 minutes, at a minimum, to several hours.
	• The steel will transform to a fully Austenitic phase, with an FCC atomic structure.
Rough Rolling	• During the stage the slab is rolled back-and-forth reduced to reduce the thickness ready for the finishing mill.
	• The material at this stage is referred to as transfer bar and is approximately 34mm thick.
Finishing Mill	• The finishing mill consists of seven consecutive pairs of rollers, each decreasing the material thickness.
	• The biggest percentage reductions are taken in the first rollers, decreasing with each consecutive pair until the material is around 2.8mm thick.
	• This operation refines the grain structure, this dictates the mechanical properties as well as reducing the product thickness.

	• For the automotive market product consistency is key, this is particularly important with regards to the texture of the microstructure to create predictable product formability.
Pickling	• The coil is passed through a liquid bath of acid, as a result hydrogen gas is produced which agitates the steel surface to remove any scale present.
	• This improves the surface quality of the strip, by removing oxides. this also improves the aesthetic appeal of the material which is important for the automotive market.
Annealing & Cold Rolling	• This stage is responsible for the ferrite and martensite phases indicative of a dual phase steel.
	• Precise heating and cooling is critical in an annealing cycle to produce the correct mechanical properties.
	• Cold rolling reduces the material to its customer defined final thickness as well and increasing the hardness of the material, which is critical for automotive applications.
Component Manufacture	• In this stage the sheet metal is formed into complex geometries, capitalising on the high formability made possible by the soft ferrite matrix.
	• Formed components are welded or bonded together to form the BIW for a vehicle.

1.4.2. Hot Mill

1.4.2.1. Slab Reheat

The role of the slab re-heat furnace is to fully normalise the slab into an austenitic phase, this removes as cast defects such as dendrite formations, as well as dissolve and alloying additions if required for the given grade. Other key considerations exist such as pacing control, surface quality and fuel usage[72]. There is a fine balance to be struck regarding the time the slab spends in the furnace and the temperature. The higher the temperature, the

more alloying elements are dissolved into the solid solution, decreasing the possibility of hard precipitates remaining in the slab. However, if the slab is left in for too long, the energy costs associated are higher in addition to this the thickness of the primary scale layer will also increase[73]. The slab reheat furnaces in Tata Steel's Port Talbot site have the unique ability to run on natural gas, which is purchased from the mains supply, or from coke oven gas (COG gas). The utilisation of COG gas reduces the plants reliability on natural gas, whilst utilising a waste product from the coke making process.

The reheat furnaces in Tata Steel Port Talbot's hot strip mill are walking beam furnaces. This configuration allows the slabs to move though the furnace on water cooled skids, travelling towards the roughing mill whilst increasing in temperature. The rate at which the slabs move through the furnace dictates the reheating time. The maximum speed a slab can travel through the 55m long furnace is 30m/hr.

The slab reheat furnace is situated after the continuous caster and before rough rolling. Slabs are heated to approximately 1250°C, this not only austenatises the grain structure but also softens the steel to reduce loads on the roughing mill. The amount of time a slab spends in the re-heat furnace depends upon the grade and the desired rolling temperature. In the case of DP grades where the slabs are transferred from the caster to the reheat furnace directly will spend less time in the reheat furnace, approximately two hours. Port Talbot utilises reheat furnaces for advantageous scheduling, reducing the time between finishing mill operations, increasing product output, as illustrated in Figure 16 by 'RHF A and RHF B'.
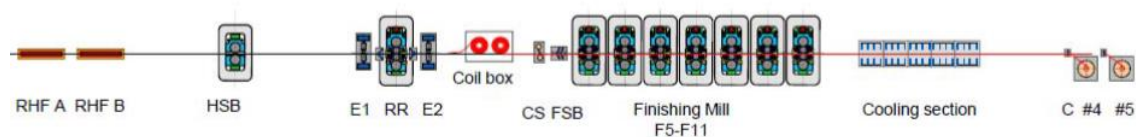
Figure 16- Tata Steel Port Talbot Hot Mill layout[72].

Temperature is controlled by an 'on-line' model which utilises plant data based upon slab surface temperature, emissivity values and time. This model is critical in correctly predicting slab core temperatures. The time each slab spends withing the reheat furnace is referred to as the soak time. Too short soak times result in undesirable microstructures, in the case of incomplete austenitisation in which pearlite or ferrite structures remain during hot rolling causing potentially high mill loads, with the possibility of increasing mill ware

and downtime. Too long of a soak time reduces production rate and increases energy costs therefore increasing plant running costs. As such optimisation of the model has been undertaken by D. F. J. Staalman and colleagues in which emissivity values were adjusted from previously empirically calculated values, therefore reducing the accuracy spread from 30°C to 15°C on average[72]. Further improvements have since been implemented though the implementation of laser pyrometers which accurately measure strip temperatures, this too has led to reported energy usage reductions[74].
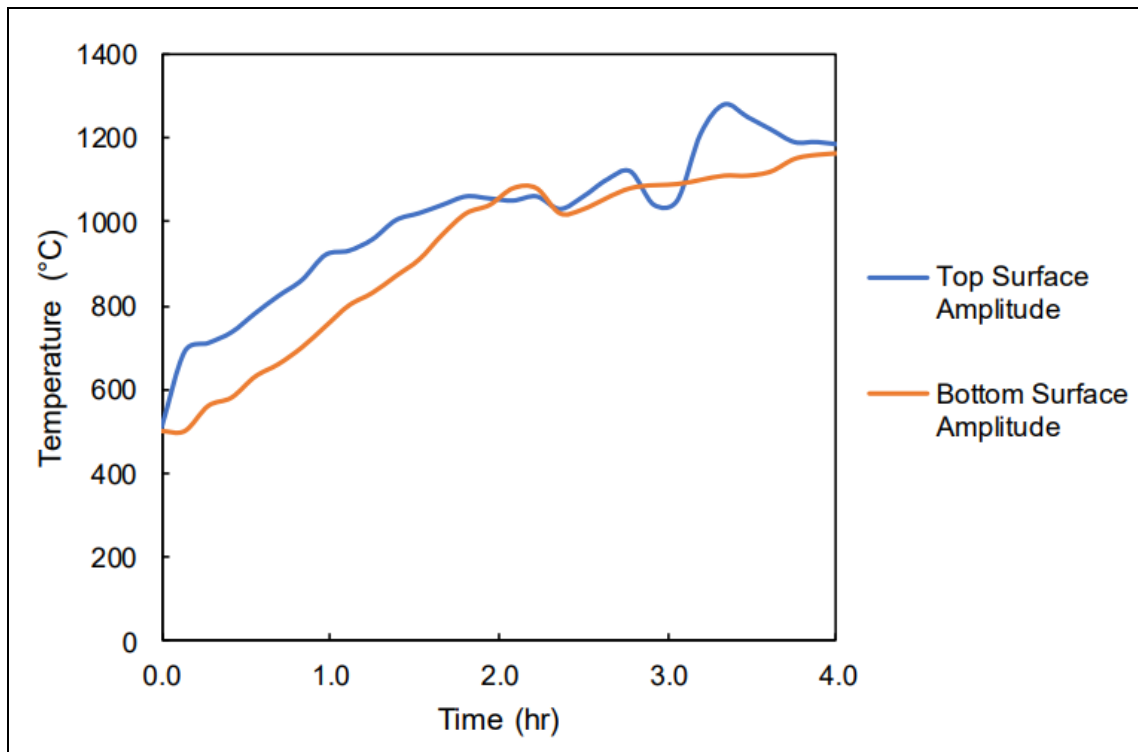
Figure 17- Plant data for a typical slab entering the reheat furnace[75].

Figure 17 shows the top and bottom temperatures for a slab entering the re-heat furnace, over a described time period. This reheat schedule is typical for most slabs, however the conditions prior to this are highly varied due to the slab yard schedule implemented. As such the temperature profile of any given slab can vary depending upon weather conditions, scheduling and the arrangement of the slabs in the yard, especially if they have been stacked. In some cases, such as DP800, slabs do not enter the coil yard and are transported directly from casting to slab re-heat, significantly reducing reheating times. This is known as a "hot-connect".

A PhD thesis by K. A. Guy investigating the 'clinking phenomena' associated with slab fractures in the slab yard, as such temperature profiles were modelled based upon extreme

case studies of slabs with varying 'journeys' thought the manufacturing route[75]. Four cases in total are presented, and the resultant internal stresses are presented, in the case of this research the stresses are not relevant, but the temperature profiles are since these will dictate the grain structure upon entry to hot rolling, and therefore potentially affect the microstructure downstream.
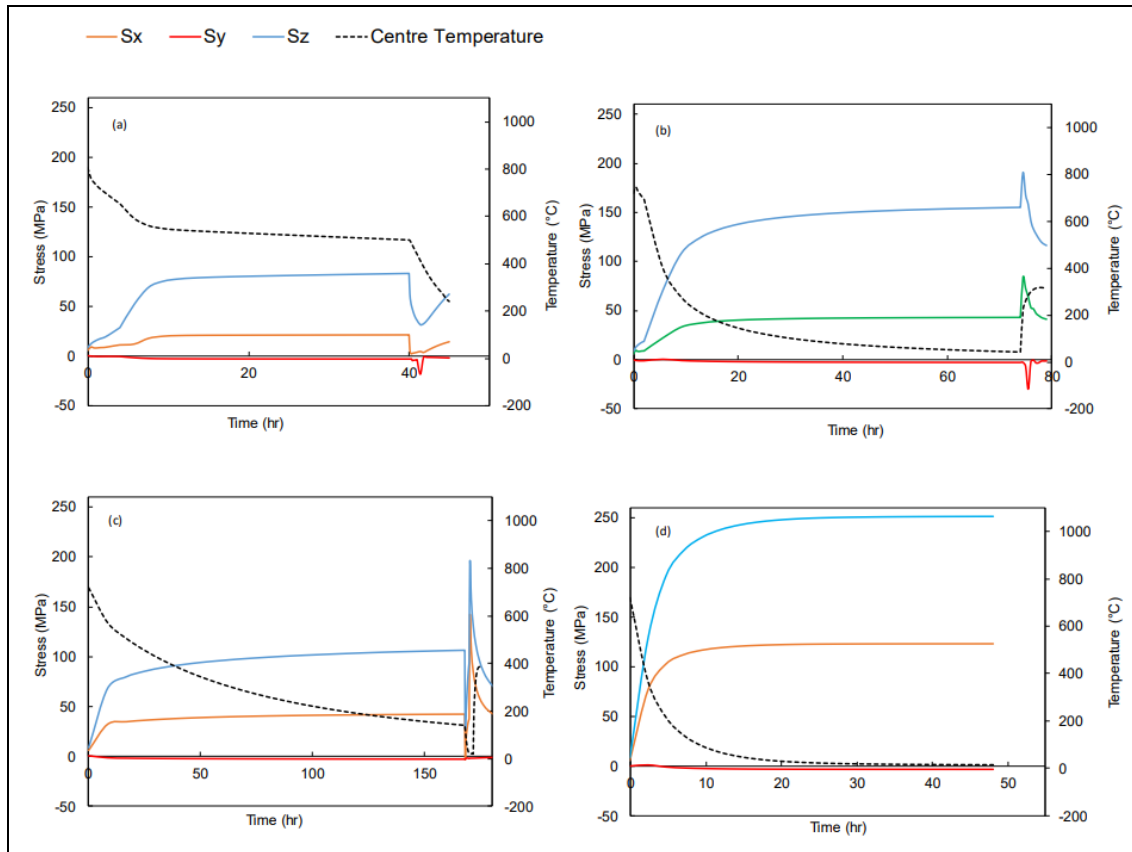
Figure 18- Variation in temperature profiles experienced by various as cast slabs, prior to entering re-heat furnace. Temperature data provided from plant, as cast microstructure assume a grain size of 500μm, Case 1 is top left, case 2 top right, case 3 bottom left and case 4 bottom right[75].

Figure 18 illustrates the four cases, core temperature data is of interest here, as well as initial as-cast grain size which was assumed to be 500μm. Notice that the variation in time spent in the coil yard can vary greatly, between 45hrs and 150hr in the above cases presented. The above plots are simulations of core temperatures for the slabs, however it should be noted that the temperature is lower closer to the surfaces and therefore microstructural properties will not be representative of the core temperature in this case. This temperature data will be key in assessing the variation in as received grain structure by the hot mill, and therefore downstream properties.

Research by Kundu into predicting the grain size of microalloyed steel grades, at the re-heat stage, found that at a temperature of 1225°C the mode grain size was 160-180µm. However heating to 1150°C results in a bi-model grain structure of 220µm and 41µm in finer areas, due to variations in temperature distribution in the furnace[76]. This shows the importance of temperature control at the slab reheat furnace stage both industrially and experimentally.

1.4.2.2.   Rough Rolling

The primary function of rough rolling is the drastically reduce the material thickness to an appropriate gauge such that it can be processed by the finishing mill. Thicknesses are reduced from a cast slab to around 34mm, in the case for DP800 automotive grade. Unlike the finishing mill the roughing mill consist of a single pair of rollers that incrementally move closer together, with the strip passing back-and-forth between them. Since large thickness reductions are experienced by the strip the length of the strip increases considerably.
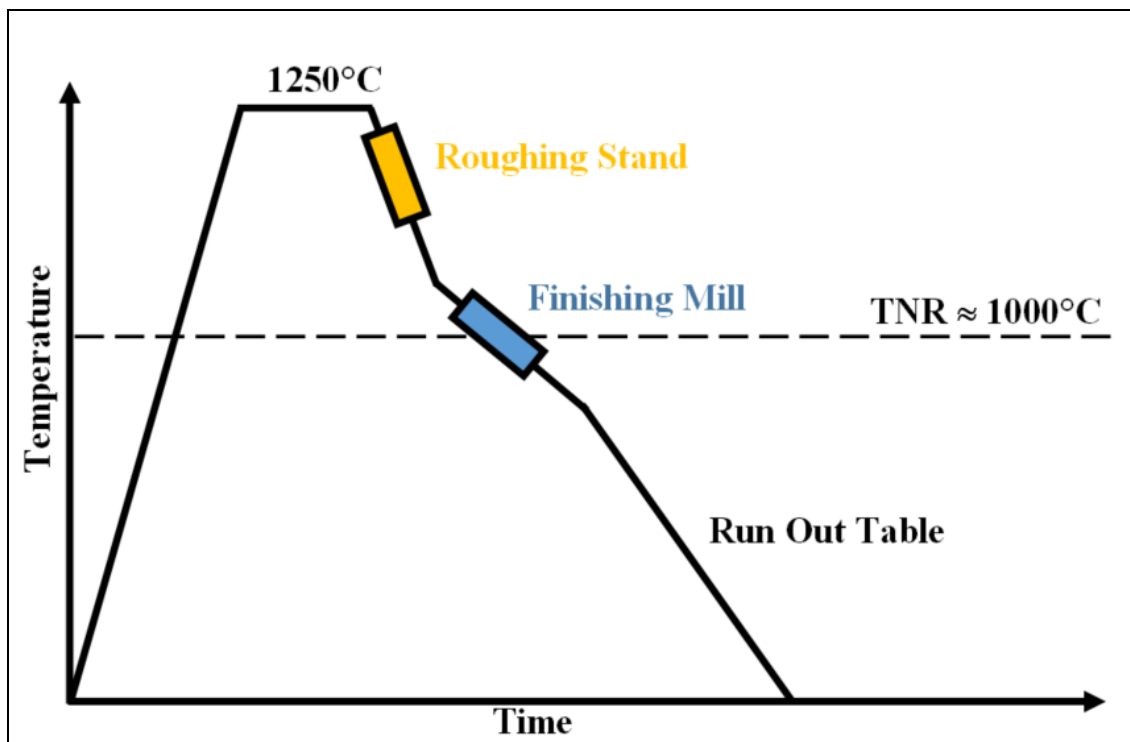
Figure 19- Illustration of temperature path for Roughing Mill and Finishing Mill.

Figure 19 illustrates the key temperatures that both rough rolling and finishing rolling occur. The T_{NR} is a key temperature to consider during hot rolling operations. Rolling either above or below this temperature has a large influence on the microstructure, especially on the aspect ratio of the grains below T_{NR}. The T_{NR} will vary as a function of chemistry and strain and therefore varies plant to plant even for the same grade[77]. However, for Tata Steel's DP800 grade T_{NR} is experienced during the finishing mill, therefore full dynamic recrystallisation occurs during the roughing mill stage. The grains are compressed, such that they are no longer equiaxed, but recrystallise into an equiaxed form between passes, but are refined, decreasing the austenite grain size. The degree of grain refinement at any rolling stage is a function of rolling parameters, such as percentage thickness reduction (strain) and chemical composition[78]. In this stage the grains should ideally be fully equiaxed and free of internal strains however the grain stricture at this stage isn't likely to have a significant degree of influence on the microstructure downstream due to the large reductions conducted in the finishing mill[73]. Once the material has been rough rolled, it is commonly referred to as 'transfer bar'.

1.4.2.3.   Coil Box

The Coil Box is a fairly unconventional addition, not common amongst many hot strip mills. Installed in the late 80s the coil box acts as an accumulator. This prevents bottlenecking in the processes since when the strip is rough rolled the length increases significantly. Figure 20 shows the location of the coil box in Tata Steel Port Talbot's hot strip mill line
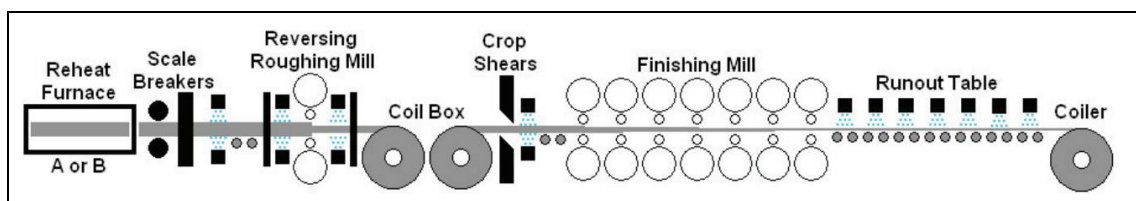
Figure 20- Diagram of the assets involved in the hot rolling process from slab to hot-band coil[79].

The presence of the coil box allows for the material to be accumulated before entering the finishing mill, which another slab can be simultaneously undergo rough rolling, see Figure 16. The coil box also has the added advantage of homogenising the strip temperature along the length, this increases the predictability of the loads experienced on the finishing mill as a result of strip temperature and its influence on the flow stress of the material. Finally prior to entering the finishing mill the ends of the coil are removed on the Crop Shear, this

'squares-off' the ends of the coil for better product shape, as well as improving the roll bite in the finishing mill.

Figure 21- A coil of 'transfer bar' on the coil box awaiting entry into the finishing mill[80].

1.4.2.4. Finishing Mill

The finishing mill is of particular interest to this research. Located after the roughing mill, here the material undergoes thickness reductions from 34mm to approximately 2.8mm depending upon the grade and requirements. The finishing mill at Tata Steel Port Talbot consists of seven roller stands, as shown in Figure 22.

Figure 22- Tata Steel Port Talbot finishing mill stands, with replacement rolls ready for changing to minimise mill down time.

At the entry of the finishing mill the steel consists of a fully Austenitic phase. In the first few passes the steel undergoes grain refinement via a mechanism of dynamic recrystallization in the reductions above the T_{NR}. Below however the grains undergo pancaking and are no longer equiaxed, as illustrated by Figure 23.

The degree of grain refinement is critical in determining the transformation kinetics on the Run Out Table, since ferrite tends to nucleate at the Austenite grain boundary, therefore the degree of refinement will increase the degree of initial Ferrite nucleation. Hot rolling is not only useful to simply reduce the net thickness of the material for processing, but rather an essential tool for grain refinement.
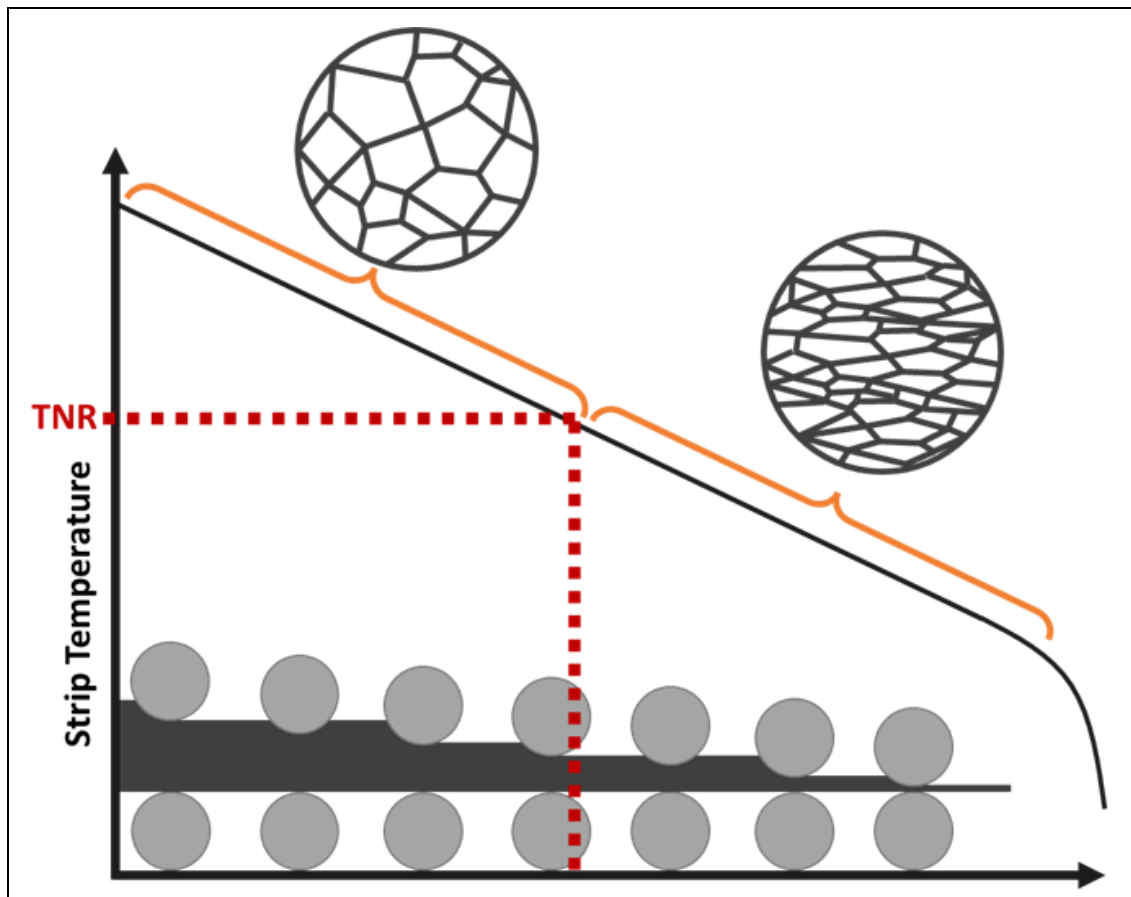
Figure 23- Illustration of nominal microstructural development on the finishing mill.

In addition to the net thickness reductions, the speed of the strip must also be carefully controlled, however both are inextricably linked through the conservation of mass since the length of the strip increases though the mill as thickness is reduced. The rotational speed of each roller stand is carefully controlled through an on-line computational model, this is key to preventing processing issues such as buckling of the strip, often referred to as a 'cobble'[73]. A cobble is the resultant 'pile-up' of strip material between rollers as a result of inappropriate roller speeds or insufficient roll bite, as shown in Figure 24.

Figure 24- Example of hot mill 'Cobble'[81].

This is a costly mill failure, which may damage production assets as well as cause significant down time resulting in further economic losses and therefore should be avoided at all costs.

Rolling loads are also a factor that must be considered carefully during the hot rolling process. This is particularly apparent in the case of AHSS grades, such as DP, where relatively high alloy additions result in higher mean flow stresses and therefore higher rolling loads[77]. Increased rolling loads result in increased roll wear, which results in increased maintenance frequency, driving up costs. It has also been reported that, for a DP grade, reducing Si additions resulted in decreased loading and increased dimensional control[82]. This illustrates the relationship between product chemistry and rolling parameter outputs, such as load. However the scope of this project is not to modify product chemistry, but rather the thermomechanical treatment however the effect of product chemistry must be carefully considered. The finishing mill at Port Talbot also has the ability to cool the strip during rolling. This is known as 'inter-stand cooling'. The purpose of this water cooling capability is to carefully control the strip temperature, as well as clear the strip of scale such that the scale does not get 'rolled into' the surface of the strip, potentially resulting in surface defects. This allows for real time adjustment of the strip temperature such that a fine balance between adequate rolling loads and an appropriate level of grain refinement can be struck.

1.4.2.5.   Run Out Table

1.4.2.5.1.   ROT Layout and Background

The ROT (Run Out Table) is the biggest driver of hot band transformation in the steel making process. The now hot rolled steel sheet travels on a roller conveyor and is actively cooled by water jets (often referred to as 'water headers') from above and below the strip, as shown in Figure 25. The steel reaches the ROT with a temperature between 800°C and 1000°C, depending on grade and requirement, upon which water cooling will occur resulting in a strip temperature between 600°C to 700°C, again depending upon the grade/chemistry. The cooling path is critical in driving appropriate transformation, to result in desired phase volume fraction, and more importantly to avoid unwanted harder phases that can be problematic for downstream processing such as coiling and cold rolling.
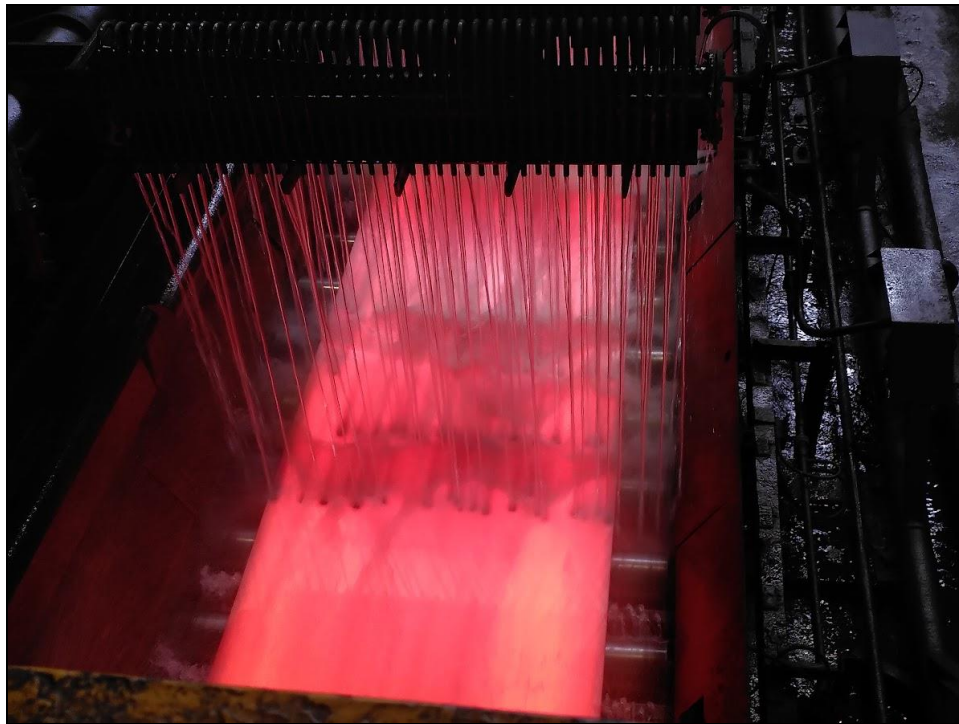
Figure 25- A photo taken from a gantry above the ROT at Tata Steel Port Talbot.

In the case of DP800, at Tata Steel Port Talbot, the desired microstructure is a combination of pearlite and ferrite, not that this is not the final microstructure of DP steel (martensite, dispersed in a ferrite matrix) since this will be achieved in the annealing process. The aim for microstructure at this stage of the manufacturing process is product consistency, quality, and formability. It is essential that the UTS does not become too high such that the product cannot be coiled and cold rolled, which can be challenging for highly alloyed

grades such as DP800, which tend to transform more slowly due to the presence of precipitate formers. This transformation is therefore dictated by the time temperature relationship experienced by the strip, which is a function of the amount of volumetric flow provided by the ROT water headers and the strip speed. The strip temperature varies to some degree within the manufacturing process, therefore an 'on-line' model is utilised to control strip temperature. This measures the strip temperature at the beginning of the ROT, and at three more points along the length of the ROT, and adjusts the cooling through the use of 'Trim Headers' to 'course correct' the strip temperature, in order to deliver the correct transformation as well as an appropriate CT (Coiling Temperature).
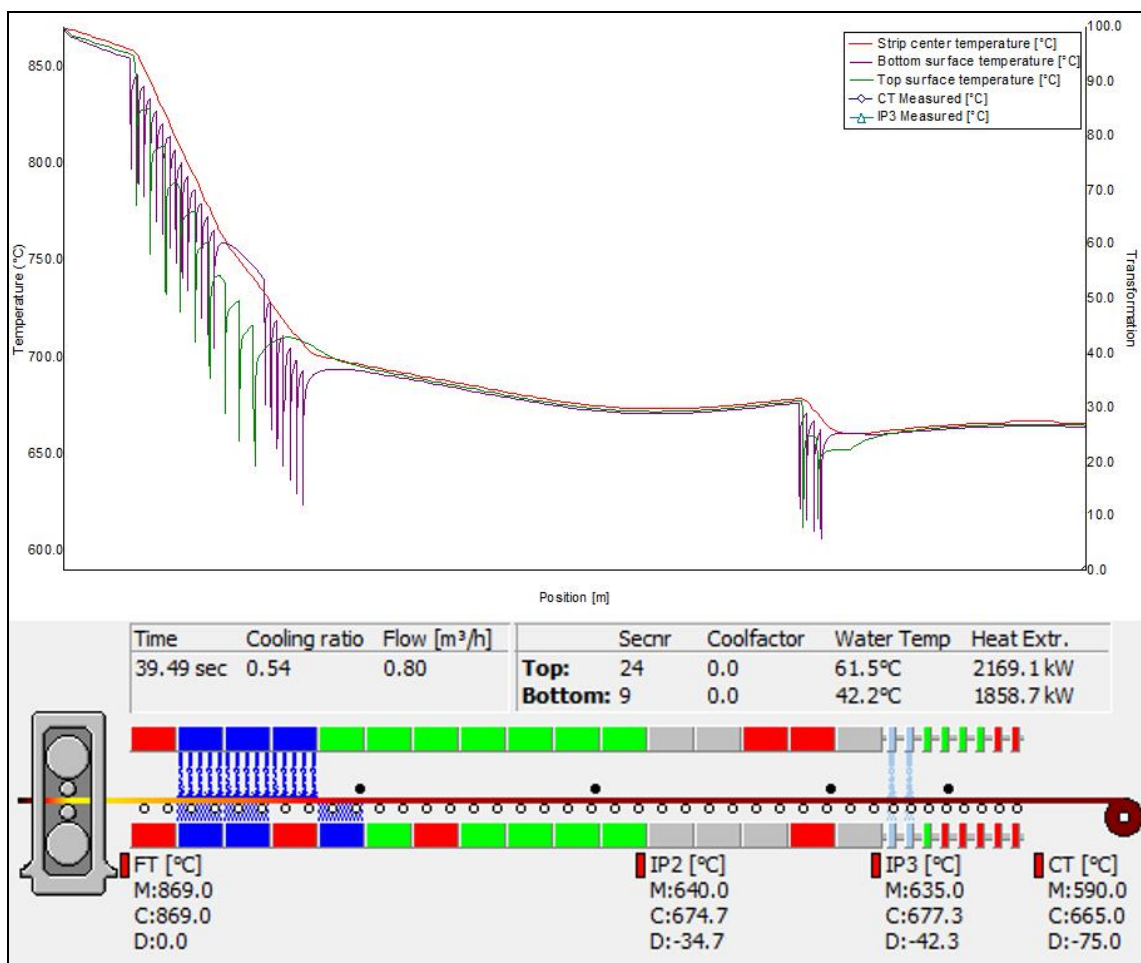
Figure 26- Titan output of a Position-Temperature relationship for a DP800 coil.

With reference to Figure 26 which shows the temperature of the strip, relative to its position on the ROT, as well as the number of headers utilised in the graphic below the graph. The trim headers are shown on the right of the ROT, detailed in a lighter blue shade, to illustrate the relatively low flow rate compared to the 'main' headers. 'FT', 'IP2' and

'IP3' denote the measured temperatures recorded on the ROT to calculate and control the cooling required to achieve a target coiling temperature (CT), and therefore desired microstructure.

1.4.2.5.2. Dynamics of Water Cooling

The degree of cooling experienced by the strip is broadly a function of the volume of water delivered to the strip surface, and the heat transfer coefficient is greater where larger volumes of water are used, generally. However the calculation of the heat transfer coefficient is complicated and is a result of the interaction between the point of impingement of the jet and the steel surface, as such this interaction has undergone extensive study[83-86]. Broadly the heat transfer coefficient is higher at the point of impingement of the water jet, and inversely the resultant temperature is less at this point, as shown in Figure 27.
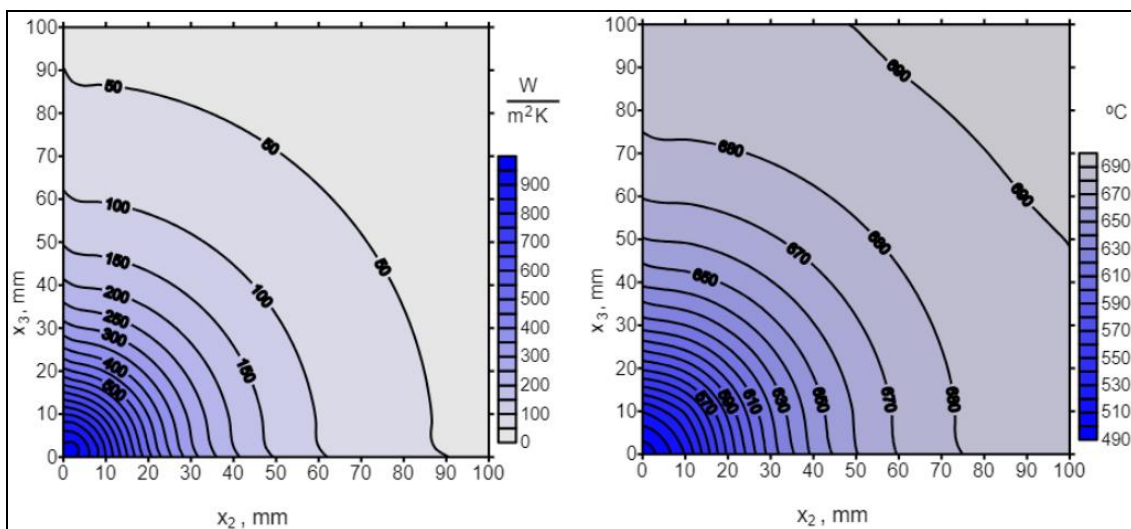
Figure 27- Heat transfer coefficient (left) and temperature (right) distribution as a function of radius, from the point of water jet impingement[83].

When considering the coefficient of heat transfer due to water cooling, the Leidenfrost effect must be considered. The Leidenfrost effect can be described as the phenomenon of a volatile liquid levitating on a vapour layer, when in contact with a very hot solid[87]. This phenomenon is commonplace on the ROT, and is also a simulated mechanism within the Titan software. An illustration of the Leidenfrost effect is shown below in Figure 28.
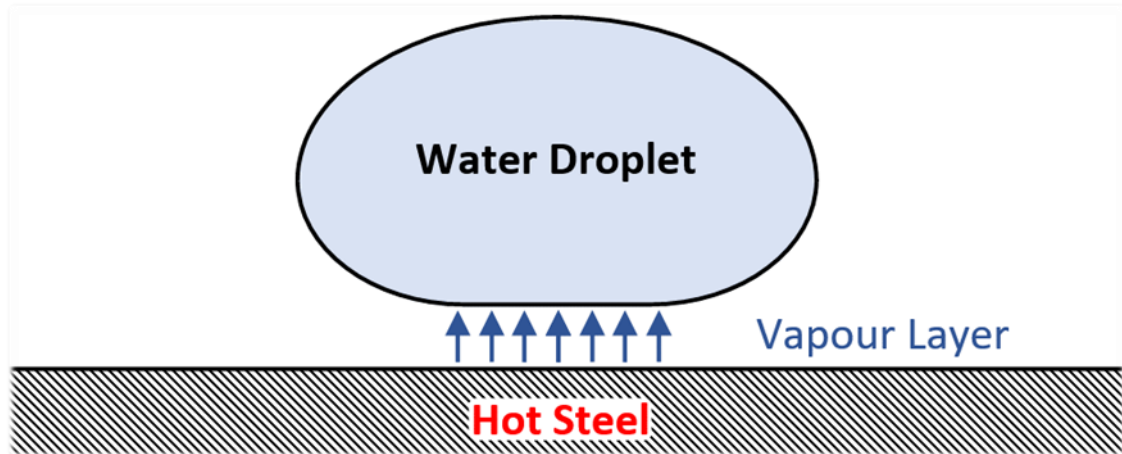
Figure 28- Illustration of the Leidenfrost Effect.

This affect limits the amount of evaporative cooling available to the strip since the water layer is 'protected' by the vapour layer. Modification to this phenomenon, via oxide formation, can have a great effect on the cooling of steel strip, as studied by O. Resl and colleagues[88]. It is therefore key that this cooling mechanism be understood when modelling, experimentally and computationally, ROT cooling operations.

1.4.2.6.   Coil-Box and Coil Yard

1.4.2.6.1.   Down-Coiler Layout and Background

The Downcoiler, situated at the end of the   ROT plays some role in the formation of the hot-band microstructure, especially in the case of AHSS steel, which transform more slowly compared to other lesser alloyed grades. In the case of DP800, at Tata Steel Port Talbot, this operation can occasionally result in undesirable phases, this will be elaborated upon in more detail in section 1.4.2.6.2. The primary role of the Downcoiler is to simply accumulate material and alloy it to be transferred to the coil yard for storage and later processing, depending upon scheduling requirements, an example of a Downcoiler can be seen below in Figure 29.

Figure 29- Photo of a Downcoiler accumulating hot rolled strip[89].

The coiler consists primarily of a mandrel, this is the central shaft which the coil wraps around, this is driven to apply tension to the coil to ensure a tight coil. At the end of the coiling process the coils are removed from the mandrel and sent to the coil yard, where they cool to ambient temperature, or when the product does not require annealing or cold rolling, they can be sent to the customer as a hot rolled product.

1.4.2.6.2.   Coil end Effects

Due to the highly alloyed composition of DP800, the transformation of the strip on the ROT can be when compared to other lower alloy grades. As a result, the strip is not fully transformed once it contacts the coiler, therefore the strip continues to transform during the coiling process. The result is that undesirable bainite formations occur at the head and tail end of the coil. The head end of the coil is the first to contact the mandrel, which is at a comparably lower temperature than the strip, and as a result the head end of the strip is subject to a high cooling rate. Once the coiling process is complete the hot coil is transported to the coil yard, the inner laps of the coil are insulated from the ambient

cooling by the outer laps, as a result the outer lap also undergoes a high cooling rate. As a result, bainite formations are present both the head and tail of the strip increasing the strength of the steel in these areas significantly. Because of this the head and tail end must be removed prior to cold rolling an annealing, in order to protect the cold mill from excessive loads. If these sections were to be used it would result in increased wear on the cold mill and possible costly breakdown. As a result it was deemed more cost effective to remove these coil ends, and have them remelted as internal scrap.

Other research has been conducted into coil cooling of strip steel. Once such example by N. Legrand and colleagues, in which a model was created for coil cooling to mitigate issues with product shape and mechanical properties[90]. This data was gathered though the use of a thermal imaging camera, tracking the temperature from multiple angles, as shown in Figure 30.
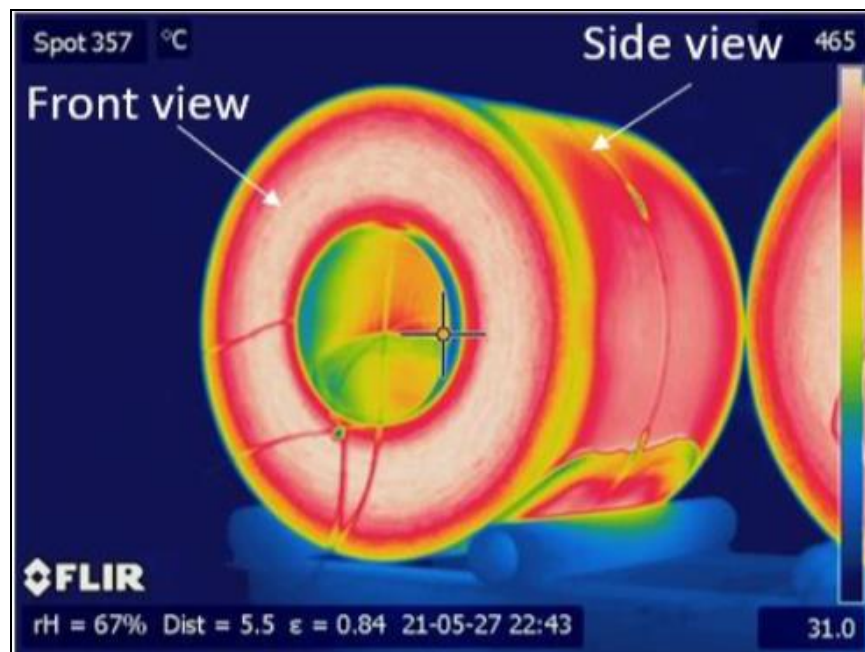
Figure 30- Thermal camera images taken from the study into coil cooling by N. Legrand and colleagues[90].

The conclusion of the trial was that central laps, within the body of the coil stay significantly warmer than the outer and core of the coil. The edges of the coil also experience higher cooling rates. Lastly the temperature gradient of the coil, through the cross section, can be considered axisymmetric[90].

With reference to the processes at Tata Steel Port Talbot; at the time of writing around 15-20% of each DP800 coil must be removed due to coil end effects. This is costing around

£50-£100/tonne with annual volumes of around 10-15kt. Therefore, the lost value is in the region of £0.5-£1.5 million. This can be compounded with the energy costs of remelting the wasted hot band coil, as well as increased CO_2 emissions. In the creation of an optimised DP800 model, will allow for investigation into possible methods for eliminating this issue, or mitigating it with the aim of reducing waste, this was one of the driving incentives behind the conception of this project.

1.4.2.7.   Cold Rolling

Cold rolling, as the name suggest, is rolling at comparatively lower temperatures to hot rolling. Similarly, to hot rolling, the purpose of cold rolling is to reduce the product thickness. Cold rolling takes place below the TNR, and therefore dynamic recrystallisation does not take place, however the temperature of the strip will increase to some degree due to the adiabatic heating due to strain. The mechanical strength of the strip will increase due to cold rolling, but will display anisotropic properties due to the 'pancaking' of the grains, as shown in Figure 31. This increase in strength is due to work hardening of the steel, which causes the UTS to rise significantly but will result in poor ductility[91].
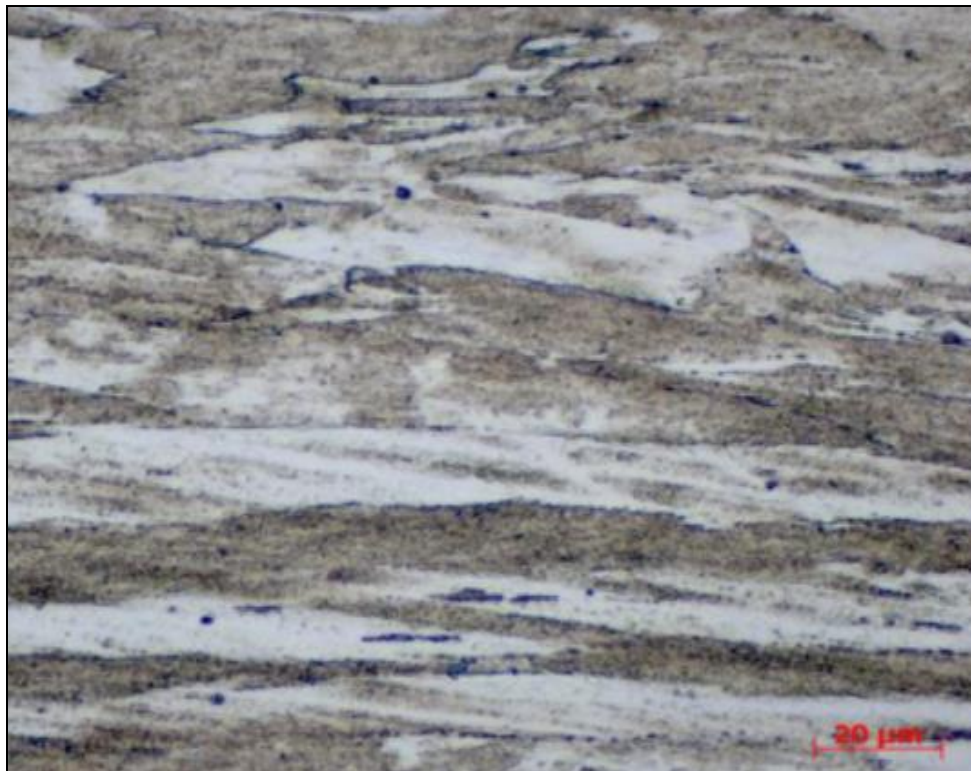
Figure 31- A micrograph of cold rolled IF steel, with a 90% thickness reduction[91].

In a post-cold rolled state the steel's ductility is far too low for body panel forming operations, due to the stresses accumulated at the grain boundaries from the strains imparted through rolling, therefore the strip must be reheated through the annealing process.

1.4.2.8. Continuous Annealing

The CAPL line (Continuous Annealing Process Line) was installed in Port Talbot in June 1998, and performed the annealing operation of steel strip in a comparatively short time, compared to batch annealing[92]. Due to this advantage the continuous annealing mechanism is the predominant method of strip annealing globally. Fundamentally annealing consists of three key stages, which are common to both continuous and batch annealing, these are;

1. Heating to a desired temperature- normally above the recrystallisation temperature, to facilitate grain growth.
2. Holding (soaking)- The holding time at the desired temperature will facilitate the degree of grain growth.
3. Cooling- The rate of cooling is key to ensure the desired microstructure is achieved, and therefore mechanical properties[9].

Tata Steel's DP800 steel alloy, as is the case will all DP steels, obtains its dual phase microstructure from the annealing stage. Therefore, it is essential that the heating and cooling pathway be carefully controlled such that the desired grain size and transformation occurs. Figure 32 shows a typical time temperature relationship for a DP800 steel in the annealing cycle. Stage one occurs at 0-300s, at 800°C, where stage two takes place, and the strip is held at this temperature for approximately 150 seconds. Lastly it is cooled in a stepped nature, initially to approximately 300°C, and then finally to ambient temperature. This process in conducted in a controlled atmosphere to reduce oxidation, commonly a mixture of nitrogen and hydrogen.
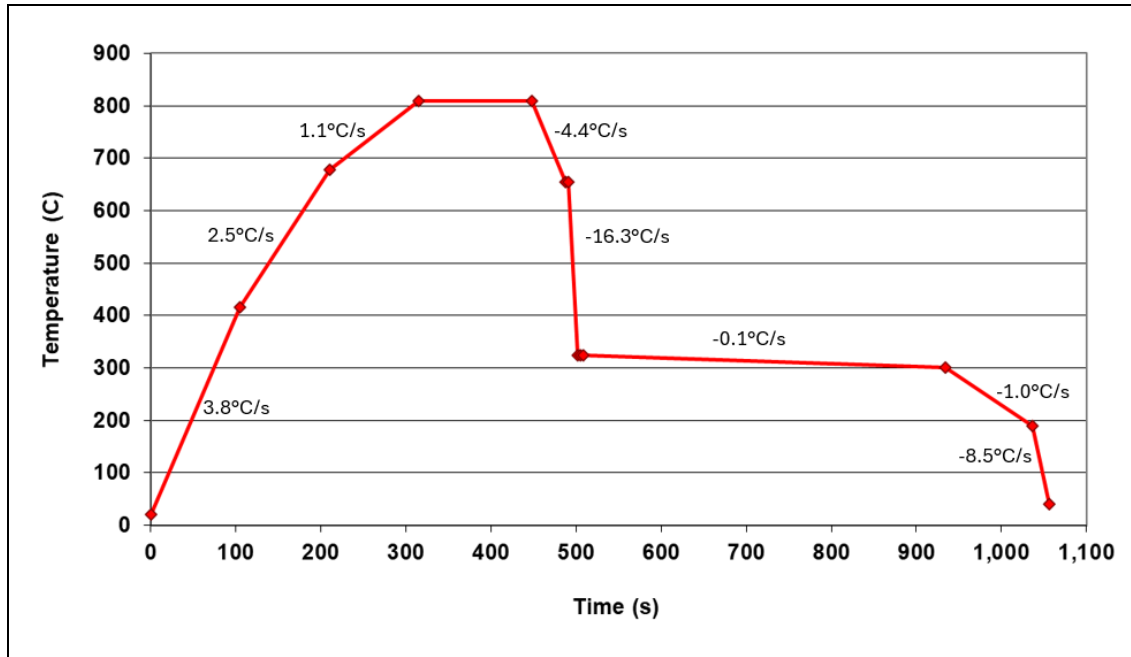
Figure 32- DP800 time-temperature relationship for an annealing cycle with heating and cooling rates..

1.5. Steel Manufacturing at the Laboratory Scale

1.5.1. Literature on Lab Scale Rolling and ROTs

Small scale, or lab scale hot mills area useful tool in the simulation of industrial hot rolling steel applications, so much so that commercially available setups are now available for purchase with experimental production in mind[93-95]. Custom one-off setups are also commonplace, such as the 'Lewis Mill' and ROT at SAMI are commonplace among other materials research institutes. Some work, internal to Tata Steel UK has been carried out in optimising this asset previously. Such as that conducted by F. Mohammed, within Tata Steel's R&D department, on this particular mill and ROT configuration, investigated the relationship between ROT velocity and plate thickness on the CT[96]. F. Mohammed tested 2, 3 and 4mm plates at a number of ROT speed settings, ranging from 1 (0.12 m/s) to 8 (0.76 m/s). This investigation will be analysed an expanded upon in the optimisation of SAMI's laboratory practices.

Similar research to this has been carried out in order to trial new alloy blends or optimise thermo-mechanical treatments, as well as optimise cooling parameters all at a smaller scale. One such example of an experimental is described in a publication by T. Taylor and colleagues[97]. Taylor presents a novel method of in situ temperature measurement, by which various input parameters are outlined such as; reheat furnace temperature, rolling

speed, roll gap, mill entry temperature, ROT water pressure, ROT water flow rate, ROT water temperature and coiling temperature. The results of these inputs are quantified the affect these have on relevant outputs such as; mill load, mill torque, mill speed, strip temperature, gauge, shape, mechanical properties, and microstructure are evaluated. From this a comprehensive numerical model was created. This level of accuracy was able to be implemented due to fine levels of control being implemented over these input parameters. Some of these include pressure regulated water headers and digitally controlled ROT and roller speed. These features are currently not available on the 'Lewis Mill' laboratory setup at SAMI, and hence measures must be taken in order to mitigate and resultant inaccuracies/ unpredictability from a more 'analogue' system.

Taylor also tackles a common problem within laboratory hot rolling: the difference between strip core temperature and surface temperature. This challenge is important in the laboratory setting and the industrial setting, since the surface temperature is often less than the core, due to ambient cooling. However the core temperature is critical in predicting microstructural evolution, particularly in ROT cooling operations. For practical reasons surface temperature is the only realistic option in a continuous manufacturing operation, and therefore infrared pyrometers are often implemented. However such pyrometers can be effected by surface water, and oxide scale which affects the emissivity of the material contributing to inaccuracies in temperature measurements. For this reason Taylor evaluates the difference in surface temperature and core temperature by embedding thermocouples within the experimental strip as illustrated in Figure 33.
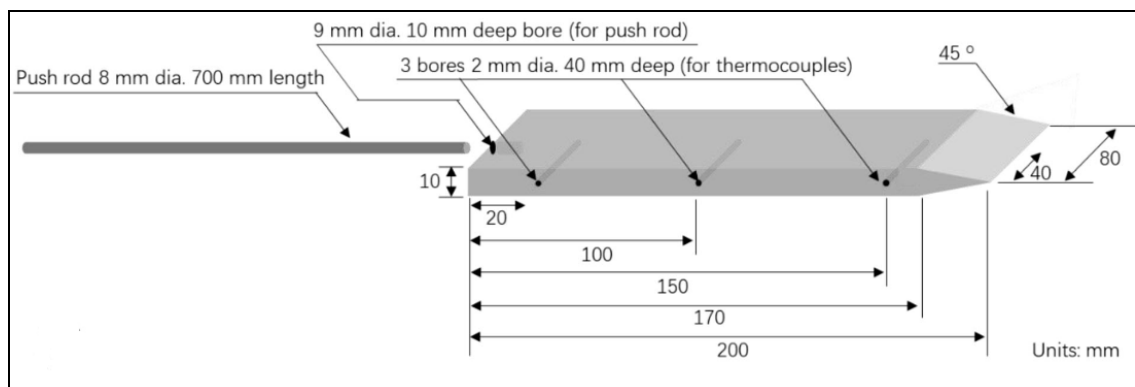
Figure 33- Novel method for strip temperature measurement at several locations for laboratory scale ROT operations[97].

This novel method proved useful for accurately measuring strip internal temperature, note the tapered nose of the sample to assist in the roll bite reliability. This novel method also allows for measurement at the head, tail and middle of the strip, this too could also prove to be a useful tool in modelling and mitigating coil end effects (see section 1.4.2.6.2).
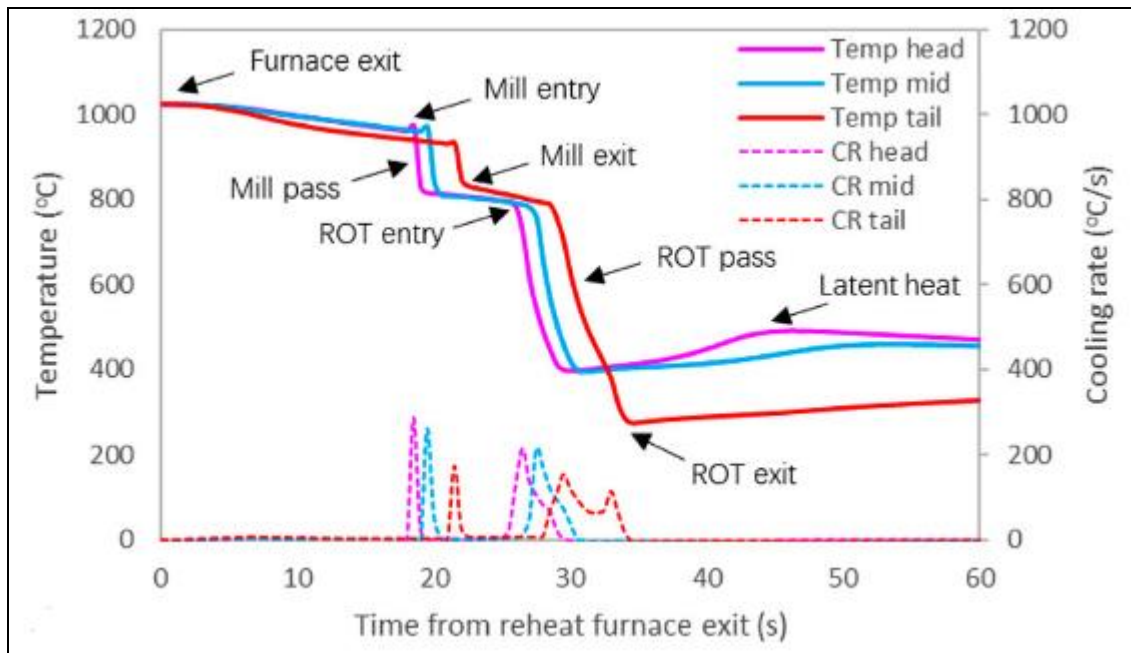
Figure 34- Sample temperature profile, against time, for Head, Tail and Middle thermocouples[97].

Figure 34 shows the time temperature profile for a given sample, and the variations in the head, tail and middle of the sample. This a key example of how strip temperature can vary, and again will be useful in modelling and mitigating coil end effects.
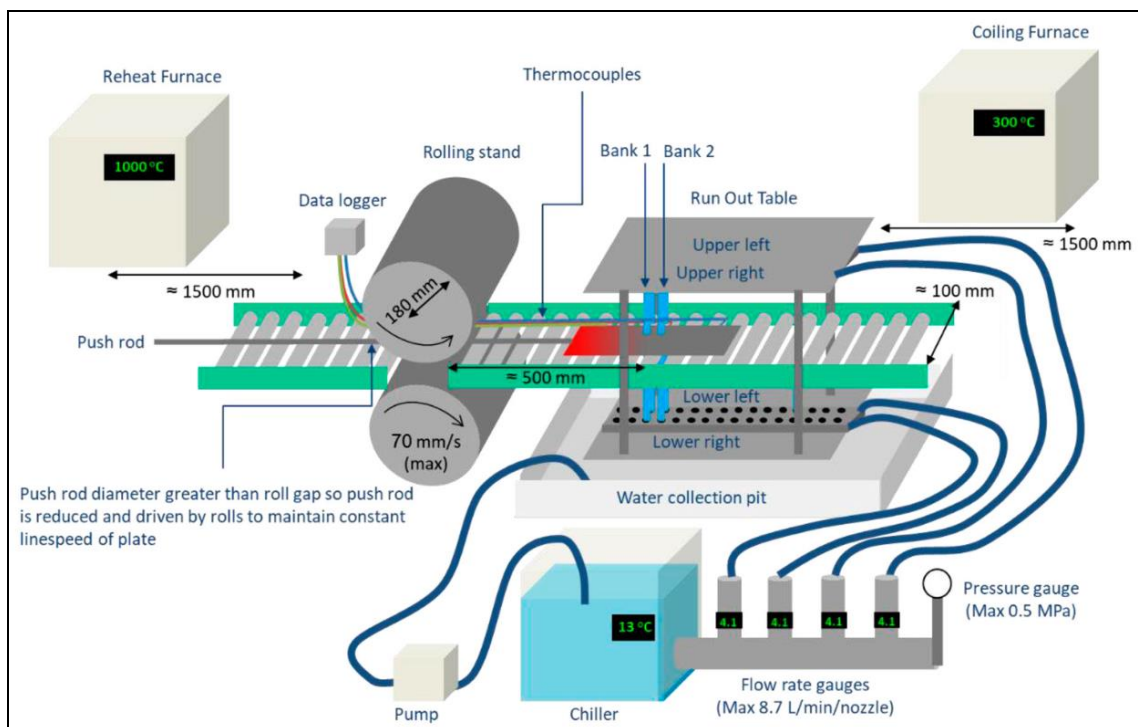
Figure 35- Diagram of experimental finishing mill setup[97].

A critique of the experimental setup described above would be the presence of only one roller stand, as shown in Figure 34. This may result in non-representative grain size and aspect ratios, when compared to a plant hot mill, which will have multiple roller stands

such that strain is being imparted into the sample above and below the T_{NR}. However single pass setups are advantageous since, and inherent issue with laboratory setups is the rapid temperature loss that the sample undergoes due to its lesser volume to surface area ratio. As a result, consecutive roller passes may result in significant temperature loss, again reducing the degree to which the study is representative of a plant scale.

Research has also been conducted at the laboratory scale in order to replicate certain industrial challenges. A paper published by Okada and colleagues investigated red scale formation on the surface of steels with varying percentage weights of silicon[98]. This was achieved by replicating plant process parameters on a laboratory scale hot mill, as shown in Figure 36.
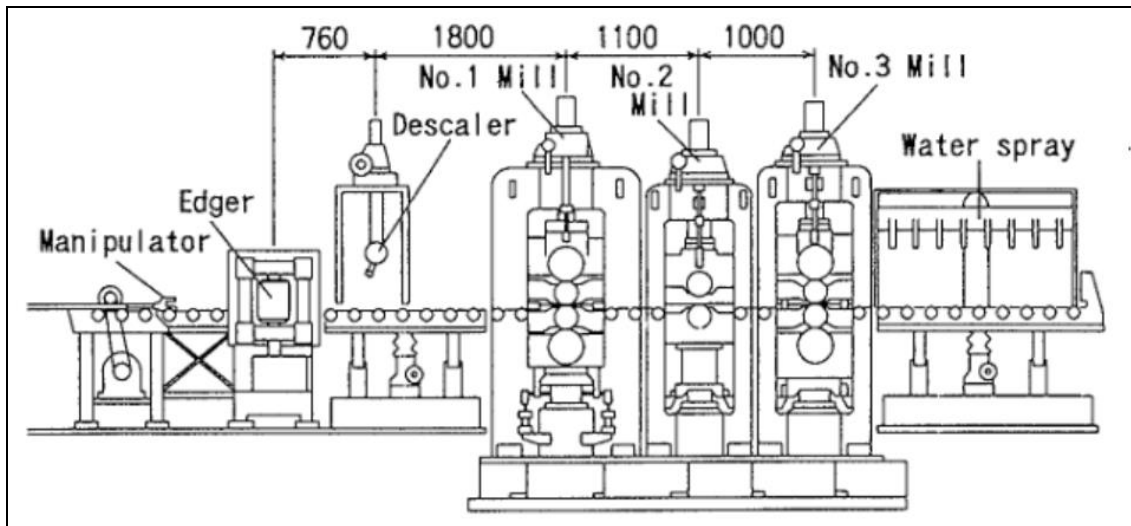
Figure 36- Diagram of Okada and Colleague's experimental setup[98].

Similarly to Taylor and colleagues' setup, this consisted of two electric furnaces, however differed in having three pairs of tandem rollers. The 1st furnace (to simulate slab re-heat) also has the added benefit of purging the chamber with a gaseous mixture of N_2, CO_2 and H_2O to accurately simulate the internal conditions of a plant slab reheat furnace. This is particularly important for replicating surface oxide formation. Okada was able to accurately replicate the formation of red scale, as well as propose measures to mitigate its formation in the future, at an industrial level. This study perfectly illustrates the capability of a laboratory hot mill to simulate industrial challenges, as well as design propositions to mitigate such challenges.

1.5.2. RAP Produced (40g)

This section details the assets and process used by Mach1 (a research institute within Swansea University) in the rapid manufacture of prototype alloys from casting to the

finished product. Although this research focuses solely on the manufacture of 'hot-band' material, the full process has been detailed here for the sake of completeness and context. A publication written by D. Farrugia and colleagues documents the full process in more detail[99].

Initially the constituent elements are weighed out in a powder form, they are subsequently compacted to reduce porosity. The powder mix is then placed into an induction coil such until the mixture is fully liquidus, where it is then left to cool. At this point the cast can be sectioned to investigate the as cast microstructure to ensure it is suitable for hot rolling and perform OES to measure the accuracy of the chemical additions.

The samples is then homogenised at the desired temperature, usually in excess of 1000°C for the desired time period. It is then removed from the furnace via single pass rolling to the desired 'hot-band' thickness.

To model the CAPL process at Tata Steel Port Talbot, heat treatment processes can be undertaken in either a vacuum or inert atmosphere via and electronically controlled furnace. Finally the product can be cold rolled in a small laboratory mill to give the desired mechanical properties. The mechanical properties and microstructure are then evaluated to assess the impact of the experimental product chemistry.
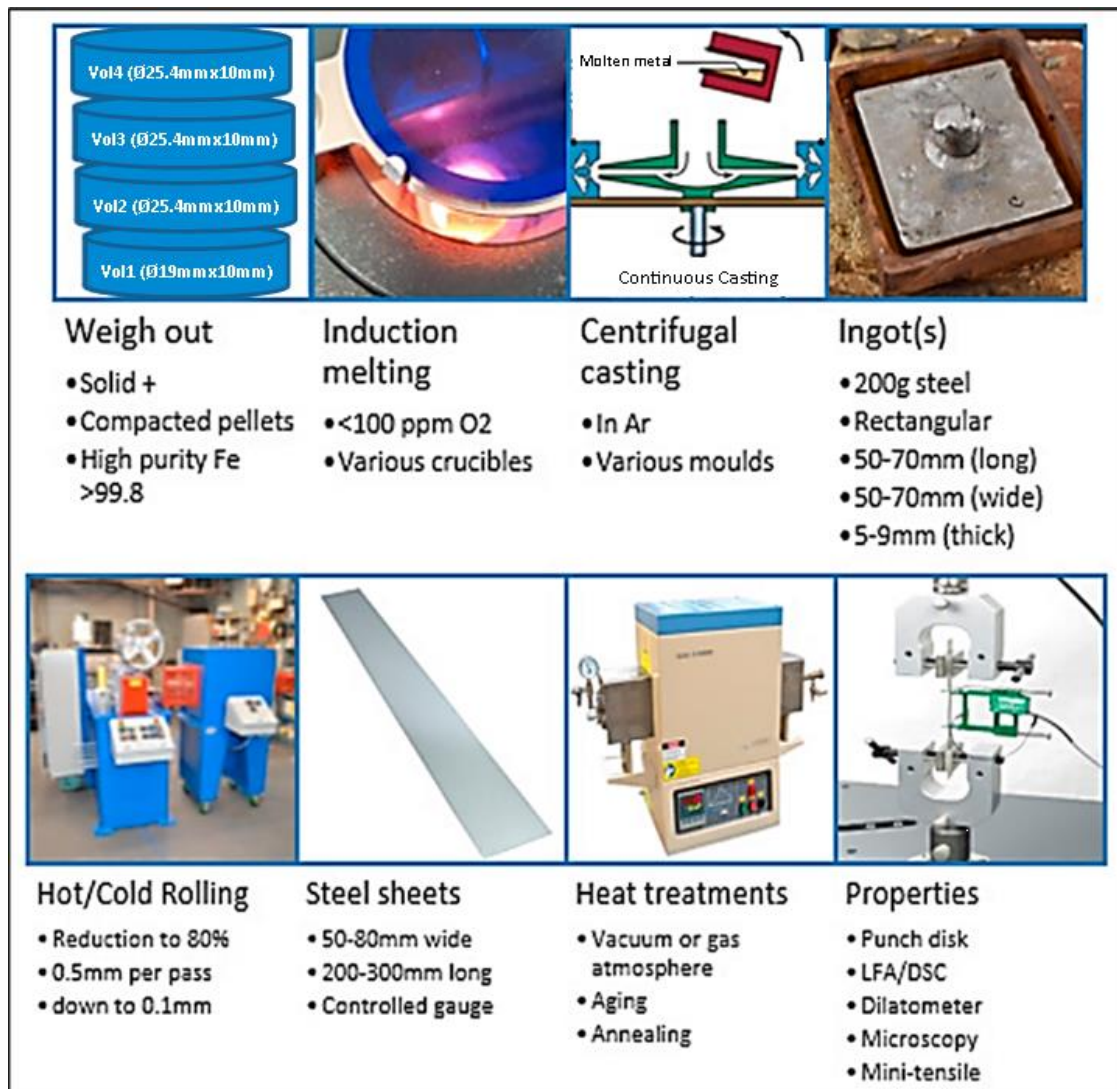
Figure 37- Outline of Mach1's RAP process route[99].

The main advantage of this manufacturing method is that the initial melt of iron and carbon (the master melt) can be sectioned such that multiple variations of thermomechanical treatments can be implemented on the same sample, and the impacts of such can be accurately assessed. This method uses limited material, and is far quicker than the following process route making it advantageous in the laboratory setting.

1.5.3. VIM Produced (2.5kg)

1.5.3.1. VIM Produced/ SAMI Produced Sample Procedure Introduction

This section details the assets used at SAMI for the 'manufacture' of steel plate, from cast blocks, in order to simulate the hot mill as Tata Steel Port Talbot in the manufacture of hot-band material. Note that both plant produced transfer bar (from Tata Steel Port Talbot) can also be processed if material is removed prior to the finishing mill, when this is not the case vacuum induction melting is used to create a replica of plant produced material. This

section is more detailed than the previous since much of the research in this thesis focusses on optimising many of the processes used in the SAMI procedure of manufacturing 'hot-band' material.

1.5.3.2. Vacuum Induction Melting

At the time of writing SAMI are currently in possession of two 'VIMs', both manufactured by Consarc, Part of the Inductotherm Group. Consarc manufacture vacuum induction furnaces for both industrial and research applications[100]. Both furnaces are bespoke items, both with the capacity of casting steel ingots up to 50kg in mass, but vary slightly in configuration and a vacuum capability.

Table 1- SAMI's VIM capabilities

	Consarc 011449-1993 (Old VIM)	Consarc 31445-2018 (New VIM)
Maximum Cast Weight (kg)	50	50
Power (kW)	125	125
Achievable Vacuum (mbar)	e^{-1}	e^{-5}
No. Coils	2	1

The benefit of VIM production is that novel blends steel alloys can be produced at an intermediate scale (when compared to a RAP procedure), as well as alloys compositions that mimic plant material. Chemical elements are added into a refractory ladle in the form of pre-weighed powders, allowing for accurate percentage weight contribution. Due to the larger volumes being produced, this allows for multi-pass hot rolling, and the manufacture of A80 tensile specimens (a tensile sample with a gauge length of 80mm with is commonplace in the tensile testing of steel), which is not possible on a RAP scale sample. This is advantageous particularly in the scope of this research since plant produced transfer bar is limited in availability. For this research VIM produced DP800 is utilised in part due to the lack of availability of plant produced transfer bar.

Figure 38- A photo of the Consarc VIM used to manufacture DP800 blocks for hot rolling.

Once the correct chemical composition by weight has been measured and placed into the crucible, the alloying elements are heated together under vacuum until they are a homogenised. The 30kg ingot is then left to cool to room temperature, where they are subsequently cut into "Transfer Bar" blocks, for hot rolling.

1.5.3.3. Re-Heat Furnace

The furnace typically used in the SAMI procedure to reheat the blocks to 1250°C is a Nabertherm N 161/13. Capable of heating to a maximum temperature of 1300°C, with internal dimensions 550 x 750 x 400 mm. This furnace is typically allowed to get to operating temperature over several hours before blocks for hot rolling are placed inside to allow for repeatable soak times. A photo of the reheat furnace is shown below:

Figure 39- Nabertherm N 161/13 Electric radiation furnace.

Once the blocks have been soaking for a sufficient period, typically two hours, they can be removed from the furnace by a operators ready for a brief descale with a pick hammer before being placed into the role bite of the mill.

1.5.3.4.   Hot Mill (Lewis Mill)

The Mill used by SAMI, in order to hot roll steel block was manufactured by the Lewis Company Canada in the 1940s. Currently the mill is used in a reverse rolling configuration with infrared pyrometers at the mill entry and exit as well a load cells on the top and bottom roller. The mill has the capability to adjust the roll gap automatically after each rolling pass, minimising inter-pass times. The below table summarised the key information regarding the mill specifications.

Table 2- Key specifications for Lewis Rolling mill.

Lewis Rolling Mill	
Maximum sample thickness	68 mm
Maximum recommended sample width	110 mm
Minimum rolling speed	0.2 m/s
Maximum rolling speed	1.3 m/s
Selected rolling speed (Used for this body of research)	0.5 m/s
Maximum Mill Load	80 T
Maximum Mill Torque	17 kNm
Maximum recommended bite angle	18°
Roller Diameter	105 mm

Below photos shows the Lewis Mill entry and exit:

Figure 40- Lewis Mill entry.

Figure 41- Lewis Mill exit.

Once the desired number of rolling passes have been completed the sample is passed onto the ROT for water cooling.

1.5.3.5.   ROT

The ROT at SAMI, designed to mimic industrial cooling operations, measured 4m long and consists of a powered roller conveyor to deliver the sample across the path of 54 water spray headers situated above and below the roller conveyor. The roller conveyor is powered by an electric motor, which is controlled by an analogue speed controller. The speed controller is operated via a rotary dial where the user can adjust the speed between 1-8, with 8 being the fastest. Under the usual SAMI operating procedure, the speed is typically set to 4, with 18 water headers open to achieve a representative coiling temperature.

Figure 42 shows the ROT with water header tank situated above it. The headers are gravity fed from the header tank, which is refilled with a ballcock valve when the water level reaches a certain height. The water is fed from a mains supply so is subject to seasonal temperature change especially if recently refilled and has not had sufficient time to tend to the room temperature, this is particularly noticeable in winter months. The ROT is also equipped with an air sprayer at the end of the water headers, to remove any excess water on the strip surface to aid in temperature measurement via an infrared pyrometer.

Figure 42- Photo of SAMI ROT with water top water headers visible and wate tank above.

1.5.3.6.   Coiling Furnace

In order to simulate the slow cooling effect of a coil of strip, a furnace is placed at the end of the ROT. This furnace is normally set to the quoted coiling temperature for the product being produced, when the experiment is finish, the furnace is switched off and allowed to cool slowly over a 24 hour period, such that the temperature profile matches that of a large coil.

1.6. Comparison of Laboratory and Industrial Processing Routes

1.6.1.   Overview

This section offers a cursory back-to-back comparison of the three manufacturing routes, highlighting the differences, outlined in Table 3. A review of literature regarding possible differences is provided here but further analysis as to the implications of these differences is provided later in the thesis.

Table 3- Comparison of SAMI and Tata Steel Port Talbot manufacturing routes.

Step No.	Port Talbot Process	SAMI Process /VIM Produced	RAP Process
1	Steel making	VIM cast	Open Cast *(Pre-weighed chemical elements are compacted and melted)*
2	Slab Reheat Furnace	Slab Reheat Furnace	Slab Reheat Furnace
3	Rough Rolling *(Reverse Rolling above T_{NR})*	Lewis Mill *(Reverse Rolling above and below T_{NR}, simulates both roughing mill and finishing mill)*	Single Pass Hot Rolling *(Reverse Rolling above T_{NR}, simulates both roughing mill and finishing mill)*
4	Finishing Mill *(Tandem rolling, above and below T_{NR})*	ROT *(water cooling on conveyor)*	"Coiling" Furnace *(Furnace to simulate slow cooling of a wrapped coil, set to CT of produced grade)*
5	ROT	"Coiling" Furnace *(Furnace to simulate slow cooling of a wrapped coil, set to CT of produced grade)*	
6	Coiling		

1.6.2. Comparison of Rolling Operations

The main fundamental difference between the plant process route and both of the laboratory manufacturing routes in the absence of a rough rolling stage. Other differences are inherent such as the time spent in the reheat furnace, among others, however these are unavoidable due to the scale of manufacture. However, the difference in hot rolling operations should be addressed, since the hot rolling schedules in all three cases as previously discussed, have a large influence on the final microstructure.

As addressed previously, the role of rough rolling is to produce enough net reductions, so the slab is suitable for the finishing mill. Upon exit of the reheat furnace, the slab temperature is around 1250-1300°C, and will exit the roughing stand at around 1150°C, after having been reduced from 250mm to 34mm in thickness. Due to these large reductions experienced by the strip it is likely some refinement of the austenite grains will take place. A report by the American Iron and Steel Institute states that during rough rolling operations, the grain size is likely to be refined from 1000μm, after a two hour soak (broadly similar to the soak time fort DP800) in the reheat furnace, to 200μm via both static and dynamic recrystallisation[101]. Research by Patil and colleagues on microalloyed API steel grades, in modifying roughing mill rolling schedules, concluded that varying the pass number did in-fact change the mechanical properties of the final

product[102]. It can therefore be reasoned that the absence of a roughing stage, in the laboratory manufacture of steel is likely to result in a larger grain size since no grain refinement is occurring. Hower this may be mitigated if meta-dynamic recrystallisation occurs in the case of the Port Talbot Roughing mill, such that sufficient accumulated strain results in transformation after the roughing passes, resulting in rapid grain growth[102].

Another key difference, that likely cannot be addressed due to the physical limitations of available equipment, it's the difference between the tandem rolling exhibited in the finishing mill at Port Talbot, and the reverse rolling in the laboratory mill at SAMI. Limited data is available regarding comparisons of tandem rolling vs reverse rolling, for like for like rolling schedules in steels, since industrially the type of a rolling mill is chosen based upon strip length or convenience. Research by Kraner and colleagues, into a comparison of reverse rolling against tandem rolling for AW-8021B aluminium alloyed reported that tandem rolling resulted in a far more homogenous grain structure over reverse rolling[103]. This may be due to variations in inter-pass times, since when reverse rolling the 'tail' end of the strip becomes the 'head' end of the strip in every other pass. This results in different inter-pass times for different positions along the strip, as the strip cools. It could be the case that the critical strain for recrystallisation is reached in some areas of the strip and not others, resulting in a spread in final grain structures. Another paper by Wang and colleagues details a comparative study of tandem against reverse rolling for SUS436L stainless steel, in the setting of cold rolling[104]. Finite element models were constructed, in both cases revealing that larger shear rates were exhibited in tandem rolling and experimentally a more refined grain structure was observed in the case of tandem rolling. This conclusion has limited relevance in the case for the comparison between Tata Steel and SAMI's production route due to difference in rolling temperatures as well as steel chemistry. However, it can be reasonably concluded that there is likely some difference, in resultant microstructures, between reverse rolling and tandem rolling. In contrast to both of these multi-pass rolling methods, the RAP route simply consists of a single pass, however due to the small sample size this is necessary since implementing additional reductions through the mill will result in large temperature losses. This shows that there is likely to be differences in the microstructure inherent to each of the three process routes, this should be considered in the analysis of any microstructural investigations that take place.

1.7. Modelling

1.7.1. Empirical Equations

1.7.1.1.   Microstructure

1.7.1.1.1.   TNR

A number of mathematical models exist of the prediction of the T_{NR}. A paper by M. N. Akhtar and colleagues helpfully outlines a number of mathematical models for predicting TNR for Niobium microalloyed grades[61]. The paper includes the Boratto Equation[105]:

$$T_{NR} = 464 - \left(644\sqrt{Nb} - 6445Nb\right) - \left(230\sqrt{V} - 732V\right) + 363Al \times 890Ti + -\text{2576i}$$
$$+ 887$$

Equation 3

A simplification of the Boratto equation by Bai and colleagues[66]:

$$T_{NR} = 174 \log\left[Nb\left(C + \frac{12N}{14}\right)\right] + 1444 \qquad \text{Equation 4}$$

The Fletcher model for TNR, created via a stepwise regression based upon laboratory measurements of 17 alloy sheets[67]:

$$T_{NR} = 849 + 349C + 676\sqrt{Nb} + 337V$$
$$(R^2 = 0.72)$$

Equation 5

The above models are simply a function of material chemistry, however it has been fond that T_{NR} is not only a function of chemistry, but is also affected by strain[66]. In response to this Fletcher and colleagues also produced a model that is a function of both steel chemistry and strain[67]:

$$T_{NR} = -310C + 657\sqrt{Nb} - 149\sqrt{V} + 683e^{-0.36\varepsilon} + 203 \qquad \text{Equation 6}$$

1.7.1.1.2.   Grain Growth (Predicting grain size during rolling)

Predicting the grain size during hot rolling is a complex task, and difficult to determine experimentally due to the high strain rates, and short time periods is which static, dynamic

69

and meta dynamic recrystallisation occur. The degree of grain refinement is largely a function of net reductions during rolling and product chemistry, but is also affected by the temperature, since as discussed previously, recrystallisation does not occur below the T_{NR}. Various mathematical models have been created in the pursuit of grain size prediction and has been studied in great depth[106-108]. An example of this equation is given, which has been previously used in the case for Nb microalloyed steels by Siciliano and colleagues [109]:

$$d_{DRX} = 1370 \times \varepsilon^{-0.13} \times e^{\left(\frac{-45000}{RT}\right)} \qquad \textit{Equation 7}$$

Where: d_{DRX} Grain size as a result of dynamic recrystallisation.

                 ε Stain impaired to the strip at the given rolling pass.

                 R The gas constant (8.31 J/mol K).

                 T Cooling rate (change in temperature between passes divided by the inter-pass time).

Similarly, Siciliano presents an expression which describes the grain growth evolution during static recrystallisation. This occurs in the unloaded case, at sufficiently high temperatures such as between rolling passes provided sufficient time has passed:

$$d_{SRX} = 1.1 \times d_0^{0.67} \times \varepsilon^{-0.67} \qquad \textit{Equation 8}$$

Where: d_{SRX} Grain size as a result of static recrystallisation.

                 d_0 Grain size at the beginning of rolling pass.

                 ε Stain impaired to the strip at the given rolling pass.

1.7.1.1.3. Critical Strain

The critical strain is also an important parameter in determining the nature of recrystallisation in hot rolling operations. The critical strain is the strain threshold at which the accumulated strain (from prior rolling passes) exceeds a given value, such that dynamic recrystallisation is initiated, resulting in a measured decrease in mechanical loading.

Therefore, this phenomena is often seen in later passes, due to strain accumulation (provided the strip is at a sufficiently high temperature). In order to measure the accumulated strain, some expression to describe it needs to be defined. Work by Siciliano and colleagues, describing the mathematical modelling of hot rolling provides the following[109]:

The accumulated strain, where the number of rolling passes is larger than 1:

$$\varepsilon_i^a = \varepsilon_i + K_{acc}(1 - X_{i-1})\varepsilon_{i-1}$$

Equation 9

Where: ε_i^a The total accumulated strain.

ε_i The initial strain.

K_{acc} Constant as a function of inter-pass time.

X_{i-1} The fraction softening.

The fraction softening, X_{i-1} ,is calculated by[110]:

$$X_{i-1} = \frac{\sigma_m - \sigma_i}{\sigma_m - \sigma_{i-1}}$$

Equation 10

Where: σ_m The flow stress at the end of the previous pass.

σ_{i-1} The stress at 20% of the strain of previous pass.

σ_i The stress at 20% of the strain of the current pass.

Note that this stresses at 20% strain are difficult to determine experimentally with novel rolling schedules on a laboratory mill, so assumptions are used in the following scenarios, where softening is expected due to drops in load. When static recrystallisation is not present, X is likely equal to 0, since there is no softening. In the case that total recrystallisation is present X can be equal to 1, or 100%[110].

1.7.1.2. Mean Flow Stress

MFS (Mean Flow Stress), or flow stress, is stress required to deform a material at a constant rate within the plastic region. Due to the work hardening characteristics of metals, flow stress is a function of the strain imparted into the strip[111]. Therefore, this a key factor to consider in the rolling mill. A number of equations have been developed with the aim of predicting mean flow stress for different materials. Typically, these area function of material chemistry, strain, strain rate and Temperature. Dimatteo and colleagues helpfully provide a concise summary of various empirical models for predicting MFS in steel, in the setting of hot strip rolling[112], where models by Misaka[113], Bruna[114], Siciliano[115], Poliak[14] and Shida[116] are compared. Dimatteo compares the data to hot strip mill data and optimises the models utilising genetic algorithms. This recent research highlights the relative importance, in an industrial setting, of accurately predicting MFS. The equations by Misaka, Bruna and Siciliano are given below:

Misaka:

$$MFS_{Misaka} = 9.8exp(fCT_{Mis})\varepsilon^{0.21}\dot{\varepsilon}^{0.13} \qquad \text{Equation 11}$$

Where: ε The strain per hot rolling pass

$\dot{\varepsilon}$ The strain rate.

fCT_{Misaka} The function of 'carbon content'

$$fCT_{Misaka} = 0.126 - 1.75C + 0.594C^2 + \frac{2851 + 2968C - 1120C^2}{T} \qquad \text{Equation 12}$$

Where: fCT_{Misaka} The function of carbon content.

C The percentage weight of carbon in the steel.

T The temperature in degrees Celsius (the inter-pass temperature).

Bruna:

$$MFS_{Bruna} = 9.81exp\left(\frac{3126 + 68C + 2117Nb + 54Mn + 152Mo}{T}\right)\varepsilon^{0.21}\dot{\varepsilon}^{0.13} \quad \textit{Equation 13}$$

Where: Nb The percentage weight of Niobium in the steel.

              Mn The percentage weight of Manganese in the steel.

              Mo The percentage weight of Molybdenum in the steel.

Siciliano:

$$MFS_{Siciliano} = 9.81exp\left(\frac{2704 + 3345Nb + 220Mn}{T}\right)\varepsilon^{0.21}\dot{\varepsilon}^{0.13} \quad \textit{Equation 14}$$

1.7.1.3.   Rolling Mills

1.7.1.3.1.   Orowan

In 1943 E. Orowan published a journal article regarding the prediction of roll pressure and roll torque in mill applications[117]. In order to do this a graphical model of the rolling scenario was developed. The distribution of pressure over the contact arc length (the length of material, in cross section, in contact with the roller). The model also accounts for frictional interactions between the rolls and the strip, which made it a superior model compared to previous attempts.

1.7.1.3.2.   Sims

What is frequently referred to as the Sims model, is another mathematical model of rolling operations[118]. The Model outlined by R. B. Sims utilises the conditions for plastic deformation outlined by Orowan[117], as well as Von Kármán's equation of equilibrium to accurately describe the roll pressure along the contact arc length[119]. Sims experimental data is derived from previous works, such as those by Orowan, as well as experimental data from rolling lead bars at room temperature, which included as well as hot rolling of steel. The following equations, outlined by Sims, are used to predict load on the rollers:

$$F = Q_p \times M_{FS} \times W \times L \quad \textit{Equation 15}$$

Where: Q_p The geometrical factor (a function of mill geometry)

            M_{FS} The mean flow stress of the material at the given roller pass

            W The sample width

            L The contact arc length (a function of the thickness reduction and roller geometry)

The geometrical factor, Q_p is calculated as a function of deformed roll diameter and thickness reduction:

$$Q_p \left(\frac{R'}{h}, r \right) = \left[\frac{\pi}{2} \sqrt{\frac{1-r}{r}} \tan^{-1} \left(\sqrt{\frac{r}{1-r}} \right) - \frac{\pi}{4} \right.$$

$$\left. - \sqrt{\frac{1-r}{r}} \sqrt{\frac{R'}{h}} \log_e \left(\frac{Y}{h} \right) + \frac{1}{2} \sqrt{\frac{1-r}{r}} \sqrt{\frac{R'}{h}} \log_e \left(\frac{1}{1-r} \right) \right]$$

Equation 16

Where: R' The radius curvature of the elastically deformed roll.

            h The thickness of the rolled strip.

            Y The thickness of the material at the plane of intersection

Q_p can also be determined graphically using Figure 43 below. The ratio of roll diameter to roll gap must be determined for each pass initially then pass reduction is used to determine Q_p.
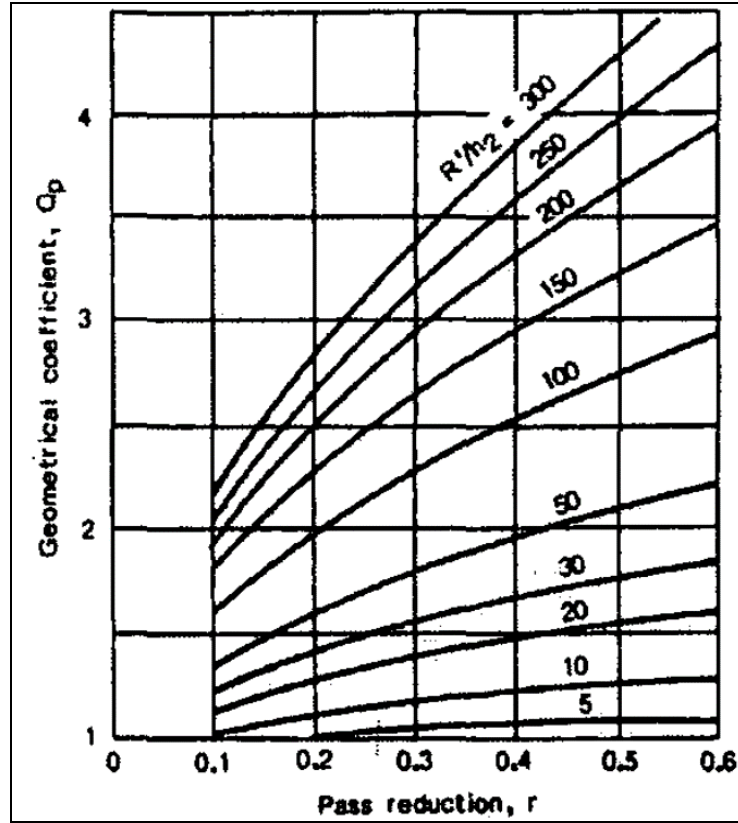
Figure 43- Q_p lookup graph from Sims model[118].

1.7.1.3.3.   Bite Angle

The equation used to calculate the bite angle for a given reduction, of a material of given thickness is:

$$\alpha = \tan^{-1}\left(\frac{\sqrt{R\,\Delta h}}{R - \frac{\Delta h}{2}}\right)$$

Equation 17

Where: R   The roller radius

            Δh The change in strip thickness in a given pass

All rolling mills have a maximum bite angle, if this angle is exceeded the mill may chatter and the material to be rolled will not pass though the rollers. Careful attention must be paid when designing a rolling schedule such that this angle is not exceeded. The maximum bite angle for a particular rolling mill is subject to the interaction between the roller surface and the material, mostly due to the friction between the two.

1.7.1.3.4. Adiabatic Heating Due to Rolling

The slab reheat furnace is not the only source of energy input into the strip during the hot mill process. The strain energy being imparted into the strip can have a significant heating effect on the strip. The effect of strain, in both the setting of the rolling and plain strain, has been previously studied on multiple steel grades[120-122]. The effect of adiabatic heating is generally considered significant at strain rates above 1s⁻¹[123].

The mathematical expression to describe the temperature change due to deformation is given as[123, 124]:

$$\Delta T = \frac{\sigma_m \delta \varepsilon}{\rho C_P}$$

Equation 18

Where: $\sigma_m \delta \varepsilon$ The area under the stress strain curve

             ρ The density of the steel

             C_P The specific heat capacity of the steel

However Equation 18 describes the temperature increase for plain strain setting, more fitting mathematical equations have been created for the setting of rolling[125]:

$$\beta = p_m \varepsilon / 427 \times 10^{-3} N c \rho$$

Equation 19

Where: p_m Average roll pressure

             ε The deformation ratio (strain)

             N Divided number contact time (dimensionless)

             c Specific heat capacity

             ρ Mass density

For reference; the total time each 'segment' is in contact with the roll, is given by $N\Delta t$, therefore β is the temperature change per unit time, for a given 'segment' in contact with the rollers.

Adiabatic heating is an important consideration when designing novel rolling schedules since it can have a significant bearing on the FRT, and therefore the transformation downstream of the finishing mill on the ROT where the strip transforms from Austenite to Ferrite and Pearlite. This is particularly relevant in laboratory hot rolling where temperature loss is a key issue due to increased surface area relative to volume ratios.

The temperature differential due to adiabatic heating can also be estimated by the equation:

$$\Delta T = (0.9/\rho C_p)\sigma\varepsilon \qquad\qquad \textit{Equation 20}$$

Where: ΔT The temperature change due to imparted strain into the strip

ρ The mass density of steel

C_p The heat capacity of steel

σ The MFS (calculated using the Misaka model, see section 1.7.1.1.1)

ε The strain due to rolling the reductions.

1.7.1.4. Thermodynamics

Due to the high temperatures of steels studied in this body of work during hot rolling processes, it is important to understand and define the mechanisms by which the samples will lose heat to their surroundings.

Convection:

$$P_{conv} = hA(T_1 - T_\infty) \qquad\qquad \textit{Equation 21}$$

Where: h Heat Transfer coefficient

A Surface area of the sample in contact with air

T_1 The surface temperature of the sample

T_∞ The temperature of the air (ambient temperature)

Radiation:

$$P_{rad} = \varepsilon\sigma A(T_1^4 - T_2^4) \qquad\qquad \textit{Equation 22}$$

Where: ε The surface emissivity of steel

                 σ Boltzmann's Constant

                 A Surface area of the block

                 T_1 Sample temperature at the beginning of a rolling pass

                 T_2 Sample temperature at the end of a rolling pass

Conduction:

$$P_{cond} = UA(\Delta T)$$ *Equation 23*

Where: U Overall heat transfer coefficient

                 A Area in contact with solid medium (mill rollers and mill bed)

                 ΔT Temperature change

Another important thermodynamic consideration in hot rolling is adiabatic heating.

2. Experimental Procedure

2.1. Materials

2.1.1. VIM Produced

Due to the limited availability of plant produced DP800 transfer bar, the VIM was used to inductively cast blocks consisting of the same chemistry as DP800, as described in section 1.5.3.2. Chemical elements are separated by weight and the target composition is obtained with high accuracy. A cast block is shown below in Figure 44.

Figure 44- VIM cast material in one half of refractory cast.

Once cast the blocks are cut into blocks measuring 34 x 80 x 100mm ready for hot rolling on the laboratory mill. The VIM cast can be partially filled, which is commonplace depending upon how much material is required. However, at full capacity (50kg), 2 x 25kg ingots can be made. These are then hot rolled on the Lewis Mill to reduce the ingot thickness (a process commonly referred to as 'cogging'), then cut on a band saw to the desired length. This can yield 8-9 blocks for hot rolling, per ingot, resulting in 19-20 blocks per VIM cast. The yield depends on the quality of cast, in the event there is some

porosity from the fill neck, then less block will result from the cast, as shown in Figure 45 below in which the furthest right ingot which contains an internal void.

Figure 45- VIM cast ingots cut for manufacture of blocks for hot rolling.

2.1.2. Plant Produced Transfer Bar

'Transfer bar' is the term given to material that has been rough rolled, but not yet hot rolled in the finishing mill. This material is periodically trimmed to extract steel of R&D purposes. As such only a limited quantity is available. In order to prepare the transfer bar for hot rolling, in the laboratory, the bar must be cut into strips then cut again into blocks measuring 34 x 80 x 100mm. Occasional machining is done on the face of these block if there is some curvature.

Figure 46- 'Transfer bar' cut ready for hot rolling, with coil ID rolling direction marked.

2.1.3. Mill Logs

In order to compare laboratory and plant rolling processes data from Tata Steel Port Talbot has been provided. For the purposes of this project finishing mill and roughing mill logs are used. Both logs provide information regarding material chemistry, product starting thickness, subsequent thickness per rolling pass, temperatures at each pass and product speed through the mills. An example of a section of a finishing mill log is given below in Figure 47. Note 'F1' refers to the 1st roller stand in the finishing mill and 'F2' the 2nd and so on. Note the section of the log detailing the product chemistry has not been included intentionally.

		CS	F1	F2	F3	F4	F5	F6	F7	FM EXIT
Stand rolling flag	( )		YES	YES	YES	YES	YES	YES	YES	
Gauge	(mm)	37.000	21.133	14.129	9.122	6.528	5.029	4.032	3.637	
Gap	(mm)		20.656	13.014	8.261	5.819	4.240	3.833	4.316	
Strip force	(Tonnes)		1908.6	1904.2	1769.2	1606.5	1486.1	1299.3	831.3	
Total force	(Tonnes)		2232.6	2228.2	2093.2	1930.5	1810.1	1563.3	1007.6	
Distrib parameter	( )		force	force	force	force	force	force	force	
Aim distribution	(%)		17.9	17.8	16.3	14.7	13.6	11.9	7.7	
Achieved dist	(%)		17.7	17.6	16.4	14.9	13.8	12.0	7.7	
Mean yield stress	(T/mm^2)		9.480e-03	1.005e-02	1.238e-02	1.684e-02	1.906e-02	1.891e-02	1.889e-02	
Recrystal factor	(%)		0.0	0.0	0.0	0.0	0.0	0.0	0.0	
Torque	(Nm)		1.424e+06	1.001e+06	7.018e+05	4.800e+05	3.012e+05	2.470e+05	1.434e+05	
Power	(kW)		3608.8	3718.7	4171.1	3863.2	3140.7	3415.2	2131.8	
Current	(Amps)		4364.7	5693.8	5660.1	5228.7	4123.8	3883.1	2880.7	
Voltage	(Volts)		839.9	658.8	756.2	770.2	784.7	893.1	750.7	
Total motor load	(%)		46.45	44.60	50.84	48.60	39.38	44.79	39.77	
Reduction	(%)		42.88	33.14	35.44	28.44	22.95	19.83	9.79	
Forward slips	(%)		11.150	8.066	8.906	7.244	5.848	5.040	2.461	
Speeds	(m/s)	0.53	0.84	1.29	1.98	2.82	3.71	4.66	5.29	5.42
Speed trim factors	( )		1.003	1.003	1.000	1.003	1.003	1.002	1.000	
Accelerated thread	(%)		0.0	0.0	0.0	0.0	0.0	0.0	0.0	
Temperatures	(C)	1111.8	961.7	966.9	953.2	937.2	921.0	905.2	892.3	868.3
Washbox /Top Flows	(%)	1 1	0.0	0.0	0.0	0.0	0.0	0.0	0.0	
Bot Flows	(%)		0.0	0.0	0.0	0.0	0.0	0.0	0.0	
Upper limit flags	(bits)		@0000	@0000	@0000	@0000	@0000	@0000	@0000	
Lower limit flags	(bits)		@0000	@0000	@0000	@0000	@0000	@0000	@0000	
Looper angle	(deg)		25.0	25.0	25.0	25.0	25.0	25.0		
Looper tension	(N/mm^2)		5.814e+00	7.231e+00	1.395e+01	1.390e+01	1.791e+01	1.685e+01		
SHAPE setup										
WR Bending	(Tonnes)		200.0	200.0	200.0	200.0	200.0	170.0	126.1	
WR Shift	(mm)		0.0	0.0	0.0	0.0	0.0	140.0	140.0	
Crown out (Cxx)	(micron)		190.6	172.3	141.9	115.0	92.3	81.7	75.2	
Crown out (quad)	(micron)		180.5	158.7	123.6	94.6	69.7	57.5	50.7	
Flatness (quad)	(pu)		1.468e-06	9.709e-06	3.746e-05	3.336e-05	-3.503e-05	3.062e-05	-5.000e-05	

Figure 47- Finishing Mill Log example.

2.1.4. Titan Journal Data

The Titan hot mill and ROT model is capable of utilising plant data and inputting this into the simulation, from which the simulation predicts downstream properties. The inputs from plant data provide the simulation with product velocity throughout the mill, the product chemistry, and an initial temperature upon entry to the ROT.

The files for each simulation is known an a 'journal', each journal is a part of an individual coil. Therefore, the simulation output shows the journal of a given section of a coil. Figure 43 shows the top section of a journal file, this details the product chemistry, rolling reductions, headers used, header flows, the time and date the coil was rolled as well as the slab ID that the coil was made from. Figure 49 shows the second half of a journal, here the data per until length of the coil is given. Note that the sample number (far left column of Figure 48) is not for a given distance of coil, the model takes 1 sample per second regardless of the rolling speed, as such the sample numbers between to consecutive coils may vary hence why 'SAMP NR' is unitless. Figure 49 shows ten lines, however each journal consists of 89 lines in total. Again, the product chemistry has been redacted.

```
+-----------------------------------------+----------------------------------------+
|     TATA STEEL PORT TALBOT              | Coiling Temperature Sample journaal    |
+-----------------------------------------+----------------------------------------+
| Date / time 21-JAN-2021 21:24:04.57    | Slabid : 65933 010      | COILW 23.73 |
+---------------+----------+--------------+-------------+-----------+--------------+
| HF7PDI  3.60 | GRTTHK  8 | QCR  6  8 | STGRAD 3751 | CEQ 447.0 | WF7PDI 1286 |
+---------------+----------+--------------+-------------+-----------+--------------+

Cooltype: Dual Flowlevel    : 0 Flowlevel m1 : 55 Flowlevel m2 : 55   Last_reduc:  8.492 Squar Dy:  0.233 Av Dy: -7.337

Pattop: X11111111X100S0S01111111  FF_T: 1  L_adap: 0.9433  delta_l: -0.0008  Labcor_alpha:  0.950  Dy_av_group:  8.518
Patbot: X11111S11H10000000111111SS  Used model: MITRON  Setup Calc Time (ms) : 669   Durbar Flag: 0

StandsUsed: 1111111
Reductions:  34.00 17.06 11.37  8.02  5.93  4.67  3.95  3.62

Flow Top:    0 158  48 157 158 156 155 153 154 160 158 153 163 153 158 167  45  53  53  49  47  47  49  49
Flow Bot:    0 198 202 204 198 197 140 203 200 100 199 198 195 195 192 204  64  66  69  63  66  67  49  17

C      MN      SI      P       AL      NB      TI      S       B       CU      CR      NI      MO      V       N

Tmpdi      : 625     Nurbgr     : 2      Cat_co     : 0      Cool_rate : 300     Coiler     : 2      TCGR       : 4
Tcpdi      : 600     SL         : 7.3    Coolmeth   : 5      Twm        : 22.3   Kprtct     : 97.9   N_samples  : 90
DTCHBase   : 7.5     DTCHAdap   : -20.0  TailCor    : 0.0    Vpattern   : 9.0    Vmax TSS   : 6.3    Coolr_M2   : 150
Lc_head    : 30      OprHeadcor : 0.0    Lc_tail    : 25     OprTailcor : 0.0    HotHeadLn  : 0.0    Grainsize  : 11.5
Npmax      : 17      Nptheo     : 72     Npcool     : 470    Vmaxct     : 2.1    Pclr       : 42.6   TF min     : 840
Npmax_M2   : 12      Nptheo_M2  : 24     Npcool_M2  : 676    Vmaxct_M2  : 4.5    Pclr_M2    : 5.3    TF max     : 880
Np         : 17      Nthrd      : 10     Nt         : 9      Nb         : 8      D IP3 CT   : -18.9  TC min     : 575
Np_M2      : 12      Nthrd_M2   : 8      Nt_M2      : 7      Nb_M2      : 5      Dy adap    : -11.3  TC max     : 625
                                                                                 dY_Badrun  : 1.150  F1safesetup: 12.00

Beta's old : -0.100478 -0.033648 0.013536 -0.025333 0.000000
Beta's new : -0.099871 -0.030812 0.011928 -0.020526 0.000000
Beta's used: -0.100478 -0.033648 0.013536 -0.025333 0.000000
```

Figure 48- Top section of a journal detailing coil chemistry, header flows and reductions.

```
Beta's old : -0.100478 -0.033648 0.013536 -0.025333 0.000000
Beta's new : -0.099871 -0.030812 0.011928 -0.020526 0.000000
Beta's used: -0.100478 -0.033648 0.013536 -0.025333 0.000000

SAMP L    HF7m VF7m Vavg Vcoil  TF7  IP2 IP2pr Ip2z IP3 IP3pr Ip3z CTm CTsp CTpr CTprFT CTz TOP    BOT    TF7 DTH IP3  CT  GAIN TOP  BOT  dYm OK S-stat  ALFA
NR                                       %              %                %  MN  T  MN  T  ff  ff  ff   fb  TRIM FLOW FLOW  %              COR_P
0    0  3.60 6.33 6.33 -1.00  860   -1 -274  -1  -1 -274  -1  600 599  599 -1  5  4  5  4  0   0   0   0.0  5.1  880 1264 -7.2  0 110000  1.000
1    4  3.58 6.33 6.33  7.17  856  699  609  12 667  617  45 611 600  599 69  6  7  5  5  0   0   0   0.0  4.7 1179 1330 -7.2  0 110010  1.000
2   11  3.62 6.32 6.32  7.20  859  695  615  13 654  625  49 598 600  600 89  6  2  5  3  0   0   0   0.0  5.2  939 1198 -7.2  1 111110  1.000
3   19  3.61 6.33 6.33  7.47  865  672  638  18 628  650  60 617 600  618 86  5  7  5  5  0   0   0   0.0  4.7 1024 1330 -7.2  1 111110  1.000
4   26  3.61 6.33 6.33  8.42  866  683  621  15 635  632  52 597 600  630 79  6  7  5  5  0   0   0   0.0  4.6 1179 1330 -7.3  0 111010  1.000
5   34  3.61 6.33 6.33  8.61  858  624  613  13 615  622  47 613 600  598 77  6  3  5  3  0   0   0   0.0  5.2  987 1198 -7.2  1 111110  1.000
6   40  3.59 6.33 6.32  9.41  866  611  637  18 616  649  59 597 600  600 87  5  3  5  3  0   0   0   0.0  5.1  832 1198 -7.1  1 111110  1.000
7   48  3.59 6.33 6.33  8.76  865  668  619  14 641  629  51 555 600  608 78  6  7  5  5  0   0   0   0.0  4.8 1179 1330 -7.3  0 111010  1.000
8   55  3.58 6.32 6.32  8.88  867  656  620  15 628  630  52 573 600  609 78  6  7  5  5  0   0   0   0.0  4.8 1179 1330 -7.3  1 111110  1.000
9   62  3.60 6.32 6.32  8.54  869  604  623  15 625  634  54 603 600  614 59  6  7  5  5  0   0   0   0.0  4.7 1179 1330 -7.3  0 111010  1.000
10  69  3.59 6.33 6.33  8.73  866  620  619  14 630  630  51 565 600  603 600 78  6  6  5  5  0   0   0   0.0  4.8 1130 1330 -7.4  0 111010  1.000
```

Figure 49- Bottom section of a journal detailing the strip velocity, header flows and measured temperature per unit length (not the journal is far longer than shown but only 10 lines have been shown).

For the purposes of this research a total of nine journals has been selected, from a variety of coils. Each file chosen has been selected from approximately the middle of each journal, the reason for this is the limit the acceleration of the strip to simplify the model, such that any changes made to the settings will result in a more predictable changes, simplifying the optimisation process since at constant velocity the model can be considered steady state. The reason for the acceleration at the beginning and end of a strip is due to limitation in 'threading' the mill and the coiler. As a result, the product velocity is varied thought the hot rolling and ROT operations, as shown below in Figure 50.

Figure 50- Illustration of percentage of maximum strip speed capacity for a coil on the ROT over time.

Table 4- Journals used for Titan analysis.

Journal File Name	Date & Time
PTROT56868-020- 301	15-SEP-2021 00:02:58.06
PTROT56869-020-300	15-SEP-2021 00:07:56.79
PTROT56870-010-301	15-SEP-2021 00:11:12.96
PTROT56871-010-302	15-SEP-2021 00:29:55.51
PTROT56873-010-304	15-SEP-2021 00:36:32.63
PTROT56874-020-303	15-SEP-2021 00:43:04.81
PTROT56876-010-303	15-SEP-2021 00:49:02.22
PTROT56877-010-300	15-SEP-2021 00:53:12.06
PTROT56879-010-308	15-SEP-2021 01:00:16.31

Strip temperatures are referenced frequently in this body of research. With reference to Figure 49, notice the headings in the table IP2, IP3 and CT, these stand for Infrared Pyrometer 2, Infrared Pyrometer 3 and Coiling Temperature. These reference physical infrared pyrometers on the ROT. Each of these record strip temperatures as it travels along the ROT. Figure 51 shows the approximate location of the IPs along the length of the ROT. IP3 is considered the most important temperature reading for most steel grades, behind CT, since failure to 'hit' IP3 requires intervention from the operators such that an adequate coiling temperature is achieved, which is a good predictor for mechanical properties.
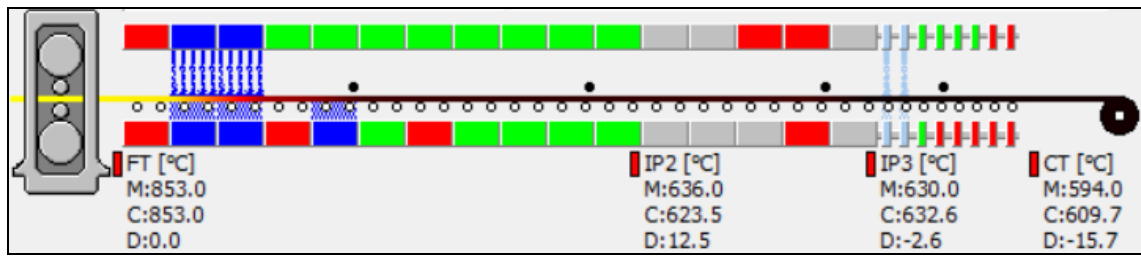
Figure 51- Titan graphics showing approximate locations of infrared pyrometers on the ROT.

2.1.5. Microscopy

2.1.5.1. Sample Prep

For this research project samples were prepared for optical microscopy via sectioning, mounting in resin, as shown in Figure 52. Once samples were mounted in the resin, they were then ground with progressively finer grits; 120, 400, 600, 1200. Samples were then polished using water based polishing mediums, with accompanying polishing cloths, using a suspended diamond solution. Again, with progressively finer solutions; 6µm, 3µm, 1µm. Colloidal silica solution was also used in some instances. Samples were subsequently also etched using 5% Nital solution to reveal a ferrite-pearlite grain structure. In some cases, a 10% solution of Sodium Metabisulphite is used since it is particularly useful in reveal multiple phases in steel microstructures at once[126, 127]. Nital differentiates Ferrite and Pearlite grains effectively, by etching the Pearlite grains to give a darker appearance. Whereas SMB (Sodium Metabisulphite) offers colour differentiation by giving Martensite a brown appearance, Bainite and blue appearance and both Ferrite and Retained Austenite a white appearance[128].

Figure 52- 30mm sample mounted in conductive resin for microscopy.

2.1.5.2. Grain Size Measurement

In the case of grain size measurement, the specification ASTM E112-13(2021)[129]. Grain size measurement is carried out using the Zeiss Zen Core software in accordance with the ASTM E112-13(2021) standard. The below table is used to convert the 'grain size number' into the mean diameter in micron:

Table 5- Macroscopic Grain Size Relationships Computed for Uniform, Randomly Oriented, Equiaxed Grains[129].

Macro Grain Size No.	$\bar{N}_A$ Grains/Unit Area		$\bar{A}$ Average Grain Area		$\bar{d}$ Average Diameter		$\bar{\ell}$ Mean Intercept		$\bar{N}_L$	$\bar{N}$
	No./mm²	No./in.²	mm²	in.²	mm	in.	mm	in.	mm⁻¹	100 mm
M-0	0.0008	0.50	1290.3	2.00	35.9	1.41	32.00	1.2	0.031	3.13
M-0.5	0.0011	0.71	912.4	1.41	30.2	1.19	26.91	1.0	0.037	3.72
M-1.0	0.0016	1.00	645.2	1.00	25.4	1.00	22.63	0.89	0.044	4.42
M-1.5	0.0022	1.41	456.2	0.707	21.4	0.841	19.03	0.74	0.053	5.26
M-2.0	0.0031	2.00	322.6	0.500	18.0	0.707	16.00	0.63	0.063	6.25
M-2.5	0.0044	2.83	228.1	0.354	15.1	0.595	13.45	0.53	0.074	7.43
M-3.0	0.0062	4.00	161.3	0.250	12.7	0.500	11.31	0.44	0.088	8.84
M-3.5	0.0088	5.66	114.0	0.177	10.7	0.420	9.51	0.37	0.105	10.51
M-4.0	0.0124	8.00	80.64	0.125	8.98	0.354	8.00	0.31	0.125	12.50
M-4.5	0.0175	11.31	57.02	0.0884	7.55	0.297	6.73	0.26	0.149	14.87
M-5.0	0.0248	16.00	40.32	0.0625	6.35	0.250	5.66	0.22	0.177	17.68
M-5.5	0.0351	22.63	28.51	0.0442	5.34	0.210	4.76	0.18	0.210	21.02
M-6.0	0.0496	32.00	20.16	0.0312	4.49	0.177	4.00	0.15	0.250	25.00
M-6.5	0.0701	45.26	14.26	0.0221	3.78	0.149	3.36	0.13	0.297	29.73
M-7.0	0.099	64.00	10.08	0.0156	3.17	0.125	2.83	0.11	0.354	35.36
M-7.5	0.140	90.51	7.13	0.0110	2.67	0.105	2.38	0.093	0.420	42.05
				×10⁻³		×10⁻³		×10⁻³		
M-8.0	0.198	128.0	5.04	7.812	2.25	88.4	2.00	78.7	0.500	50.00
M-8.5	0.281	181.0	3.56	5.524	1.89	74.3	1.68	66.2	0.595	59.46
M-9.0	0.397	256.0	2.52	3.906	1.59	62.5	1.41	55.7	0.707	70.71
M-9.5	0.561	362.1	1.78	2.762	1.33	52.6	1.19	46.8	0.841	84.09
M-10.0	0.794	512.0	1.26	1.953	1.12	44.2	1.00	39.4	1.00	100.0
M-10.5	1.122	724.1	0.891	1.381	0.994	37.2	0.841	33.1	1.19	118.9
M-11.0	1.587	1024.1	0.630	0.977	0.794	31.2	0.707	27.8	1.41	141.4
M-11.5	2.245	1448.2	0.0445	0.690	0.667	26.3	0.595	23.4	1.68	168.2
M-12.0	3.175	2048.1	0.315	0.488	0.561	22.1	0.500	19.7	2.00	200.0
M-12.3	3.908	2521.6	0.256	0.397	0.506	19.9	0.451	17.7	2.22	221.9
M-12.5	4.490	2896.5	0.223	0.345	0.472	18.6	0.420	16.6	2.38	237.8
M-13.0	6.349	4096.3	0.157	0.244	0.397	15.6	0.354	13.9	2.83	282.8
M-13.3	7.817	5043.1	0.128	0.198	0.358	14.1	0.319	12.5	3.14	313.8
M-13.5	8.979	5793.0	0.111	0.173	0.334	13.1	0.297	11.7	3.36	336.4
M-13.8	11.055	7132.1	0.091	0.140	0.301	11.8	0.268	10.5	3.73	373.2
M-14.0	12.699	8192.6	0.079	0.122	0.281	11.0	0.250	9.84	4.00	400.0
M-14.3	15.634	10086.3	0.064	0.099	0.253	9.96	0.225	8.87	4.44	443.8

2.1.5.3. Volume fraction measurement

In order to measure the volume fraction of given phases the open-source image processing software ImageJ was utilised. Images are converted into an 8-bit image (black and white), the 'threshold tool' is then used to select all shades within a given range. allows the user to select all pixels of a given phase and therefore calculate the volume of the image (microstructure) selected, therefore calculating the volume fraction of that phase. An example of this process is shown below in Figure 53, with the original micrograph shown on the left and the processed micrograph on the right.
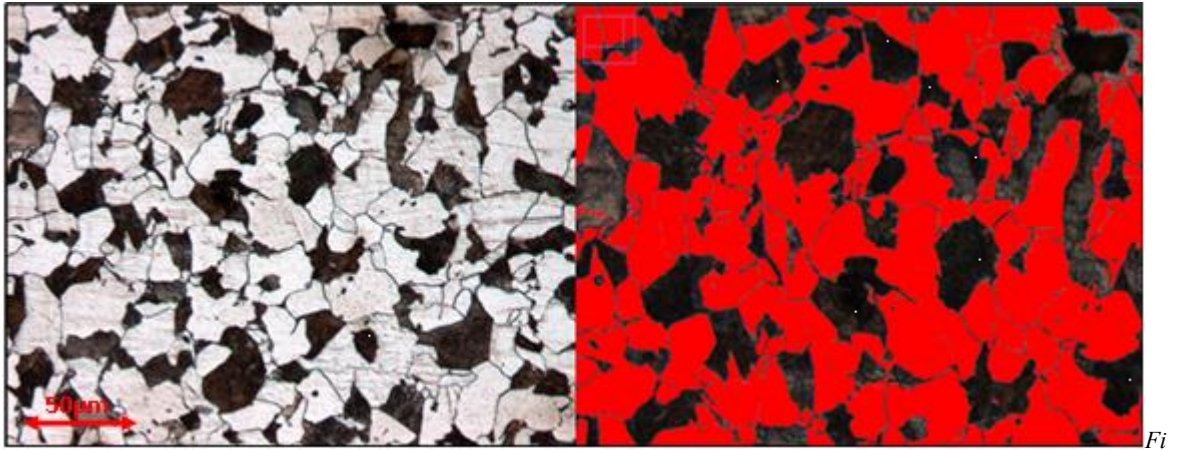
gure 53- Dual phase micrograph processed using ImageJ to select all ferrite grains.

2.2. Tensile

2.2.1. A80 Geometry

A80 tensile samples were prepared for processing of plant produced hot-band material. Tensile samples were water jet cut, so not to create a heat affected zone, potentially affecting the microstructure. Figure 54 shows the drawing from which the tensile samples were manufactured.
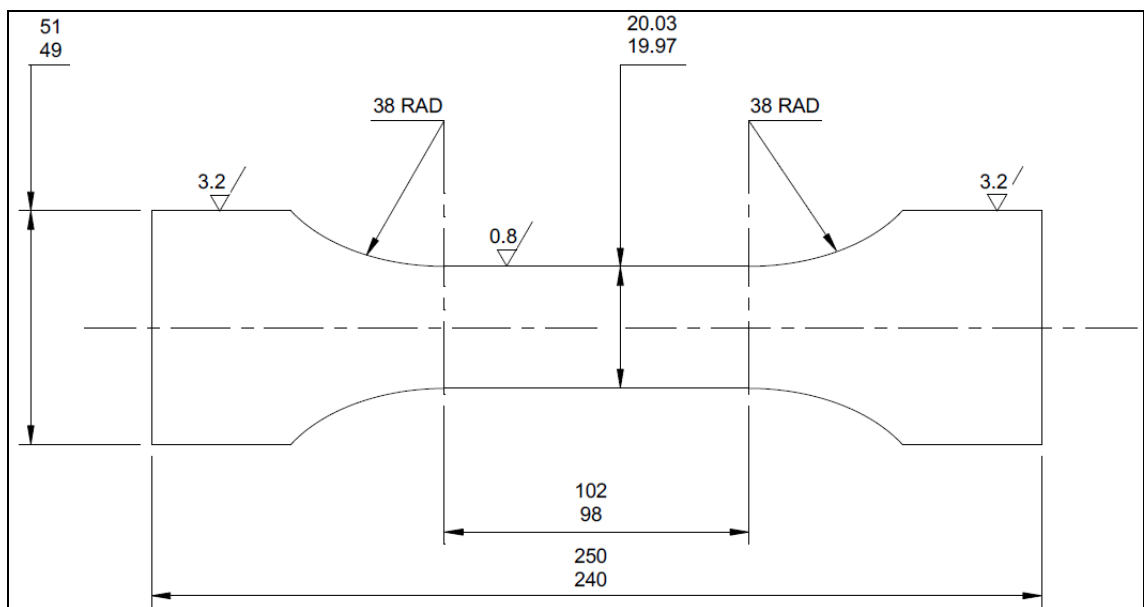
Figure 54- A80 tensile specimen drawing.

All tensile testing was conducted in accordance to BS EN ISO 6892-1:2016[130]. A Dartec universal tensile tester was used to test the tensile specimens. Samples were securely clamped in each end. Sample design a procedure was followed in accordance to BS EN ISO 6892-1:2016, with exception of the use of an extensometer due to the tendance of the

samples to fail rapidly and extensometer was not used, instead the stroke of output from the tensile tester was recorded over time. In any case UTS was used for analysis where extension is not concerned. All samples were extended at a rate of 1mm/minute in order to fully capture the modulus of elasticity as described in BS EN ISO 6892-1:2016.
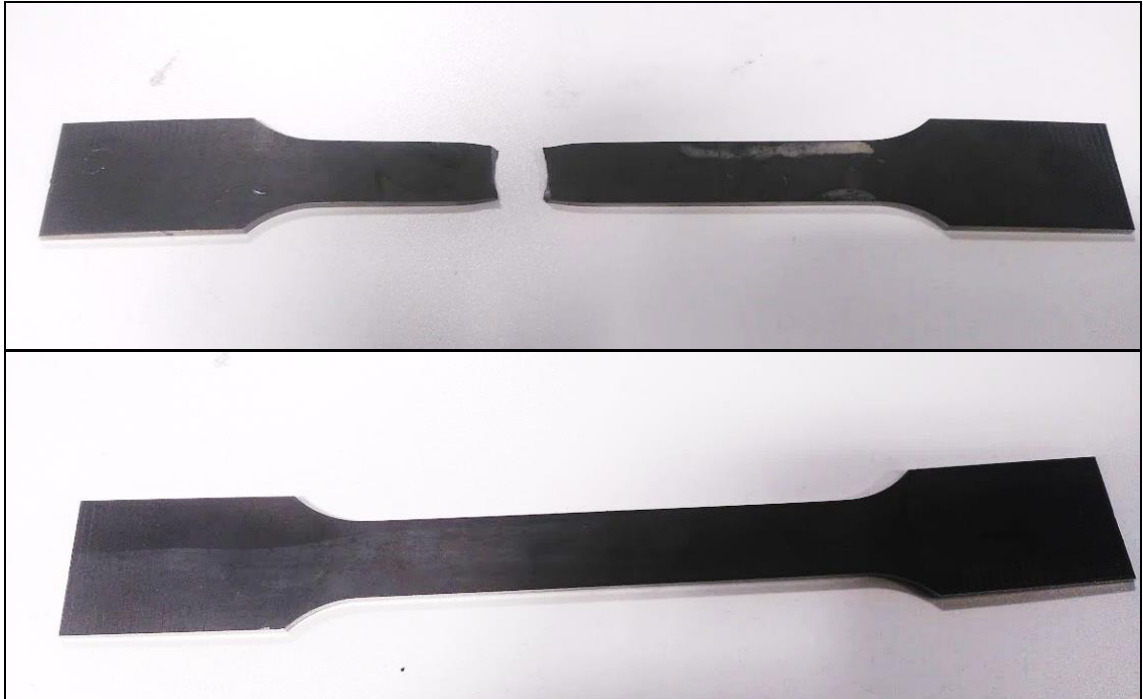
Figure 55-A(top) fractures tensile sample, B(bottom) untested tensile sample, both manufactures from plant produced DP800.

Stress-strain graphs were then plotted, with extension values adjusted to account for mechanical compliance in the system, as well as accounting for the slight curvature in the sample due to previously being coiled after cooling on the ROT. Impact of backlash and sample curvature shown by red circle on Figure 56 below.
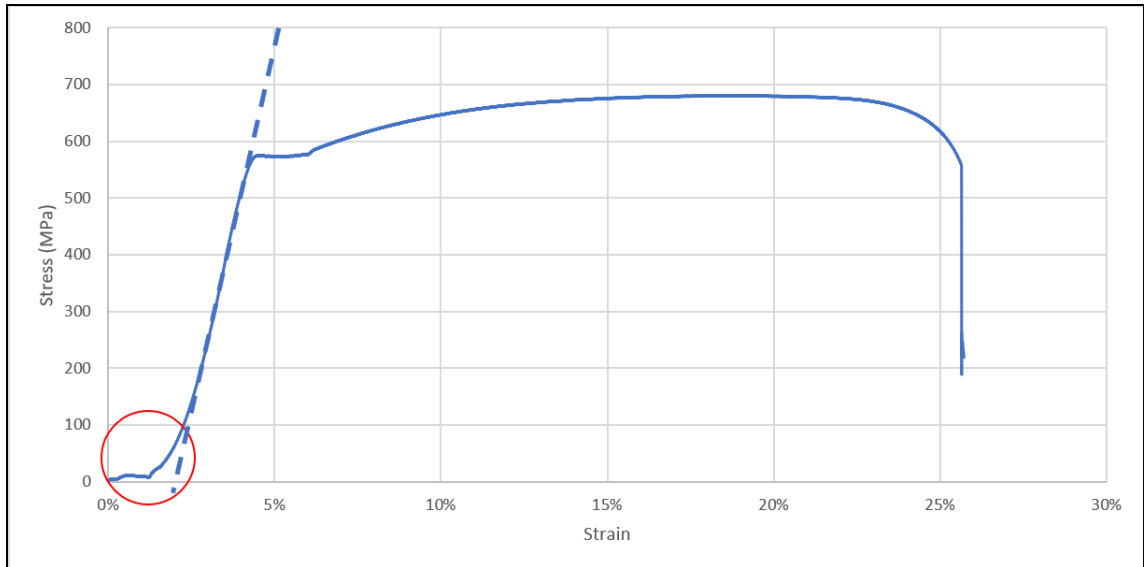
Figure 56- Example of tensile curve without 'backlash' correction.

In order to correct the effect of backlash and sample curvature, the displacement value, at which the proportional rection intercepts the x-axis is offset against the data set. The result of this practice is shown below in Figure 57:
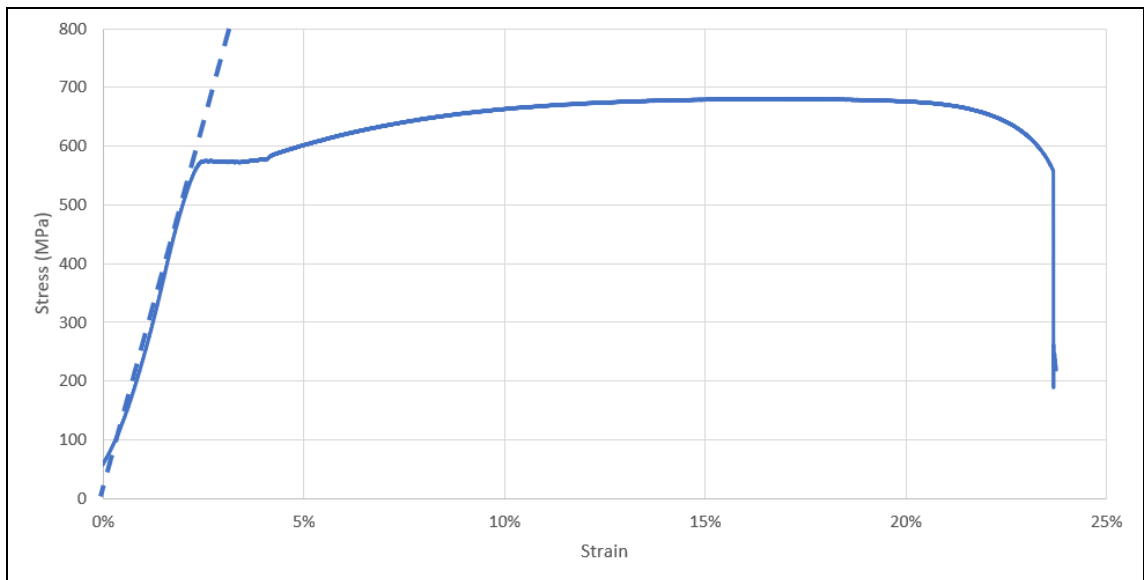
Figure 57- Corrected stress strain curve.

2.3. Plastometry

2.3.1. Introduction to PIP

Plastometry is a novel method of obtaining stress strain curves from material though an indentation type method, similar to a hardness test. Data collected from the materials resistance to indentation, and the profile of the displaced material is input into a finite

element simulation which in turn generates a simulated stress strain curve. A labelled diagram of the plastometer is shown below:

Figure 58- Labelled diagram of plastometer[131].

This allows smaller samples, which cannot be manufactured into larger A80 type tensile specimens, to be analysed and approximate mechanical properties determined. Two indenter tips are available, the larger indenter is generally preferable but limited to samples with a thickness of 3mm or more. The smaller indenter tip is suitable for samples of 1.5mm thickness or greater. More details of sample requirements are given in Table 6.

Table 6- Plastometrex Sample Requirements, adapted from PIP user manual[132].

Feature	Requirements
Sample Dimensions (1mm radius tip)	Thickness range ~3mm to 70mm Lateral range ~6mm to ~150mm
Sample Dimensions (0.5mm radius tip)	Thickness range ~1.5mm to ~70mm Lateral range ~3mm to ~150mm
Required Surface Finish	$R_z <~3\mu m$. This can be obtained using a relatively coarse abrasive paper. Polishing is not needed, although of course a polished surface is fine.
Sample Surface Tilt	Preferably low, although about 1° is acceptable.
Sample Material	Metallic only
Sample Mounting	Mounted or Unmounted

This piece of equipment has potential to be hugely beneficial to the Prosperity Partnership's goals of Rapid Alloy Prototyping, by allowing stress strain data to be rapidly determined for a range of samples. This is particularly beneficial in the laboratory setting in which is it far more convenient to create small amounts of novel alloys, whereas previously in order to make A80 tensile samples, much larger amounts of material would have to be cast.

2.3.2. Sample Requirements

Experimentation carried out by students at Swansea University has determined that for steel samples, a grinding operation using '1200 grit' griding paper is the minimum requirement for surface finish, without compromising results. It has also been determined from previous experience that when testing rolled, or previously coiled material, as seen in the steel manufacturing process, that the curvature of the material can prove problematic. The curvature can provide compliance in the specimen, allowing the sample to flex when indented, which in turn affects the accuracy of the measurement. Therefore, in this case samples should be sectioned and mounted.

2.4. Laboratory Hot Rolling

2.4.1. Pre-Heat

The Nabertherm furnace is typically switched on four hours prior to samples being placed inside the furnace, in order to heat to 1250°C to replicate the slab reheat furnace. Sample are then left placed in typically for two hours to allow any precipitate forming elements to fully dissolve, 2 hours is also chosen to provide a repeatability to all samples. The first hour allows the block to reach a homogenous temperature, the second hour allows sufficient normalisation of the grain structure to a fully austenitic phase. The samples are then removed, with two operators; one to open the furnace door and the second to remove the sample with steel tongs. The sample is then placed on a bench and hit with a pick hammer to remove any scale that has built up on the block surface.

2.4.2. Hot Rolling

The roll gap per pass, often referred to as the 'rolling schedule' is programmed by the user prior to rolling. In theory infinite passes can be programmed in by the user. In practice no more than ten passes are typically used, due to decreases in strip temperature resulting in large rolling loads.

Once the sample is descaled it is placed in the roll bite, with the roll gap at the first pass setting. Once the sample has passed through the rollers, it is received by the second operator. Once received by the second operator, the first operator reverses the rolling direction, triggering the mill to automatically reduce the roll gap to the second pass position, previously programmed into the mill. This process continues until the lass pass, typically seven in total. Then the sample is transferred by and operator to the ROT. During the rolling process, mill loads and temperatures at the entry and exit are recorded and later exported for analysis. Inter-pass temperature varies as a function of strain, sample size and number of rolling passes.

2.4.3. ROT

Once the final pass is completed, the operator moves the sample directly to the ROT where the conveyor-rollers are rotating ready to deliver the sample under the path of the water headers. The setting available for the user to vary on the ROT, similarly to the Port Talbot ROT, is the roller speed and the water delivery. Unlike the Port Talbot ROT the flow rate cannot be controlled, however the number of headers open can be changed. Each header can be individually isolated by a ball valve, for both the top and bottom banks. The roller speed is controlled by an analogue motor controller, the speed is selected via a dial, reading between 1 and 8, with 8 being the fastest. Increasing the speed of the ROT is

associated with a decreased cooling effect of the water, alternative the number of headers can be also decreased. Figure 59 shows a sampled after being immediately placed on the ROT entering the water headers.

Figure 59- Hot rolled sample entering the ROT water sprays.

2.4.4. 'Coiling' Furnace

Once the strip has been water cooled, and the surface temperature logged, an operator will remove the strip from the roller conveyor and place it into the 'coiling' furnace. The furnace is typically set to 610°C where it remains for approximately five minutes, then switched off and allowed to cool slowly. Figure 60 shows operators placing the water-cooled sample into the Carbolite furnace. Similarly to the reheat furnace this is also switched on several hours prior to rolling to allow the furnace to reach the desired coiling temperature for the steel grade being rolled.

Figure 60- Operators placing rolled sample into 'coiling' furnace for a slow cool.

2.4.5. Mill Output- Results Interpretation

Much of the experimental results of this research will be focussed upon the temperatures at which the samples are being hot rolled. Therefore, the method used to determine these temperatures is described. Below shows a typical Mill temperature readout for a 7-pass schedule, with temperature measured at the mill entry and exit.
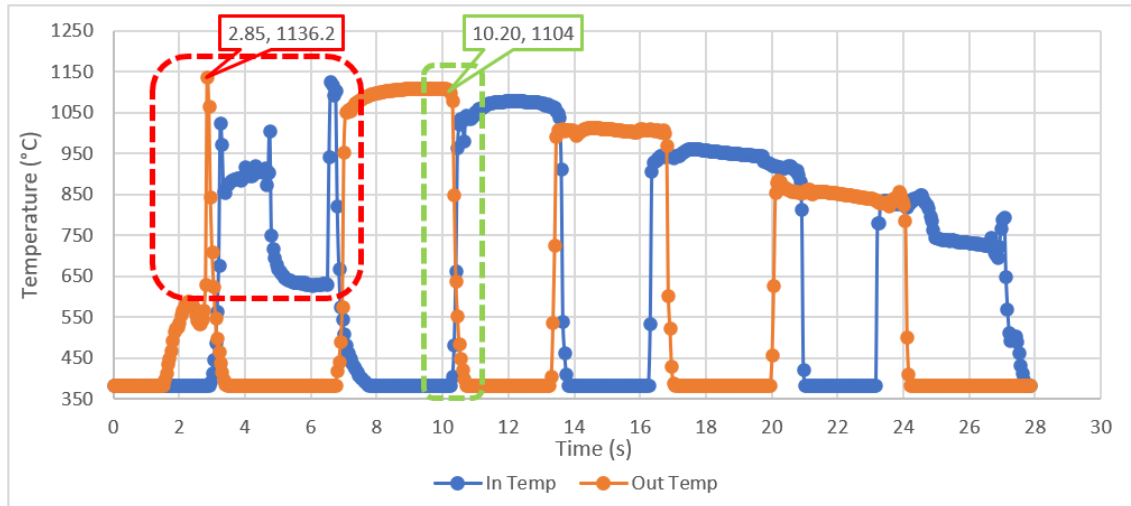
Figure 61- Example of a typical 7-pass temperature output from the laboratory hot mill.

The blue and orange lines on the above graphs shows the temperature readouts of the mill entry and exit respectively. Note the default reading of the sensors is 385°C, this reading is given when a material is less than the minimum temperature that can be detected by the sensors, so should not be used considered when evaluating hot rolling temperatures. The green dashed box denotes the 3rd rolling pass, since the point at which there is a temperature reading from both the mill entry and exist is when the approximate centre of the strip is between the rollers, therefore for the purposes of this research the maximum temperature in this rection is considered to be the inter-pass temperature (as shown by the data point call-out box in the above figure). The red dashed box shows a region of apparent instability in the temperature measurement. This can be due to a number of factors, such as the sample not being rolled in the centre of the mill and therefore only momentarily passing under the IR pyrometer, or the presence of surface scale affecting the emissivity of the strip. In this case the maximum reading should be taken since this will likely correspond most strongly with the core temperature of the strip which is the most critical temperature when evaluating hot rolling operations with respect the recrystallisation.

The load output for the mill is evaluated in a similar fashion. The below figure shows the load readout for the same sample shown in Figure 61, as a function of time:
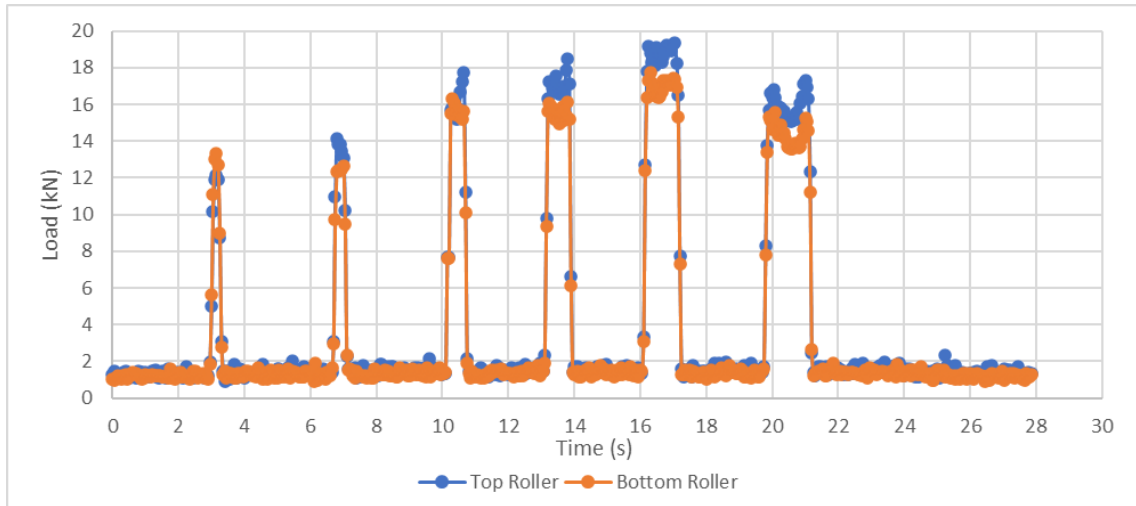
Figure 62- Load readout for a 7-pass schedule from laboratory hot mill.

As denoted by the key in the above figure, the load outputs from the load cells, for both the top and bottom rollers are shown for a typical seven pass rolling schedule. The peaks in the readings show when the steel sample is between the rollers. For the purposes of experimental analysis, the peak loads for each roller passes are summed and used for any subsequent calculations. (Note this particular rolling trail implemented a 'dummy-pass' on the last pass, in which the sample was passed forward through the mill so a temperature reading is recoded, but no reductions are imparted to the strip, meaning no load is output from the load cells is registered).

These peak values can be processed and compared with other rolling schedules for a like for like comparison, allowing for a more convenient analysis of results. An example of this is given below:
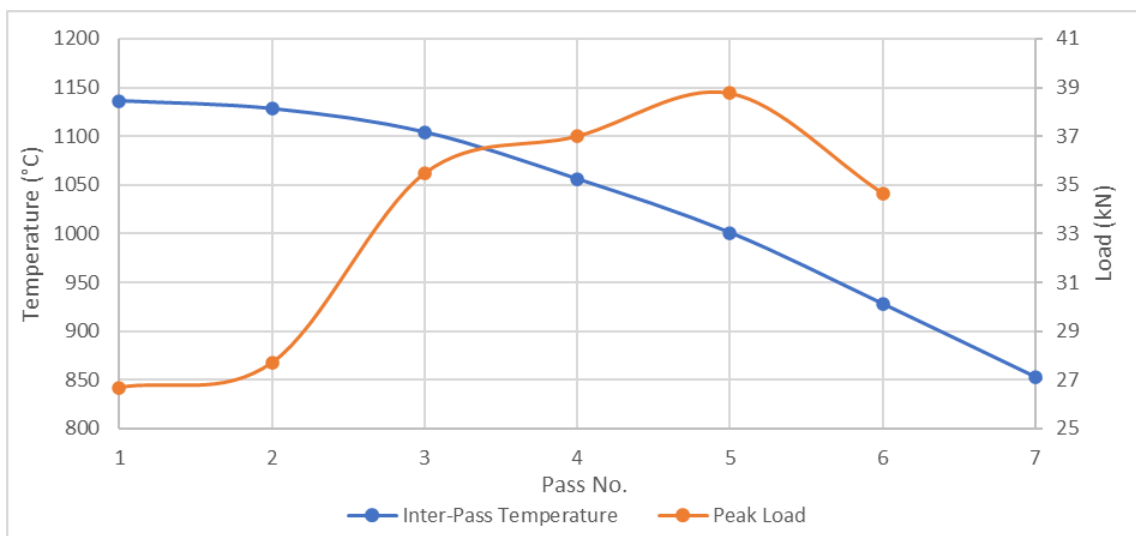
Figure 63- Inter-pass temperature and peak load output from laboratory hot mill for a typical 7-pass rolling schedule.

2.5. Titan Model Setup

In order to use titan for the desired application, the user must first replicate the industrial section to be studied. The setup used for the majority of the research described in this thesis uses the '*ROT Port Talbot LC.xml*' Setup. The '.xml' is a file format used by Titan to describe the assets within the model, assets include but are not limited to; roller stands, coilers and run out tables.

The setup shown in Figure 167 is '*ROT Port Talbot LC.xml*', note that despite the hot rolling process not being modelled, a 'stand' is still required to initial the simulation. Additional assets can be added to the simulation by clicking on the asset icons in the 'General' tab, for instance several roller stands could be added in order to model a hot mill.

Once the desired assets are in place, the journals from which the simulation receives its key inputs, such as chemical composition, must be uploaded, as shown below:

Once the journals are uploaded to the setup, numerous files will appear on the left-hand pane. If studying one coil, numerous files will appear for that coil with each file representing a 'section' of that coil. Further explanation is given in section 2.1.3. Much of the comparative analysis undertaken in this thesis utilised graphs of ROT outputs. In order to create such a graph, the user must define the both the x and y axis. With reference to Figure 169, the x axis is defined by 'Base axis'.

A typical output from Titan is shown below, listing strip temperature at the top, bottom, and middle of the strip. The transformation is also listed for both ferrite and pearlite which are the expected phases in at this stage in the manufacturing process.
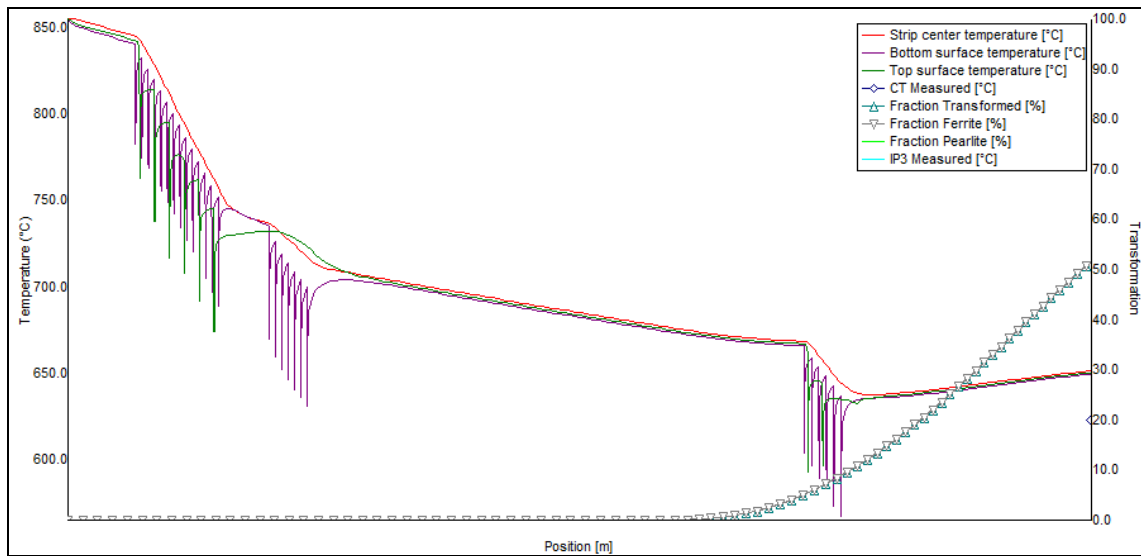
Figure 64- Typical Titan output, displaying both strip temperature, and transformation for a given position at default settings.

Lastly a 'Cumulative' file was created, this has the benefit of being able to compile the results of multiple journal files in one table, summating the variables or reporting the final variable (such as final transformation, or final temperature). As shown in Figure 170, the cumulative file is created under output options, file options.

The variables to be recorded are then selected. Figure 171 shows the available outputs that can be included in a similar method to the creation of the graph shown earlier.

2.6. Jmat Pro

JMatPro is a simulation tool used for calculating various material properties based upon a chosen chemical composition[133]. It is capable of modelling a range of material alloys, including Aluminium Alloys, Magnesium Alloys, Cast Iron, General Steels, Stainless Steels, Cobalt Alloys, Nickel Based Superalloys, NiFe Based Superalloys, Titanium Alloys, Zirconium Alloys, Solder Alloys and Single Crystal Systems[133]. The work in the following Thesis will utilize the General Steels model of the software. Once the desired chemistry is created a number of simulations can be performed allowing the user to extract various outputs. JMatPro is capable of creating CCT and TTT curves, based on chemistry, which is useful when designing new alloys with a particular heat treatment in mind. Mechanical properties can also be modelled based not only on chemistry but also a design heat treatment. The mechanical properties available to the user are; strength (yield), hardness, flow stress-curves, creep and rupture/life strength, conversion between strength and hardness, forming limit diagrams and processing maps[133]. Unlike other programs, JMatPro does not include data from literature within the models, it utilises physically based

models which have been validated. The claimed advantage is that the model 'avoids' variation in results due to experimental differences, resulting in a consistent and predictable material model[133].

In order to setup the Jmat Pro software the user must create a material file, this simply describes the steel chemistry to be studied. The composition can be saved for analysis later on or modified. Many of the simulation tools in JMatPro require a user defined starting grain size, for the purpose of this research, based upon industry recommendations, the initial grain size, upon entry to the hot mill is assumed to be 10μm.

2.7. OES

OES (Optical Emission Spectroscopy) is an analysis method used to determine the elemental composition of materials, in this case steel. In order to confirm the cast chemistry of VIM produced DP800 samples OES is conducted in instanced incorrect chemistry is suspected. OES works by creating a high voltage current between the samples in question, and a conductor close to the material surface. As a result of this high energy interaction, the surface of the material is vaporized and electromagnetic energy is released, broadly between the infrared and ultraviolet range. These wavelengths are separated by an optical sensor in which each wavelength corresponds to a specific element. This process is repeated a number times to create an average result over the length of the sample such that a reliable mean can be created. The standard operating procedure for the SAMI labs, when conducing OES is to complete a total of eight emissions and the mean and standard deviation is recorded. Samples should be free of contaminants and measure at least 20mm by 20mm. The specific equipment used in this research, within the SAMI laboratories, is a SPECTROLAB Spark OES, shown in the image below:

Figure 65- SPECTROLAB Spark OES [134].

3. Benchmarking

3.1. T_{NR}

In order to attempt to control and influence transformation characteristics in the finishing mill and Run Out Table, the key temperatures must be determined. Mathematical models to predict T_{NR}, as a function of chemistry as well as both chemistry and strain are outlined in section 1.7.1.1.1. As discussed previously, the TNR is essential in determining downstream grain refinements and 'pancaking'. Therefore in order to predict this the product chemistry is input into the equations described in section 1.7.1.1.1:
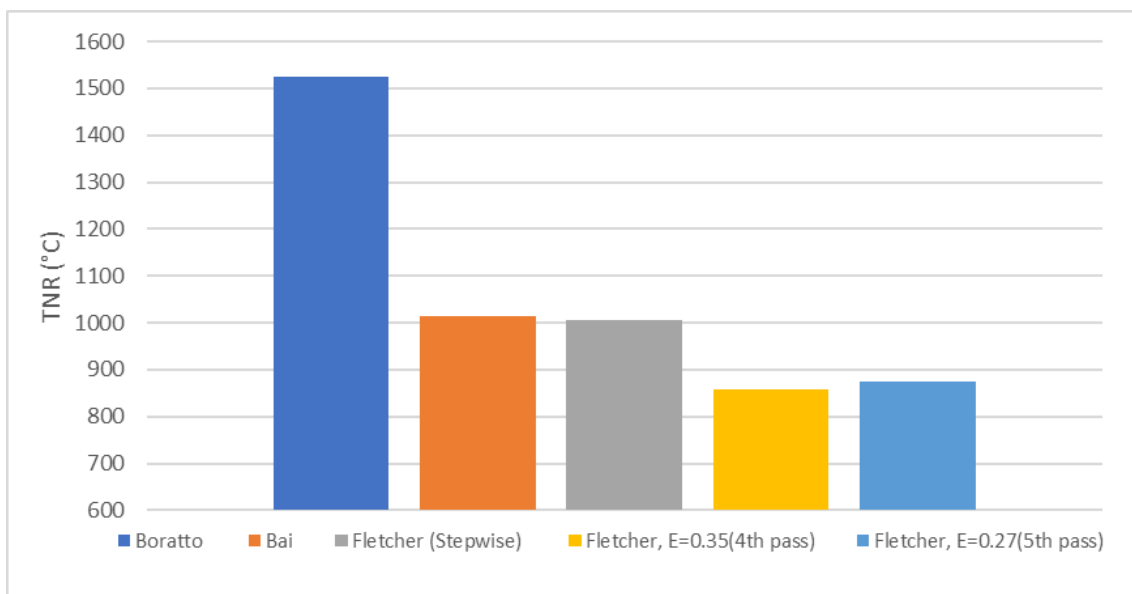
Figure 66- Comparison of reported T_{NR} values, based upon Tata Steel DP800 product chemistry using different proposed mathematical models by Boratto, Bai, Fletcher (with stepwise regression), Fletcher (considering strain in the 4th mill pass) and Fletcher again (considering strain in the 5th mill pass).

The T_{NR} of Nb bearing microalloyed steels has been successfully determined experimentally by M. N. Akhtar and colleagues, which DP800 can also be considered[61]. Through multi hit compression testing it was determined that the T_{NR} of studied grade was 951°C. It is therefore likely that the result for the Boratto equation is incorrect, whereas the results determined from the Bai and Fletcher models are more likely to be correct. This is in alignment with the findings of Homsher and colleagues, when studying Nb bearing steels, the Bai equation was found to be the best match when compared to experimental data, also utilising multi hit compression testing[60]. Therefore for the purpose of this work the T_{NR} is assumed to be in the range of 990°C and 1010°C.

3.2. Mechanical Testing of Hot-Band Material and Plastometry

3.2.1. Justification and Background

One key processing parameter on the ROT is the water header flow rate. This has a large bearing on the strip microstructure and by extension the mechanical properties. Plant produced transfer bar material was provided by Tata Steek UK, from the Port Talbot Hot Mill. 20 Samples total were provided, each has undergone a slight variation in heat treatments. FRTs and CTs were provided for each sample. These were cut into A80 tensile samples and tested. This initial investigation into plant produced material provided insight into hot bad microstructure as well as a mean of validating the novel mechanical testing method (Plastometry) for DP800 material. The material chosen was removed from a plant produced DP800 coil, from a section of the coil that would otherwise be discarded due to local temperature variation, such that no compromise in quality reaches the customer and other downstream processes.

3.2.2. Tensile Results
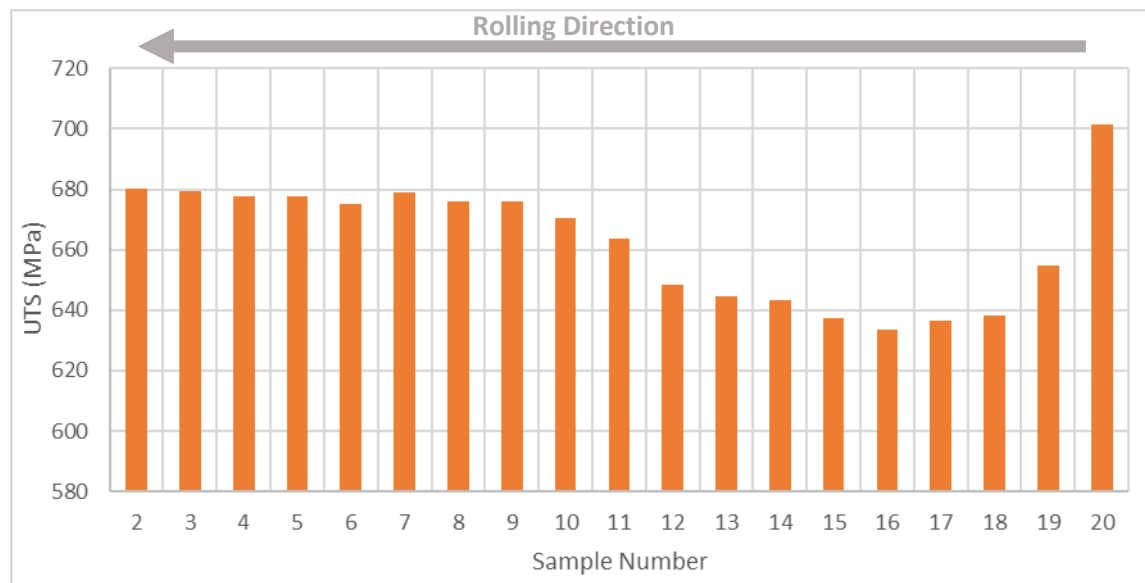
Figure 67- UTS of TSUK Hot-Band samples.

Figure 67 shows the measured UTS from the A80 tensile samples. Sample No. 1 slipped from the jaws of the tensile tester, therefore the result was omitted, since some elongation had occurred, likely work hardening the sample and therefore compromising the accuracy.

It can be seen the UTS is stable between samples 2 and 10, remaining between 670 and 680MPa, however dips quickly with the lowest being sample 16 with a UTS of 633MPa, but then rising sharply again to where it peaks at the rear of the sample to 701MPa. For

reference the expected UTS for DP800 strip (hot band material) is expected to be approximately 680 MPa.

3.2.3. Micrographs

Grain size analysis was conducted on the tab ends of samples; 2, 4, 8, 16 and 20. The tab end of the tensile samples were used, to ensure that any grain size analysis was done outside the deformed gauge length of the tensile specimen. These samples were chosen to capture the majority of the 'stable region', spanning from sample 2 to 9, as well as capture the highest and lowest UTS samples which are 20 and 16 respectively. The average grain size measurement for each sample is given below:

Table 7- Grain size analysis across hot band sample width.

Sample No.	ASTM Grain Size No.	Equivalent Grain Size (μm)
2	14.0	2.8
4	14.0	2.8
8	13.5	3.3
16	13.0	4.0
20	13.0	4.0

As expected, all samples exhibited a ferrite pearlite dual phase microstructure, one such example is given below at both 10x and 100x magnification. With reference to Figure 68 the banded microstructure is evident from sample 8 as a result of hot rolling. The darker grains seen in sample 8 are perlite formations and the lighter ferrite.

Figure 68- Micrograph of tensile sample 8, at 10x magnification.
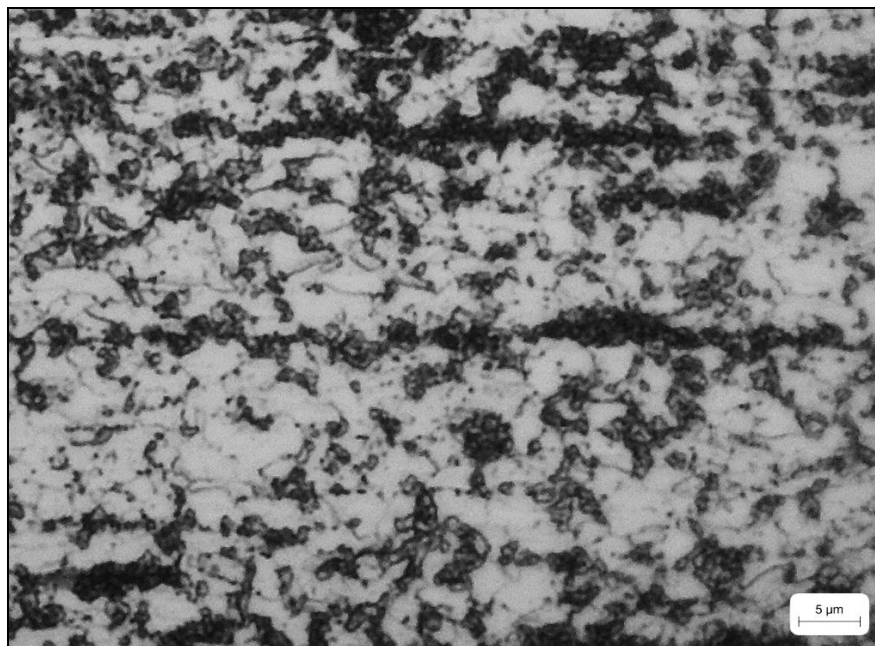
Figure 69 -Micrograph of tensile sample 8, at 100x magnification.

Volume fractions of each phase for samples 2, 4, 8, 16 and 20 were also analysed using ImageJ, using the process described in section 2.1.5.3. 50x magnification was used to ensure that areas would capture a mixture of ferrite and pearlite formation, due to the nature of the banded microstructure using too high of a magnification would result in unrepresentative volume fractions being reported.

Table 8- Microstructural volume fractions from tensile samples.

Sample No.	Pearlite Volume Fraction (%)
2	21.74
4	23.45
8	22.81
16	18.30
20	28.56

3.2.4. Temperature Profiles

Temperature profiles, provided by Tata Steel UK are given below such that the temperature profile of each tensile can be compared.
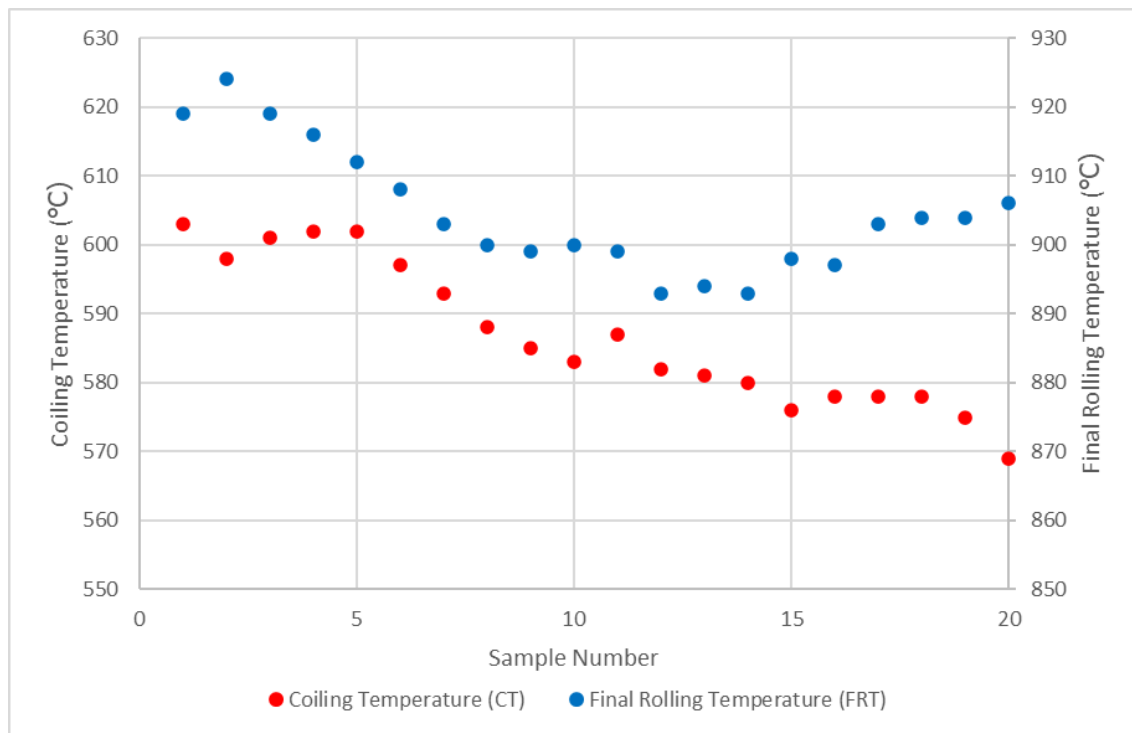
Figure 70- Comparison of coiling temperature variation and finishing temperature variation, for each DP800 sample.

3.2.5. Discussion

The relationship between the coiling temperature and finishing temperature seem to be proportional relationship on the left-hand side of the graph (between samples 1-8) broadly. However, this relationship does not continue beyond sample 12 interestingly. With reference to the average grain size analysis conducted and shown in Table 7 it is clear that the grain size is somewhat constant in, with a slight increase in average grain size in

samples 16 and 20. Interestingly samples 16 and 20 reported the lowest and highest UTS results respectively. It could therefore be suggested that the mechanical properties are a result of variations in phase volume fractions of pearlite. This would be expected, with reference to a DP800 CCT curve, as seen in Figure 81, since higher cooling rates would be associated with larger volume fractions of Pearlite. In order to confirm this, the cooling rate was illustrated by the difference in Finishing temperature and Coiling temperature, both of which are shown in Figure 70 and the volume fraction of pearlite was compared below:

Figure 71- Comparison of temperature change over ROT (FRT - CT) and measured perlite volume fraction for samples 2, 4, 8, 16 and 20.

It can be seen from the above figure that there is some correlation between the total temperature loss over the ROT (for each given sample), which can be considered to be a proxy for cooling rate (since strip speed was constant in this region of the strip), and the phase volume fraction of ferrite. This is particularly apparent in samples 16 and 20. However there is some discrepancy regarding this trend especially in sample 8 which does not follow this trend as closely.

3.2.6. Plastometry Validation

The purpose of this study is two-fold; to analyse plant produced strip properties, and to validate Plastometry as a novel method for validating mechanical properties of steel samples. Firstly, in order to compare the A80 tensile samples and the Plastometry method the tab ends of the tensile samples were cut off, mounted and ground to 1200 grit finish. As shown below in Figure 72.
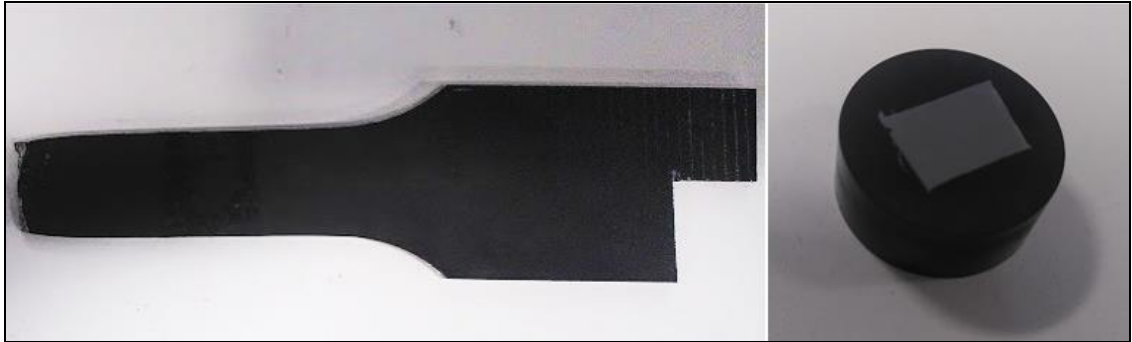
Figure 72- Tensile tab end sectioned and mounted in resin.

Each mounted sample underwent indentation and profilometry three times, ensuring appropriate spacing was used such that it satisfied the recommended requirements outlined by LPX, as shown below in Figure 73.
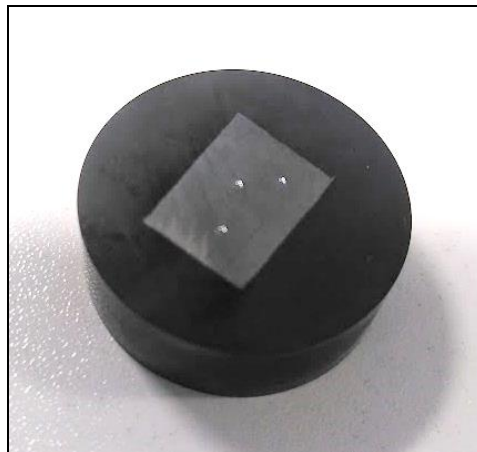
Figure 73- 32mm mounted sample with Plastometry performed 3 times, with 6mm spacing.

The average of the UTS readings are shown below and overlayed with the UTS readings from obtained from the A80 samples. Note all mounted samples in this study were taken from the bottom of the tensile bars.
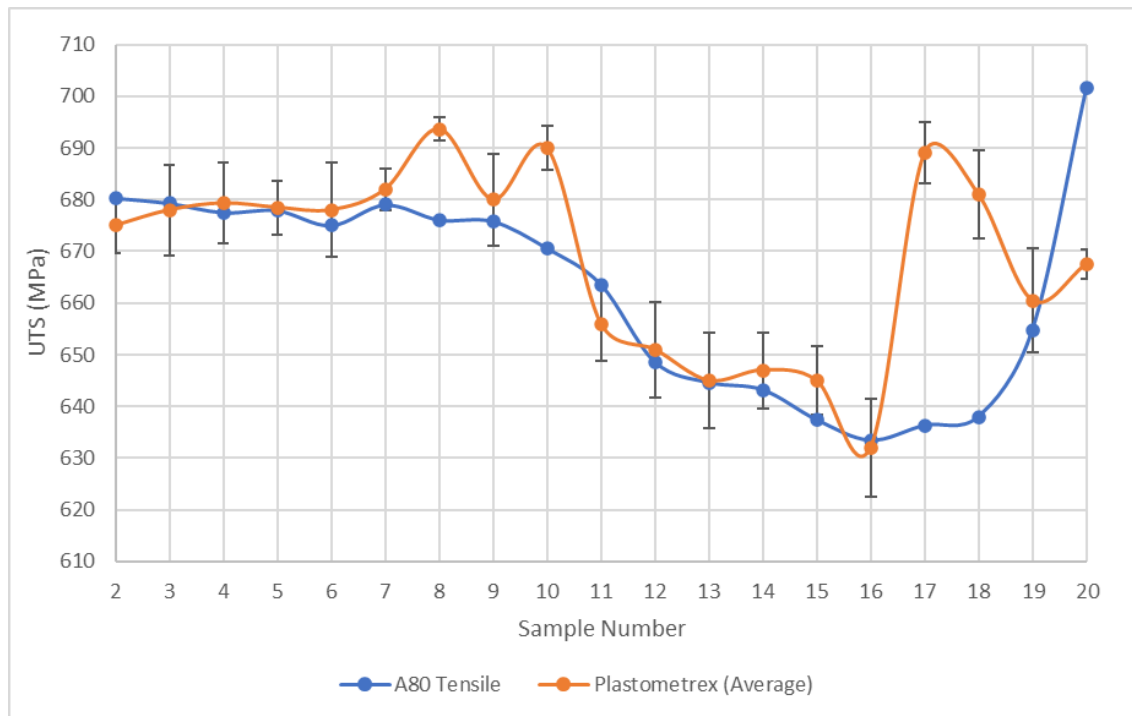
Figure 74- Comparison of Plastometry values and A80 tensile UTS values.

It can be seen that generally a good convergence was seen between the Plastometrex results and the A80 UTS, with the exception of samples 8, 10, 17, 18 and 20. Excluding the named samples a percentage difference of less than 1% was achieved. Note that the standard deviation (obtained from the averages of the three results) does not extend or overlap the respective A80 tensile result. Assuming the rest of the samples are an accurate prediction of UTS, this bi-modal relationship would suggest that the properties at the tab ends deviate from the properties in the gauge length of the sample, showing that the mechanical properties and therefore microstructure also varies along the length of the tensile bar to some degree.

In order to investigate this further the top end of sample 17 was again cut off and prepared for Plastometry, allowing for comparison of results at the top, middle and bottom of a single tensile sample, shown below in Figure 75.
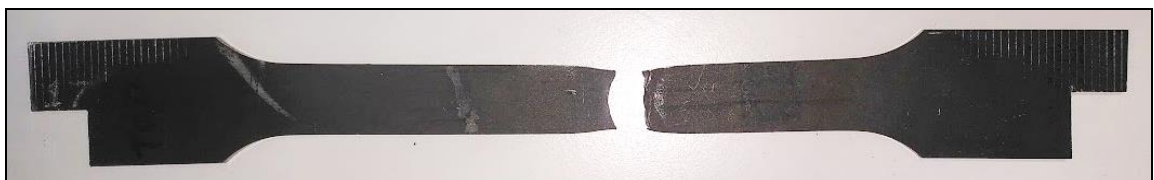
Figure 75- Tensile sample with both top and bottom sectioned.

The results are shown below, again with the standard deviation obtained from the average of the three indents performed per sample.

107
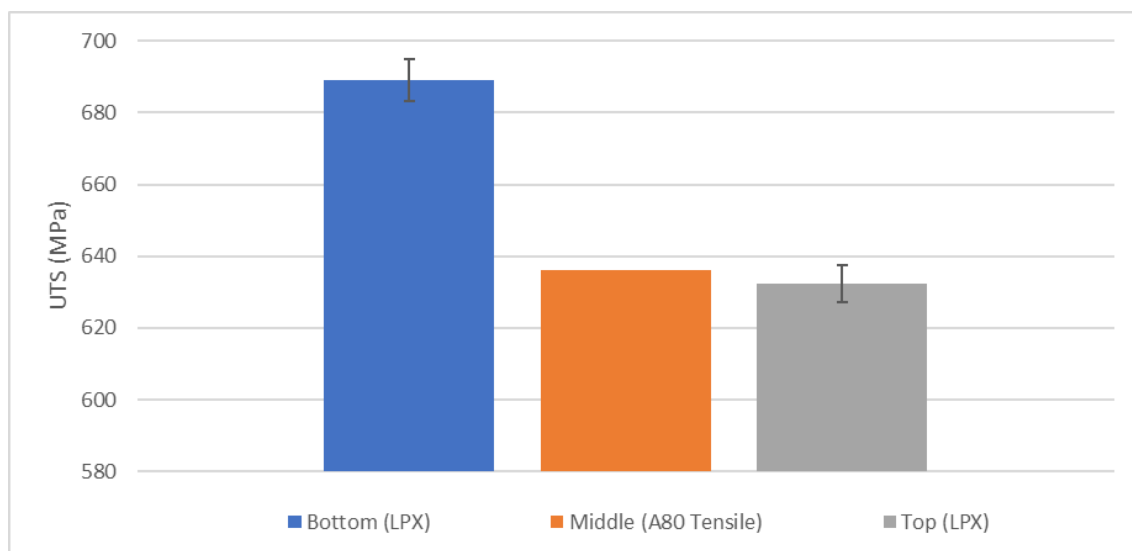
Figure 76- Comparison of UTS from bottom, middle (gauge length) and top of A80 tensile specimen No. 17.

The above figure illustrates the bi-modal nature of the mechanical properties along the length of the tensile, with the top of the tensile samples conforming much better to the UTS measured from the A80 samples, whereas there is a difference of approximately 50 MPa between the bottom of the sample and the A80 UTS.

3.2.7. Conclusion

To conclude this section shows that strip mechanical properties can vary to some degree locally for a section of plant produced DP800 tensile bar, in some areas (since this phenomenon was not present on all tensile samples in the plant produced strip). This shows that differences observed in UTS between the LPX and the standard A80 tensile, are not due to inaccuracies of the plastometry method, but rather due to the difference in material properties in the gauge section of the tensile vs the tab ends. Despite these variations in mechanical properties this is not a commercial issue for DP800 since in order to obtain its final microstructure (described in section 1.1.3) and associated mechanical properties is much be annealed which 're-sets' the microstructure making properties at the hot band stage irrelevant. In addition to this, this section of the strip is routinely discarded since it is known to have varying mechanical properties, but was well suited to evaluate the LPX. Some correlation was seen in the volume fraction of pearlite and the UTS determined by both Plastometry and A80 tensile.

In addition to this Plastometry is also a successful method in capturing mechanical properties locally which otherwise would not be possible, particularly in the case for small samples were it is not possible for tensile samples to be made. For this reason, Plastometry

is performed in assessing the mechanical properties quickly and efficiently for laboratory produced hot band material for the remainder of this thesis. It has also been noted, that for small sample sizes, such as those produced by the RAP route, Plastometry provides a key method of evaluating the mechanical properties quickly when there is insufficient material to produce a tensile sample.

3.3. Lab Scale Hot Rolling

3.3.1. Water Flow Rate Study

Water flow rate in run out table cooling operations is a key parameter in dictating the cooling rate, and therefore transformation of the steel sample. As such it is essential to benchmark the water flow rates from the headers, to compare to plant processes and therefore compare theoretical cooling rates. The flow characteristics of the laboratory ROT are to some degree affected by its design, since it is a gravity fed system.
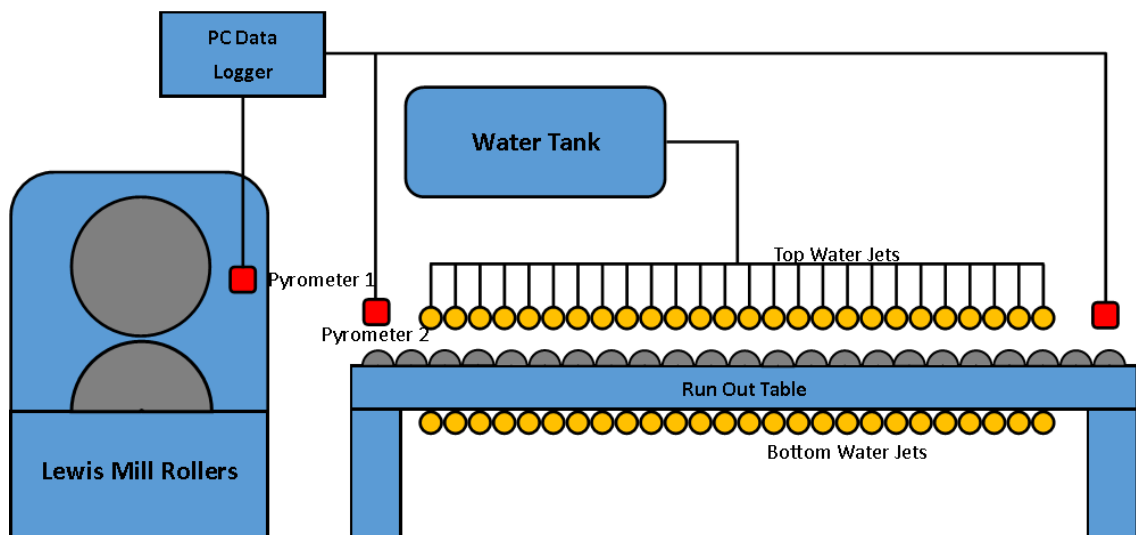
Figure 77- Laboratory Mill and ROT Diagram, showing header tank, pyrometer location and water spray headers.

Figure 77 shows the layout of the lab mill and ROT. The water headers are situated above and below the ROT, mimicking an industrial plant setup. They are fed by a header tank situated approximately 2m above ground level. In standard operation the ROT automatically opens the users chosen headers after the 4th mill pass. This design feature was implemented so that the tank wouldn't prematurely empty, and therefore effect the flow rate since the height of the water in tank is proportional to the pressure at the header outlet. As described by the hydrostatic pressure equation:

$$P = \rho g h \hspace{6cm} \textit{Equation 24}$$

Where: P   Fluid Pressure

                     ρ Fluid Density

                     g   Acceleration due to gravity

                     h   Height of the fluid

However, a flaw in the system is that the headers will open regardless of the degree to which the tank is full/ empty, therefore if consecutive runs are carried out without leaving adequate time for the tank to fill this may result in insufficient flow rates and therefore cooling. To mitigate the effect of this possibility a study was conducted to observe the pressure variation in the water flow rates over time:
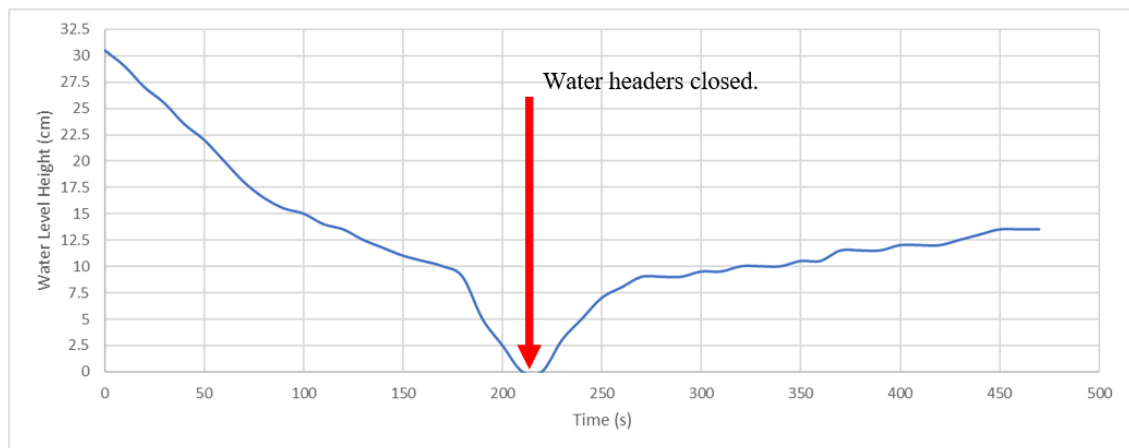
Figure 78- Variation in water level height in tank over time, with top bank open and bottom bank closed.

During the study only the top header bank was left open in order to slow the total flow rate out of the tank so height measurement could be recorded more easily. The water level height was recorded every ten seconds. The tank was allowed to fully drain, until 210 seconds. Then the headers were shut off so the water tank could refill. Measurements stopped after 480 seconds, however based on the flow rate from the fill pipe the time taken to fill the tank from empty was estimated to be approximately 850 seconds.

In addition to the above study, and investigation was carried out to compare the flow between the top and bottom headers. It was speculated that the flow rate from the bottom headers was higher than the top due to the difference in pressure heads, since height is proportional to pressure and therefore flow rate, see equation 11. This was confirmed by again recording the time for the tank to drain, with the only he top headers open, then the

bottom open and then both open, and the flow rate determined by dividing the volume of the water by the total time. This experiment was repeated with different combinations of headers open and closed to record the flow rate in these configurations. It was noticed that the sum of both the top and bottom individual flow rates was greater than the flow rate of both headers being open, this is likely due to increased velocities in the pipe at the outlet of the tank resulting in a 'bottle neck' due to a uniform tube diameter being used throughout the system. As shown in Figure 79 and Table 9.
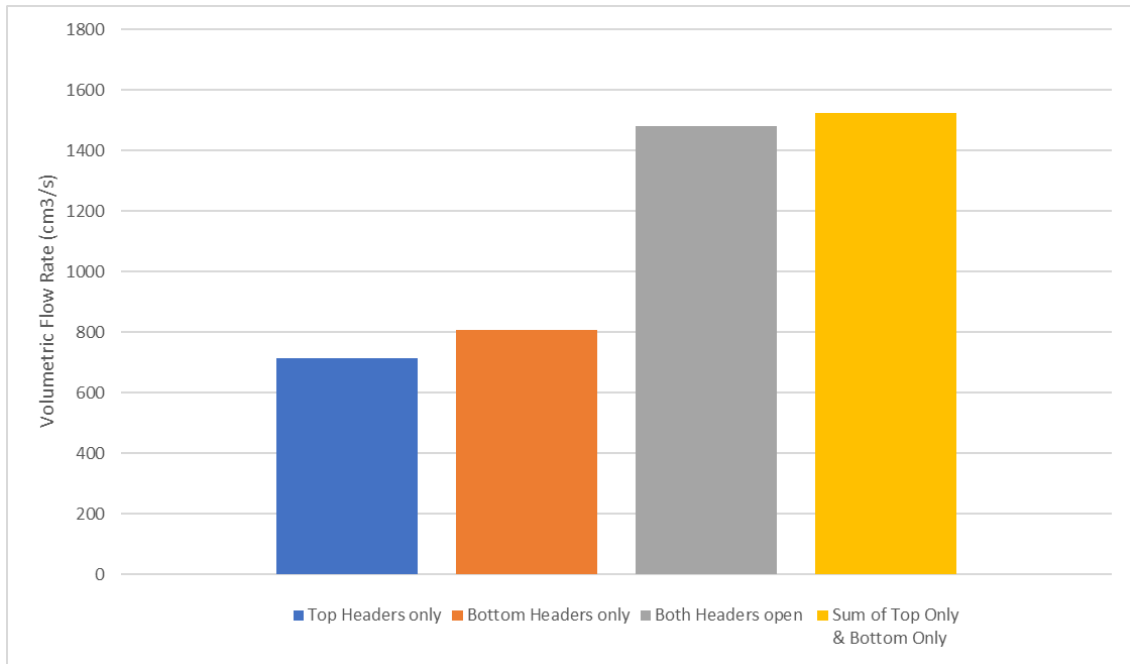
Figure 79- Comparison of Laboratory ROT header flow rates.

Table 9- Water header flow rates for Laboratory ROT.

	Drain Time (s)			Average	Volumetric Flow (cm³/s)	Flow per Header	Flow per Header (m³/hr)
	1	2	3				
Top Headers only	102.0	100.0	100.0	100.7	715.2	27.5	0.099
Bottom Headers only	89.0	89.0	89.0	89.0	809.0	31.1	0.112
Both Headers open	49.0	48.0	49.0	48.7	1479.5	28.5	0.102

The data collated in this section is used to compare the ROT parameters between the laboratory ROT and Port Talbot ROT. This is therefore critical when designing cooling schedules for laboratory produced steel samples.

3.3.2. ROT Roller Speed Velocity Study

In addition to the previous benchmarking exercises on the Lewis Mill, the ROT speed needs to be quantified. The ROT is powered by and DC motor, controlled with an analogue motor controller, operated via a dial. The dial reads 0-9, 9 being the fastest speed that the ROT is capable of. Currently the standard speed setting, determined via previous experience, is 4. However with the intention of adjusting various ROT parameters, the dial settings must be quantified in terms of velocity. In order to investigate this a sample was placed on the ROT, and the time taken to reach the end of the ROT at each dial position. This was converted into velocity, by dividing by the length of the table; 4m. The results are recorded in Table 35.

This fitted second order polynomial equation was used to determine the relationship between dial position and ROT velocity, as shown in Figure 80:
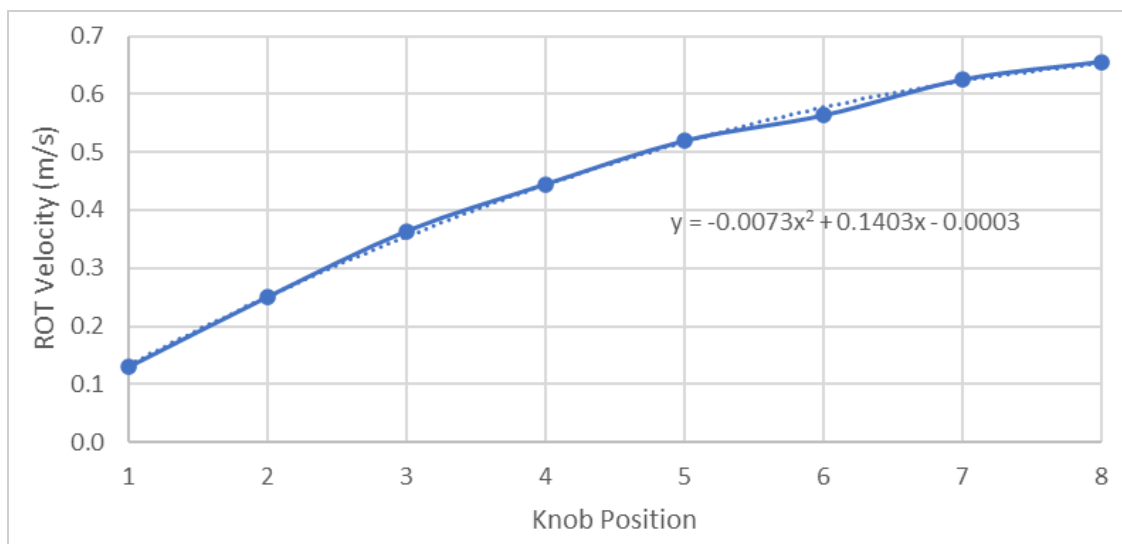
Figure 80- ROT speed for a given dial position.

It is clear from Figure 80 that the relationship between dial position and speed is not linear. It has therefore been recommended that the above graph should be consulted when designing novel ROT cooling schedules. This will avoid the previously held assumption that twice the value of the dial position will double the resultant speed. This information will be key when replicating Titan model rolling operations to ensure the correct ROT speed is used.

3.3.3. Time Temperature Relationship

3.3.3.1. Method

As discussed previously the time temperature profile that a steel undergoes during thermomechanical treatments dictates its final microstructure. As such it is necessary to benchmark the time temperature relationship that strip material undergoes during processing on the Lab Mill. In order to achieve this the typical operation carried out by operators of the Lab Mill was observed a total of five times, and the time at which each operation was conducted was recorded, as well as the variation in each time to understand the inevitable degree of variance that occurs in such manual handling operations. The time stamp for each operation was recorded once it had begun to the nearest 0.5s.

Table 10- Time taken for each Laboratory Rolling and ROT operation.

	Remove from furnace	De-scale	Mill 7th Pass & Transfer to ROT	Transfer from Mill to ROT	Arrival at End of ROT (Dial Position 4)	Into Coiling Furnace	Sample Remains in Coiling Furnace Overnight
1	0	11	40	43.5	52.5	55	
2	0	9.5	39	44	52.5	54.5	
3	0	9.5	38.5	43	54	57	
4	0	11	39.5	43.5	53	55	
5	0	10.5	41	44.5	53	57	
Average (s)	0	10.3	39.6	43.7	53	55.7	
AveDev (s)	-	0.64	0.72	0.44	0.4	1.04	

In addition to this the temperature per, operation was also recorded from previous experiments of similar chemistries as shown in Table 11.

Table 11- Approximate Temperature 'journey' of strip rolling on Lab Mill.

Operation	Remove from Furnace & De-Scale	Hot Rolling (7 Passes)		Transfer from Mill to ROT	End of ROT & Transfer to Coiling Furnace
Temperature (°C)	1250	1150 (Initial Rolling Temperature)	812 (Final Rolling Temperature)	812	625

The average time temperature relationship was overlayed on a CCT curve to approximate the transformation occurring in the sample, as a function of surface temperature, as shown in Figure 81. In order to generate this curve using Jmat Pro the DP800 chemistry with a grain size of 10µm, the software then uses internal thermodynamic and kinetic models to predict the phases as a result of different cooling rates subject to the users input starting grain size and chemistry. This value for grain size was suggested by Tata Steel based on previous research of the estimated grain size upon entry to the hot mill[135].
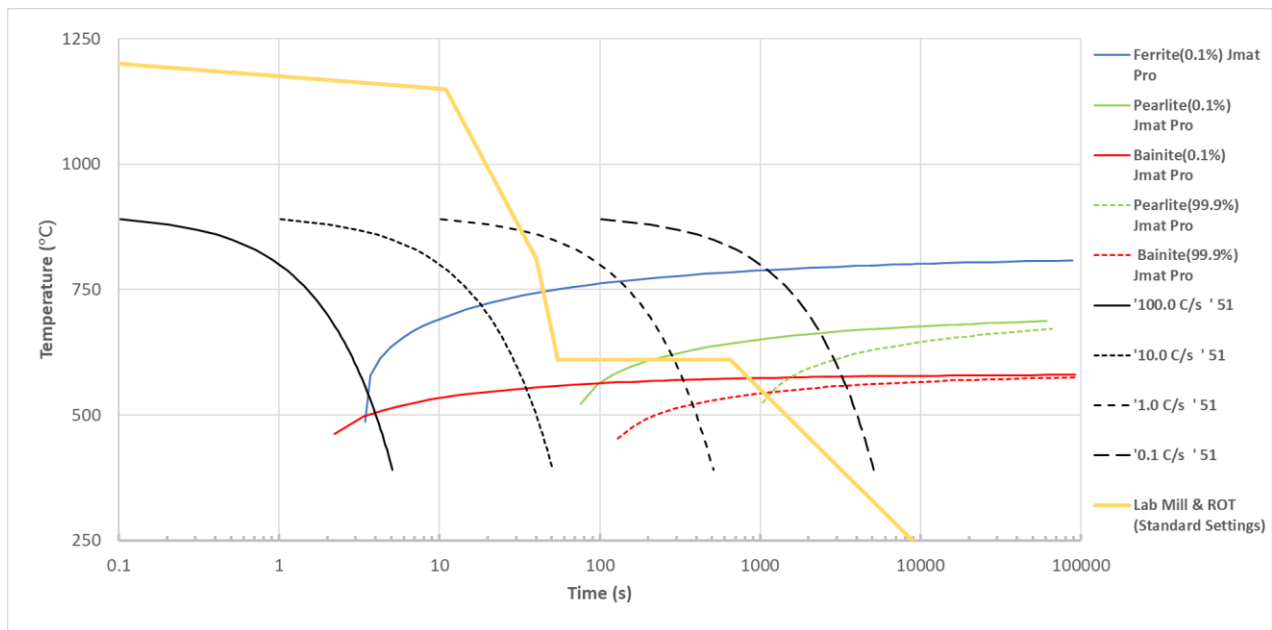
Figure 81- Time Temperature 'journey' overlayed onto DP800 CCT curves generated using Jmat pro.

3.3.3.2. Comparison to Port Talbot Steel Works

In order to obtain a good estimation of a time temperature relationship, research was conducted into the into the various departments around the Port Talbot steel works to detail to each relevant process, as well as collate data obtained from relevant literature. Figure 82

shows a time-temperature profile of a typical DP800 strip, obtained from Titan, which is derived from plant pyrometer data. This time-temperature profile is used as a relevant benchmark with the aim of simulating the Port Talbot ROT in the laboratory setting. It can be seen that upon entry to the ROT the strip temperature is approximately 850°C, and 650°C at the exit, prior to coiling and each unit length of steel spends just under 15 seconds from the entry of the ROT to the exit. Therefore, these parameters should be aimed for when replicating plant processes.
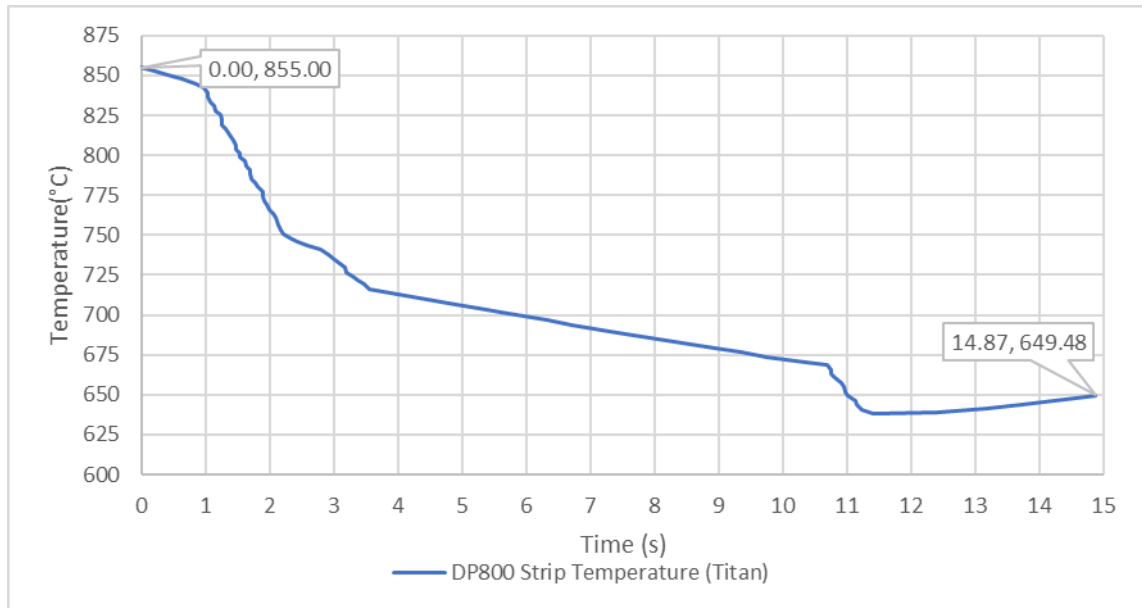
Figure 82- Simulation of ROT temperature profile from Titan software for a typical DP800 strip.

In order to compare the observed time temperature relationship, detailed in Table 11, the two were overlayed, as shown below in Figure 83. Note that the time stamp for the lab profile was modified such that the beginning of the ROT operation was set to 0s in order to compare against the Titan (Port Talbot) data.
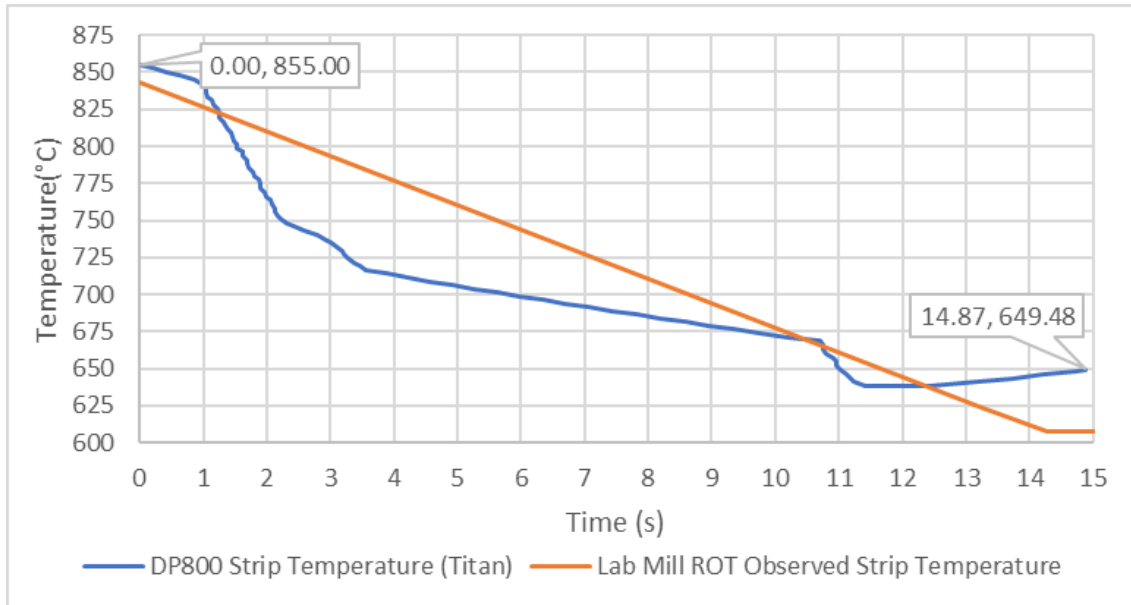
Figure 83- Comparison of temperature profiles and Titan temperature profiles (reflective of plant process), for a DP800 strip.

It is clear from the above that the time temperature profile above does not provide sufficient resolution in comparing the profiles. Since the transformation within the strip is largely influenced by the cooling rates, it is important to clarify the true time-temperature profile of the strip, in the experimental setting.

For this reason a thermocouple was mounted into a section of pre-rolled strip in order to track the temperature down the ROT, as shown below in Figure 83.

Figure 84- Previously hot rolled DP800 strip, with k-type thermocouple mounted in the centre.

Due to the high loads and thickness reductions experienced by the strip, it is not possible to conduct hot rolling with a thermocouple in situ. Therefore, the process was simulated by simply heat the pre-rolled strip to above FRT (900°C), then de-scaled with a wire brush and placed on the ROT where the usual water-cooling procedure was conducted.
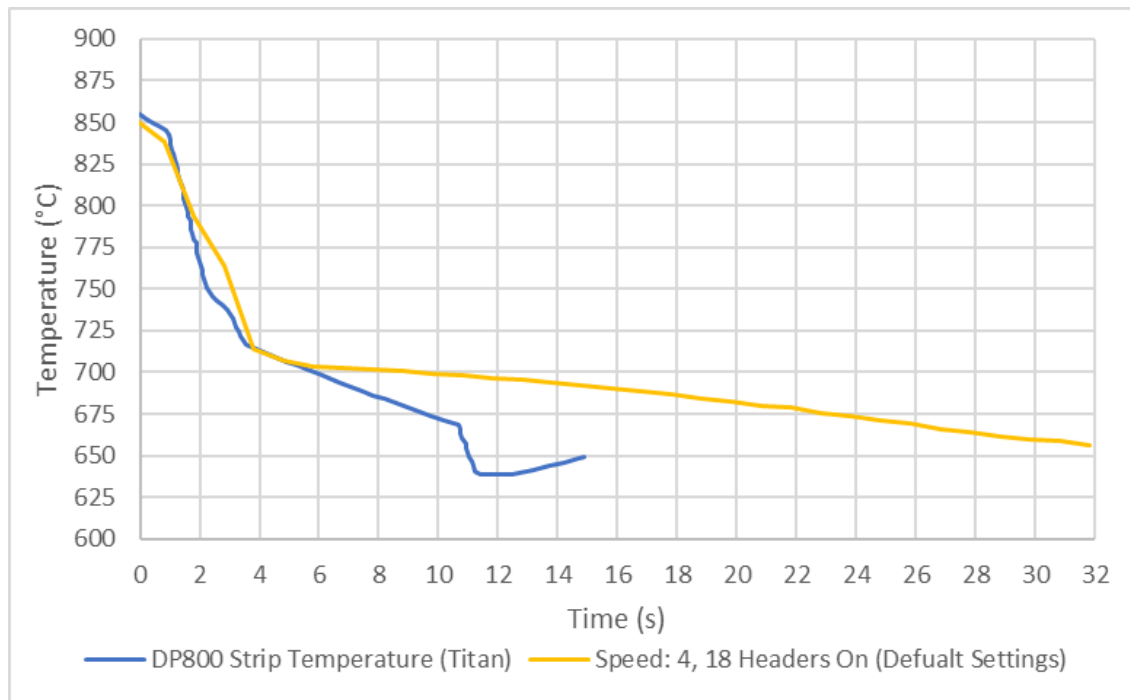
Figure 85- Comparison of thermocouple temperature profiles and Titan temperature profiles (reflective of plant process), for a DP800 strip.

Figure 85 shows the time-temperature profile for a Port Talbot produced DP800 strip, compared with the profile obtained using the experimental procedure described by the yellow line. The initial water-cooling phase of the schedule appears to achieve a good match for the Port Talbot schedule, achieving a similar temperature gradient in the first 4 seconds of approximately 42°C/s. However, when the strip, in the experimental setting reaches the air-cooled section of the ROT (where no water headers are switched on), it appears to retain heat more effectively than the plant process according to the Titan model. This is shown by the difference in temperature gradients between the 4 and 11 seconds for the Plant model and the experimental setup are 7.3°C/s and 2.2°C/s respectively. This results in the temperature deviating largely towards the end of the process. Lastly in the experimental procedure it is common practice for the strip to be held in front of the coiling furnace (see section 2.4.4) until a representative CT is reached (650°C), via air cooling, then placed into the coiling furnace for several hours. It can take several seconds for this temperature to be reached as shown in Figure 85. This causes some deviation in the time-temperature profile between the experimental process and the plant process. In contrast to this the practice industrially it to implement the trim headers, which adjust the trip temperature towards a target temperature for coiling. This is shown in the dip in temperature at around 10.75s, which results in an ideal CT of 650°C at the end of the ROT.

3.4. Titan Assessment

3.4.1. Default Settings Output

The Titan software was run for the journal files outlined in section 2.1.3. One such output from the graph described is shown below:
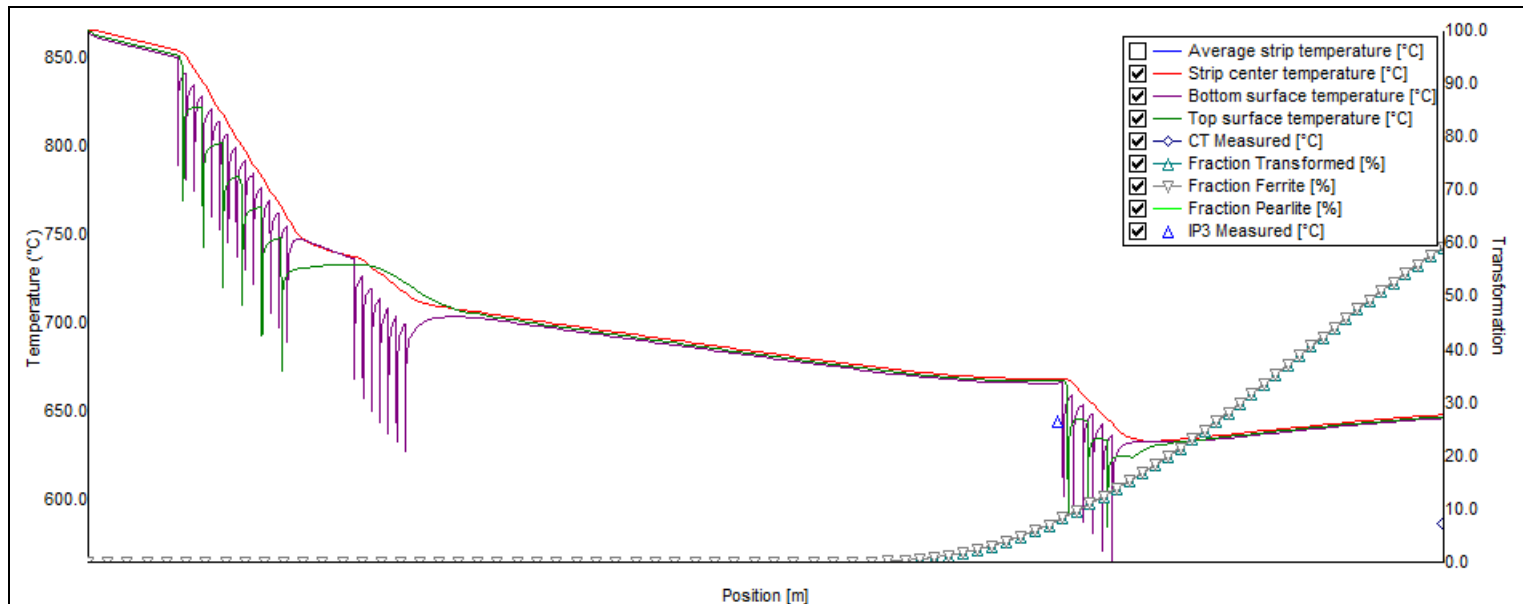
Figure 86- Titan output for 56868-020-301 at default settings, showing modelled temperatures for the top and bottom surfaces, and strip core, as well as the predicted transformation, and measured temperature at IP3 on the ROT for a selected point on a selected coil.

The simulated temperature paths for a given position along the strip length are shown as well as the simulated resultant transformation. The IP3 Measured (Blue triangle), is shown, this pyrometer is plant data and is not subject to simulation settings. This graphs shows the temperature 'journey' for a given point on a given coil and the transformation that likely would have resulted due to the chemistry of the strip and the cooling parameters applied to it. The oscillating temperature traces that are seen on the graphs are the response in surface temperature due to the impingement of the water jets on the strip. The IP3 temperature point has been chosen as a target for the optimisation.

It is clear in this case that the software over predicts the temperature at this point on the ROT. The reported transformation during cooling operation on the ROT is also shown by the grey and turquoise triangle plots. At the end of the ROT the total transformation is reported to be 60%, and 60% ferrite, with no pearlite reported, since the strip is not fully transformed. As a result the remaining 40% is still austenitic and becomes pearlitic when the strip is a coil, since the core of the coil is cooled slowly.

Table 12-Cumulative file at default settings.

Calculation	CTc	CTm	IP3c	IP3m	Frac.T	Ferr	Per	Bain
56868-020-301.00	646.9	587	667.07	645	59.28	59.28	0	0
56869-020-300.00	655.12	589	673.1	634	74.8	74.8	0	0
56870-010-301.00	649.46	591	668.07	638	46.38	46.38	0	0
56871-010-302.00	630.38	591	665.38	638	31.17	31.17	0	0
56873-010-304.00	659.76	592	680.18	635	78.33	78.33	0	0
56874-020-303.00	661.15	598	675.28	635	74.85	74.85	0	0
56876-010-303.00	657.35	595	670.61	642	63.89	63.89	0	0
56877-010-300.00	652.67	594	662.29	630	65.37	65.37	0	0
56879-010-308.00	652.67	594	662.29	630	65.37	65.37	0	0

The cumulative file shown above also confirms the no pearlite transformation is reported in the strip. IP3c and IP3m shows the calculated (simulated) and measured values respectively for the strip temperature, at the position the pyrometer is located on the Port Talbot ROT. Likewise, CTc and CTm show the coiling temperatures, again both calculated and measured. both of these temperatures are used on plant to achieve the correct microstructure at the coiler, to improve processability. For example, it is critical bainite formation does not occur such that the strip cannot be cold rolled, due to the resultant loading being far too high. Figure 87 shows the difference between the IP3 reading and CT readings for both calculated and measured values, as well as an average for all journals studied. The values shown are not absolute values, but rather true values, since in every case the calculated temperature is higher than the measured. the average difference across the nine journals was 59°C for the coiling temperature and 33°C for the IP3 temperature.
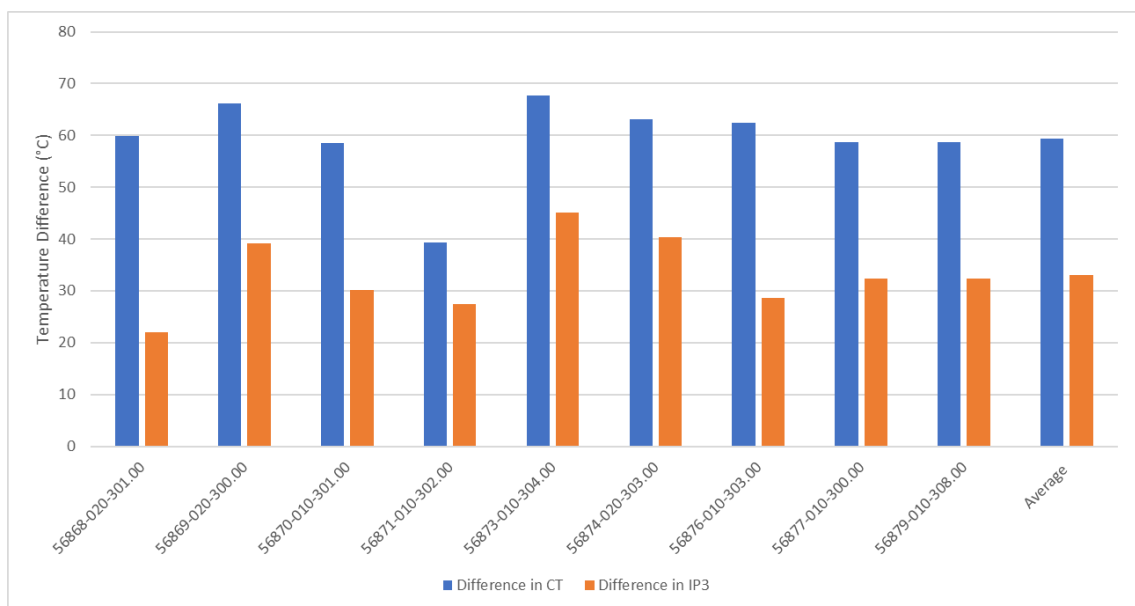
Figure 87- Difference in simulated IP3 and CT for each journal and average for all.

This shows that in its current unoptimized configuration the Titan package is not capable of modelling strip transformation on the ROT, in correctly reporting volume phase fraction, percentage transformed, or correct temperature prediction of the plant process.

3.4.2. CCT Curve Comparison

In order to gain an understanding of the transformation kinetics within the Titan model, a process was designed to 'extract' the conditions at which transformation would occur a given temperature. This would result in the creation of a TTT curve for the Titan software (at default settings). Arguably a CCT curve would be a more practical representation of ROT transformation kinetics, however due to limitations with the Titan package a CCT curve could not be extracted. As a result, a TTT curve is used for comparison reasons.

In order to set up Titan to track when transformation of a given phase occurs, the 'Roll It' package was used, as shown below in Figure 88. This allowed or the temperature to be held at a user defined value for any length of time, then an output file could be created that reported the phases present in the strip over time. The first instance (0.1%) of any phase was recorded with the time stamp. This process was repeated for a number of temperatures in order to build a TTT diagram over time.
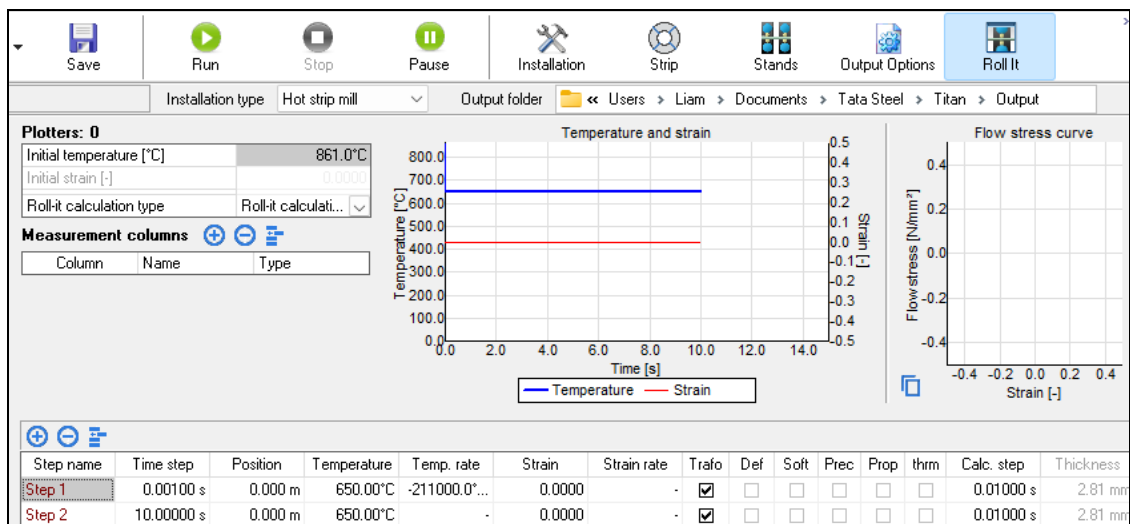
Figure 88- Titan- Roll It simulation.

The results of this operation are shown below, with the first instance of bainite, ferrite and pearlite at 0.1%.
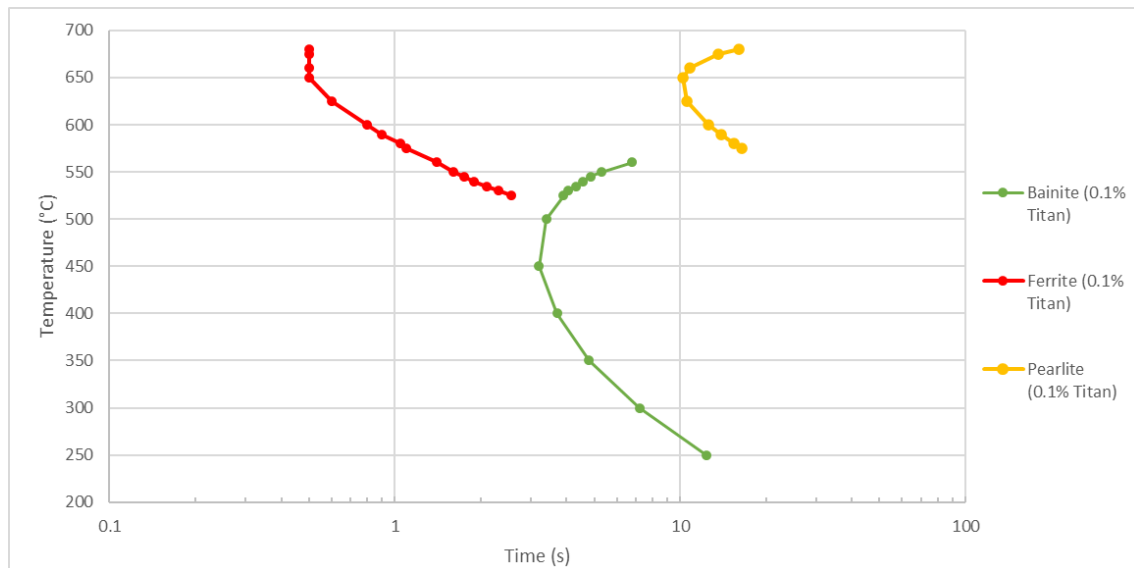
Figure 89- TTT curve extracted from Titan at default settings.

In order to benchmark the initial transformation kinetics of Titan, this TTT curve was overlayed with one from Jmat Pro, using Tata Steels D800 product chemistry and an initial grain size of 10µm. The results are shown below:
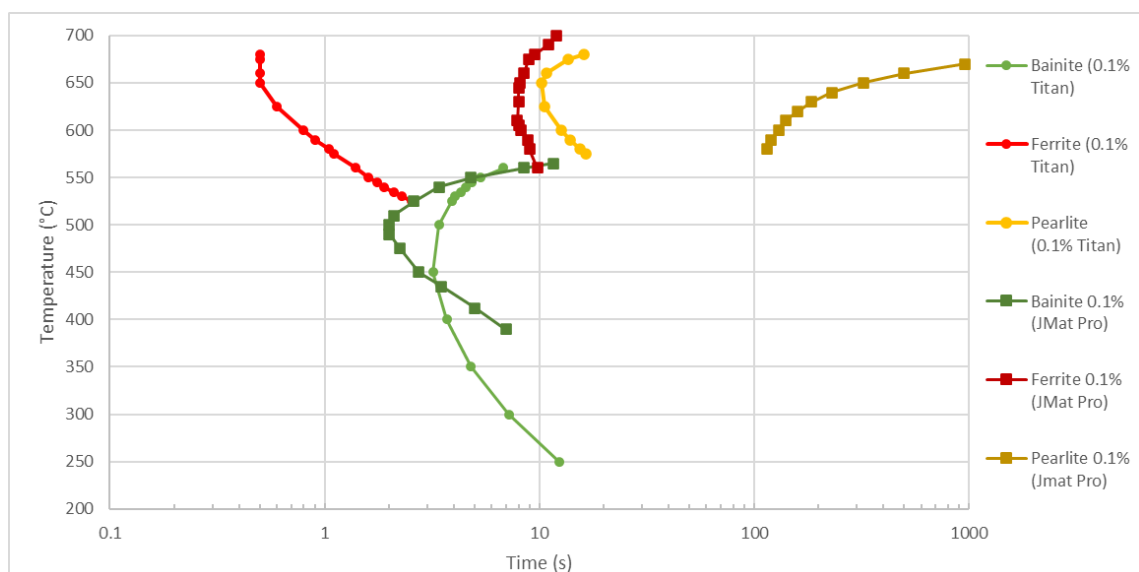
Figure 90- Titan TTT and Jmat Pro TTT comparison.

It is clear from Figure 90 that, at default settings, according to this comparison the Titan simulation models transformation of austenite to ferrite earlier than the Jmat Pro simulation by a significant degree. At a temperature of 650°C, in the case of Titan, ferrite formation initiates as 0.5 seconds, however in the case for Jmat Pro, ferrite formation doesn't initiate until eight seconds. Despite no pearlite formation being reported in the cumulative file, pearlite formation is in fact present in this study using the 'Roll It' tool. Similarly to ferrite, the simulated pearlite formation is also earlier, when compared to Jmat Pro. Interestingly

121

the bainite nose is noticeably higher in temperature and the bainite curves appear to present different shapes. Unlike both ferrite and pearlite however, bainite in the instance of the Titan simulation appears to form earlier than Jmat Pro. Assuming Jmat pro is a more accurate representation of DP800 transformation, this may be an explanation as to why the transformation reported on the ROT is incomplete.

3.4.3. PAGs Sensitivity Study

At the time of writing, the Titan simulation has one input regarding the grain structure at the entry of the ROT: 'Initial (centre) grain size'. There are also additional settings to describe the grain structure; 'Top grain size' and 'Bottom grain size'. These describe the grain size at the top and bottom section of the strip, by default these are set to 0 since in this configuration only strip centre is studied. These settings can be found under strip, Metal Matrix, Phase properties:
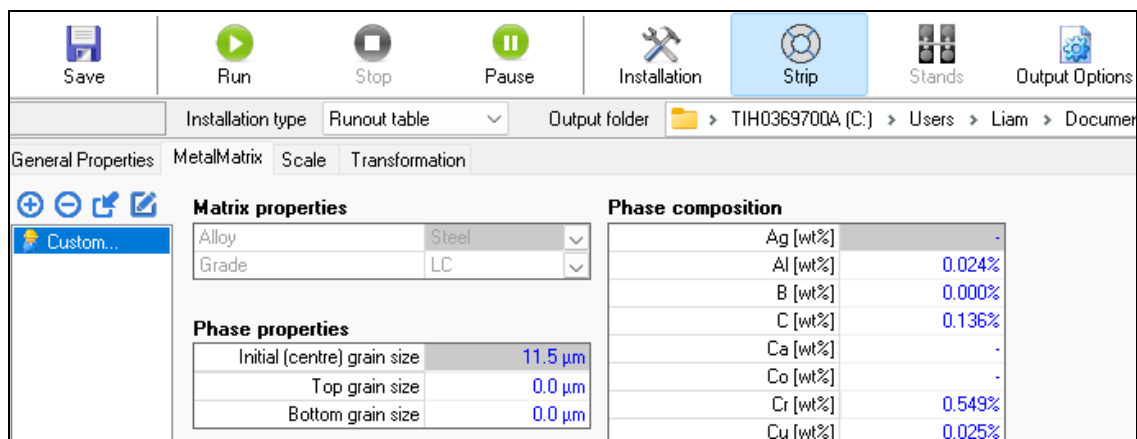
Figure 91- Initial grain size settings.

As shown above the default grain size is set to 11.5µm, which aligns with the industrial recommendation of 10µm. Additionally, the software does not allow for the possibility that the grain structure may not be equiaxed, as can be the case when hot rolling below the T_{NR}. In order to see the affect the initial grain size would have on the key outputs of the Titan model, a sensitivity study was conducted regarding grain size. The grain size was increased and ran for all nine of the journals, the average; simulated coiling temperature, the simulated IP3 temperature and the simulated total transformation at the end of the ROT.
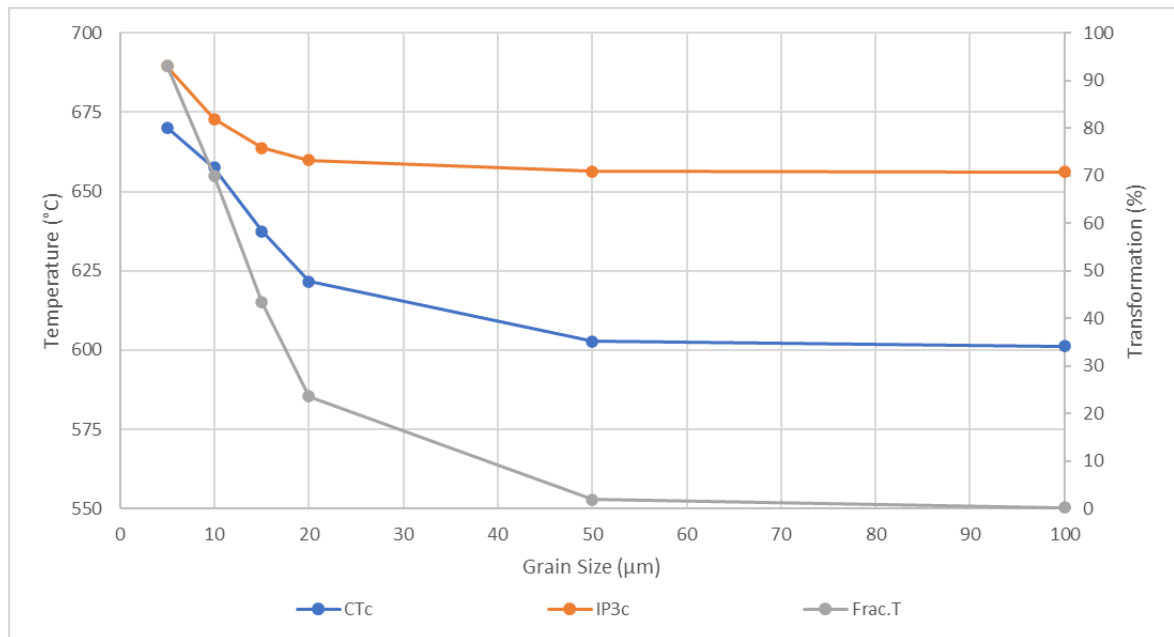
Figure 92- Effect of varying grain size in Titan on the coiling temperature (CTC), the IP3 pyrometer temperature (IP3C) and the total transformation of the strip at the end of the ROT (Frac.T).

It can be seen from the above results that modifying the grain size, particularly between 5 and 20µm, results in a significant difference in both calculated temperatures and percentage transformed. This range is likely the grain size in which the representative grain size exists. Therefore investigation into the initial grain size (upon entry to the ROT) has been conducted in section 4.3.1.

4. Optimisation

4.1. Mill Optimisation Chamfer Study

4.1.1. Justification of Chamfered samples

Previous research conducted using the laboratory scale hot mill at SAMI had been conducted with the following rolling schedule:

Table 13- Resultant material thickness per pass and percentage thickness reduction.

Existing DP800 Rolling Schedule								
Roller ID	0	1	2	3	4	5	6	7
Material Thickness (mm)	34	29.5	21.5	13.9	9.5	6	3.7	2.3
% Reduction	-	15.3	37.2	54.7	46.3	58.3	62.2	60.9

This design was chosen in order to create satisfactory thickness reduction, within seven passes whilst limiting the loads subjected to the mill. However, the strain (or percentage reduction) per pass varies greatly, shown by Figure 93.
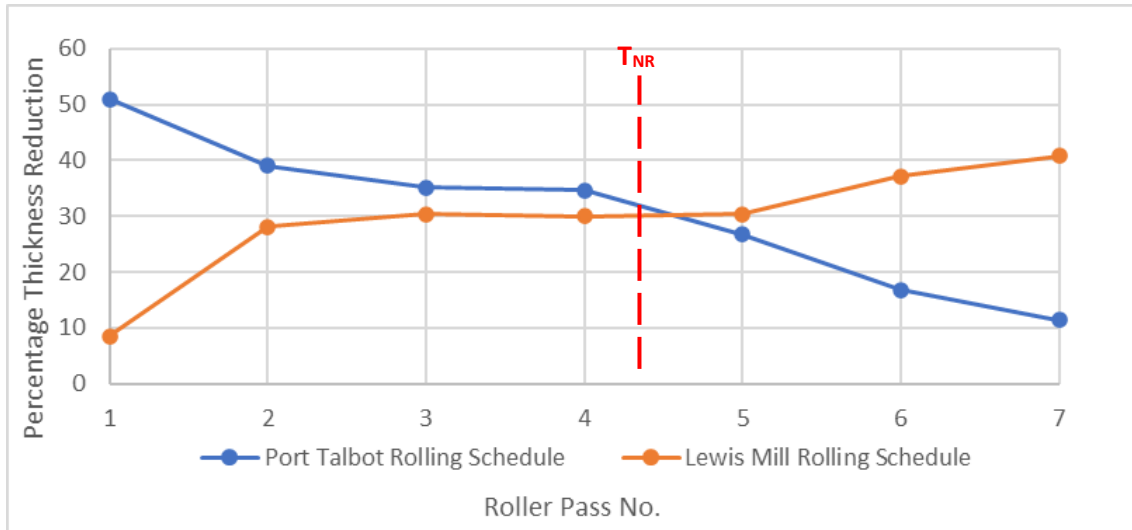
Figure 93- Comparison of percentage reduction per pass of existing laboratory setup and Tata Steel's rolling schedule for DP800.

This particularly an issue since the material is being rolled, in part, below the TNR. As a result, the microstructure between the experimental route is likely to vary between the plant route, since larger reduction in later passes will result in a greater degree of pancaking of grains, which in turn will affect ferrite nucleation on the ROT. It was found, from analysis of historic data using this mill by S. Kumar and colleagues at Swansea University's SAMI [136], that TNR occurred between roller passes four and five, as highlighted on Figure 93.

It has also been noticed by colleagues, that the existing rolling schedule, when implemented in other grades, has generated strain induced ferrite which is discussed in section 1.3.2.4. This was noticed because of a mismatch in the grain structures of experimentally produced steel samples, vs those produced on plant. Since the grain structure was non representative, amendment must be made to the rolling schedule must be made, therefore justifying this body of work.

Ideally the rolling schedule, seen in Table 13 would be implemented in the lab setting. However due to a geometrical constraint, that is a challenge for many rolling mills, the bite angle will not allow this. The bite angle is the minimum angle for a given mill setup which allows for material to be 'drawn in' by the action of friction. If this angle is exceeded, the

material will not 'bite' and result in potentially catastrophic consequences on and industrial scale.

This is a particular limitation in the laboratory setting since a roller diameter is a contributing factor to this limitation. This phenomena was characterised mathematically by Orowan[117], in the setting of cold rolling mills.

Since the roller diameter on Tata Steel's Port Talbot hot mill is 700mm, thicker gauges and larger reductions are able to be processed. Table 14 shows the resultant bite angle, per roller pass, for both the Tata and SAMI rolling schedules, when applied to the SAMI laboratory (Lewis Mill).

Table 14- Bite angle of Tata and SAMI rolling schedule, based upon SAMI lab mill geometry.

	Resultant Bite Angle (Degrees)						
Mill Pass No.	**1**	**2**	**3**	**4**	**5**	**6**	**7**
Tata Steel Port Talbot Schedule	23.07	14.08	10.43	8.32	5.91	4.01	3.02
SAMI Lab Mill Schedule	9.55	16.58	14.61	12.09	10.17	9.39	7.79

The maximum bite angle for a given roller set up is a function of friction between the roller and the sample, as a result this is a complex relationship that depends upon surface properties, use of lubricant and temperature[137]. Based upon previous work conducted on the lab mill, the minimum bite angle was found to be 18°. This value was observed to be reliable for several years for the mechanical processing of steels at SAMI. It is clear from Table 14 that if Tata's schedule were to be implemented, on the SAMI laboratory mill, this would far exceed the bite angle criteria.

In order to overcome this, a chamfered sample was designed. This would allow for an appropriate initial bite angle, whilst maintaining representative material reductions per pass to replicate Tata's industrial process. The first iteration is shown below:
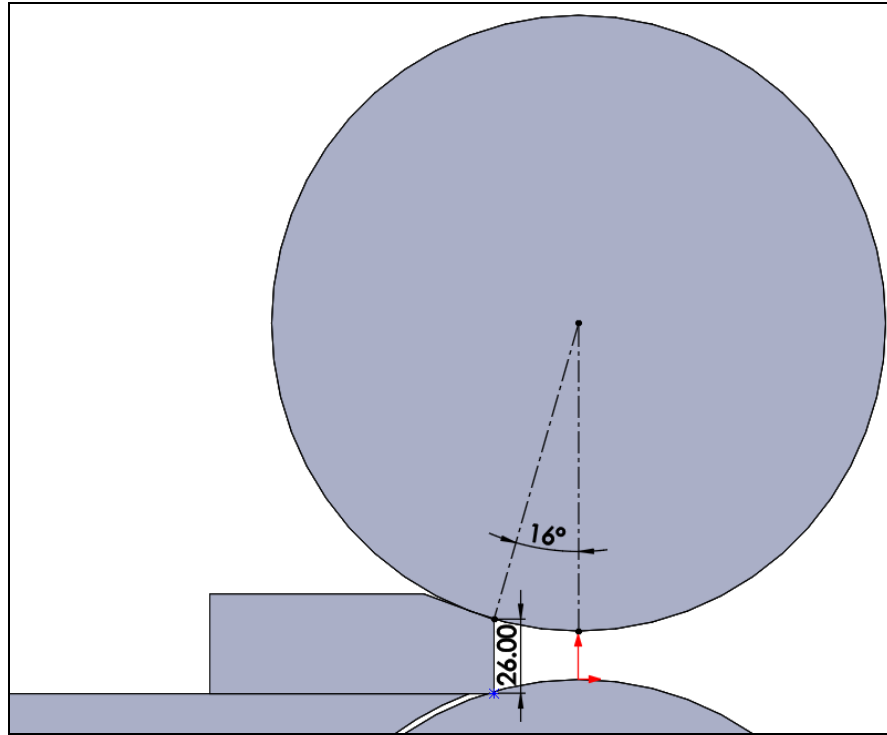
Figure 94-Tapered design of hot rolled sample.

Figure 94 shows 'Sample 1' with a chamfer applied to the top edge. The initial thickness of the 'nose' of the sample is 26mm, this results in a bite angle of 16°, allowing for a margin of safety in the bite angle limitation.

4.1.2. Load Prediction

Before 'Sample 1' could be trialled, other limitations of the experimental setup had to be accounted for. The Load on the Mill. Mill load is a function of percentage reduction, therefore since larger reductions are being made in the 1st pass, this had to be estimated to prevent exposing the mill to loads beyond its calculated limit (70kN). To estimate the Load, equations from the Sim's model were employed, see Equation 15 and Equation 16[118]. A detailed description of the Sim's model is given in section 1.7.1.3.2. For the purposes of this load estimation Q_p was set to 1, since the in order to estimate this the "Radius of curvature of the elastically deformed roll[118]" must be known, which is not possible for the given laboratory setup. Substitution of R' with undeformed roller radius (R) was attempted but this did not produce realistic results, hence substituting Q_p with 1 was deemed to be appropriate considering load estimation was the goal, and a conserve margin of safety is included to mitigate any uncertainties in load estimation. MFS was calculated using the Misaka model, (see Equation 11 and Equation 12) as described in section 1.7.1.2, was also utilised in the load estimation model. Other models for MFS

(Bruna and Siciliano), however little difference was found in their application when assessing the previous laboratory rolled data, as shown in Figure 95. However negligible difference was observed, therefore Misaka was chosen due to its simplicity and was deemed adequate.
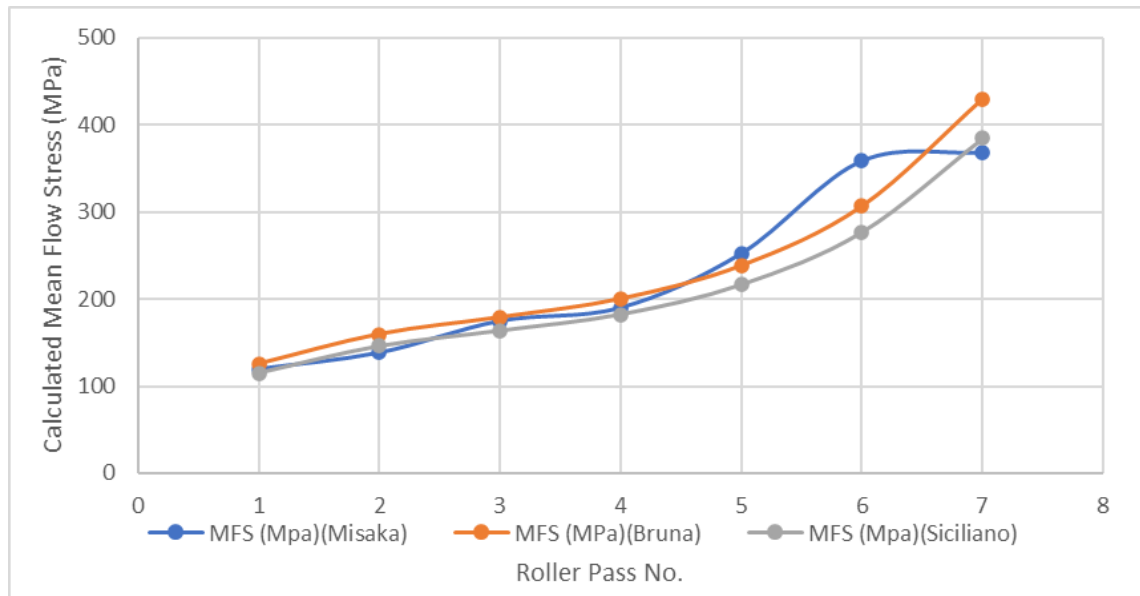
Figure 95- Comparison of different MFS models when applied to laboratory rolling procedures.

In order to test the validity of the mathematical model for the given setup, historic data from the lab-scale mill was collected. This data allowed product chemistry to be accounted for the in the collection of MFS data, as well a load reading for each given trial, and a given temperature for each pass. This load reading was compared against the calculated load to validate the model over six different experiments, one such example is shown below:
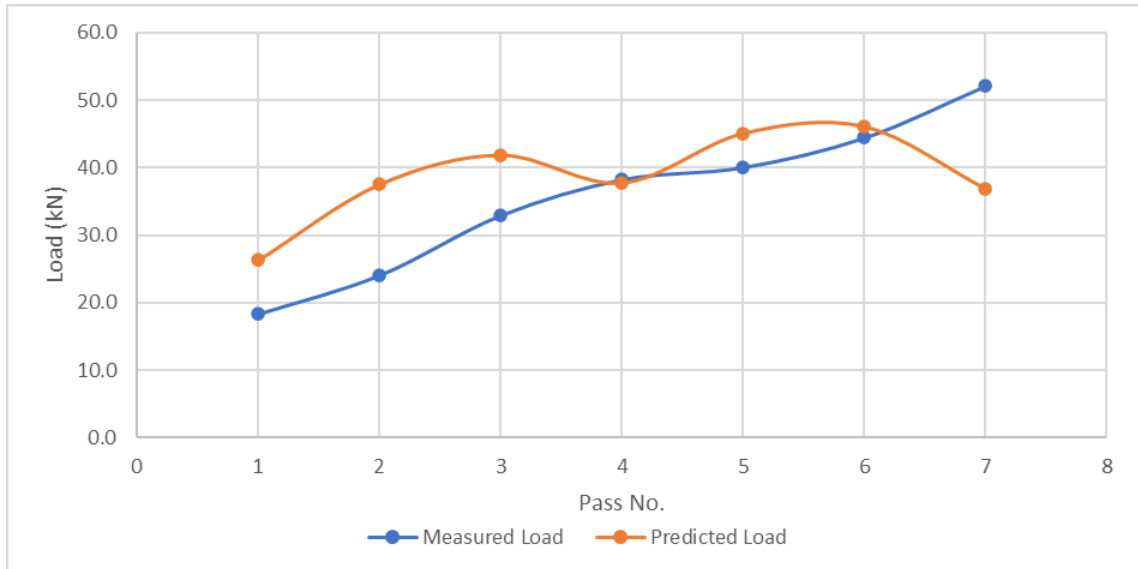
Figure 96- Modelled load compared with measured load for DP600 grade, rolled using existing SAMI rolling schedule.

Figure 96 shows one such example of the modelled load for a previously rolled DP600 grade using the SAMI lab mill rolling schedule, as described in Table 14. A reasonable match was achieved utilising the mathematical models. In each case the model was found to over predict the peak load on the 1st pass, by a significant degree, which was viewed as advantageous since this would provide some margin of safety.

Table 36 (appendix) shows the comparison between the measured loads and calculated loads for six previously rolled DP600 samples. The highest difference observed across all passes is for pass two at 14.2kN, and the lowest being for pass four at 5.1kN. Generally, the model tends to over predict the load.

4.1.3. Geometry Design 1 (Single Chamfer)

Slight variations in rolling schedules were trialled during the experimental period in an attempt to limit mill loads and improve reliability. Rolling schedules of each sample are given below, however all mimic the Port Talbot schedule, with slight differences in percentage reduction in the first four passes (above T_{NR}), hence the predicted load varies for each sample.

Table 15- Sample 1A rolling schedule details and measured temperature.

Sample 1A	Pass Number							
	0	1	2	3	4	5	6	7
Roll Gap (mm)	34	22	14	8	4.3	3.16	2.63	2.33
Bite Angle (°)	-	15.87	15.87	13.73	10.77	5.97	4.07	3.06
Inter-pass Temp (°C)	-	1160.0	1113.8	1113.8	1018.0	976.9	866.5	817.2
Strain (%)	-	35	36	43	46	27	17	11
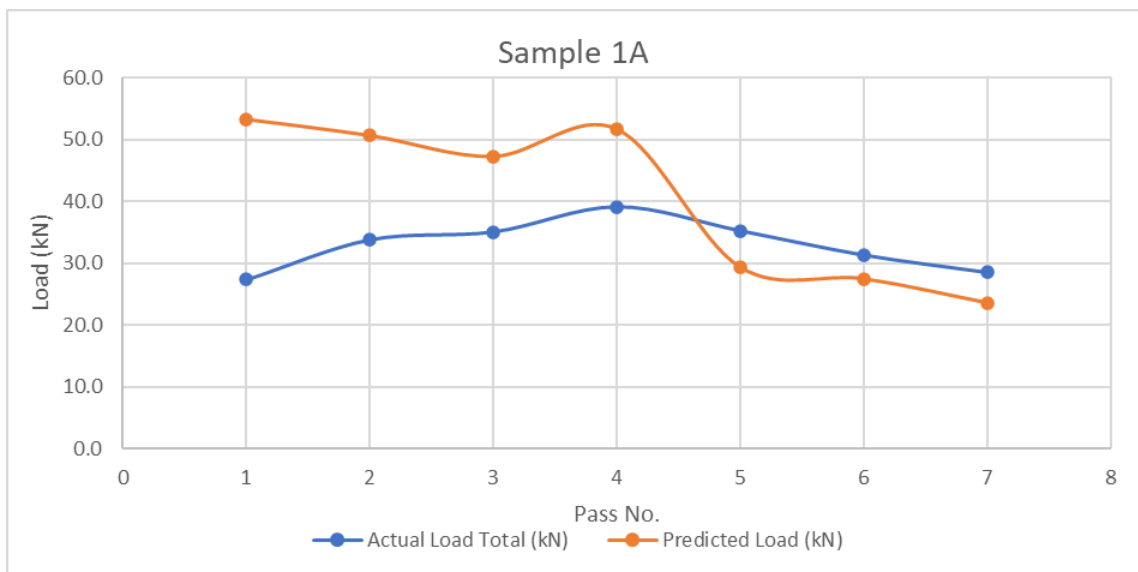
Figure 97- Sample 1A, 1st attempt of sample 1, peak load from both rollers, per roller pass.

Table 16- Sample 1B rolling schedule details and measured temperature.

Sample 1B	Pass Number							
	0	1	2	3	4	5	6	7
Roll Gap (mm)	34	18	11	7	4.31	3.16	2.63	2.33
Bite Angle (°)	-	15.87	14.84	11.20	9.18	6.00	4.07	3.06
Inter-pass Temp (°C)	-	1160.2	1117.4	1079.8	1017.9	824.6	760.3	662.3
Strain (%)	-	47	39	36	38	27	17	11
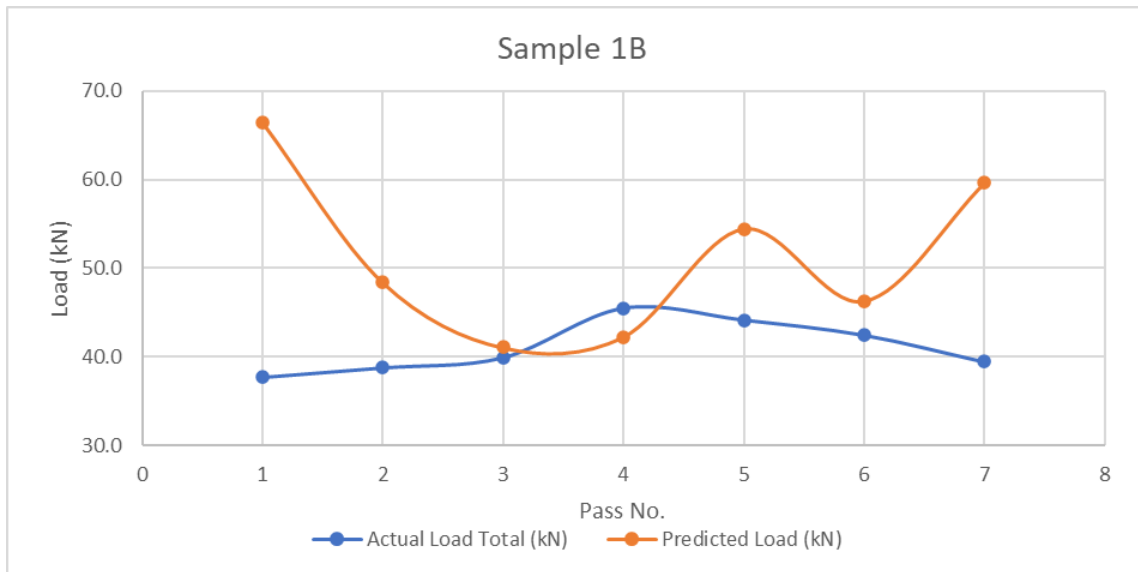
Figure 98- Sample 1B, 2nd attempt of sample 1, peak load from both rollers, per roller pass.

Table 17- Sample 1C rolling schedule details and measured temperature.

Sample 1C	Pass Number							
	0	1	2	3	4	5	6	7
Roll Gap (mm)	34	19	12	6.8	4	2.8	2.3	2
Bite Angle (°)	-	15.87	14.84	12.78	9.37	6.13	3.95	3.06
Inter-pass Temp (℃)	-	1154.0	1117.1	1054.9	1024.6	916.7	838.3	733.8
Strain (%)	-	44	37	43	41	30	18	13
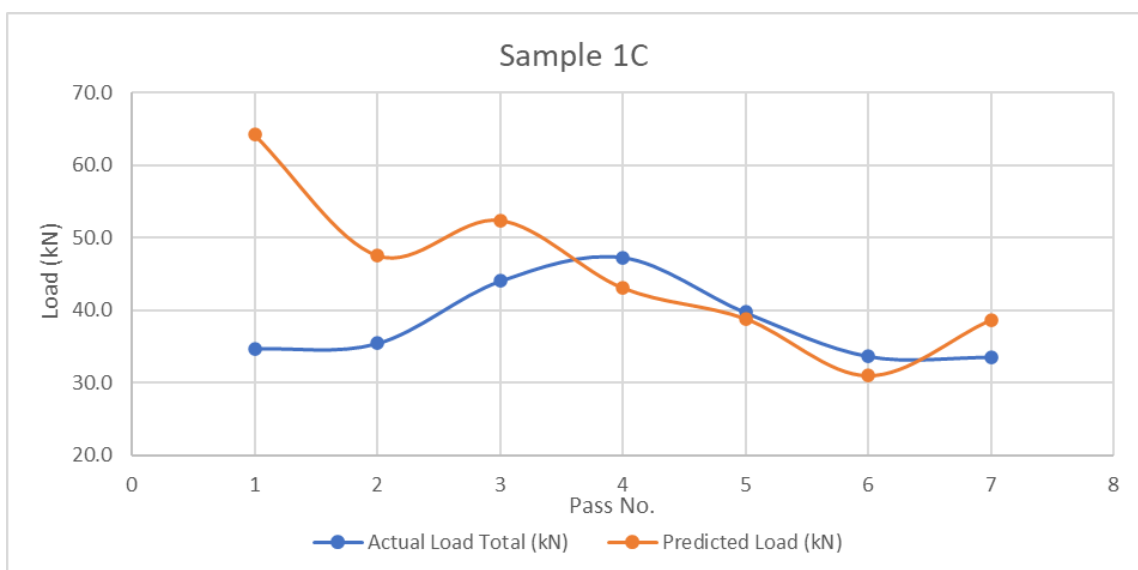
Figure 99- Sample 1C, 3rd attempt of sample 1, peak load from both rollers, per roller pass.
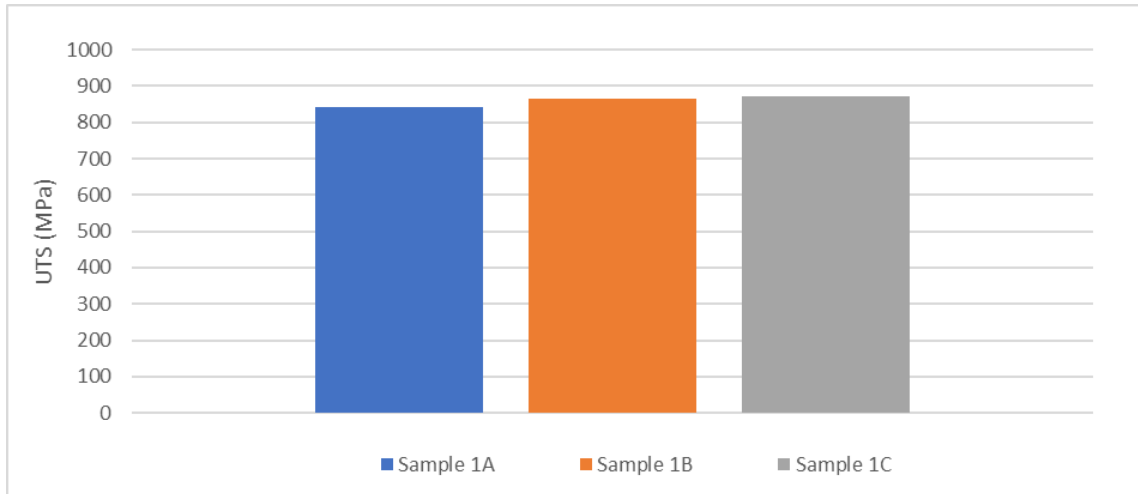
Figure 100- UTS of samples, obtained via Plastometry, after finishing mill and ROT operations, including 'coiling furnace' cooling.

Table 18 -Details of experiments for 'Sample 1', including Final Rolling Temperature, Coiling Temperature and general notes regarding biting reliability.

	Slab Re-heat Furnace Temperature (°C)	No. of Water Headers Open	Final Rolling Temperature (°C)	Coiling Temperature (°C)	Notes
Sample 1A	1250	18	817	540	All passes were successful. Second pass was reluctant to bite and required some force to push it though.
Sample 1B	1250	18	662	410	All passes were successful. Issue with touchscreen to reverse rollers between pass 2 and 3, resulting in delay.
Sample 1C	1250	18	733	540	All passes were successful.

Three samples were manufactured in total, each with identical geometry. All three samples were successful in completing the finishing mill schedule. The second was repeatably unreliable in creating a successful bite without the user applying significant force to force the sample to bite. For this reason, Sample 1B and C had modified rolling schedules such that the bite angle was reduced below 15 degrees to improve bite reliability. This proved to be a successful measure in improving bite reliability. Similarly, when validating the model, as discussed in section 4.1.2, the loads typically were an over prediction of the experimentally measured value. This was regarded to be a net positive outcome since the goal of the model was to ensure the maximum mill load was not exceeded. This tend was most prolific on the 1st pass, in which the largest loads were expected, a reason for this

may be due to the large contact arc length (see Equation 15) due to the large percentage reductions in the 1st pass, resulting in extremely large torque values (especially for the top roller). This therefore could have caused the motor controllers in the mill to limit the current draw, resulting in a reduced mill speed which in turn would reduce the strain rate, in turn reducing the MFS and therefore Mill Load. For this reason it has been recommended that a torque meter be fitted to ensure the calculated maximum mill torque value is not exceeded (17kNm).

It is clear from Table 18 that the temperatures exhibited are not representative of plant values. As such microstructural analysis of these samples would not give useful data, so was not performed. It is also worth noting that the decreased FRT would likely have resulted in increased loads, since temperature is inversely proportional to MFS. It was suspected that these lower temperatures likely caused bainitic formation and possibly martensitic formations within the samples and as such are not representative of plant produced material. This was confirmed by measuring the UTS though Plastometry, see Figure 100. The recommended UTS for material as this stage in the manufacturing process would be approximately 680MPa. It is clear that all three of these samples far exceed that due to the incorrect temperatures.

The rolling schedule for Sample 1C was deemed to be the most successful schedule. The reason for this largely due to the bite angle at the 2nd pass being below 15 and therefore being the most reliable, since it was found that bite issues were common on the second roller pass. Despite this modification it still achieves a good match, particularly below the T$_{NR}$, as illustrated in Figure 101.
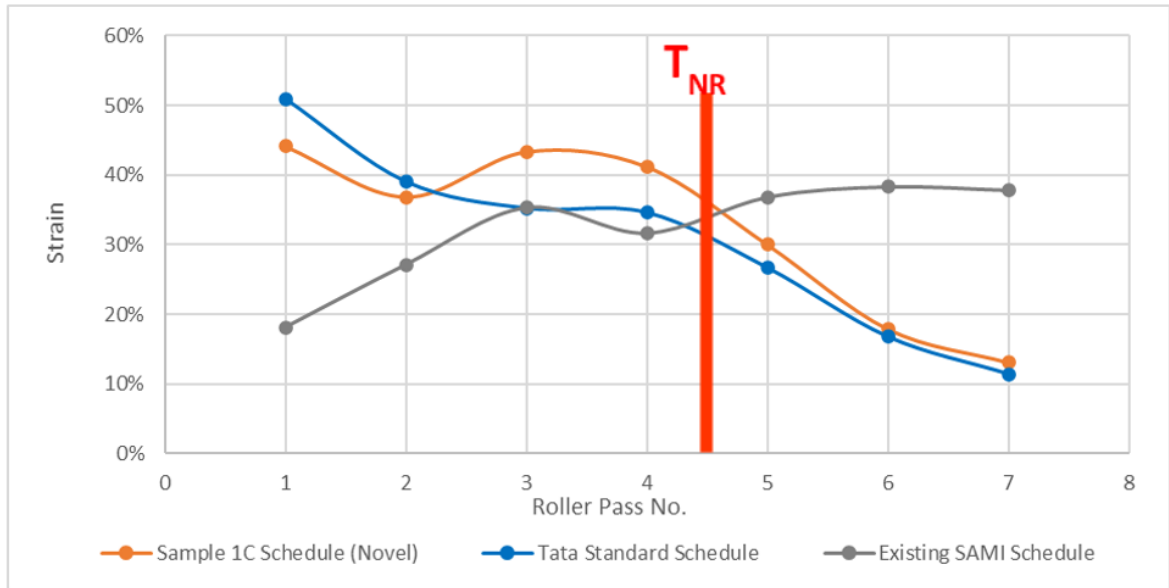
Figure 101- Comparison of rolling schedules, with T_NR overlayed for the new experimental chamfered sample (Sample 1C) and the Tata Steel Port Talbot rolling schedule and the existing SAMI practice for the manufacture of laboratory produced hot rolled samples.

4.1.3.1.   Strip Properties across length

Due to the geometry of the sample, only the parallel section of the sample undergoes representative thickness reductions, and therefore only this section is likely to exhibit representative microstructure, therefor this is of significant interest to the experimental procedure undertaken at SAMI, since some material can be considered 'invalid'. One of the samples rolled in this body of work was sectioned along its length as shown below in Figure 102. This sample was a successfully rolled 6-pass chamfered schedule with a representative coiling temperature, and was a laboratory produced DP800 chemical composition. Note head end, tail end and rolling direction have been marked on the figure but this is only with reference to the ROT and every other mill pass since these the Lewis mill utilises and reverse rolling and not tandem rolling.
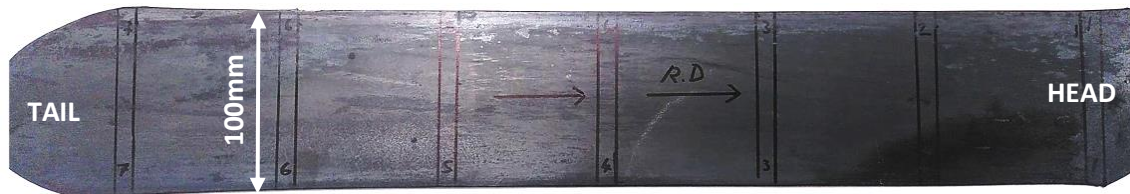
Figure 102- Sample 1 rolled plate with samples 1-7 marked on top surface, with rolling direction shown.

Figure 103- Sample 1 rolled plate samples cut into strip for analysis.

Note that additional samples were taken from the strip after the above photos were taken, for greater resolution along the length of the sample. The total number of samples taken for analysis was 10, including the very nose of the sample. Plastometry was utilised the evaluate the mechanical properties along the length of the sample. The results are shown below in Figure 104.
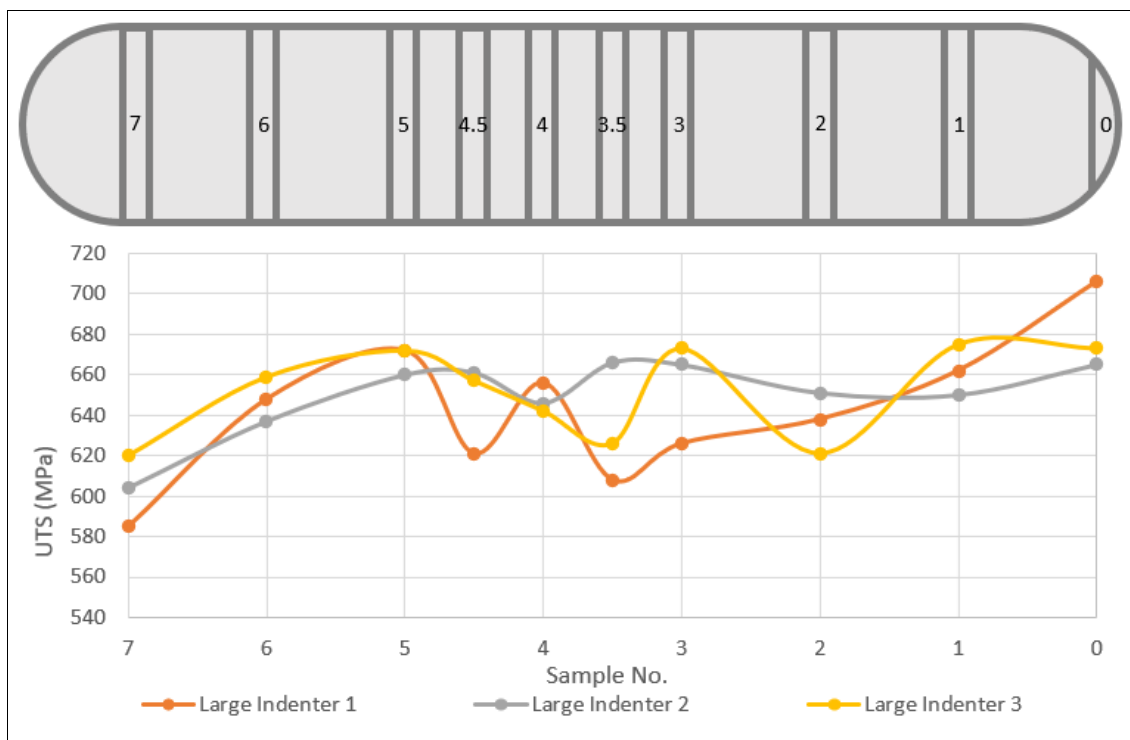
Figure 104- Simulated UTS from Plastometrex with sample location shown.

A total of three indents were performed on each strip cut from the plate, all within the innermost 30mm of the centreline, so the edge effects were not affecting the results due to higher cooling rates at the extreme edges.
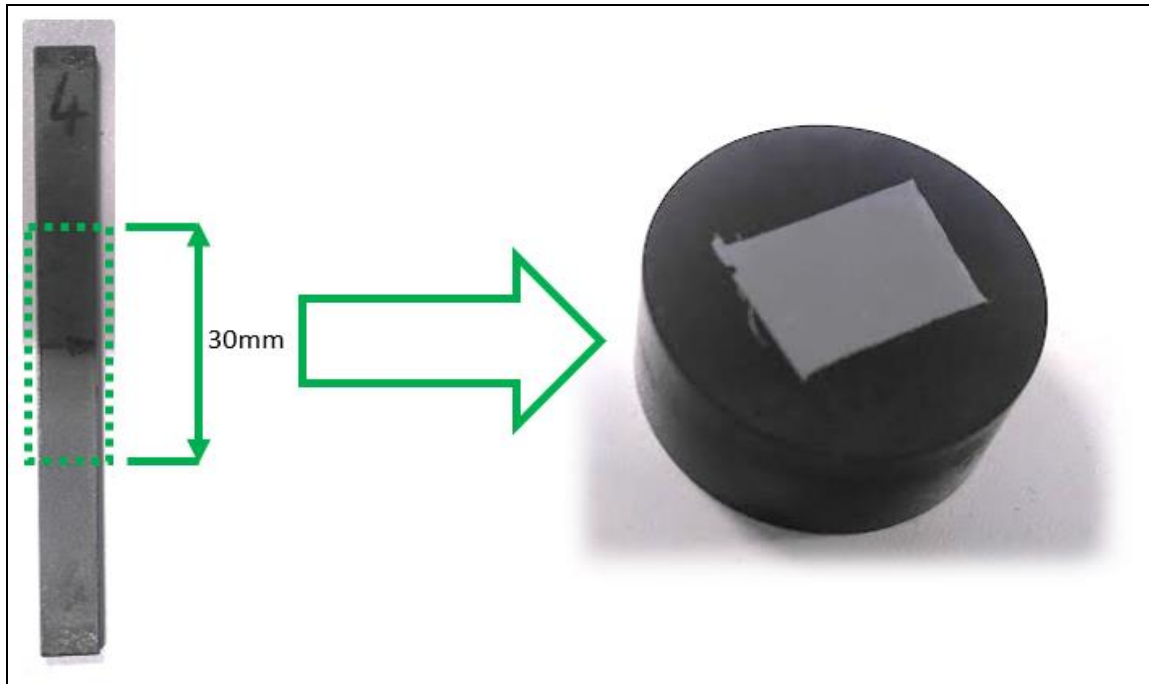
Figure 105- Illustration showing sample location for each strip.

An average of the simulated UTS results, from the three indentations are shown below in Figure 106.
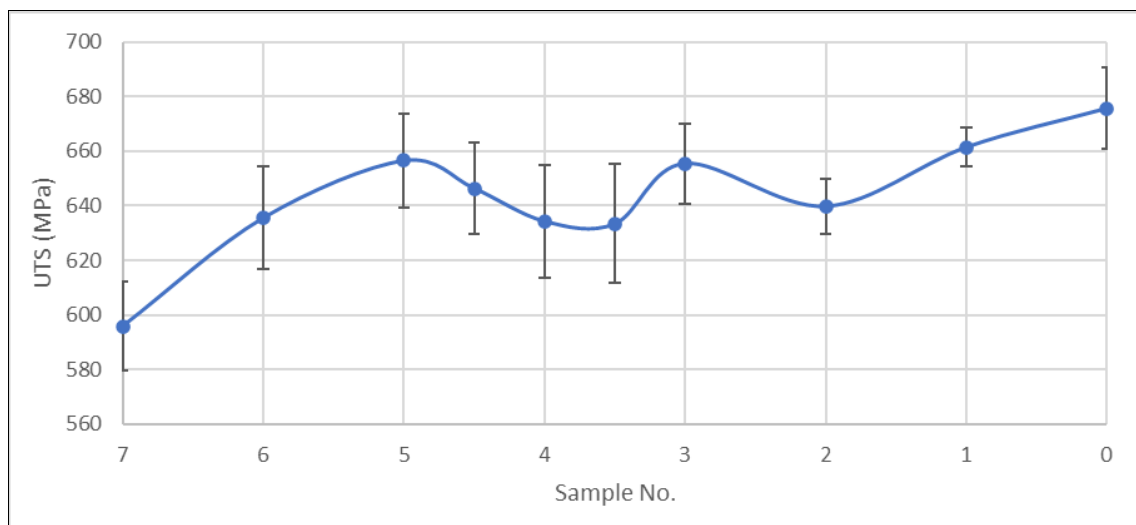
Figure 106- Average UTS results from plastometer, with average deviation shown in error bars.

Generally higher UTS results are associated with higher cooling rates due to smaller grain sizes and possible bainitic formations, if cooling rates are sufficiently high. This may explain the highest UTS measured at sample No. 0 at 675.7 MPa, due to the larger surface area at the very tip of the plate. However, this is also true for the tail end of the strip, where the UTS is the lowest measured at 595.8 MPa. Therefore, it may be the case that the rolling reductions are responsible for the difference in mechanical properties, since Sample No. 7 underwent the full rolling reductions, due to being at the tail end of the sample, where as

135

Sample No. 0 would not have received any reductions in the first pass due to the sample geometry, but also likely experienced a faster cooling rate due the to surface area to volume relationship at the very nose of the sample. To gain a further insight into this, microscopy was conducted on each of the strips cut from the plate.

Grain size analysis was performed for each of the strip microstructures, in accordance with ASTM E112-12 2021, the results are shown in the graph below:
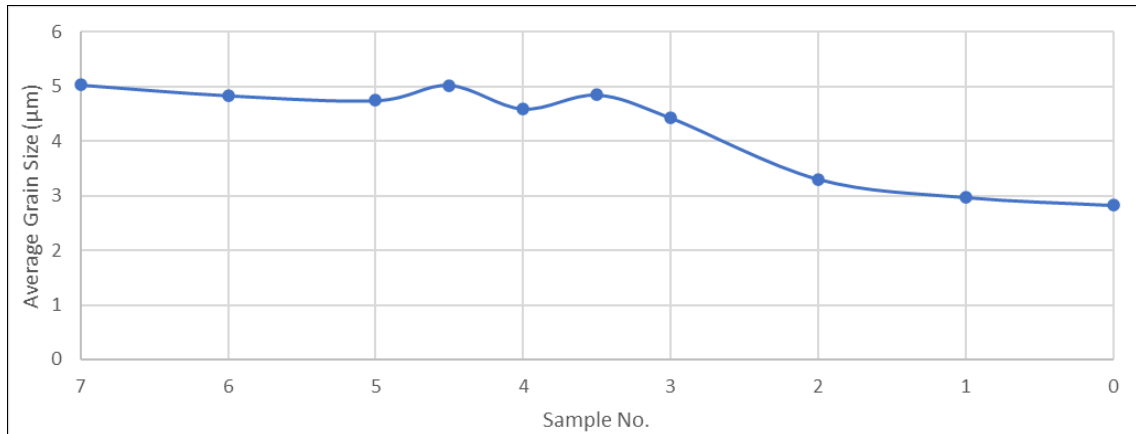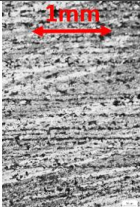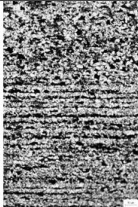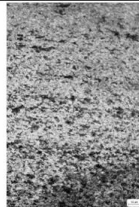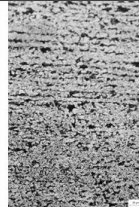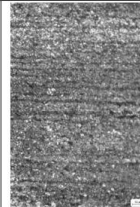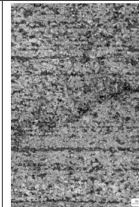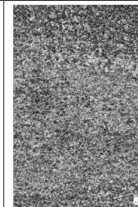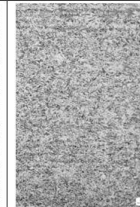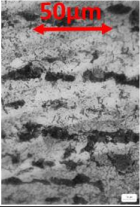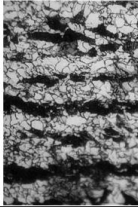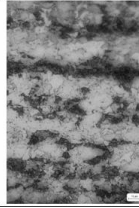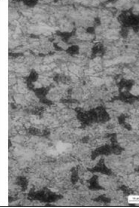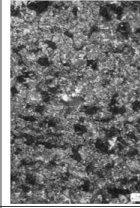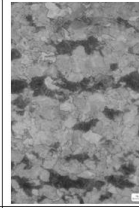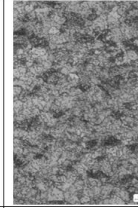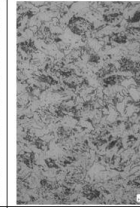
Figure 107- Average grain size along strip length.

A smaller average grain size is observed nearer the nose of the sample, which is in agreement with the results shown in Figure 106. The finer average grain size in this region is likely responsible for the higher UTS measured. However it is contrary to the fact that the nose of the sample experiences less strain reductions than the rest of the strip, less reductions should result in a larger grain size since grains are refined during hot rolling operations.

It was also noticed that the phenomena of banding was not observed at the nose of the sample, but was present throughout the remainder of the strip, shown below in Table 19. The first presence of banding is shown clearly in sample No. 2 with longitudinal pearlite formations shown by the darker regions in both magnifications. Due to the chamfered geometry, the nose of the sample does not undergo the same reductions that the rest of the sample experiences. However after the 1st reduction, the sample is of uniform thickness and therefore the whole length of the strip is subject to the same strain from the 2nd pass onwards. It can therefore be reasoned that the presence of the banded microstructure is formed in the 1st pass.

Table 19- Micrographs at 50 and 1000 times magnification across sample length.

50x Mag								
1000x Mag								
Sample No.	7	6	5	4	3	2	1	0

Interestingly the tail end of the sample has comparable average grain size with the strip centre, however with reference to Figure 106 there is a significant difference in the UTS, with the tail end of the strip being significantly weaker. To investigate this further the volume fraction of pearlite was measured for each strip sample. Three images were taken from each sample and the average volume fraction of Pearlite is presented below:
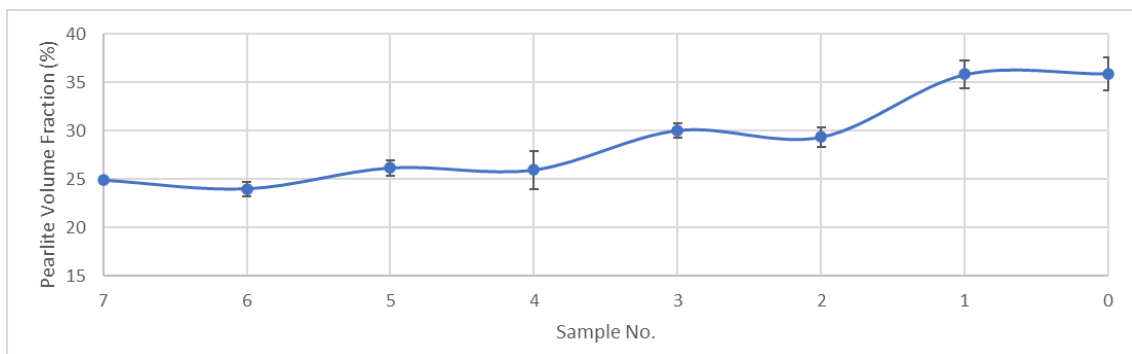
Figure 108- Pearlite volume fraction across sample length.

The volume fraction of pearlite appears to correlate with grain size along the strip length. Therefore the increased UTS at the nose of the strip is likely due to a combination of both the increased volume fraction of pearlite and a more refined grain structure. However the investigations performed do not account for the especially low UTS exhibited at sample No. 7. This may be due to the limitations of the strip areas selected for microstructural grain size and volume fraction analysis, since there may be local areas of microstructural variation. This could be attributed to variable temperatures during rolling or on the ROT, perhaps due to scale or varying levels of water impingement on the strip.

In any case this study shows that with reference to the UTS, volume fraction and grain size analysis conducted that the both the front and back of the sample strip should be avoided. Ideally all samples should be taken between strips 5 and 3 (with reference to Figure 102). For experimental reference this 'window' measures 250mm in length and is in the centre of mass of the strip (since final strip length can vary as a function of final rolling thickness and starting block size). This study has also shown some degree of variation in strip properties for both microstructure and mechanical properties, in this particular study the UTS varies, within this 'stable' region by a maximum of 23 MPa, the average grain size varied by 0.6 μm, and the perlite volume fraction by 4.1 %. Therefore, differences in these values between consecutive experiments conducted on the lab mill should only be regarded as relevant if they are larger than the percentage difference described previously.

One possible reason for the potential differences between the front and the back of the sample was due to the different inter-pass times, experienced by the front and the back of the sample, that are inherent in this reverse rolling method. In order to gain an insight into this possibility a Jmat Pro simulation was designed, utilising the multi-pass hot rolling package. Two rolling schedules were created to simulate the front and the back of the plate, using Tata Steel's DP800 product chemistry. These were generated through analysis of the multi-pass trace of the load reading from the laboratory mill:
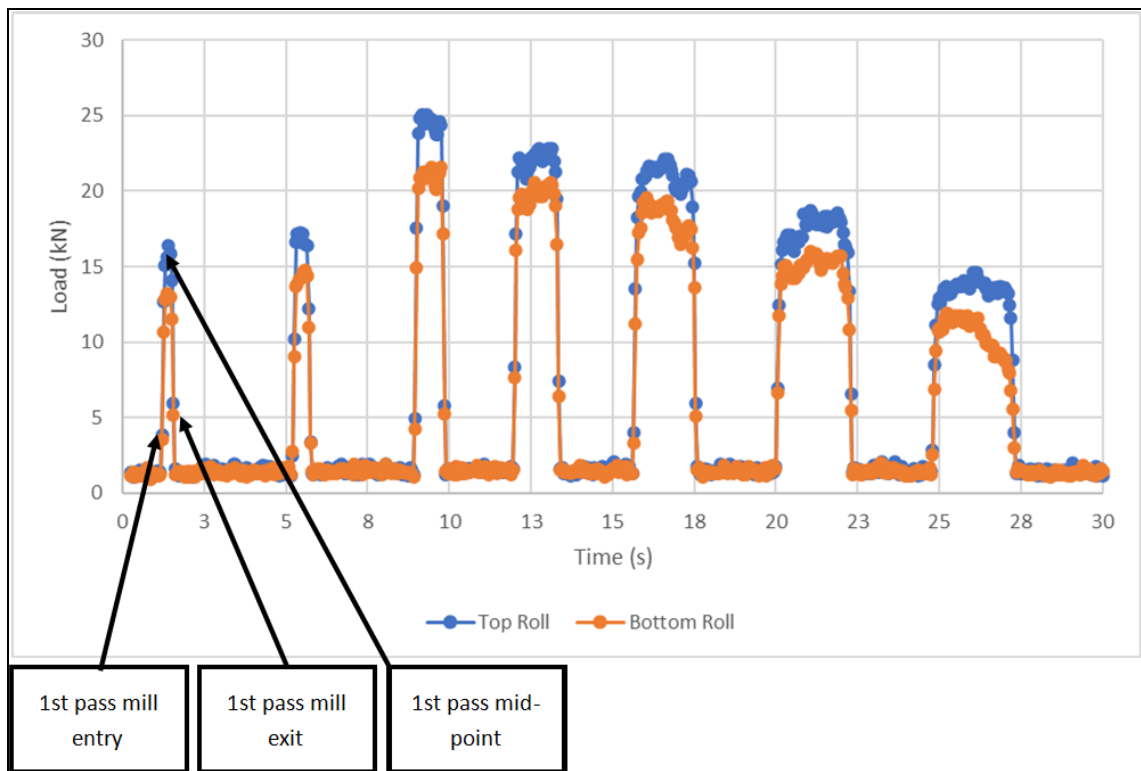
Figure 109- Front Back and strip Middle Inter-pass time analysis.

A rolling schedule, with inter-pass time was generated from these measured readings by subtracting the difference in the time stamps for each roll pass:

Table 20- Difference inter-pass times between consecutive rolling passes for the front middle and rear of strip.

	Inter-pass Times (s)					
Pass No.	**"1 - 2"**	**"2 - 3"**	**"3 - 4"**	**"4 - 5"**	**"5 - 6"**	**"6 - 7"**
FRONT	4.55	3.20	4.40	2.30	6.65	2.55
BACK	3.65	4.65	2.15	5.55	2.50	7.25
MIDDLE	4.1	4.2	3.3	3.75	4.45	4.95

Below these results are presented graphically for better illustration:
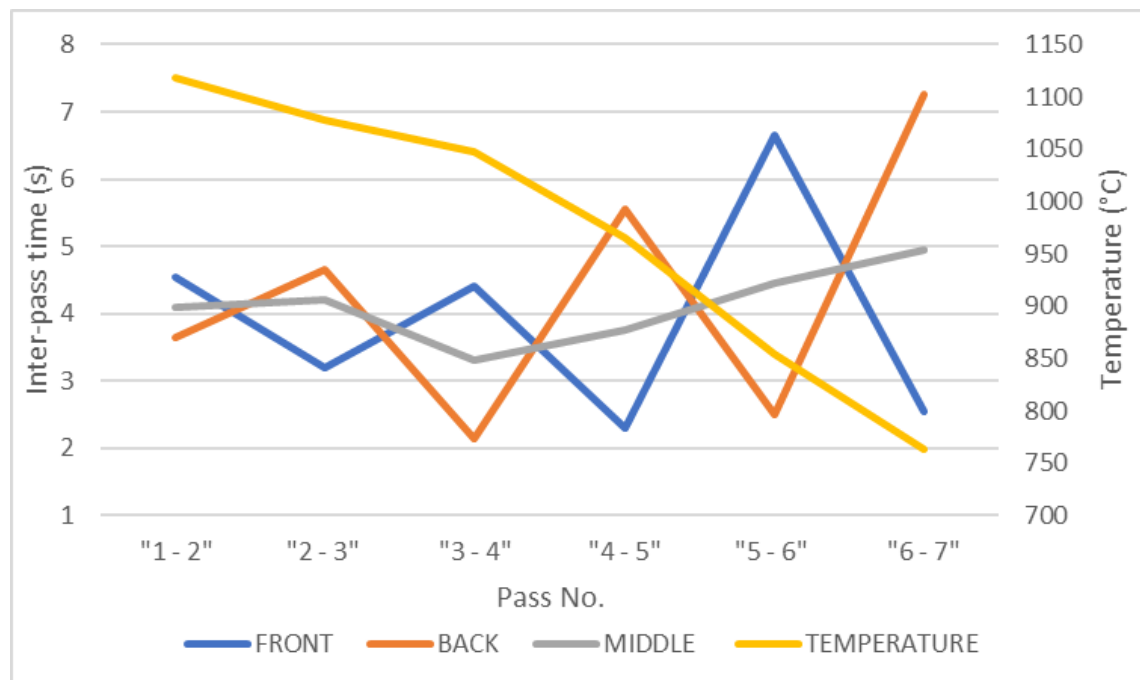
Figure 110- Graphical presentation of inter-pass times for each roller pass front, middle, and back of strip, as well as strip temperature for each of the roller passes.

These results were then input into Jmat Pro's multi-pass hot rolling simulation to see the influence on grain size for all three of the rolling schedules. With the starting grain size set to 700μm based upon the findings of section of 4.1.7.1.
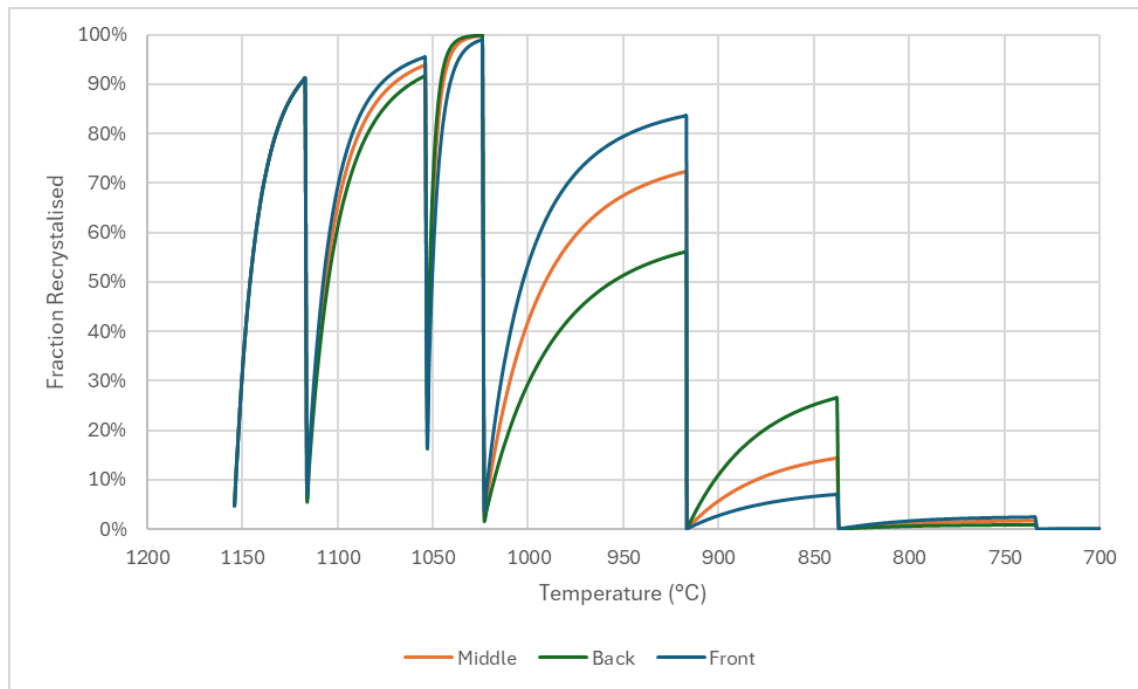
Figure 111- Simulated fraction recrystalised as a function of temperature based on the different inter-pass times derived from experimental data, using Jmat Pro.

It is evident from the above figure that there are some differences in the modelled recrystallisation as a result of varying inter-pass times. It is worth noting that for this simulation the same temperature was used for each roll pass, however in reality it is likely there was some temperature variation through the length of the strip. It is likely that the temperature was highest in the middle of the strip and somewhat lower at the front and back. However, due to limitations in the data acquisition rate of the pyrometers this cannot be confirmed.

Each peak shown in Figure 111 corresponds to a rolling pass, where recrystallisation is present, since the recrystallisation is in response to straining of the microstructures. As expected there is full recrystallisation in earlier passes since the material is well above the TNR. The first three roller passes provide similar levels of recrystallisation, this is likely due to the high temperature of the strip as well as the plate being relatively short, and as a result the inter-pass times are somewhat similar to one another. With reference to Figure 110, it can be seen that after the 3rd pass the inter-pass times become more varied between the passes, and as a result the recrystallization seen in Figure 111 also become more varied between the front, middle and back of the strip.

The variation in fraction recrystallisation through the roller passes is likely to have some effect upon the final grain size. One would expect where there is more recrystallisation

before the TNR, the resultant grain size is likely to be finer and more uniform. This is the case with the front of the sample, as shown by the 3rd peak in Figure 111 which reports approximately 84% recrystallisation, where as the middle and the back are 73% and 56% respectively. This shows good agreement with the microstructural findings shown in Figure 107 showing a lower average grain size nearer the front of the sample. This investigation, using Jmat Pro therefore shows that a likely reason for property variation along length is due to variations in inter-pass timings due to reverse hot rolling.

4.1.4. Geometry Design 2 (Symmetrical Specimen)

A novel design was sought after concerns were raised regarding the useful length of "Sample 1" since only the 'non chamfered section' will undergo representative thickness reductions. For this reason, a symmetrical sample was created. As shown in Figure 112.
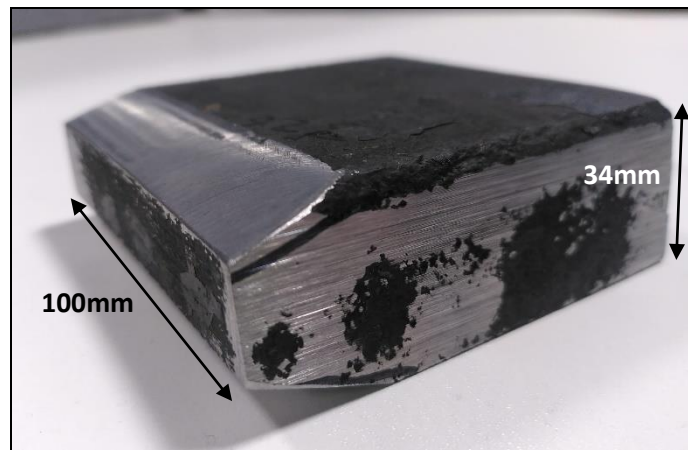
Figure 112- Symmetrical Sample Design

This allows for the initial 'nose' of the sample to have adequate initial bite, however the thickness increases on two faces rather than one, at a similar angle, therefore reducing the tapered length, therefore increasing the amount of material available for analysis. This is particularly useful when using plant produced transfer bar, which is costly to obtain, allowing for increased experimental yield.

Two blocks with the 'Sample 2' geometry were trialled experimentally. Heating and resultant temperatures are shown in Table 21.

Table 21- Details of experiments for 'Sample 2', including Final Rolling Temperature, Coiling Temperature, and general notes regarding biting reliability.

	Slab Re-heat Furnace Temperature (°C)	No. Water Headers Open	Final Rolling Temperature (°C)	Coiling Temperature (°C)	Notes
Sample 2A	1250	18	763	570	All passes were successful. Much quieter than Sample 1 blocks, likely due to reduced chatter.
Sample 2B	1250	18	752	558	All passes were successful. Much quieter than Sample 1 blocks, likely due to reduced chatter.

It was generally accepted based upon the experience of the operators and the audible report of the processing of the blocks that the 'Sample 2' was the preferable design of the two, therefore this design was taken forward.

Figure 113 shows the load outputs for 'Sample 2A', again the trend seen previously was repeated in that the predicted load far exceeded the measures load, but seemed to nominally align for the latter passes, with exception on the last pass where a 15kN difference was seen. It still remains unclear why this is the case. However, in any case the loads were lower than the upper limit of 70kN, so this was a satisfactory result.
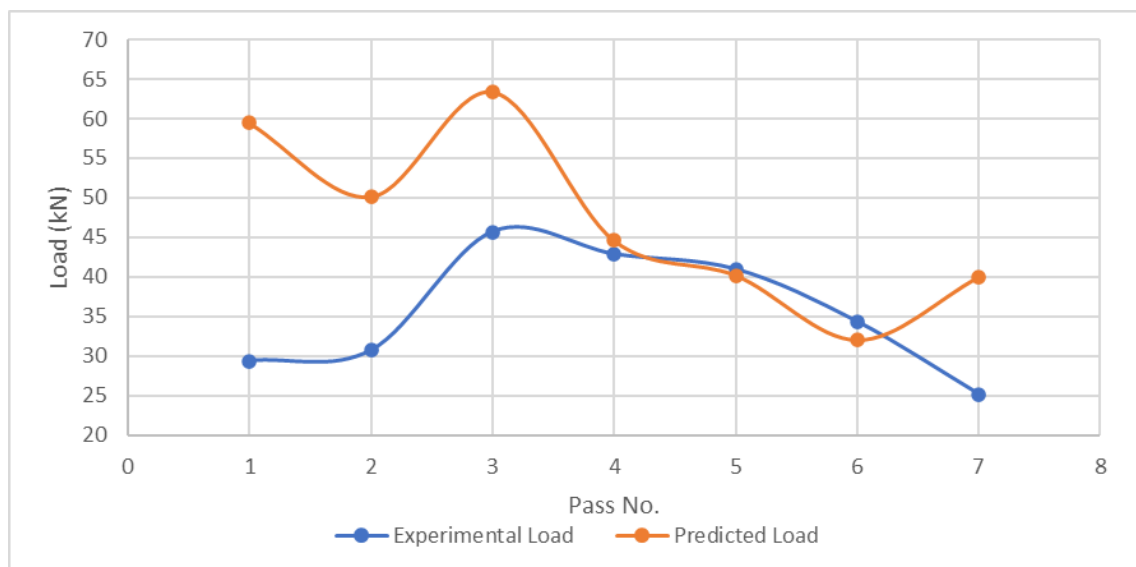
Figure 113- Predicted and Measured Load for 'Sample 2A'.

Similarly to 'Sample 1' the UTS was approximated using Plastometry, with both blocks exceeding 700MPa due to the low CT shown in Table 21.

Despite successful mechanical processing of the sample between the rollers, a less than appropriate FRT was still observed, similarly to the trend seen in 'Sample1'. Despite the operators' best efforts to mitigate temperature loss over the rollers (by pre heating the rollers by passing a heated iron block between them for 20 passes, this resulted in a roller surface temperature of 60-70°C, prior to rolling). This trend of insufficient FRT seemed to exclusively exist for this particular rolling schedule, therefore further investigation was warranted.
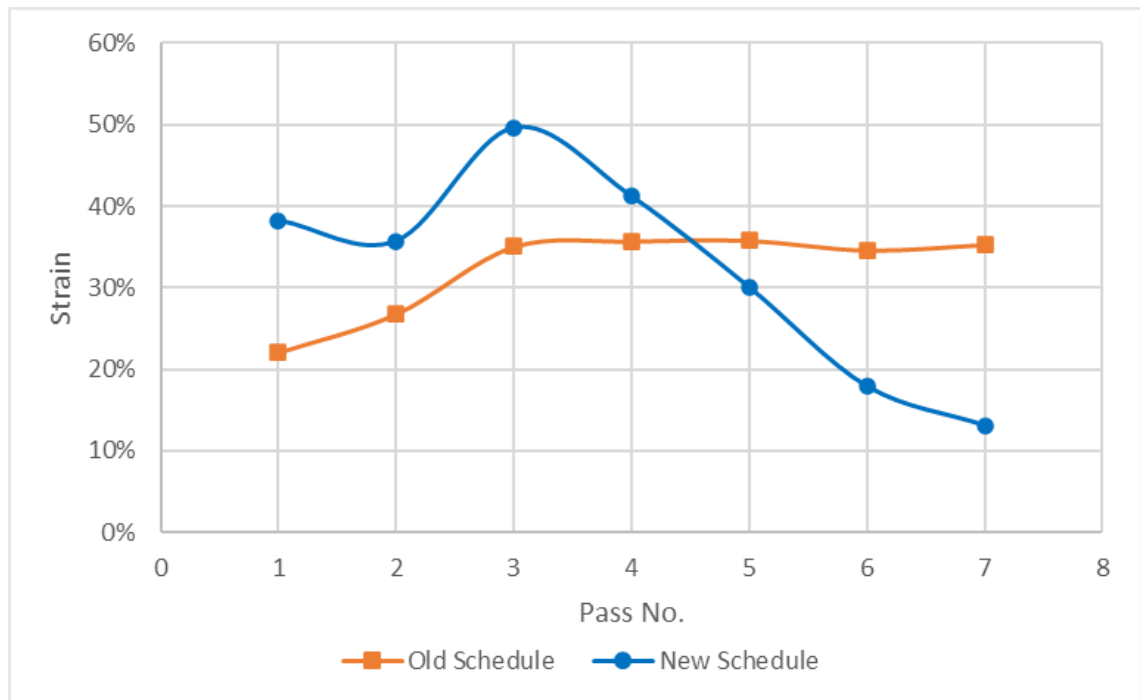
Figure 114- Strain per pass of new schedule (aligned with Port Talbot plant) and old rolling schedule, previously used experimentally

Figure 114 shows the percentage strain imparted into the schedule per roller pass, for the new aligned rolling schedule against the older schedule previously used. It is evident that in the last three passes, decreased strain is used, as was the intention for this body of work, however due to the phenomena of adiabatic heating this is likely to have an influence on strip temperature, as shown below:
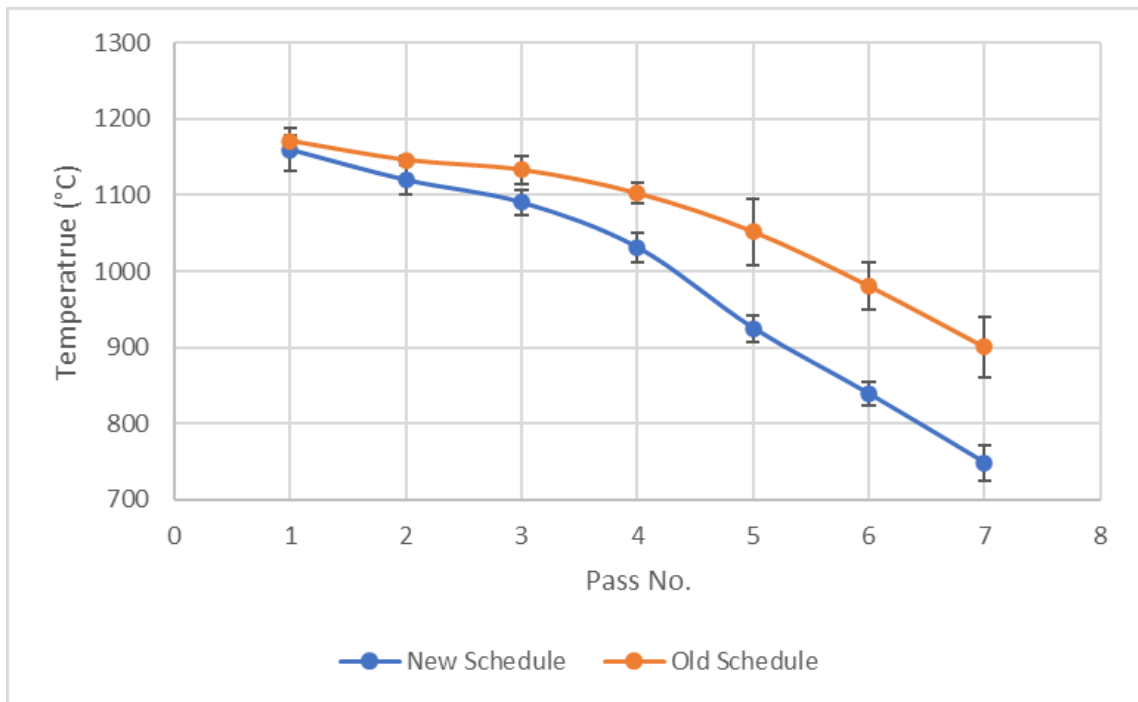
Figure 115- Average inter-pass temperature from all 'New Schedule' experiments, and inter-pass temperature from 6 previously rolled DP grades using the 'Old Schedule'.

Figure 115 shows the average inter-pass temperature from all trails conducted using the 'New Schedule' with an average of six DP600 blocks previously rolled using the 'Old Schedule'. It is evident from this trend that the 'New Schedule', with reduced strain in the later passes, does affect the inter-pass temperature, in particular the FRT which is a major driver in dictating representative transformation on the ROT.

For this reason, it was decided that a 6-pass schedule should be implemented to overcome this issue.

4.1.5. Geometry Design 2 (Symmetrical Specimen) 6-Pass Schedule

As discussed above, a reduced number of rolling passes was attempted in order to better retain strip temperature. The reasons that this approach was theorised to be beneficial was largely due to a decreased rolling time, eliminating the last pass would mean less heat is lost due to radiation. This factor was thought to also be compounded by the fact that one less pass would result in less physical contact between the strip and the rollers, allowing for less opportunity for thermal conduction. Some of these affects were expected to be mitigated by the fact that a 'dummy' pass had to be implemented so that the sample ended up on the 'exit' side of the mill, for ease of entry into the ROT, however this process is quicker than an equivalent 7th rolling pass since the sample can be passed between the

rollers without touching them and therefore relying upon the roller speed to feed to sample to the operator on the exit end.

The rolling schedule was also adjusted to retain the degree of deformation below the TNR, but with a total of six passes. Therefore, higher rolling reduction were introduced into earlier passes, details of the roll gap programmed into the mill and resultant percentage reductions are shown below in Table 22.

Table 22- 6 Pass schedule rolling reductions.

6 Pass Schedule							
Pass No.	**0**	**1**	**2**	**3**	**4**	**5**	**6**
Roll Gap (mm)	34	20	12	6	3.3	2.6	2.3
Reduction (%)	-	0.41	0.40	0.50	0.45	0.21	0.12
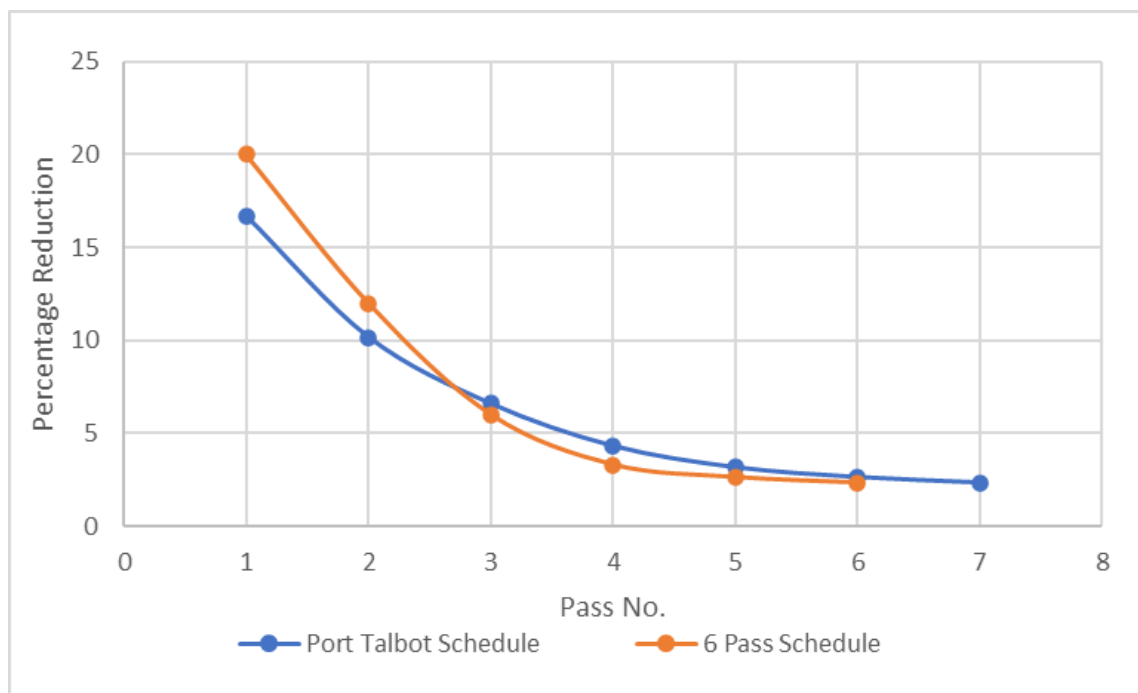
Figure 116- Comparison of relative reduction per rolling pass of 6 pass Laboratory schedule and Tata Steel Port Talbot schedule.

Figure 114 shows the relative reduction, for each rolling pass, between the Port Talbot Hot Mill Schedule and the novel six pass laboratory schedule. Note that good convergence between the two schedules is achieved below the fourth pass, which is approximately the region that the TNR occurs.

Three blocks were trailed utilising the 'Sample 2 Design' geometry. All loads were within limits and a reasonable degree of repeatability was observed, as shown in Figure 117.
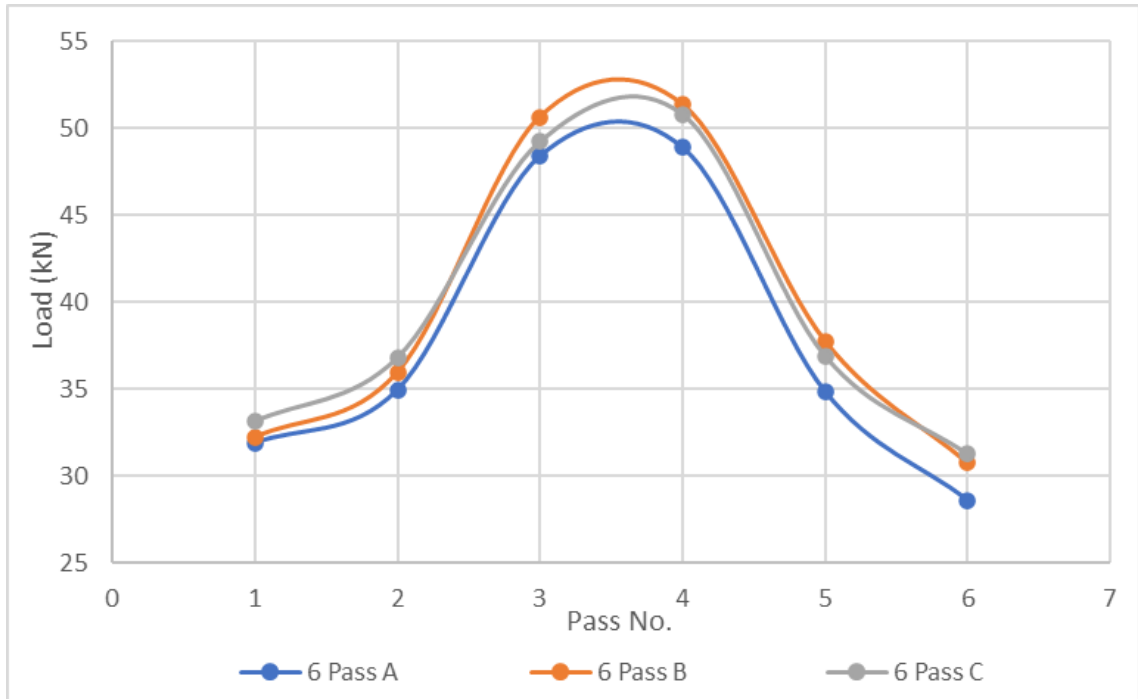
Figure 117- Load Output from 6 Pass Schedule, with identical geometries and reheat times (repeats).
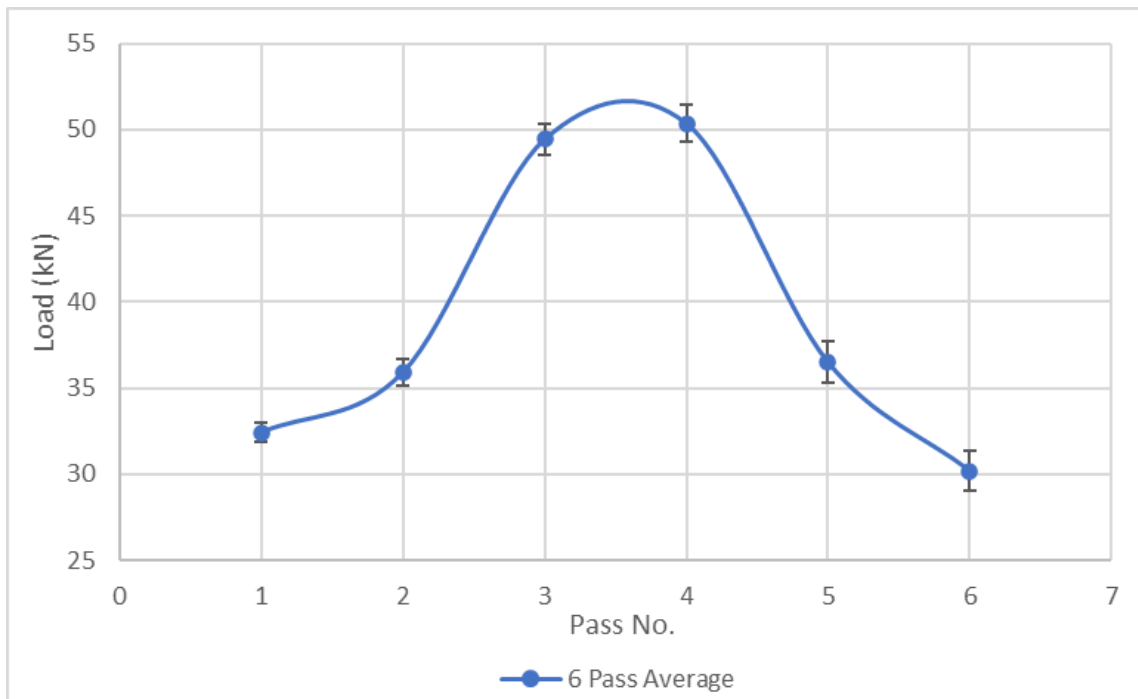
Figure 118- Average Load outputs with error bars depicting standard deviation.

Temperature outputs were more variable than the loads, this is likely due to slight variations in inter-pass times resulting in more temperature loss. However interestingly a good converge was seen at the FRT (Pass 7), shown in Figure 119. Note that the 7th 'Pass' is simply the temperature reading from the 'dummy' pass as the sample was passed back from the entry side to the exit side of the mill, under the pyrometers, provoking a reading.

This is useful since it allows for the capture of the temperature loss resulting from the dummy pass.
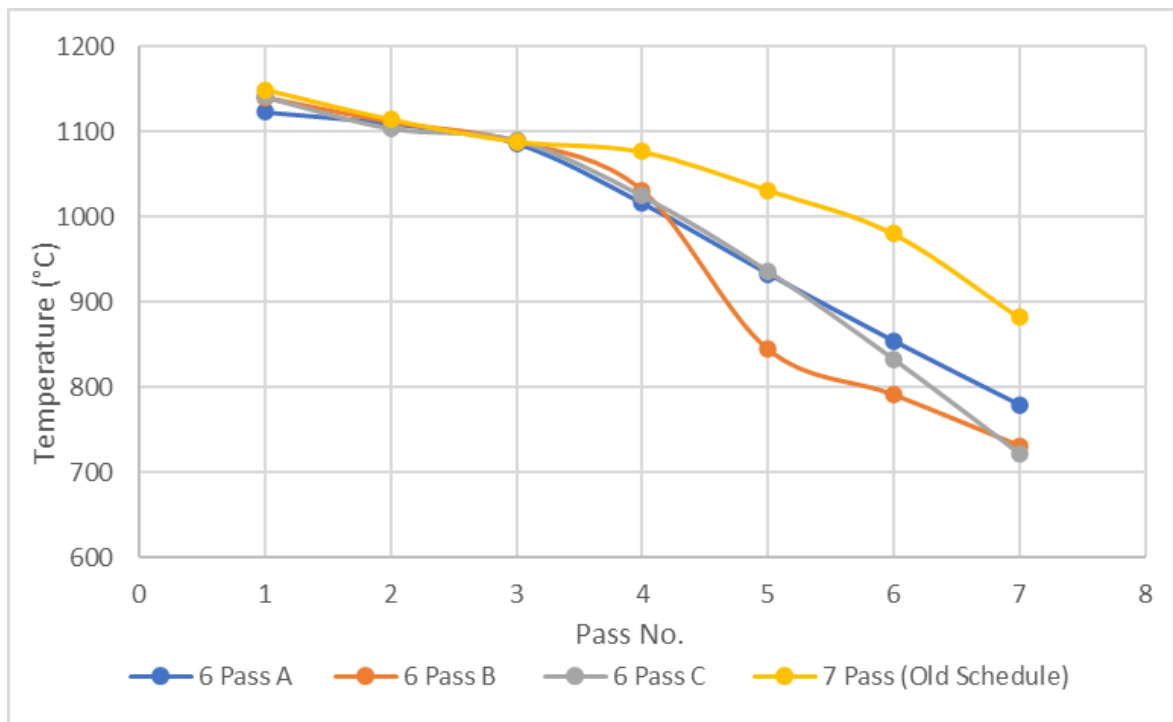
Figure 119- Inter-pass temperature of all 3 6 Pass blocks with a previously rolled 7 pass schedule overlayed.
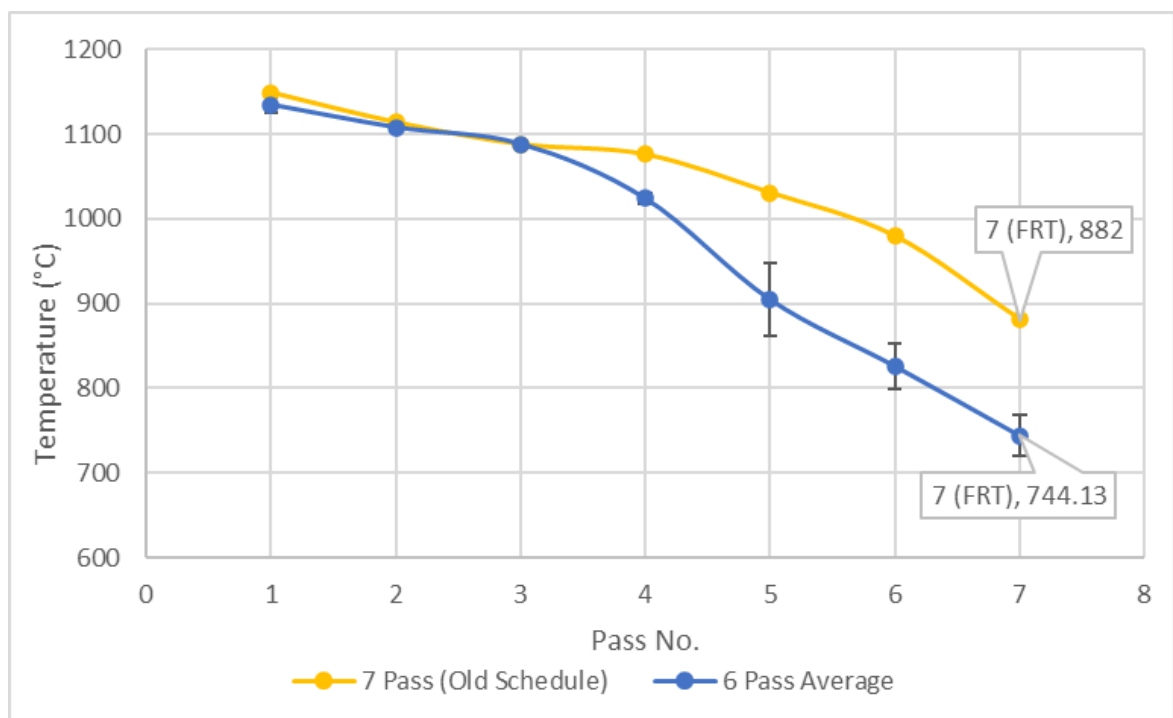
Figure 120- Average inter-pass temperature of the 3 6 pass blocks, with the inter-pass temperature of a previously rolled 7 pass schedule.

Figure 120 Illustrates the relative difference between the two schedules. It is clear that despite efforts made to decrease the difference in FRT, by implementing fewer rolling passes, the temperature at the exit of the mill remained too low and therefore unsuitable in modelling the Port Talbot Hot Mill.

Due to the persistent temperature difference between the two rolling schedules, it was deemed that a greater understanding of the possible differences between the two schedules should be sought. The possible causes for temperature difference could not be attributed to experimental variation, such as varied inter-pass time since, with reference to Figure 119, the FRT tended to converge regardless. This trend of lower temperatures in later rolling passes, was also observed repeatedly across a total of five samples with the 'new' rolling schedule, with greater rolling reductions in the earlier passes. Two key avenues were identified for possible temperature loss; decreased adiabatic heating and difference in sample geometries at subsequent rolling passes due to variations in the two rolling schedules.

Equation 20 was used to estimate the amount of temperature increase attributed for each rolling pass, as shown in Figure 121.
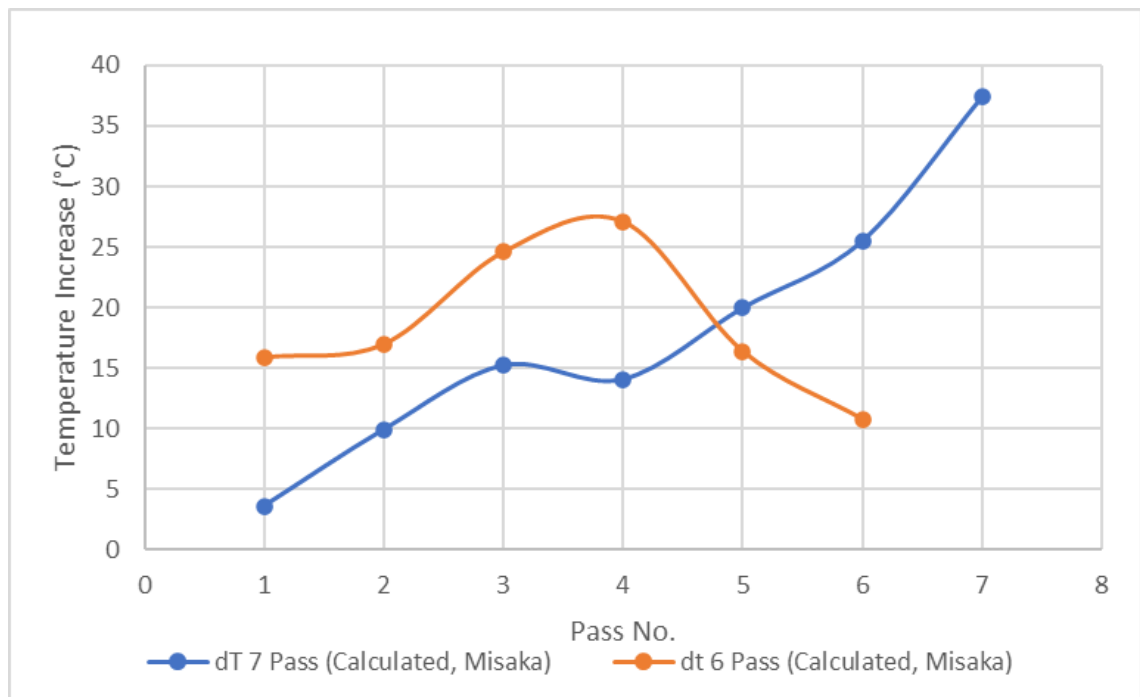
Figure 121- Calculated temperature increase due to strain imparted into the sample, Misaka model used to estimate MFS for each rolling pass.

As expected the degree of adiabatic heating experience by the sample rolled with the seven pass schedule, was larger than that of the six pass in the later rolling passes, due to the higher strain imparted in this part of the schedule. However the larger difference in any single pass, according to this model is approximately 15°C, which does not explain the large difference seen in the FRTs, shown in Figure 120, of approximately 170°C.

Therefore, the difference in temperatures is likely due to differences in sample geometries at relative rolling passes. The below equations describe the three mechanisms in which any object, at an increased temperature relative to it's surroundings, will expel thermal energy (per second):

Equation 22 describes the heat radiation energy emitted from the sample over time. The term 'A' describes the total surface area of the sample, which is the only independent variable, in the case of radiation, between the two rolling schedules. To illustrate this, the surface area of the samples, for each rolling pass was plotted and compared, see Figure 122 below. The sample was assumed to be a constant width of 100mm and modelled as a straight length with semi-circular ends, and the volume was assumed to be constant throughout, this allowed the surface area of the sample to be calculated mathematically.
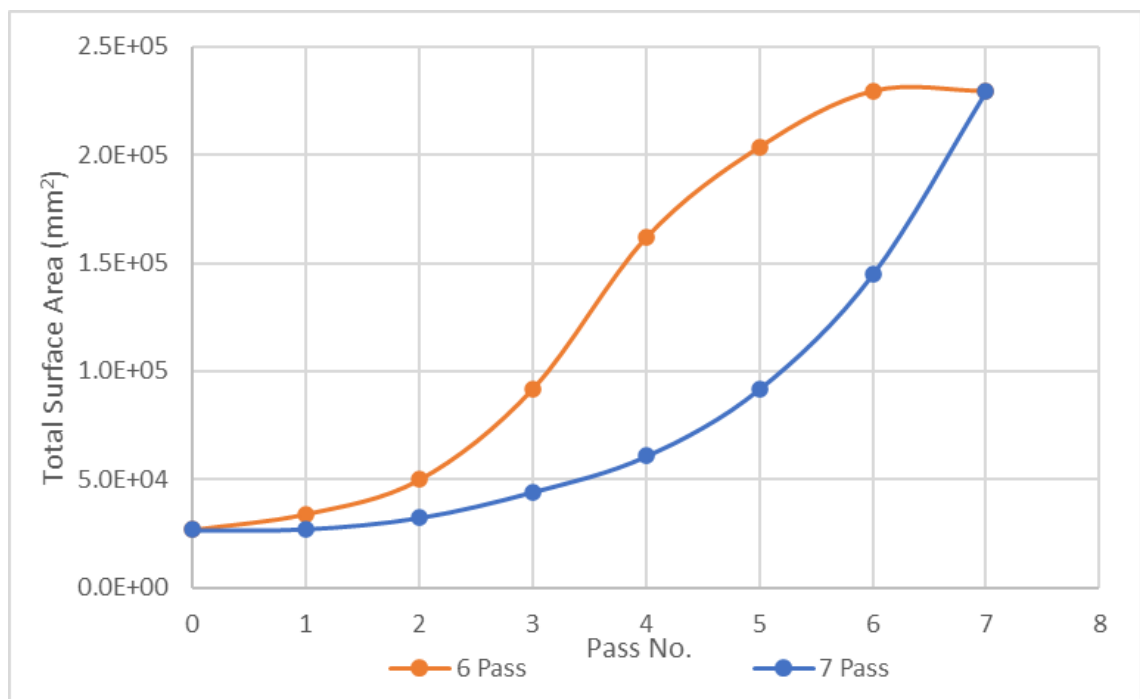
Figure 122- Surface area of each sample, per roll pass.

The largest deviation in total surface area was observed in pass five with a total difference of approximately 62%. Despite the surface area at pass seven being identical, since both samples are being rolled to the same gauge, the opportunity for radiation and convection is increased significantly for the six pass schedule. Likewise the opportunity for conduction is also increased in the six pass schedule. Heat loss through conduction can be attributed to two areas; the area in contact with the roller, and the area in contact with the bed (the bottom surface of the strip). In the six pass schedule, greater reductions are being made in earlier rolling passes, therefore the contact arc length will be greater, likewise the resultant length, and therefore bottom surface of the strip will also be larger, for a given pass.

In conclusion, in attempting to replicate the Port Talbot rolling schedule, in achieving greater rolling reduction, in later rolling passes, temperature loss is inherent to this process. Therefore a 5-pass schedule is the only feasible method by which a representative FRT can be achieved, this too will have the added benefit of not needing a 'dummy' pass, since the sample will finish on the exit end of the mill.

4.1.6. Geometry Design 2 (Symmetrical Specimen) 5-Pass Schedule

4.1.6.1. Sample Justification

Similarly, to previous attempts the reduction in total passes was utilised in order to better retain strip temperature, throughout the hot rolling process and therefore achieve the target FRT. However, with the approach it was clear that moving away from a 7-pass schedule to a 5-pass would be a less representative schedule when compared to the Tata Steel Port Talbot rolling schedule. It was suggested that removing the last pass, due to the percentage reductions being low, would be advantageous completely omit this reduction as well as 'compress' the earlier reduction (above the T_{NR}) into fewer passes. The aim therefore was that a representative rolling schedule could be achieved (with the exception of the last pass), whilst maintaining lower reductions below the T_{NR}. In order to protect the Mill, as was the case in previous schedule designs, a balance was obtained in order to achieve the most representative rolling schedule, whilst minimising mill loads and torques to an acceptable level. The proposed schedule is shown below in Table 23.

Table 23- 5 Pass schedule rolling reductions.

5 Pass Schedule						
Pass No.	0	1	2	3	4	5
Roll Gap (mm)	34	20	12	6.5	4	3
Reduction (%)	-	41	40	46	38	25

A comparison between the Port Talbot hot mill schedules and the proposed five pass schedule is shown below in Figure 123. Note the pass numbers have been offset, illustrating that the last pass has been effectively removed, allowing for a pass by pass comparison of the two schedules.
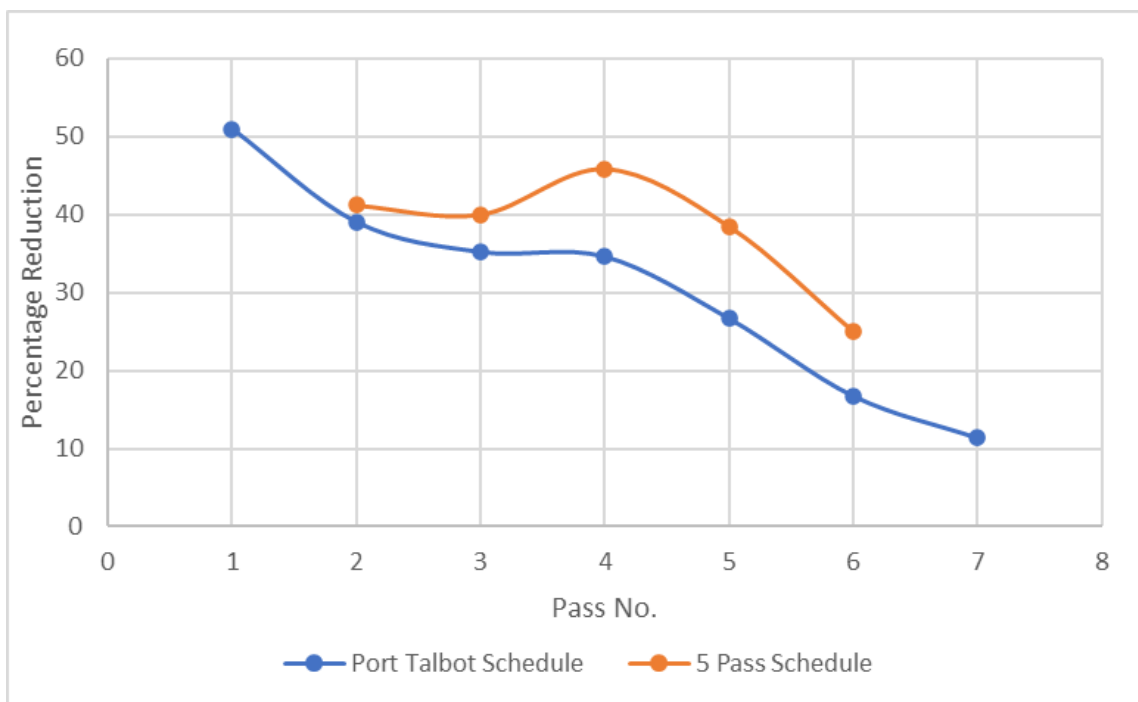
Figure 123-Comparison of strain per pass for Port Talbot rolling schedule and 5 pass experimental schedule.

4.1.6.2.   Results

Two blocks were rolled with the above rolling schedule, with identical cooling paths used. The peak load output and inter-pass temperature, per pass, for both blocks is shown below.
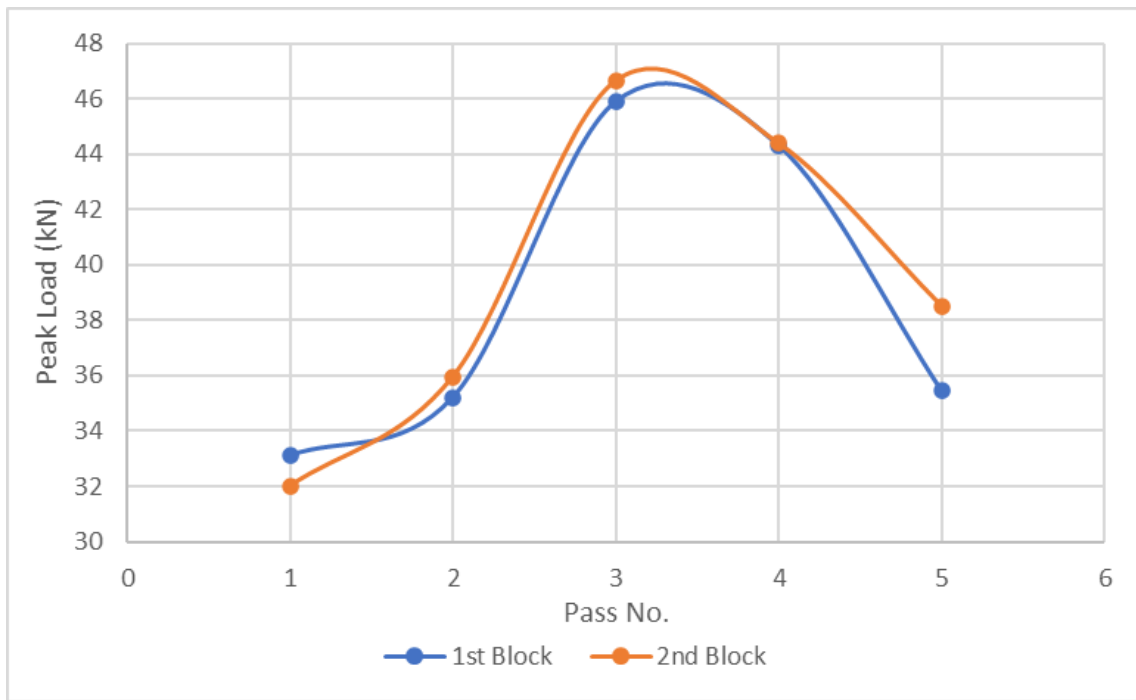
Figure 124- Peak load outputs for 5 pass schedule.
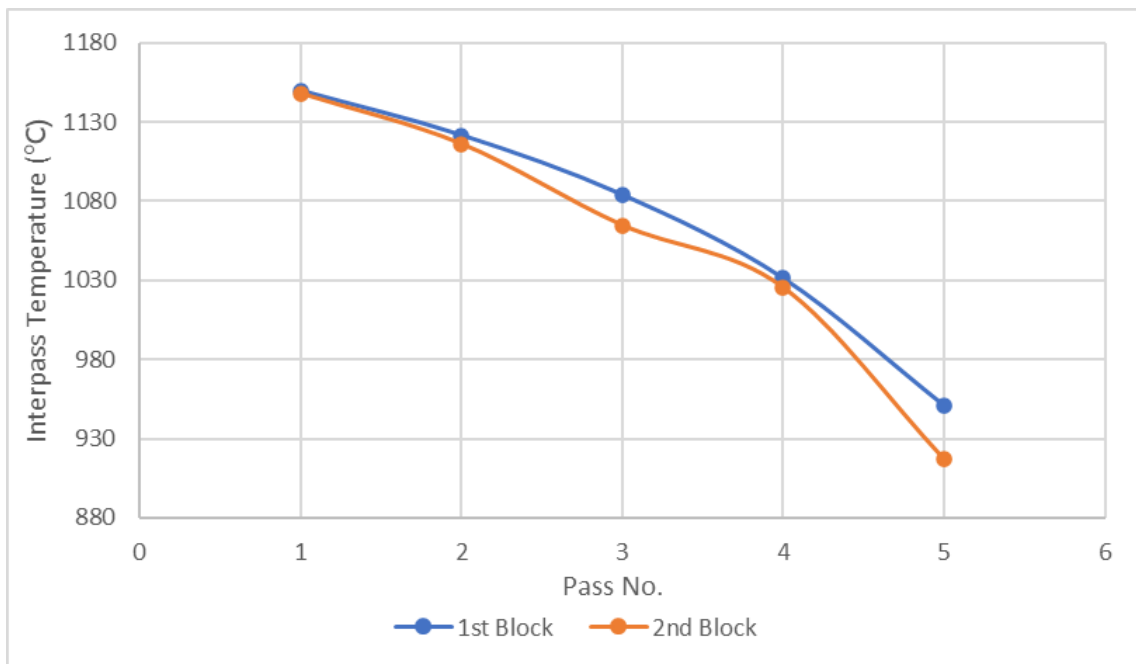
Figure 125- Inter-pass temperature outputs for 5 pass schedule.

It is clear from the above figure that the target FRT was exceeded by a significant degree. Due to this, the strip was held in air before entering the ROT, so that the cooling path utilised resulted in the correction coiling temperature, which was a successful approach in achieving the correct coiling temperature. Peak load and inter-pass temperature was also reasonably repeatable, with a maximum variation, in any given pass, of 3.1kN and 33.7°C respectively. Both of these variations occurred on the last pass. It is likely that this increase

in temperature resulted in an increase in the MFS, and therefore resulted in an increase in peak load.
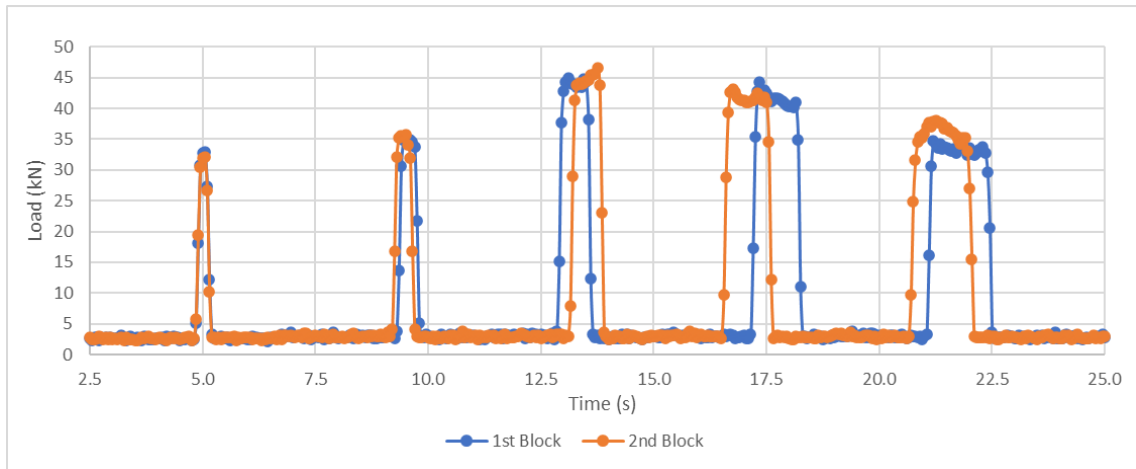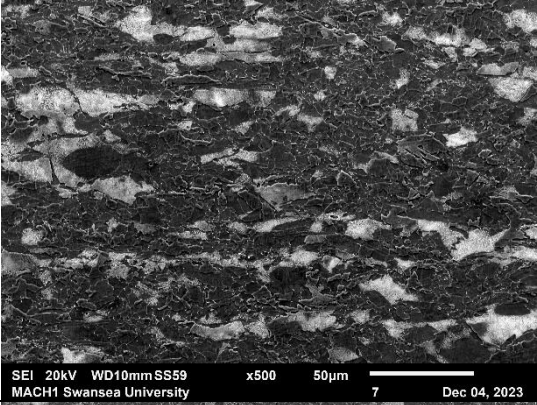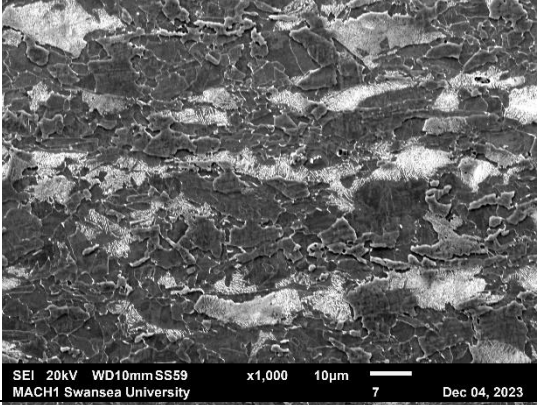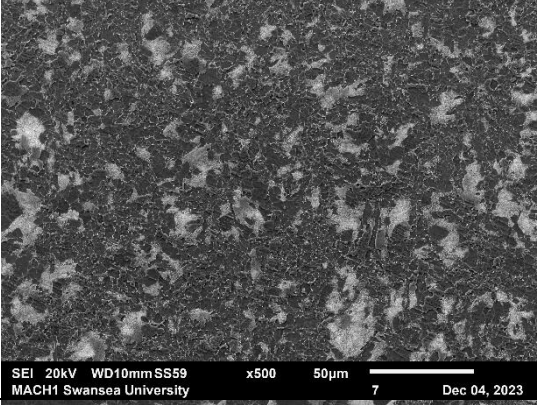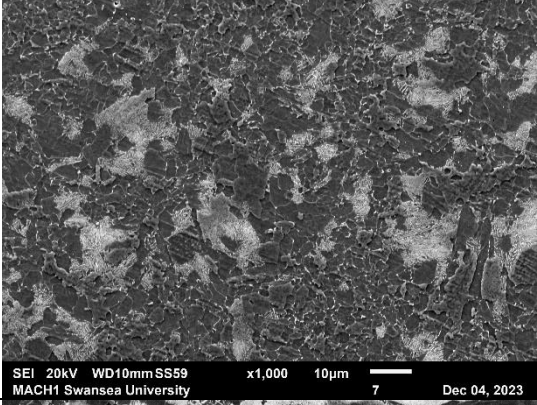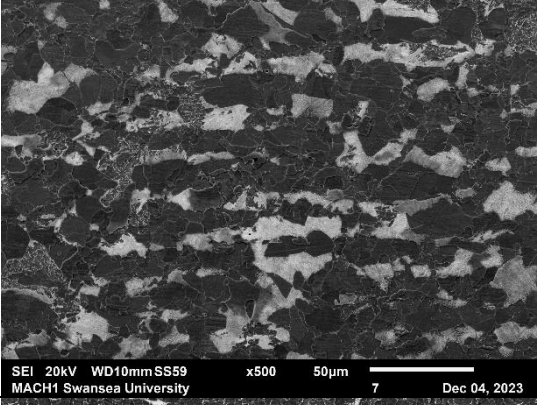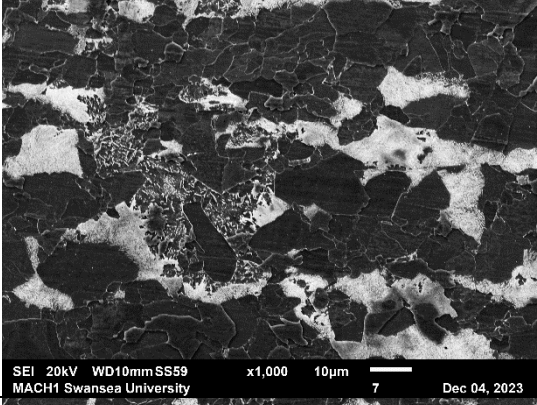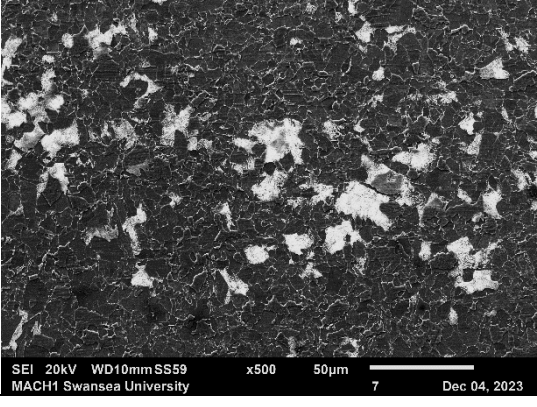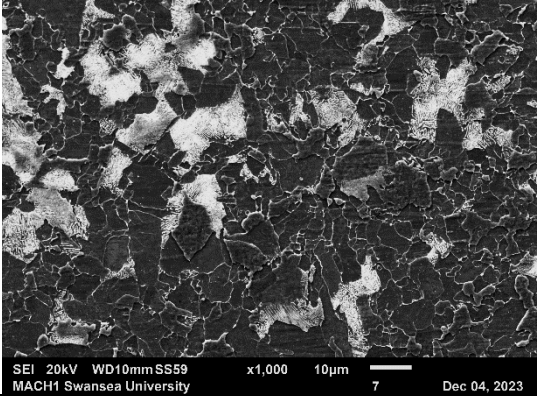
Figure 126- 1ˢᵗ and 2ⁿᵈ of two identical blocks over time.

Figure 126 shows the load readouts over time, for each rolling pass, for both the 1ˢᵗ and 2ⁿᵈ blocks. From the loading profiles, it is clear that the inter-pass times for the 1ˢᵗ block were slightly longer than that of the 2ⁿᵈ, with the exception of the 3ʳᵈ pass. This resulted in the total rolling time for the 1ˢᵗ block being slightly longer than the second. This may have been the cause of the lower temperature at the 5ᵗʰ pass, and therefore the higher load exhibited. However this method allowed for increase strain to be imparted in the initial roll passes and did not result in an unacceptable low FRT.

4.1.7. Microstructural Comparison of Process Routes

Due to the fact that this novel five pass schedule was the only trial that succeeded in achieving the correct FRT, to microstructures have been investigated and compared with the 'old' seven pass schedule and Tata DP800 hot band material. Micrographs were taken using an SEM in direction parallel to the rolling direction and from the top of the sample in order to measure the average grain size. All sample were taken from the very centroid of each of the hot rolled strips, in accordance with the findings in section 4.1.3.1.

Sample Name	Magnification	
	500x	1000x
7 Pass 'Old' Schedule (Rolling Direction)		
7 Pass 'Old' Schedule (Sample Surface)		
5 Pass 'Novel' Schedule (Rolling Direction)		
5 Pass 'Novel' Schedule (Sample Surface)		

Sample	Magnification
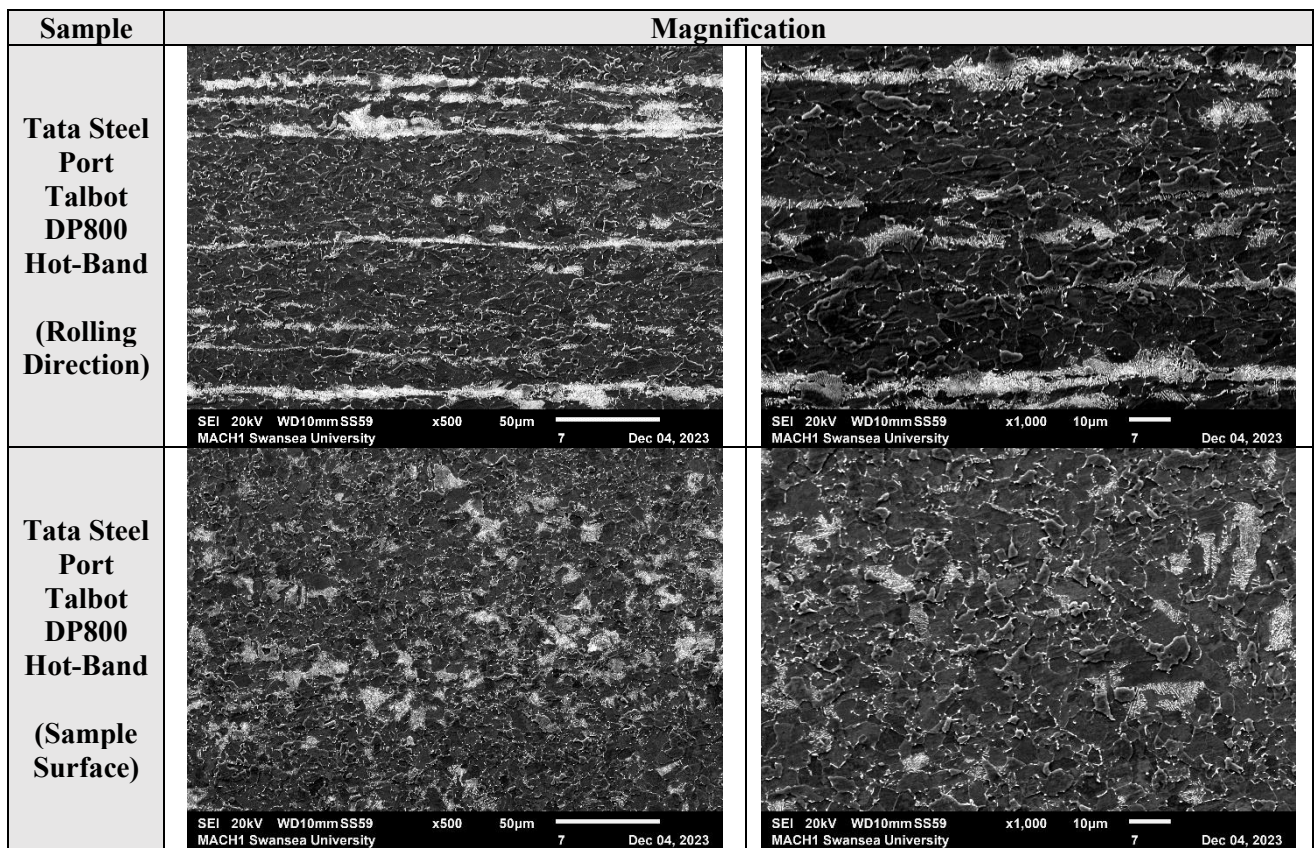
Figure 127- SEM microstructural comparison between 5 pass, 7 pass and Tata Steel Port Talbot 'Hot-Band- material, at 500x and 1000x magnifications

The average grain size was also measured from the sample surface of each micrograph, note that a total of three micrographs were used in order to obtain a more accurate aggregate reading of average grain size. Plastometry was also performed on the samples to obtain a reading of the macroscopic mechanical properties. And lastly the average volume fraction of pearlite was also calculated, using ImageJ. The results are shown below:

Table 24- Summary of results from laboratory produced hot band material and Tata Steel Port Talbot produced hot band material.

Sample Name	Average Grain Size (µm)	Volume Fraction Pearlite (%)	UTS (Plastometry) (MPa)
7 Pass 'Old' Schedule	3.86	36	735
5 Pass 'Novel' Schedule	5.71	32	712
Tata Steel Port Talbot DP800 Hot-Band	3.66	21	721

4.1.7.1. Discussion and Jmat Pro Simulation of Process Routes

The most distinct difference between the laboratory produced and the plant produced material is the presence of banding. The plant produced sample exhibits continuous pearlitic structures traveling longitudinally, parallel to the rolling direction. These structures appear to be continuous and measure between 5µm and 10µm thick, with a highly varied band spacing. In contrast to this the laboratory produced samples do not exhibit continuous banded structures, however the pearlitic formations are nominally arranged in longitudinal patters, with additional pearlitic structures dispersed throughout. This can be seen more clearly at lower magnification, as shown below in Figure 128 (Note that due to the Nital etchant used the Pearlitic structures appear dark against the ferritic matrix). The reason for the reduced banding seen in the laboratory produced samples, for like for like chemistries was likely due to differences in the hot rolling parameters. Although this experimental study aims to align the net reductions per pass, the strain rates are problematic to match due to the higher speeds at which the strip is rolled in the industrial setting compared to the laboratory.
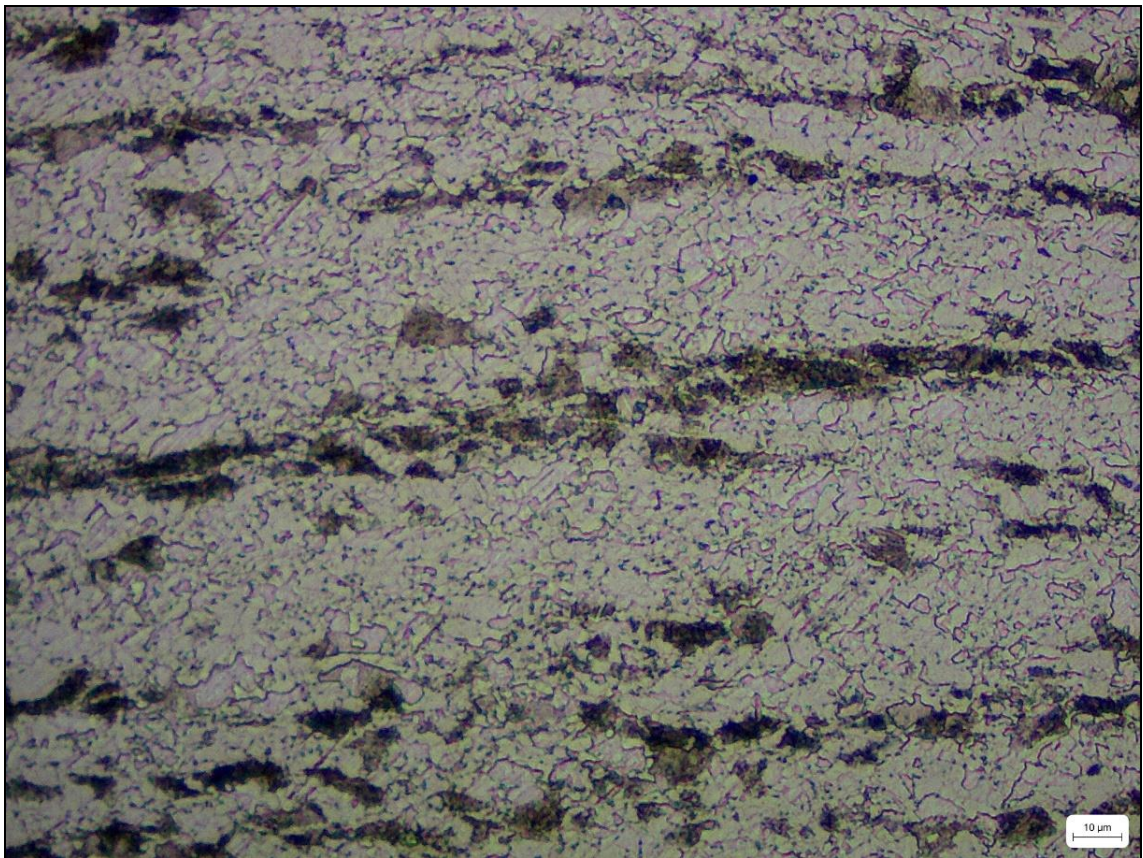
Figure 128- Micrograph of 7 pass "old" schedule, parallel to the rolling direction etched with Nital to reveal pearlitic structures.

The second most noticeable difference between the two manufacturing methods is the level of grain refinement. On average the laboratory route produced a 65% larger average grain size, when compared to the plant route. This is likely due to the presence of the roughing mill, reducing the slab thickness by 6-fold resulting in a significant level of grain refinement.

The level of grain refinement obtained from the roughing mill was simulated by using the 'Multi-Pass Hot Rolling' model in conjunction with the 'Reaustenisation' model in Jmat Pro. First the properties of the Slab Reheat Furnace were modelled based upon the temperature profile shown in Figure 17, as reported by Khosla [75]. This resulted in a final grain size of 466 μm, which was in turn used as the starting grain size for the roughing mill simulation. The reductions, temperatures and inter-pass times were obtained from a roughing mill log were used. The output of grain size, per roughing pass is shown below:
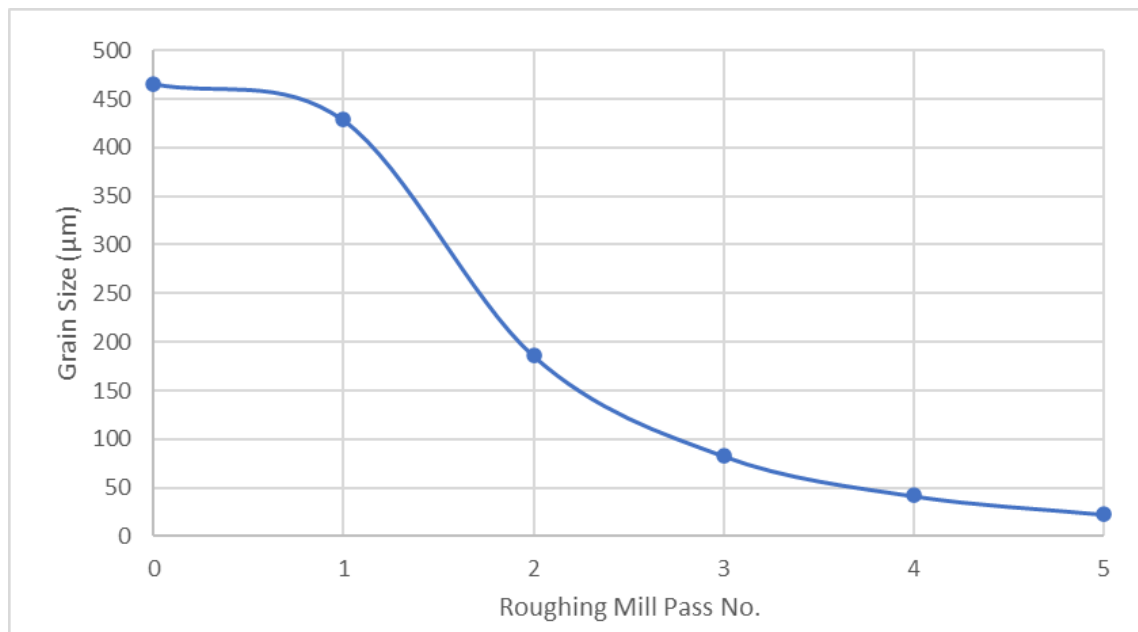
Figure 129- Simulated grain size per pass for the Port Talbot Roughing mill, using JMat Pro.

The final grain size, post rough rolling, was reported to be 23 μm. This is a 20x reduction in grain size, from the starting grain size. It is difficult to quantify the grain size exactly when entering the finishing mill, since upon exit of the roughing mill the strip temperature is in the region of 1100°C, which is well above the TNR and therefore recrystallisation and grain growth is likely to occur before entry into the finishing mill.

However previous research conducted by Tata Steel Port Talbot has estimated the starting grain size, upon entry to the finishing mill to be 120 μm[135], as a result of grain growth due to high slab temperatures. In any case the simulation for the finishing mill was

conducted in the similar fashion, using the temperature, strains, and inter-pass times from a finishing mill log as shown in Figure 47. This showed a total convergence, for both grain sizes, in at 13 μm as shown in Figure 130. In any case the laboratory process route, using the DP800 chemistry is not currently capable of achieving a representative grain structure, when compared with plant produced hot-band material. Despite the strains being well aligned in the case of the 5-pass schedule, with the Port Talbot schedule, the difference in the rollers used can account for changed in the microstructure, since the Port Talbot rollers approximately 700mm in diameter, compared to the 105mm rolls in the laboratory mill. Ouchi and colleagues found that, for Nb bearing steels an increase in roller diameter resulted in a significant reduction in grain refinement[78], likely due to differences in strain rate. This likely explains the large difference between both the laboratory produced samples and the plant produced samples.
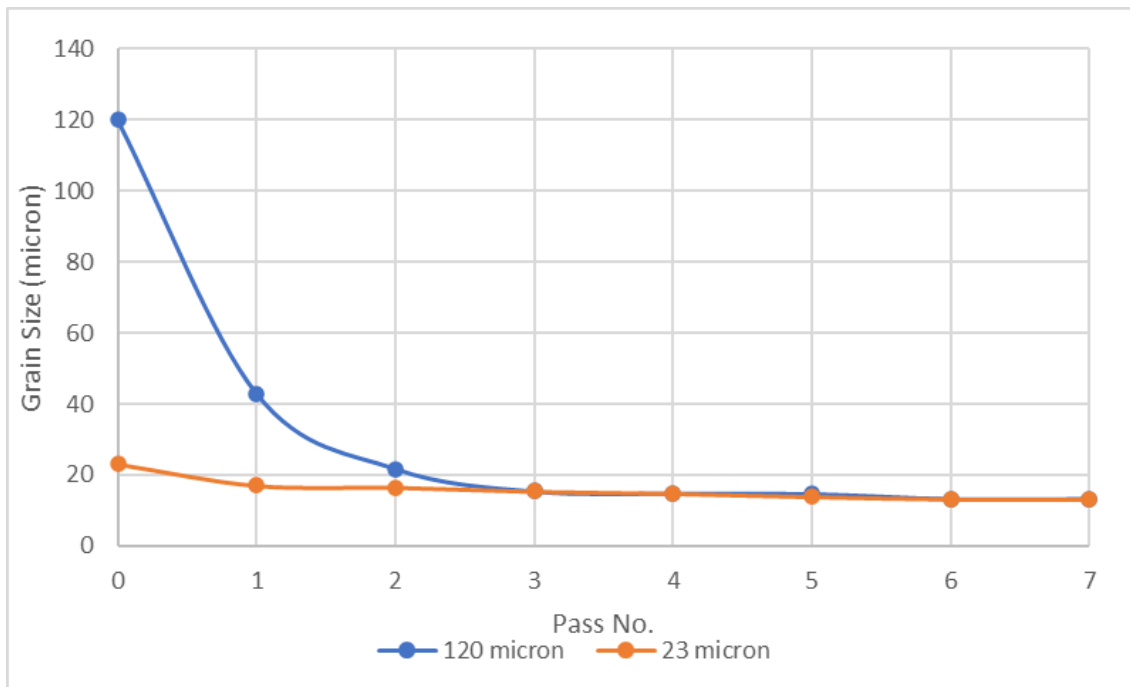
Figure 130- Grain size comparison, per pass, for the finishing mill based on simulated and reported starting grain size (upon entry to the ROT), using JMat Pro.

When comparing the laboratory produced samples against one another it is clear that the 'old' 7-pass produces a coarser microstructure when compared with the novel 5-pass schedule. This is likely due to the increased ability for the grain structure to recover between rolling passes for the 5-pass schedule. The nature of the strains also likely plays a role, since the 'old' 7-pass schedule (with reference to Figure 114) is characterised by large reductions in the latter passes, likely below T_{NR} and as such would refine the

microstructure to a greater degree than the novel five pass schedule, where a larger portion of the net reductions occur above the T_{NR}.

To further investigate the microstructural evolution, during the laboratory hot rolling procedure, both the schedules were replicated in Jmat Pro. To determine the starting grain size, the temperature profile of a typical block had to be determined. This was achieved by mounting a thermocouple into the centre of a block (see Figure 131) and observing the temperature over time using a data logger as per the standard practices observed in SAMI.
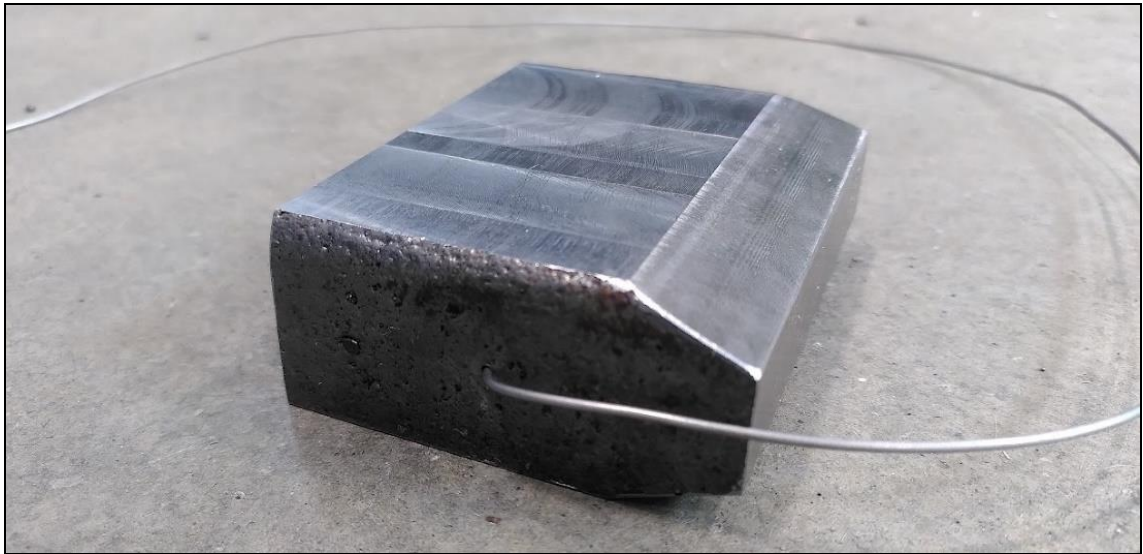
Figure 131- DP800 block with thermocouple mounted in the centre of mass.

The results of the time temperature profile are shown below.
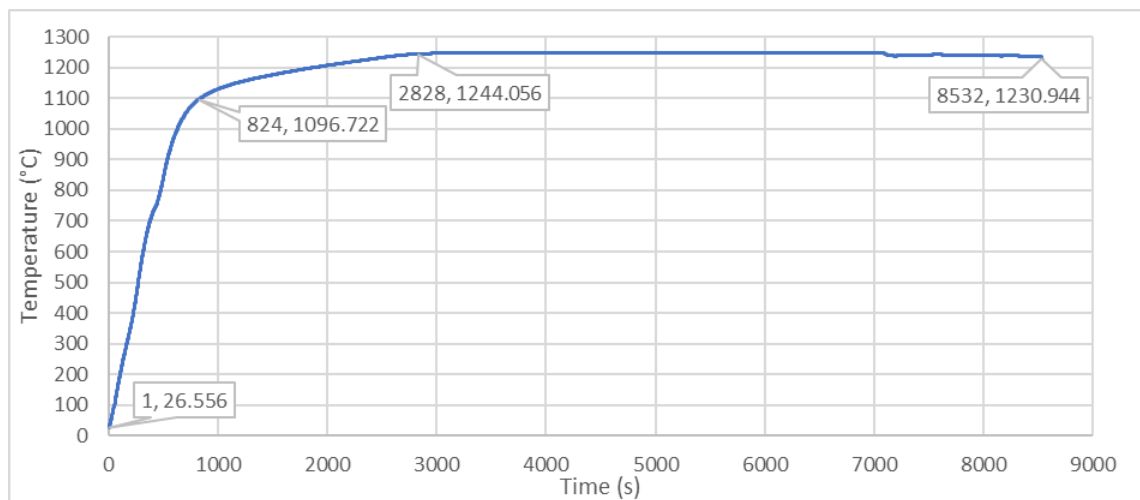
Figure 132- Time temperature profile of a lab produced DP800 block for hot rolling.

The time temperature profile was approximated as two heating rates and a soak time in which the temperature did not change, as described by the four points shown on the above

graph. The resultant simulated austenite grain size is shown below in Figure 133 with a final grain size of 702 μm.
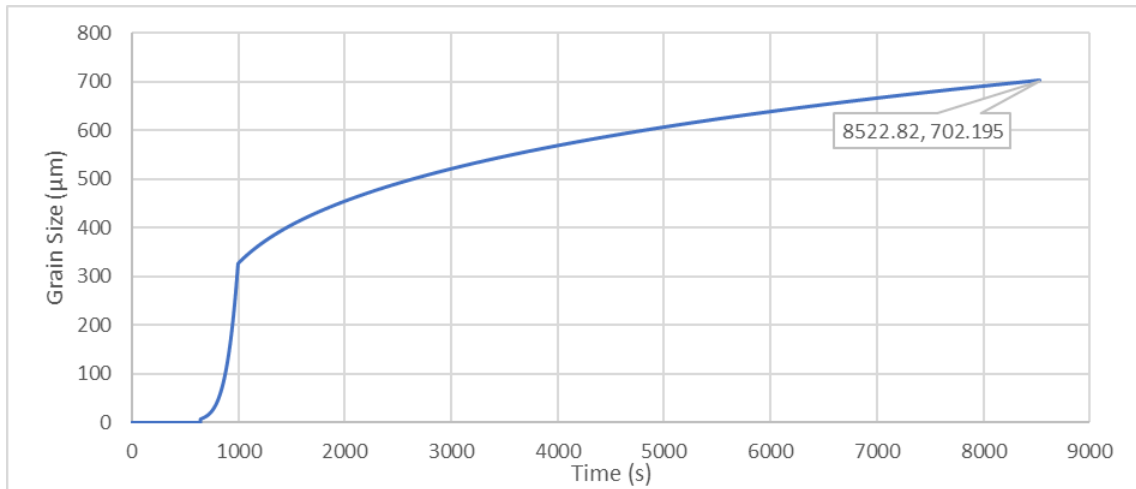
Figure 133- Jmat Pro simulated austenite grain size from reheat furnace for a DP800 lab produced block.

Subsequently this grain size was input into Jmat Pro's multi-pass hot rolling simulation for both the novel 5-pass and 'old' 7-pass rolling schedules with the strain inter-pass times and temperatures determined from the respective experiments. The simulated grain size per pass is shown below:
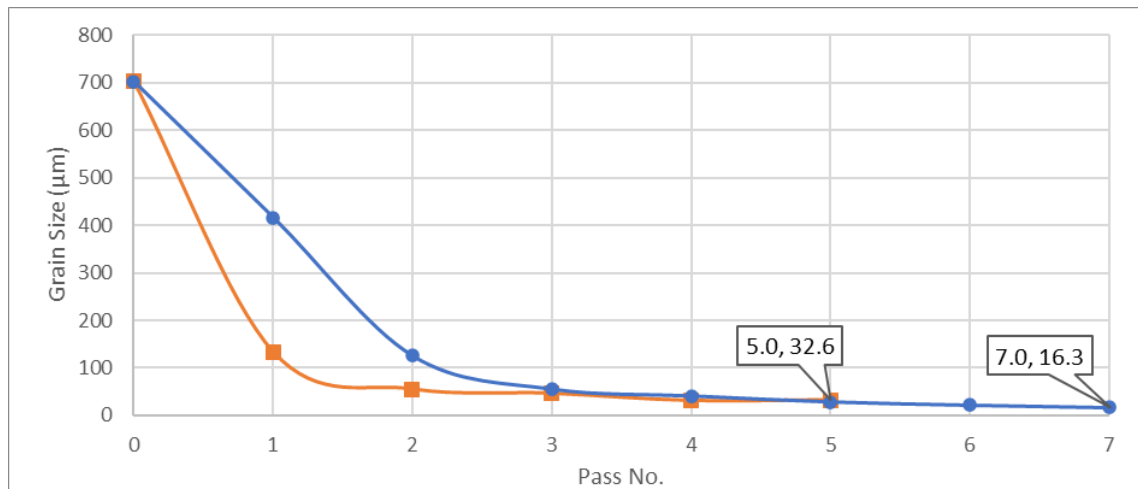
Figure 134- Simulated grain size per pass for both 5 and 7-pass laboratory hot rolling schedules.

The results of this simulation show, that according to the recrystallisation models in within Jmat Pro, that the 7-pass schedule does in fact refine the microstructure to a greater degree than the five pass. It is worth noting that this grain size is the austenite grain size and not the average grain size of the ferrite matrix with pearlite formation seen in the micrographs above, so they cannot be quantitatively compared but the trends observed are valid, since a more refined grain structure achieved below TNR would result in a more refined grain structure on the ROT.

4.1.8. PAGS Comparison

4.1.8.1.1. Study Justification

To finish this body of work a comparative study was conducted to compare the grain sizes upon exit of the ROT for both the 5-pass and 7-pass rolling schedules. This insight will provide further clarity into the laboratory process routes, as well as a comparison between the Jmat Pro simulations of the process routes.

4.1.8.1.2. Method

The rolling section of this study is identical to the previous experimental work discussed in this thesis, with the exception of the absence of the ROT. Instead the samples are quenched to 'freeze' the austenitic microstructure. To do this, after the last rolling pass the plates were placed into a bucket of water until cool. This results in a fully martensitic microstructure, that when etched with picric acid, reveals the prior austenite grain boundaries.

4.1.8.1.3. Results
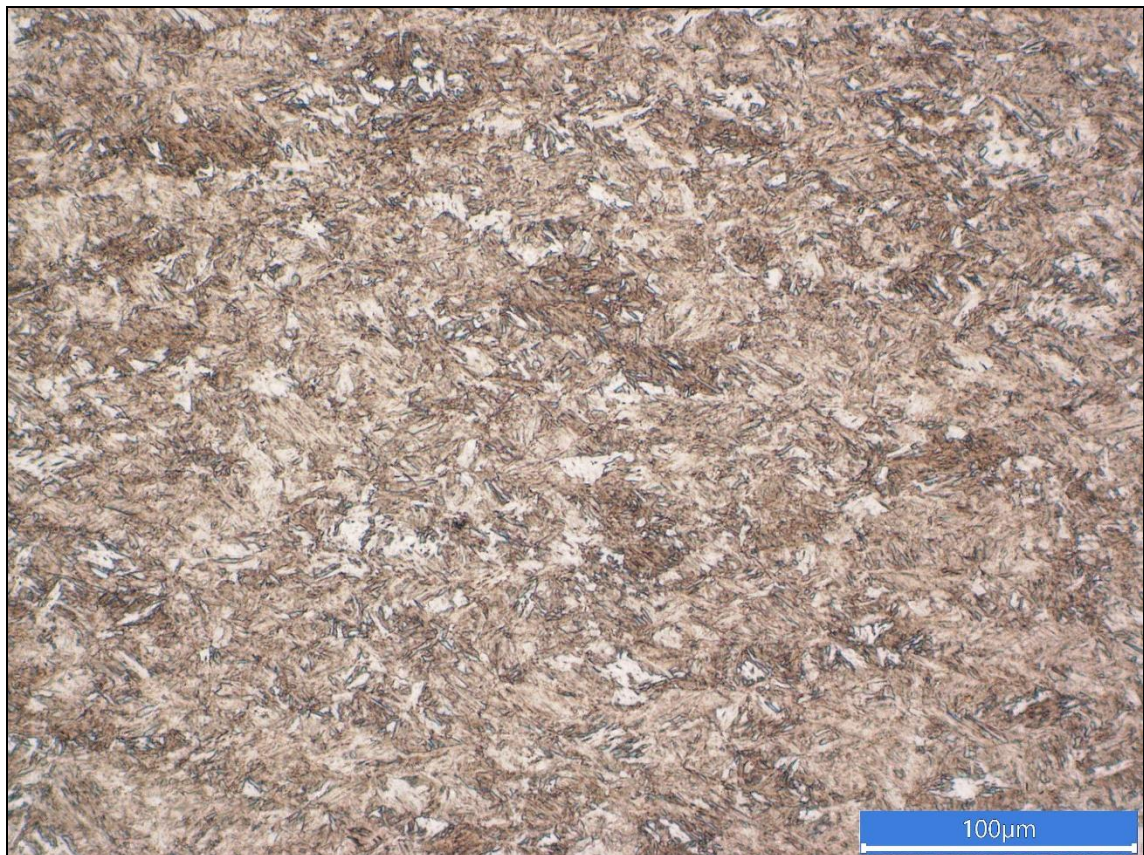
Figure 135- DP800 7-pass cross section plane at sample centre.
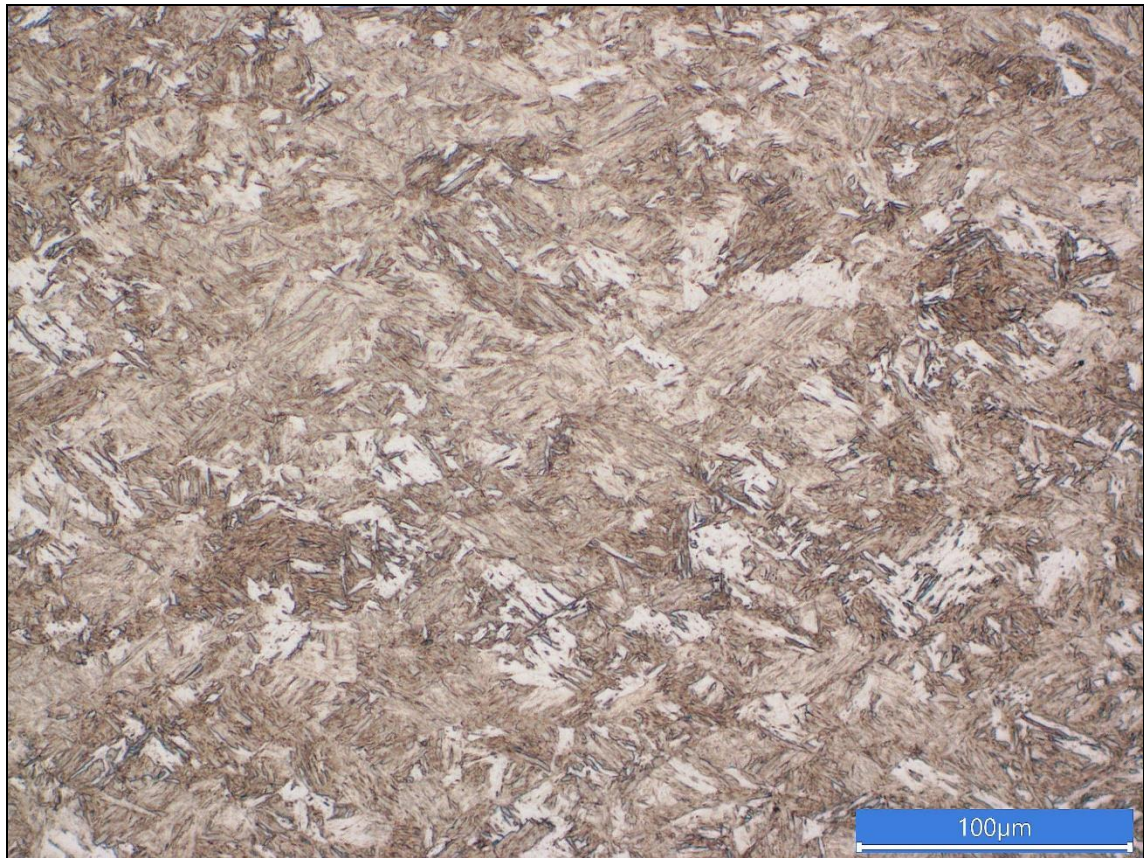
Figure 136- DP800 5-pass cross section plane at sample centre.

Initially the grain size could not be determined using picric acid, despite the microstructure being fully martensitic, even after full immersion for over one minute. Etching with the aim of revealing prior austenite grain boundaries is often problematic, particularly in the case of lower carbon microalloyed steels[138]. Instead Marshall's reagent was used, since this has been shown to be successful in revealing prior austenite grain boundaries where picric acid has previously failed[139]. However this also proved unsuccessful, but did reveal the martensitic and bainitic structures in the quenched samples with good clarity.

Unfortunately as a result the prior austenite grain size could not be measured between the five and seven pass samples. However by visual comparison that the martensite grain structure in the seven pass sample is significantly finer than the five pass sample, which is in agreement with the findings of Table 24.

There are currently tools software tools available to calculate the prior austenite grain size from martensitic structures, however these tools often require and EBSD map of the microstructure[140]. Further work could be conducted in the manor to experimentally determine the austenite grain size for both hot rolling schedules.

4.2. ROT Optimisation- Embedded Thermocouple

4.2.1. Study Justification

In order to determine the most optimal cooling path for the laboratory ROT, the temperature profile must be tracked accurately. In light of the findings in section 3.3.3, the default settings appear to match the Port Talbot schedule to a reasonable degree. However some improvement was sought. The procedure to achieve this is the same as was used in section 3.3.3. However the velocity and the number of headers was modified in an attempt to best match the cooling path. The DOE is given below:

Table 25- Laboratory ROT experimental matrix, with different variations of ROT speed and number of water headers open.

Test No.	Number of Headers open	ROT Speed Setting	Resultant ROT velocity (m/s)
1	18	5	0.52
2 (Default)	18	4	0.44
3	18	3	0.36
4	22	5	0.52
5	22	4	0.44
6	22	3	0.36
7	16	5	0.52
8	16	4	0.44
9	16	3	0.36

The plates used measured 3mm in thickness and were produced using the standard laboratory hot rolling procedure with a thermocouple embedded in the centre of mass of the plate. The temperature was recorded from the first instance of the plate reaching 850°C (FRT), then placed on the ROT for water cooling. The recording was stopped once the plate had reached the end of the ROT, this temperature was subsequently recorded as the resultant 'coiling temperature'. The maximum data acquisition rate for the data was 1Hz.

4.2.2. Results
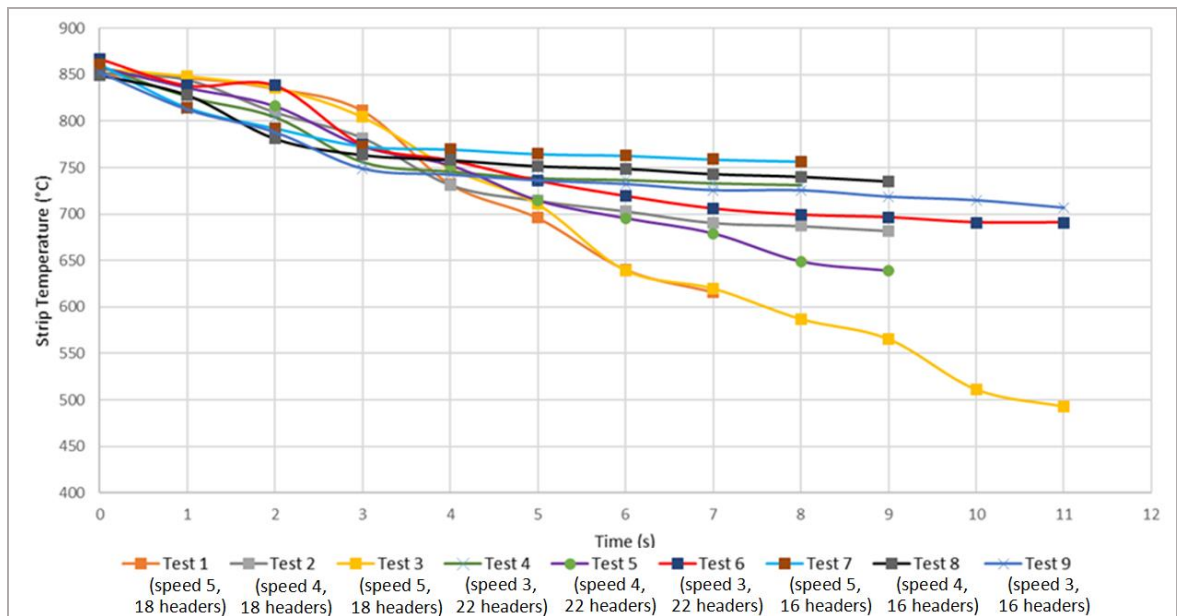
Figure 137- All tests, with all variations of ROT speed and number of headers open.

Figure 137 shows all tests carried out with different combinations of ROT speed and water header configurations. Note that the tests with slower ROT speed settings spent a longer duration of time on the ROT. The predicted time for the plates to spend on the ROT was referenced from Table 35. The initial metric for success, with respect to experimental procedure, was to achieve the target CT, which is 650°C, for this particular grade. For this reason any combination of settings that fell outside of this were eliminated from consideration. All temperature profiles that satisfy this metric are shown below:
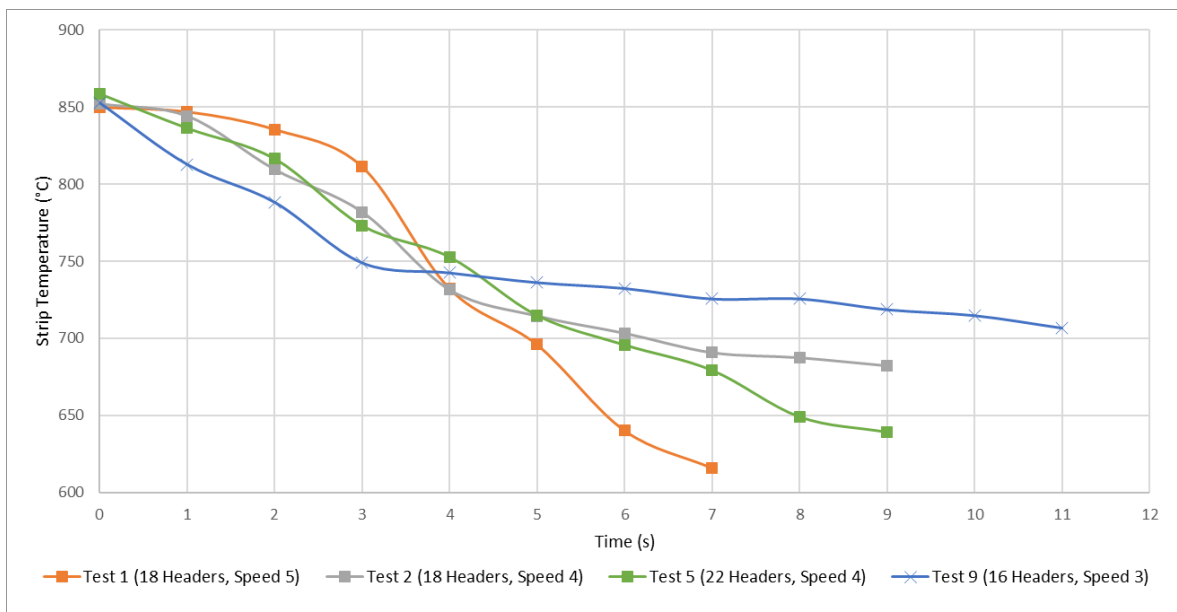
Figure 138- All temperature profile with appropriate target CTs.

In order to assist in future work for SAMI, using this particular mill and ROT configuration, the relationships between CT, ROT speed and header configurations were investigated:
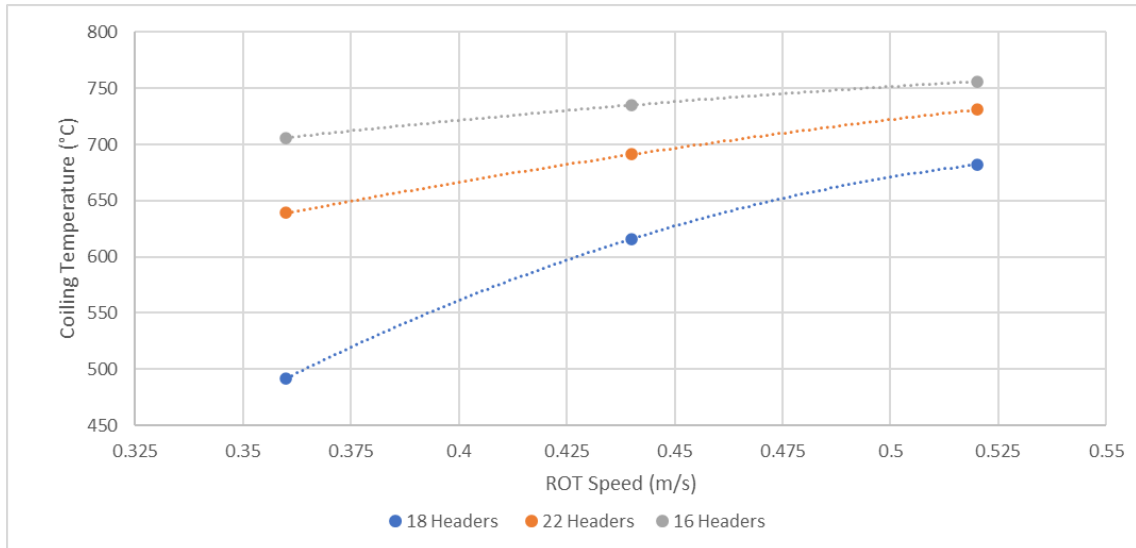
Figure 139- Relationship between ROT speed for a given number of headers, on CT.

As expected, the lower the number of water headers opened the higher the CT at the end of the ROT. A polynomial line of best fit has been overlayed on the above figure, in order to highlight the trend, however the relationship cannot be relied upon to be a 1st order polynomial due to only three data points being present for this particular study. A broarder experimental matrix, with a larger number of data points, would likely highlight the mathematical relationship between these variables.

The relationship between the CT as a function of the number of headers open was also evaluated:
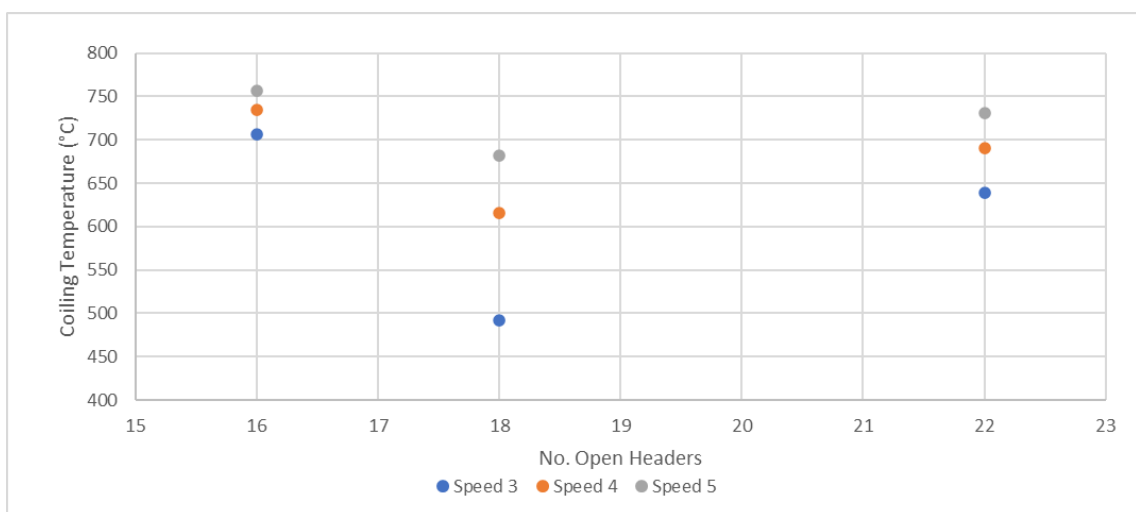
Figure 140- Relationship between the number of headers open and coiling temperature for a range of ROT speeds.

Interestingly, across all ROT speed settings, the 18 headers configuration achieved a lower coiling temperature (relative to both the 16 and 22 header configurations), as shown in the above figure. This is likely do to the change in pressure at the exit of the nozzle when more headers are open. This effect is especially prominent ion the bottom bank when decreased pressure results in a decreased waterjet height, and therefore likely a decrease in the volume of water impinging on the bottom of the plate, thereby decreasing the cooling rate of the ROT

4.2.3. Discussion

This study does not account for material thickness since all plates used were 3mm thick. Due to the limits of the thermocouple diameter, plates thinner than 3mm could not be used. However, in order to assess the relationship between plate thickness and CT, thicker plates could be utilised in a similar way, since this experimental procedure is proved to be effective in evaluating strip temperature profiles as a function of ROT settings.

With reference to Figure 140, and the results for CT for the 18-header configuration being lower than anticipated. This result may be due to the limitations of a water tank fed system. It was noticed that with an increase in the number of water headers open the height of the bottom header jets decreased, as a result of a pressure decrease. This decrease in height therefore could result in a decrease in the mass of water impinging on the on the bottom surface of the strip. It therefore seems a threshold pressure in which maximum water cooling can be delivered to the strip as a result of the water jet height limitations from the bottom bank. This, in addition to the findings in section 3.3.1 show that care must be taken when setting up the laboratory ROT in order to achieve the desired amount of cooling.

With reference to section 1.5.1, Research previously carried out by F. Mohammed, within Tata Steel's R&D department, on this particular mill and ROT configuration, investigated the relationship between ROT velocity and plate thickness of the CT, using a similar experimental procedure[96]. As previously described F. Mohammed tested 2, 3 and 4mm plate at a number of ROT speed settings, ranging from 1 (0.12 m/s) to 8 (0.76 m/s). However in this body of work, all the headers (26 total) were open for all tests. It was reported that the difference in CT, between the 3 and 4mm plates was almost negligible, especially above speed setting 2. This may provide opportunity in the future for rolling to a larger final thickness, whilst achieving appropriate coiling temperatures. However, it is worth nothing that the results from F. Mohammed, are only the quoted CTs and a

temperature profile is not given, therefore, despite the possibility that the CT may be acceptable, the temperature profile may not be representative. In addition to this the through thickness temperature gradient may also be greater for a thicker plate, and therefore the surface temperature may not be as indicative of the core temperature, a problem raised buy Tailor and Colleagues in their optimisation of laboratory rolling conditions[97]. Therefore further experiments should be conducted, with an embedded thermocouple, in order to measure the core temperature profile over time, before a 4mm plate is considered. The results from Figure 139 were overlayed with F. Mohammed's for 3mm plate thickness are shown below:
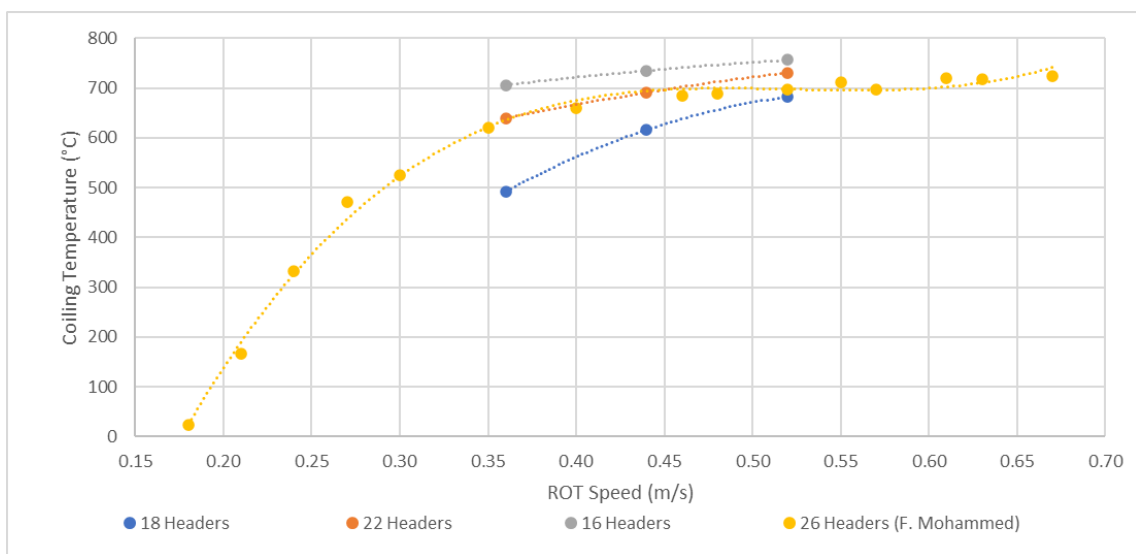
Figure 141- Comparison of F. Mohammed's data with ROT experimental data for 3mm plate thickness.

Good alignment was achieved between the 22 and 26 header data. Despite falling outside of the 'useful' range for coiling temperatures, this does provide interesting insight into to cooling characteristics of the ROT at the extremes. For example this data illustrates that there is little change in CT with increasing ROT speed, for the 26 header configuration. When comparing the two data sets it is essential to consider the differences in data collection methods. For example, the data provided by F. Mohammed was collected using an infrared pyrometer, and therefore measures surface temperature. This technique also may be less accurate one water and oxide scale has formed on the surface of the sheet. Little detail is provided regarding the specification of the pyrometer, which may be subject to interference from steam and water on the surface of the strip. The data gathered in Figure 139 and Figure 140 was collected over a single day, in which the water temperature was recorded to be 19.2°C, with little variation throughout the course of the day. In contrast to this the data gathered by F. Mohammed does not reference the incoming water

temperature, nor the ambient temperature, which may modify the net heat transfer coefficient and therefore the CT to some degree. A criticism of both data sets in predicting ROT cooling outcomes, as a function of ROT settings, is the fact that the microstructure is not representative of a hot rolled plate, therefore like for like transformations are not occurring in trials described above vs a plate that had been reheated and hot rolled. This may have a small effect on the strip temperature due to the endothermic and exothermic nature of some phase transformations[141].

Lastly, in a similar method fashion to section 3.3.3.2 the temperature profiles from this study were overlayed with a temperature profile, from the Titan software which is simulated from pyrometer measurements from Tata Steel's Port Talbot ROT. The most 'acceptable' temperature profiles, shown in Figure 138 used:
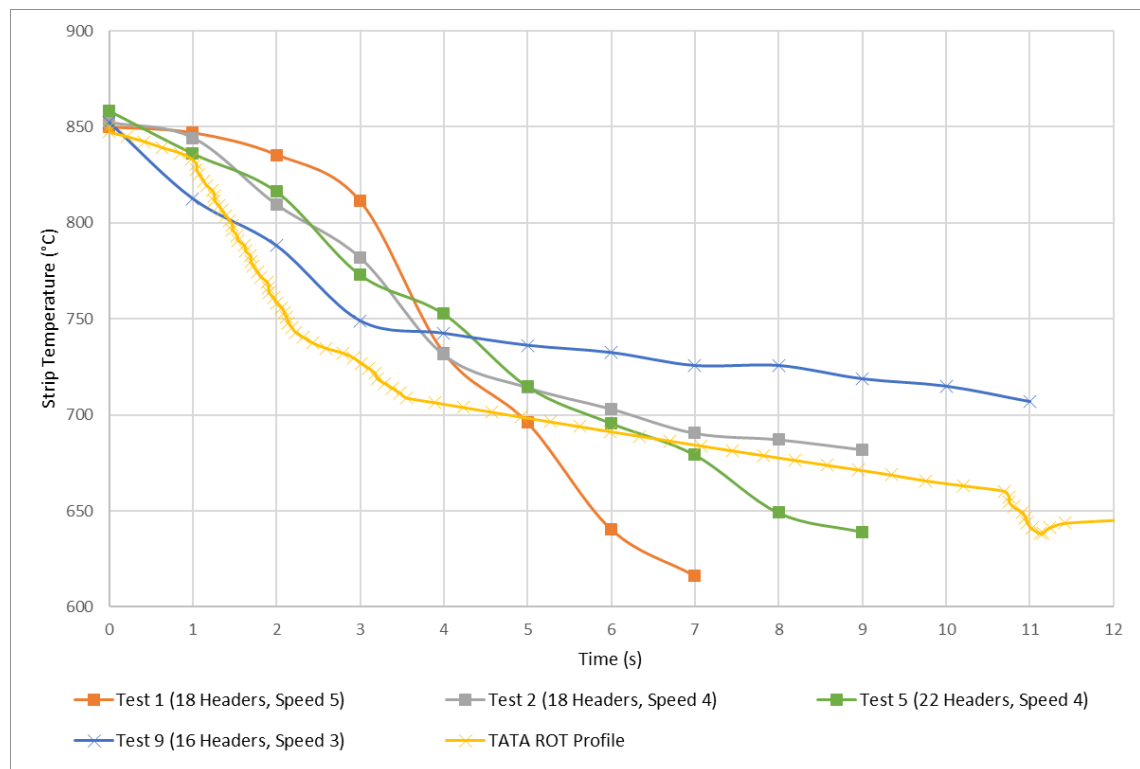
Figure 142- All temperature profile with appropriate target CTs and Tata Steel Port Talbot ROT temperature profile.

It is clear from the above figure that no combination tested achieves a representative cooling rate when compared to the Tata Seel Port Talbot, which is important in controlling the correct volume fractions of both ferrite and pearlite. The cooling rate achieved by the Port Talbot ROT between one and four seconds is approximately 52°C/s. The average cooling rates for the temperature profiles shown in Figure 142 are shown in the table below:

Table 26- Comparison for average cooling rates for experimental and Plant profiles in the first few seconds of ROT cooling.

Temperature Profile Name/No.	No. of Headers Open	ROT Speed Setting	Average Cooling Rate (°C/s)
Test 1	18	5	39
Test 2	18	4	38
Test 5	22	4	28
Test 9	16	3	35
Tata ROT Profile	-	-	52

The average cooling rate for the experimental tests, in all cases, is significantly lower than that of the Port Talbot ROT. However, when accounting for both cooling rate and CT it is clear that 'Test 5' provides the most optimal conditions in replicating the PT ROT.

4.3. Titan Software Optimisation

4.3.1. Initial grain size

With reference to section 3.4.3, it is clear that the grain size has an impact on both the transformation kinetics, and therefore the calculated temperatures also. For this reason investigation has been undertaken to determine a likely starting grain size for the ROT. As stated previous the default grain size used for the ROT in the DP800 model in Titan is 11.5 μm. This is referenced from the approximation determined by the product final thickness, as shown in Figure 15.

With reference to section 4.1.7.1, where the grain size was approximated from slab reheat to roughing mill, to finishing mill. It was found that, according to the JMatPro simulation (using plant data), the reported average grain size was 13μm. This was input into the Titan model and the effects on the predicted temperatures, a phase volume fractions were found to be negligible. This is likely due to the increase in starting grain size to be only 12%. However it does confirm a good agreement with the findings of section 4.1.7.1 and the default initial grain size of 11.5μm proposed by the Titan software.

4.3.2. TTT curve alignment

This section outline the simulations undertaken in the Titan software in an attempt to better align the transformation curves of Titan with those extracted from Jmat Pro. Two methods

are tried in this section to modify the transformation properties; modifying the M0_Baseparameter and modifying the Niobium Slow Down parameter.

4.3.2.1. M0_Base Modification

The section outline the M0_Base parameter modification and the resultant effect on the temperature and transformation outputs.

4.3.2.1.1. Method

M0_base the first chosen parameter to vary in the optimisation of the transformation curves shown in section 3.4.2. M0_base, also known as the mobility pre-factor. This tuning parameter affects the rate of the transformation front in the MITRON transformation model, this factor is combined with a few other factors such as the percentage weight of Nb to calculate the effective rate of transformation. This mobility factor also accounts for the difference in growth rate between ferrite and pearlite from austenite[68]. As such there are two different equations for each phase.

In the case of Ferrite transformation:

$$Mobility = \frac{M0\_Base}{1 + NbSlowDown \times NbEffective}$$

Equation 25

And in the case of Pearlite transformation:

$$Mobility = \frac{M0\_Base}{PeaerliteSlowDown \times (1 + NbSlowDown \times NbEffective)}$$

Equation 26

Therefore the modification of the M0_Base parameter was chosen to align the transformation curves for both Ferrite and Pearlite to align them with the curves exported from Jmat Pro.

Within the Titan software the M0_base parameter was modified for a given temperature and the time at which the first instance of both Ferrite and Pearlite (0.1%) of this was recorded.

4.3.2.1.2. Results

It was found that modifying the M0_Base factor from 1.75 to 0.1 gave the best alignment with the Jmat Pro curves for both Ferrite and Pearlite. Although the shape of the Pearlite transformation curve does not align as closely when compared to Ferrite:
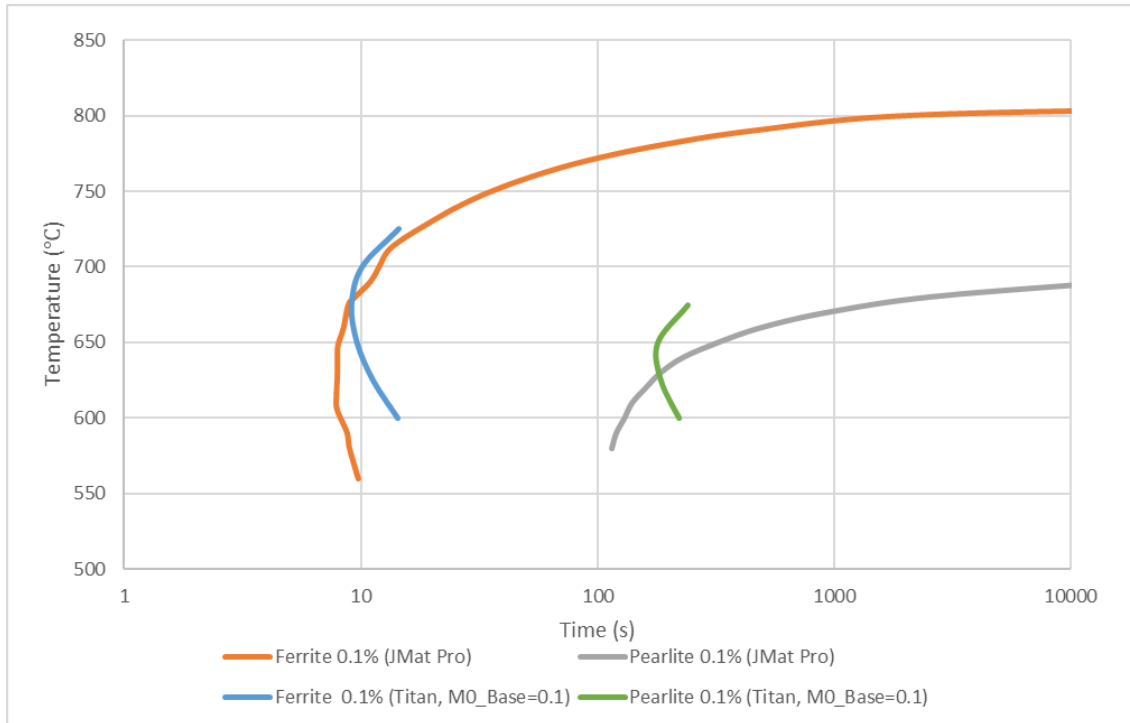
Figure 143- Transformation curves for both Ferrite and Pearlite with modification to M0_Base parameter from 1.75 to 0.1.

In light of these findings, M0_Base was modified in the ROT model within Titan and ran for the selected nine journals outlined previously. Despite the curves alignment on the 'Roll It' model, decreasing the M0_Base setting from 1.75 to 0.1 resulted in almost no transformation occurring on the simulated ROT. For each of the nine journals none resulted in a fraction transformed larger than 1%, shown below in the below table. Therefore M0_Base modification is not an acceptable parameter for optimising simulation transformation on the Titan ROT.

Table 27-Fraction transformed for each of the 9 journals for 1.75 and 0.1 M0_Base settings.

	PTROT568 68-202-301	PTROT568 69-202-300	PTROT568 70-010-301	PTROT568 71-010-302	PTROT568 73-010-304	PTROT568 74-020-303	PTROT568 76-010-303	PTROT568 77-010-300	PTROT568 79-010-308
Fraction transformed M0_Base = 1.75	59	75	46	32	77	75	64	66	66
Fraction transformed M0_Base = 0.1	0	0	0	0	0	2	0	0	1

4.3.2.2.   NbSlowDown Modification

The section outline the NbSD parameter modification and the resultant effect on the temperature and transformation outputs.

4.3.2.2.1.   Method

In light of the findings of the above section it was decided that NbSlowDown should be attempted as a tuning parameter to align the transformation curves. M0_Base was kept at its default value (1.75) for this study. The method was repeated in the same manner as the above study.

4.3.2.2.2.   Results
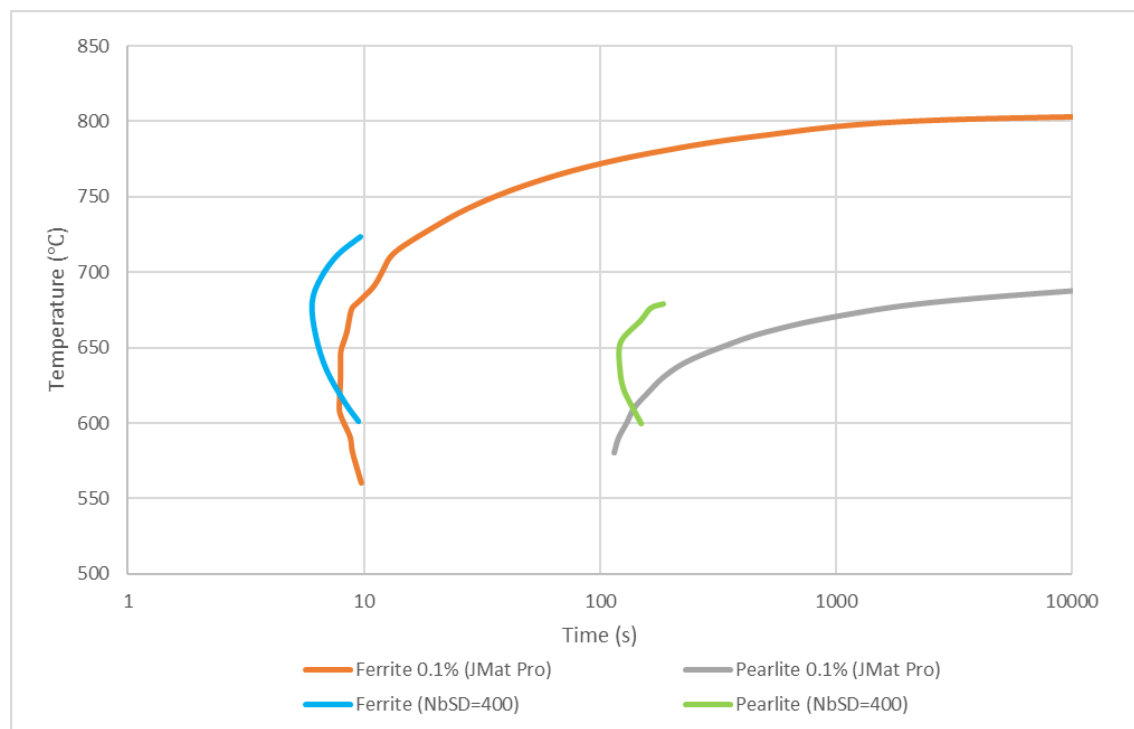
Figure 144- Transformation curves for both Ferrite and Pearlite with modification to 'NiobiumSlowDown' from 4 to 400.

Modifying NbSD to 400 was found to give the best match for both the Pearlite and Ferrite transformation lines. In order to assess the impact of this on the ROT simulation this setting was included into the MITRON transformation model for the Port Talbot ROT model in Titan in a similar manner to the above study, the results are shown in the table below. It is evident that this also is not an appropriate method in optimising transformation parameters for the ROT simulation.

Table 28- Fraction transformed for each of the 9 journals for 4.0 and 400.0 NiobiumSlowDown settings.

	PTROT568 68-202-301	PTROT568 69-202-300	PTROT568 70-010-301	PTROT568 71-010-302	PTROT568 73-010-304	PTROT568 74-020-303	PTROT568 76-010-303	PTROT568 77-010-300	PTROT568 79-010-308
Fraction transformed NbSD = 4.0	59	74	46	32	78	75	64	66	66
Fraction transformed NbSD = 400	0	0	0	0	0	0	0	0	0

It was clear that this approach has not been successful in increasing the total transformation in the model. It is evident that, with reference to Equation 25 and Equation 26, increase NiobiumSlowDown and decreasing M0_Base decreases the net mobility of the transformation front, and therefore decreases the product transformation in the cumulative file. It was decided that the method outlined in section 3.4.2, using the 'Roll It' package, to extract the transformation curves, from Titan was not an appropriate method to compare against Jmat Pro transformation curves, and optimise with the intent of improved transformation in the cumulative file. The decision was then made to attempt to optimise the temperature prediction of the strip rather than improve the transformation performance. This is addressed in the next section.

4.3.3. Temperature Optimisation (CE)

4.3.3.1. Method

In light of the results of the previous section, a metric was created the measure the effect of the parameter adjustment on each of the journals. The chosen temperature selected was IP3, this is the pyrometer that is situated near the end of the ROT, the last being the coiling temperature pyrometer. IP3 is considered to be a good aim for temperature alignment since, it encapsulated much of the heat due to transformation at this position on the ROT.

In order to generate an overall score for temperature prediction, of the nine journals, the difference between the measured temperature (at IP3) and the predicted temperature, at the same point on the ROT. Of the nine journals, the average difference was taken, the lowest difference was assumed to be the best. The average deviation of the difference in temperature provide a measure of how accurate the 'tuned' parameter is for all of the nine journals. For example, if the 'tuned' parameter was found the be the most accurate, on average, for the group, but had one outlier which exhibited a larger difference in the measured vs the predicted temperature, then this would not be considered and accurate or

helpful optimisation. Lastly the product of the average deviation and the minimum difference was also taken to provide an overall score.

The first setting trialled was the 'Cooling Efficiency' or CE. In the Titan manual, the Cooling Efficiency is defined as "the cooling efficiency in the laminar flow sections". The default setting for the CE was 97%. The CE was adjusted iteratively until the lowest score for both average difference and average deviation was found, to the nearest 12.5%.

4.3.3.2. Results

Table 29- Results of adjustment of Cooling Efficiency on the 9 selected journals.

Journals	Measured Temp °C	Cooling Efficiency 97.0%		150.0%		50.0%		200.0%		250.0%		300.0%		350.0%		275.0%		225.0%		212.5%		237.5%		Min
56868-020-301	645	662	17.3	668	22.6	695	50.4	650	4.6	633	12.4	635	10.0	626	18.6	636	9.5	641	4.4	646	0.8	637	7.9	
56869-020-300	634	660	25.7	654	19.9	690	56.2	630	4.3	610	23.8	599	35.3	588	46.0	604	30.2	621	13.0	624	10.3	616	18.3	
56870-101-301	638	667	28.6	666	27.8	699	61.2	657	18.6	642	4.3	631	7.3	635	3.4	637	1.3	649	11.0	653	15.0	646	8.4	
56871-010-302	638	665	27.1	656	17.5	698	60.2	654	15.6	639	1.0	627	10.7	620	18.2	633	4.8	646	7.7	650	12.1	643	5.0	
56873-010-304	635	666	31.0	661	25.7	691	55.9	637	2.0	619	16.1	608	26.8	597	38.0	615	19.9	630	5.1	634	1.5	624	10.7	
56874-020-303	635	662	26.9	664	29.5	687	52.4	646	11.0	642	6.5	630	5.4	621	14.2	634	0.8	644	8.5	640	4.9	644	9.1	
56876-010-303	642	664	22.1	671	28.6	694	51.9	655	13.0	640	1.7	644	1.8	636	6.0	642	0.0	647	5.5	652	9.8	645	2.7	
56877-010-300	630	655	24.8	660	30.4	686	55.6	641	11.2	624	6.2	627	3.1	619	11.1	631	0.5	633	2.6	637	6.7	628	2.3	
56879-010-308	630	655	24.8	660	30.4	686	55.6	641	11.2	624	6.2	627	3.1	619	11.1	631	0.5	633	2.6	637	6.7	628	2.3	Min
Average Difference (Degrees)		25.37		25.82		55.48		10.16		8.70		11.51		18.51		7.49		6.73		7.54		7.39		6.73
Standard Deviation		3.70		4.49		3.40		5.20		7.00		11.01		13.54		10.09		3.41		4.47		4.87		3.40
Product of Std-Dev & Avg Diff		93.77		116.05		188.49		52.81		60.91		126.73		250.62		75.64		22.92		33.66		36.00		22.92

Figure 145- Explanation of scoring for CE simulation trial.

A CE setting of 225% was found to be the most desirable (to the nearest 12.5%). It offered to lowest average difference across the nine journals, with an average deviation of 3.41% (the second lowest). The below graphs show this aswell as the other values trialled. Note the error bars for each point illustrate the average deviation of that given cooling efficiency for the group.
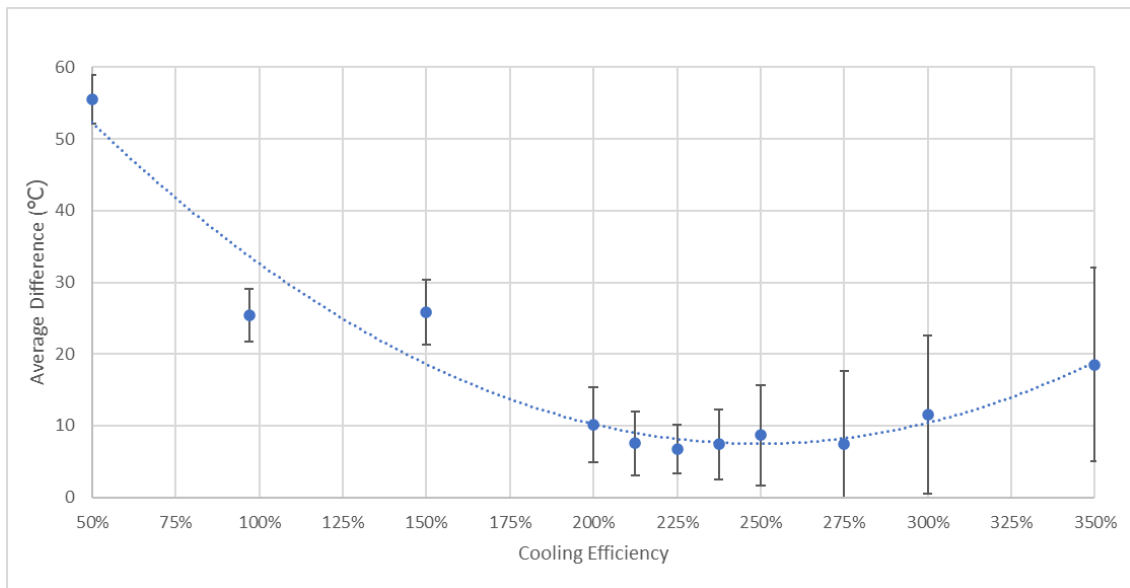
Figure 146- Cooling efficiency against average difference between measured temperature and predicted temperature for IP3.

In order to evaluate the changes to the wider model with regards transformation, the simulation was repeated with the request to model the full transformation kinetics, the results are shown below for each journal:
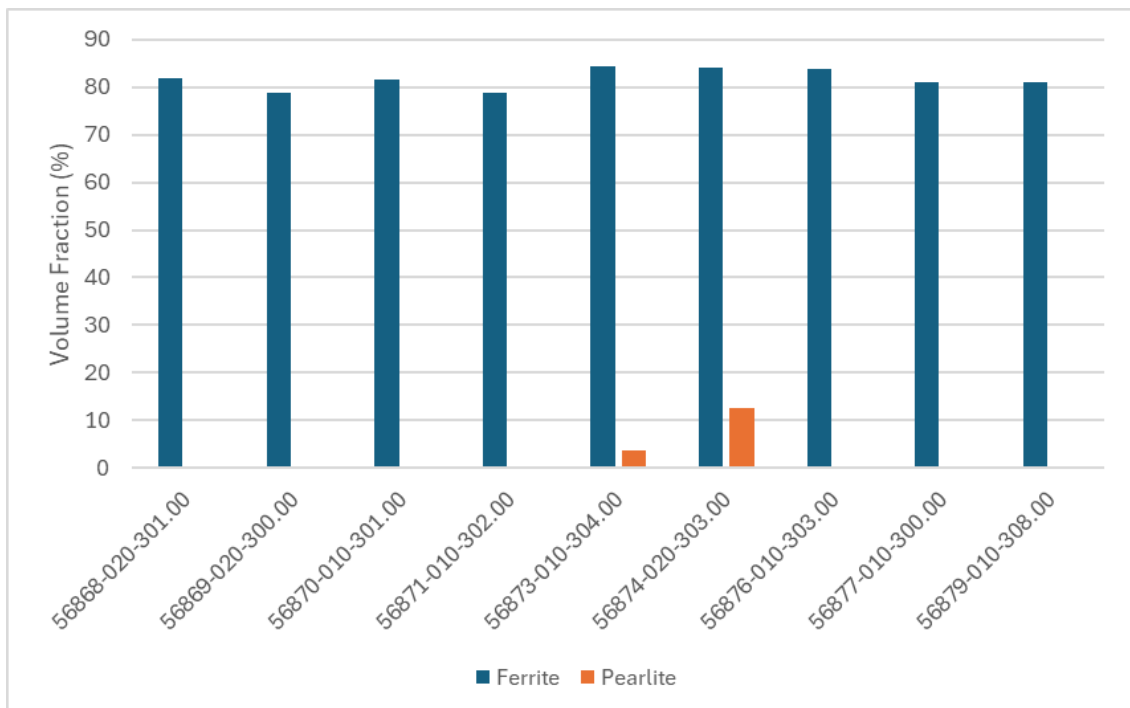
Figure 147- Ferrite and Pearlite volume fractions for CE 225%.

It is clear from the above figure that optimising for IP3 temperature alignment, using CE, improved the transformation output significantly, especially when compared to the optimisation carried out using NbSD (see section 4.3.2.2). However, it still remains a point

175

of concern that the Pearlite transformation is still so low. With reference to section 3.2.3 and Table 8, as well as recommendations from colleagues at Tata Steel Port Talbot, the volume fractions of Pearlite for a successful DP800 coil should be in the region of 20-30%. However much of this transformation only occurs during the coiling process, and not on the ROT, which is not modelled on the Titian ROT simulation. In any case, as mentioned in the previous sections, the model cannot be optimised for transformation using journal data since there is no measured transformation data included within the journal data.

To further assess the success of this temperature optimisation the simulation was repeated with more measured temperatures; CT (Coiling Temperature), IP2 (the second Infrared Pyrometer on the ROT) as well as IP3, a more in-depth description of this is given in 2.1.4. The below figure shows the absolute difference in measured and calculated temperatures post CE optimisation:
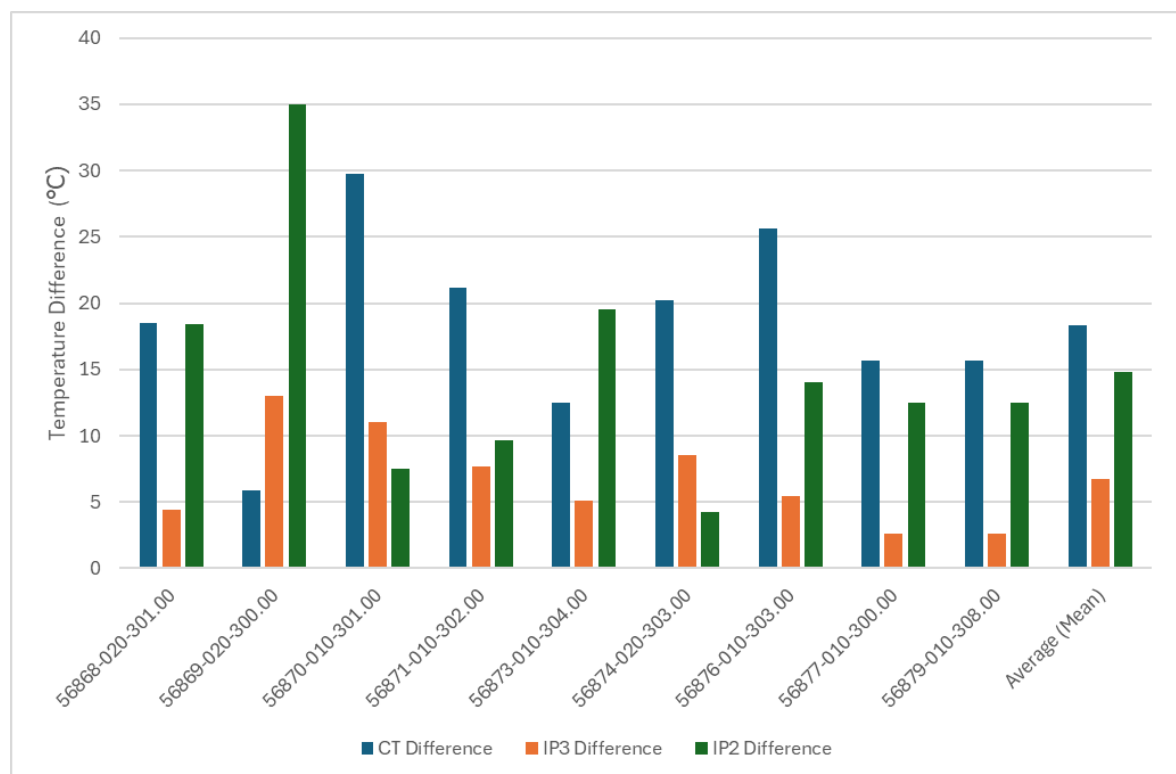
Figure 148- Absolute difference in measured temperature and predicted temperature at difference locations along the ROT for all 9 journals studied, as well as the average of each journal where cooling efficiency (CE) is being adjusted.

It is clear from the above figure that large variations in calculated and measured strip temperatures are present. As expected, the lowest average difference of the three pyrometer readings is IP3 (6.7°C), since this was the metric by which the CE was optimised for. However, CT Difference and IP2 Difference are much larger at 18.3°C and 14.8°C respectively.

For this reason the simulation trial was repeated, in the same way, but aiming for a lowest combined average temperature, the results are shown below:

Table 30 -Adjustment for CE for lowest average of IP2, IP3 and CE.

Journals	CTm	IP3m	IP2m	Cooling Efficiency 97.0% CTc	IP3c	IP2c	CT diff	IP3 diff	IP2 diff	150.0% CTc	IP3c	IP2c	CT diff	IP3 diff	IP2 diff	200.0% CTc	IP3c	IP2c	CT diff	IP3 diff	IP2 diff	250.0% CTc	IP3c	IP2c	CT diff	IP3 diff	IP2 diff	300.0% CTc	IP3c	IP2c	CT diff	IP3 diff	IP2 diff
56868-020-301	587	645	649	618	662	682	31	17	33	635	668	660	48	23	11	615	650	640	28	5	9	596	633	623	9	12	26	597	635	623	10	10	26
56869-020-300	589	634	646	636	660	668	47	26	22	629	654	644	40	20	2	604	630	620	15	4	26	583	610	602	6	24	44	569	599	592	20	35	54
56870-101-301	591	638	647	625	667	687	34	29	40	641	666	662	50	28	15	629	657	648	38	19	1	614	642	633	23	4	14	600	631	622	9	7	25
56871-010-302	591	638	647	612	665	687	21	27	40	625	656	658	34	18	11	621	654	646	30	16	1	604	639	630	13	1	17	590	627	620	1	11	27
56873-010-304	592	635	637	645	666	670	53	31	33	635	661	650	43	26	13	612	637	625	20	2	12	593	619	608	1	16	29	581	608	598	11	27	39
56874-020-303	598	635	636	641	662	674	43	27	38	640	664	656	42	29	20	622	646	635	24	11	1	614	642	630	16	7	6	603	630	617	5	5	19
56876-010-303	595	642	651	630	664	682	35	22	31	644	671	663	49	29	12	628	655	645	33	13	6	613	640	630	18	2	21	614	644	632	19	2	19
56877-010-300	594	630	636	625	655	673	31	25	37	637	660	653	43	30	17	618	641	632	24	11	4	600	624	616	6	6	20	602	627	615	8	3	21
56879-010-308	594	630	636	625	655	673	31	25	37	637	660	653	43	30	17	618	641	632	24	11	4	600	624	616	6	6	20	602	627	615	8	3	21
Average Difference (Degrees)				31.94						27.48						14.58						13.92						16.67					
Average Deviation				6.07						4.70						6.42						7.83						9.24					
Product of Std-Dev & Avg Diff				193.92						129.02						93.62						108.97						154.08					

Journals	CTm	IP3m	IP2m	Cooling Efficiency 350.0% CTc	IP3c	IP2c	CT diff	IP3 diff	IP2 diff	225.0% CTc	IP3c	IP2c	CT diff	IP3 diff	IP2 diff	275.0% CTc	IP3c	IP2c	CT diff	IP3 diff	IP2 diff	237.5% CTc	IP3c	IP2c	CT diff	IP3 diff	IP2 diff	262.5% CTc	IP3c	IP2c	CT diff	IP3 diff	IP2 diff	
56868-020-301	587	645	649	587	626	614	0	19	35	605	641	631	18	4	18	599	636	623	12	9	26	601	637	627	14	8	22	595	632	621	8	13	28	
56869-020-300	589	634	646	554	588	583	35	46	63	595	621	611	6	13	35	575	604	596	14	30	50	589	616	606	0	18	40	576	605	598	13	29	48	
56870-101-301	591	638	647	603	635	623	12	3	24	621	649	639	30	11	8	607	637	627	16	1	20	618	646	636	27	8	11	609	638	629	18	0	18	
56871-010-302	591	638	647	580	620	613	11	18	34	612	646	637	21	8	10	598	633	625	7	5	22	609	643	634	18	5	13	602	637	628	11	1	19	
56873-010-304	592	635	637	567	597	590	25	38	47	605	630	617	13	5	20	588	615	604	4	20	33	599	624	613	7	11	24	589	616	605	3	19	32	
56874-020-303	598	635	636	595	621	608	3	14	28	618	644	632	20	9	4	608	634	622	10	1	14	617	644	633	19	9	3	611	638	626	13	3	10	
56876-010-303	595	642	651	607	636	623	12	6	28	621	647	637	26	5	14	614	642	630	19	0	21	618	645	634	23	3	17	612	639	628	17	3	23	
56877-010-300	594	630	636	594	619	607	0	11	29	610	633	623	16	3	13	606	631	618	12	1	18	605	628	619	11	2	17	604	628	617	10	2	19	
56879-010-308	594	630	636	594	619	607	0	11	29	610	633	623	16	3	13	606	631	618	12	1	18	605	628	619	11	2	17	604	628	617	10	2	19	Min
Average Difference (Degrees)				21.59						13.30						14.62						13.28						14.51						13.28
Average Deviation				12.23						6.18						8.29						7.41						8.04						4.70
Product of Std-Dev & Avg Diff				264.08						82.16						121.24						98.41						116.73						82.16
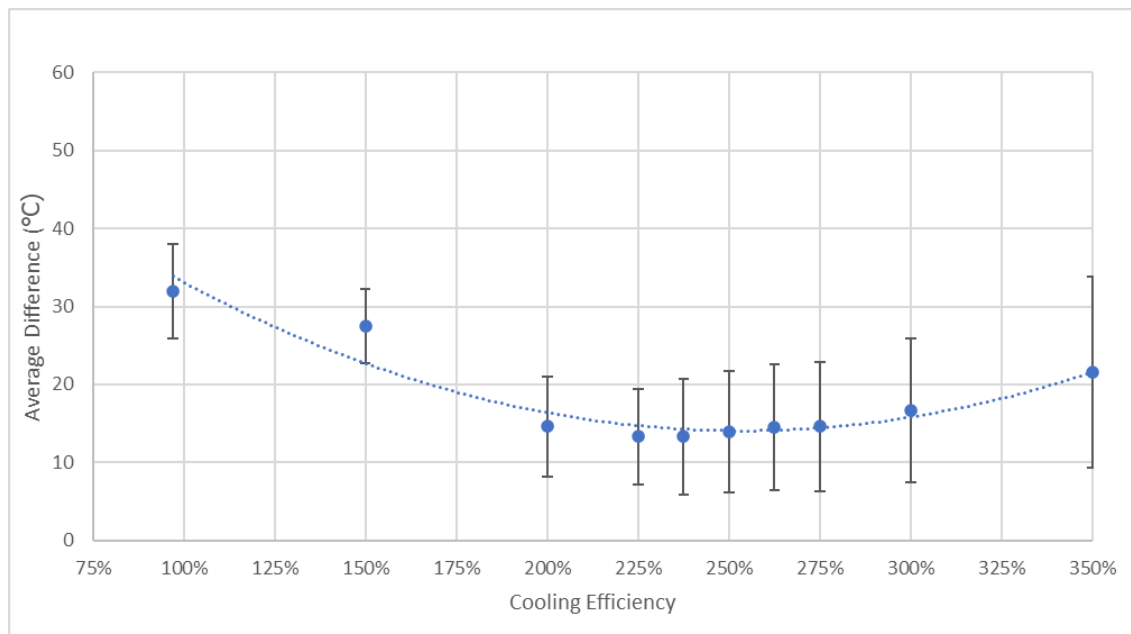
Figure 149- Cooling efficiency against minimum average difference between measured and predicted; IP2, IP3 and CT.

When optimising, using CE, for all pyrometer readings there is significantly more variation in the results, as shown by the magnitude of the error bars, meaning the average deviation

of the results is far higher. Therefore, tuning for cooling efficiency is not a reliable parameter for optimising the temperature prediction of the transformation model (MITRON) within Titan.

4.3.4. Titan Optimisation Conclusion

4.4. Optimisation Conclusions

This section lists the conclusions of the optimisation process for the Laboratory (Lewis) Mill, the investigation into the starting grain size for the Titan ROT model, Laboratory (Lewis) Mill ROT optimisation and optimisation of the Titan model.

Mill Optimisation Chamfer Study:

Two designs geometries were created for improved initial bite in the mill, with the pursuit of higher initial reductions in the first pass. Design geometry 2 was proved to be the preferable design. A 5-pass schedule proved the most effective in increasing the initial reductions in the first passes, and maintaining strip temperature, despite this temperature was retained too well and the slab had to be paused before entering the ROT to prevent quenching. Microstructural analysis against the 'Old' 7-pass schedule and the 'New' 5-pass schedule revealed that the older schedule was more representative of plant produced DP800 hot band material. Despite this, this research has been key in providing a novel geometry for the research conducted by Tata Steel and Swansea University in hot rolling of novel steel alloys, with rolling schedules that were not previously possible.

Prior Austenite Grain Size Comparison:

An experimental method was sought to analyse the PAGS of the VIM produced DP800 hot rolled specimens for both the 'Old' 7-pass schedule and the 'New' 5-pass schedule, via analysis of quenched samples, to revel the as rolled microstructure in order to asses the microstructural impact of the 2 rolling schedules. Unfortunately, the experiment was not successful in revealing defined grain boundaries for measurement, but the microstructure of the 'Old' 7-pass schedule not noticed to be finer than the 5-pass, which was largely expected do to the increased number of mill passes, limiting the opportunity for recrystallisation. However this approach proved successful in the IF grade (see section 6.0), and was used to successfully validate the JMat Pro® model of the laboratory process.

ROT Optimisation Thermocouple Study:

It was evident that the ROT likely required upgrade to provide a representative cooling rate, regarding the Port Talbot Mill. This too will assist in the elimination of water jet height inconsistencies, as a function of the number of headers open. These recommendations are given in detail in section 8.2.

Titan Software Optimisation:

It was hoped at the conception of this work that the Titan package could be both optimised for temperature prediction and transformation prediction of Tata Steel's DP800 grade on the ROT with the aim of improving product formability. Optimisation attempts using parameters related to strip transformation such as; M0_base and Niobium Slow Down, proved unsuccessful in improving transformation prediction within the simulation for the nine journals chosen. For this reason an approach that optimised temperature prediction was sought. Adjusting the Cooling Efficiency of the headers, in the simulation appeared to yield positive results, improving the group average of the nine journals for temperature prediction, as well as some improvement in initiating pearlite formation. However this resulted in a poor prediction for IP2 and CT , meaning this optimisation failed in creating an accurate prediction of strip temperature along the ROT. Ultimately a successful optimisation of this model would require accurate transformation information, due to the interplay of heat released upon the austenite to ferrite transformation as the system transitions from to a more stable state during cooling, as such the free energy is released as heat. In addition, a larger data set would be beneficial in improving the reliability of the findings. At the time of writing transformation monitors are being fitted to Tata Steel's ROT and will be able to provide accurate transformation data of the degree or ferrite formation in the strip by measuring the magnetic permeability. This therefore make future optimisation of the Mitron model possible.

5. Industrial Challenges- Coil End Effects

5.1. Justification (Economic & Environmental)

This experimental section outlines a possible approach to reduce coil end effects by experimental means. The phenomenon of coil end effects, which has previously been described to some detail in section 1.4.2.6.2 is the occurrence of excessively hard bainitic structures within the nose and tail end of hot rolled hot-band coils due to higher cooling rates. If these were to be subsequently cold rolled, this would place excessive loads on the cold mill and cause possible breakage and a pause in production. Due to the nature of the manufacturing process the cooling rates at the nose and tail of the coil cannot be modified since the nose of the coil cools more rapidly due to a quenching effect when coming in contact with the mandrel, and the tail cools more rapids due to the outermost lap being air cooled to a greater degree than the rest of the coil. As a result these are discarded and remelted, reducing product yield and increasing energy consumption. In order to combat this more transformation is therefore required on the ROT to reduce bainitic structures in the strip.

At the conception of this project, as mentioned previously it was hoped that an optimised transformation model, within Titan, would provide a useful tool to model possible process adjustments to improve the product yield by reducing product end effects. However, since this approach was not successful a experimental approach has been substituted.

A possible experimental method to increase transformations on the ROT has been suggested; to modify the FRT above and below normal conditions (850°C). A lower FRT may promote a lesser degree of a cooling requirements on the ROT cause a greater degree of transformation of the strip. However rolling at lower temperatures may refine the grain size further such that less opportunity for grain recovery is present, which could promote and increase in UTS, making for less favourable cold rolling conditions. Rolling at a higher FRT would likely result in an increase in grain size due to an increased ability for the austenite grain to recover above TNR, but the elevated temperature upon hitting the ROT may be difficult to cool sufficiently. For this reason, an experiment was designed to modify the FRT experimentally, with a 'standard' ROT cooling procedure to replicate Port Talbot as much as possible, despite the limited cooling rates achievable (as shown in Figure 142).

5.2. FRT Adjustment- Experimental procedure

A total of five chamfered samples were prepared and rolled with the same rolling schedule used in section 4.1.6. Despite the microstructure offering an arguably less representative microstructure when compared to the plant produced hot-band material. The higher FRT allowed for an increased opportunity to roll to at temperatures where the material can recrystalise (above the T_{NR}), which would not be possible with a seven pass schedule. Therefore, the trends in UTS and microstructure have been evaluated against like samples to determine the degree of transformation rather than compare against plant produced hot band material.

In order to achieve a varied FRT a 'pause' was implemented in the rolling schedule to allow to sample to cool between passes two and three, meaning subsequent passes would be at a lower temperature with increased duration of the 'pauses'. The below table shows the pauses used in each schedule, for each sample:

Table 31- Pause in schedule and anticipated temperature loss for each block.

Block No.	Pause Duration (s)	Anticipated Temp loss°C	Anticipated FRT°C
1	0	0.0	870.0
2	1	13.3	856.7
3	2	26.6	843.4
4	3	39.9	830.1
5	4	53.2	816.8

The anticipated FRT was estimated based upon the average cooling rate, per pass, for the experiment outlined in section 4.1.6, which was approximately 13°C/s. The blocks were then subject to cooling using the settings which best matched the Port Talbot ROT, as described in section 4.2.

5.3. Results

Plastometry and microscopy were performed at the centre of mass of the hot rolled sample, in accordance with the findings of section 4.1.3.1. The results for the Plastometry are presented in the table below, as well as the measured FRT.

Table 32- Predicted and Measured FRTs and UTS of samples achieved using Plastometry.

Block No.	Anticipated FRT°C	Measured FRT°C	UTS (MPa)
1	870	951	502
2	856.7	946	498
3	843.4	945	512
4	830.1	926	504
5	816.8	903	504

5.4. Discussion

Despite the predictions for temperature loss being based upon previously rolled DP800 block, the measured FRT was higher than expected, by and average of 91°C. however the expected trend regarding temperature loss, for a given delay was nearly achieved. The below graph shows the expected FRT, as a function of delay time, for both the measured and expected values:
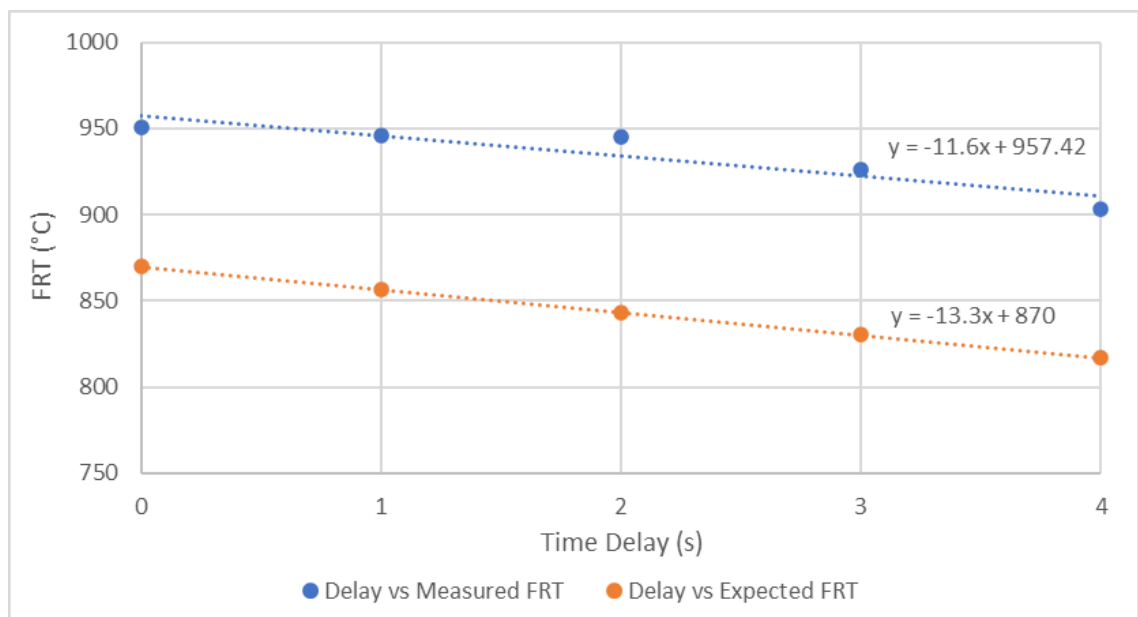
Figure 150- Final Rolling Temperature as a function of time delay, in seconds, between the 2nd and 3rd rolling passes.

It can be seen from the equations of the lines that the temperature loss, per second of delay achieved experimentally was approximately 12°C/s, which is near the expected value of 13°C/s. Despite this a range of FRTs was achieved for a like for like rolling schedule across five samples. In each case the target CT of 650°C was achieved by implementing the standard cooling schedule on the ROT and waiting a number of seconds whilst reading the strip temperature, until 650°C was reached before placing the sample in the coiling

furnace. This allowed for a somewhat representative cooling profile to be implemented on the strips. Interestingly there appeared to be some variation in the initial rolling temperature (the temperature measured at the first rolling pass), with a variation of 12°C between extremes.
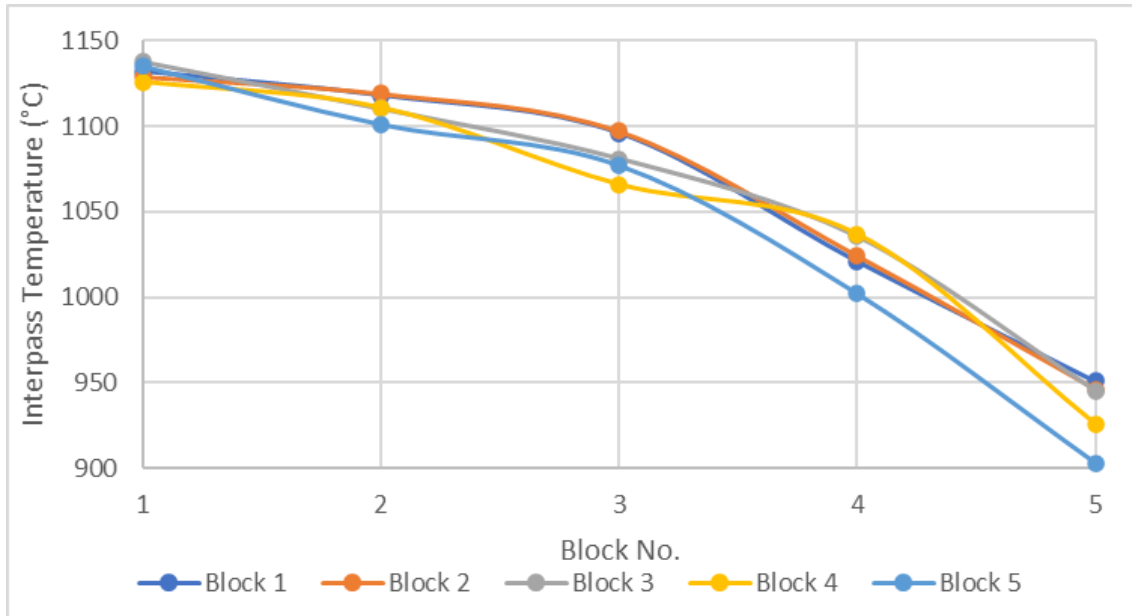
Figure 151- Inter-pass temperature per pass for Blocks 1-5 with increasing delays between pass 2 and 3.
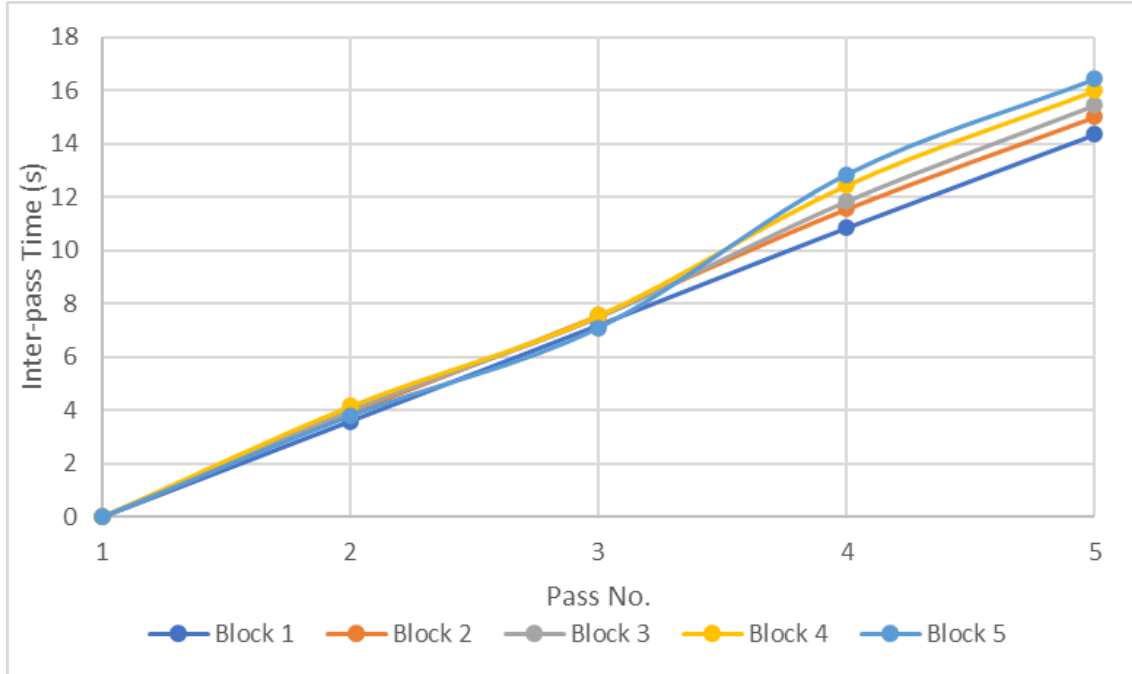
Figure 152- Normalised Inter-pass times per pass for Blocks 1-5.

Figure 151 shows the temperature per roller pass. Interestingly there appears to be a significant amount of temperature variation at the 2nd pass (22°C between extremes).

However, the resultant FRT does appear to increase proportionally to delay time, as shown in Figure 150. The variations observed in the earlier passes may be attributed to slight errors in the temperature measurement possibly due to a combination of the course data acquisition rate and the presence of scale, which appears to be more prominent in the earlier passes. Despite these inconsistencies the method of implementing a delay does appear to be successful in adjusting the FRT.

Despite the success in achieving a variation in the FRT the mechanical properties seem somewhat stable despite this. With respect to the UTS, which was estimated using Plastometry, the maximum variation in results was only 14 MPa, with and average measurement of 504MPa. This is significantly lower than expected. When compared to the values in Table 24 it is clear that this particular experiment was not successful in replicating the plant process. Despite 'Block 1' being an exact mimic of the 5-pass schedule that was conducted in section 4.1.6, and therefore the control, it is evident that the mechanical properties are not comparable.

It was suspected that the mechanical properties were as a result of the chemistry being incorrect. The blocks in question were designed to be a mimic of a Tata Steel produced DP800 transfer bar, however is was suspected that this block in particular was a 'mis-cast' and therefore had an incorrect chemistry. To confirm this OES was conducted on the samples, outlined in section 2.7. The elemental composition is shown below in Table 33.
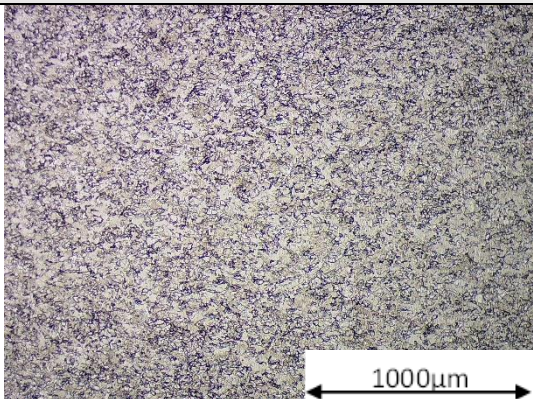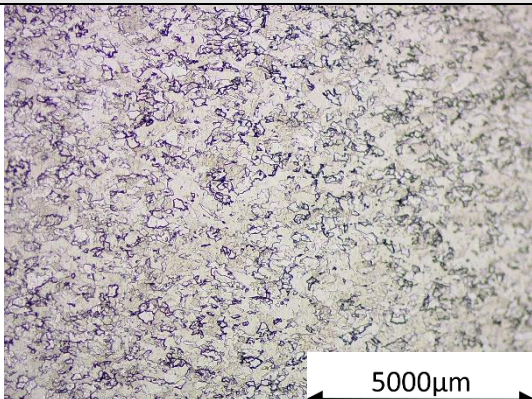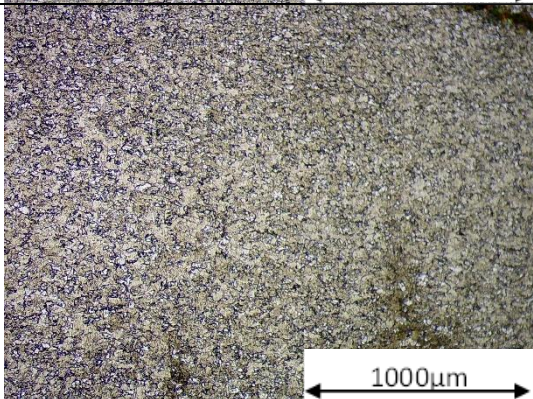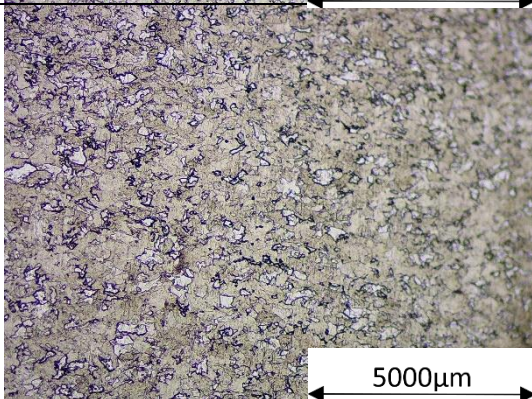
Table 33- OES data from 5 pass FRT variation study.

Element	C	Si	Mn	P	S	Al	N	Ti	Fe
Mean	0.003	0.009	0.075	0.010	0.006	0.068	0.001	0.060	99.75
SD	0.000	0.001	0.001	0.001	0.022	0.022	0.001	0.002	0.025
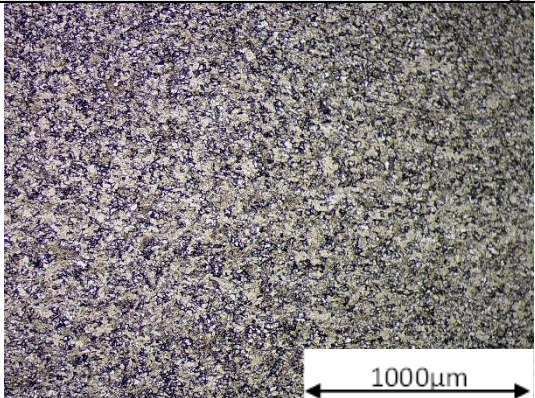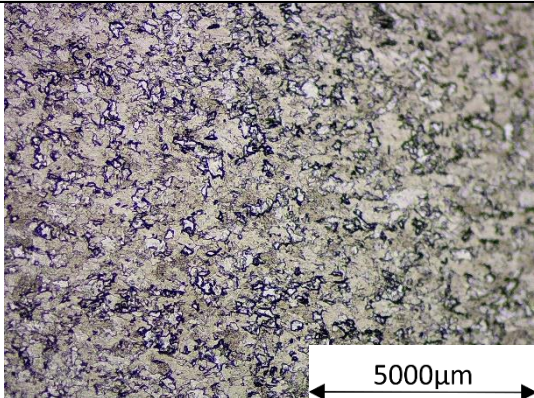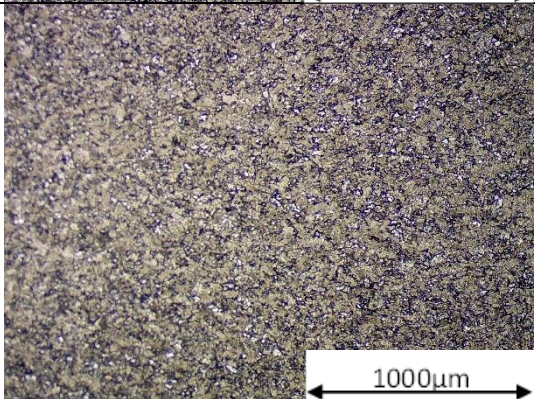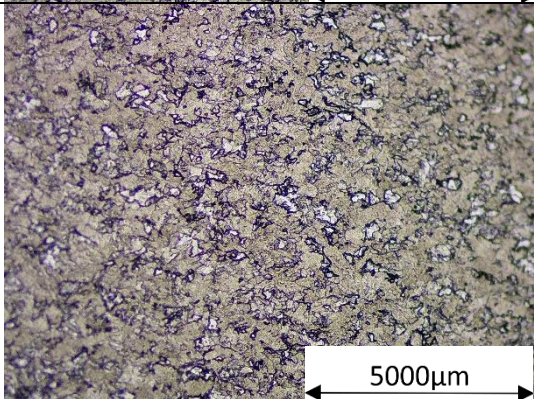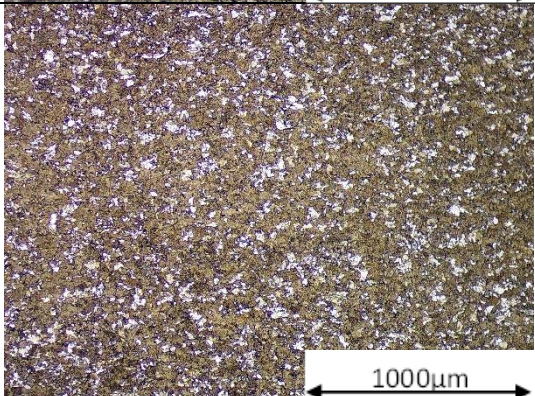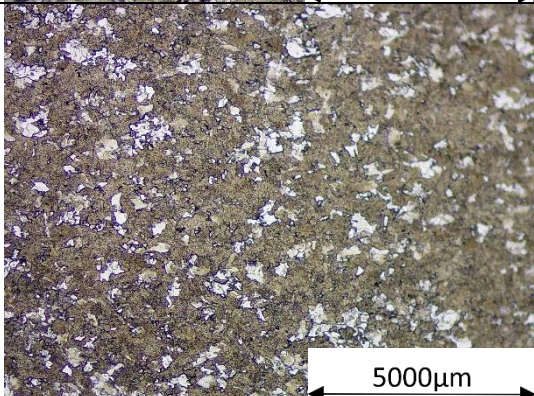
It is clear from the above data that the elemental composition varies greatly from the PD800 composition which was intended. It is likely that an issue with the VIM method caused this or some error in the addition/ measuring of the alloying elements. Concerningly this cast contained no Nb, which is a key element in the transformation of DP800, as well heavily influencing the recrystallisation characteristics. As suspected, the percentage weight of carbon is 40 times less that the target value for Tata Steel's DP800 grade. The DP800, being a AHSS (with a higher carbon content) as such is able to readily form carbon rich phases such as pearlite, whereas low carbon steels, such as the composition outlined in the above table, this is not the case, see section1.3. The presence of perlite in any quantity,

in a ferrite matrix, will result in a significantly stronger material due to the presence of cementite, see section 1.3.4. There is also significantly lower percentage weights and numbers of microalloying elements. This will also reduce the strength of the material significantly, due to the absence of precipitate formers and their associated strengthening mechanisms; both precipitate hardening and grain refinement, see section 1.2.1. Both of these factors explain the low simulated UTS results found. The chemical composition was more reflective of and IF steel grade, in any case microstructural analysis was conducted to see the effect of the processing parameters on the final microstructure.

Table 34- Optical micrographs of samples with pause between roll passes, etched with 2% Nital, showing 5x and 10x magnification.

Sample Name/ Block No.	Magnification	
	5x	10x
1	1000µm	5000µm
2	1000µm	5000µm

Sample	Magnification	
3	1000μm	5000μm
4	1000μm	5000μm
5	1000μm	5000μm

Figure 153- Average ferrite grain size of samples 1-5.

It can be seen from Figure 153 that there is little variation in the grain size, nor can any discernible trends be observed in the small variations that are shown. This was also found with the simulated UTS determined by Plastometry for all five samples. Despite the experimental procedure being successful in carrying final rolling temperature, not discernible effects were recorded in doing so. Unfortunately this means that this approach in investigating the effect of the transformation rate, as a function of final rolling temperature was not successful.

Since the incorrect material was used for this experiment, there is some question as to whether using DP800 instead would have yielded different results. Due to constrains on time and facility availability this particular experiment could not be repeated experimental. Instead a Jmat Pro simulation was performed for using Tata's DP800 chemical composition, as well as the experimental chemical composition determined by OES in Table 33. The starting grain size for the experimental chemistry was also recalculated using Jmat Pro using the furnace heating profile determined in section 3.3.3, shown in Figure 131. The inter-pass times, and temperatures, were taken from the mill output data to ensure a close replication of the conditions experienced by the strip, the results are shown below:
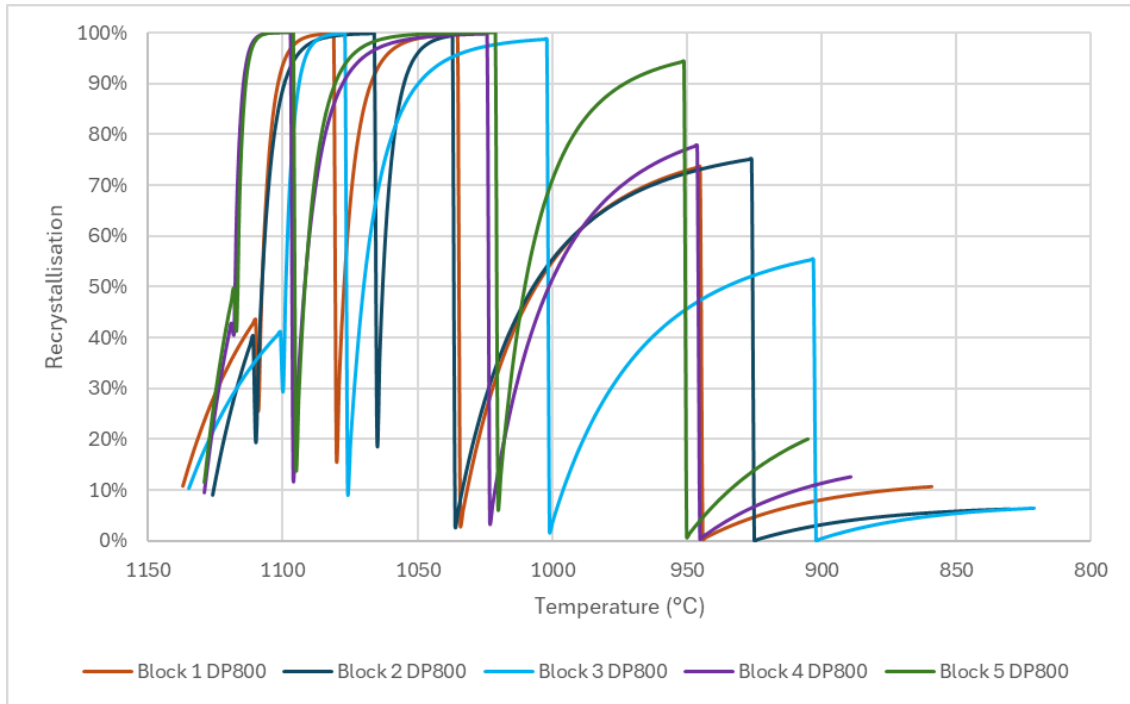
Figure 154- Jmat Pro simulation of fraction recrystallisation for DP800 blocks 1-5, as a function of temperature.
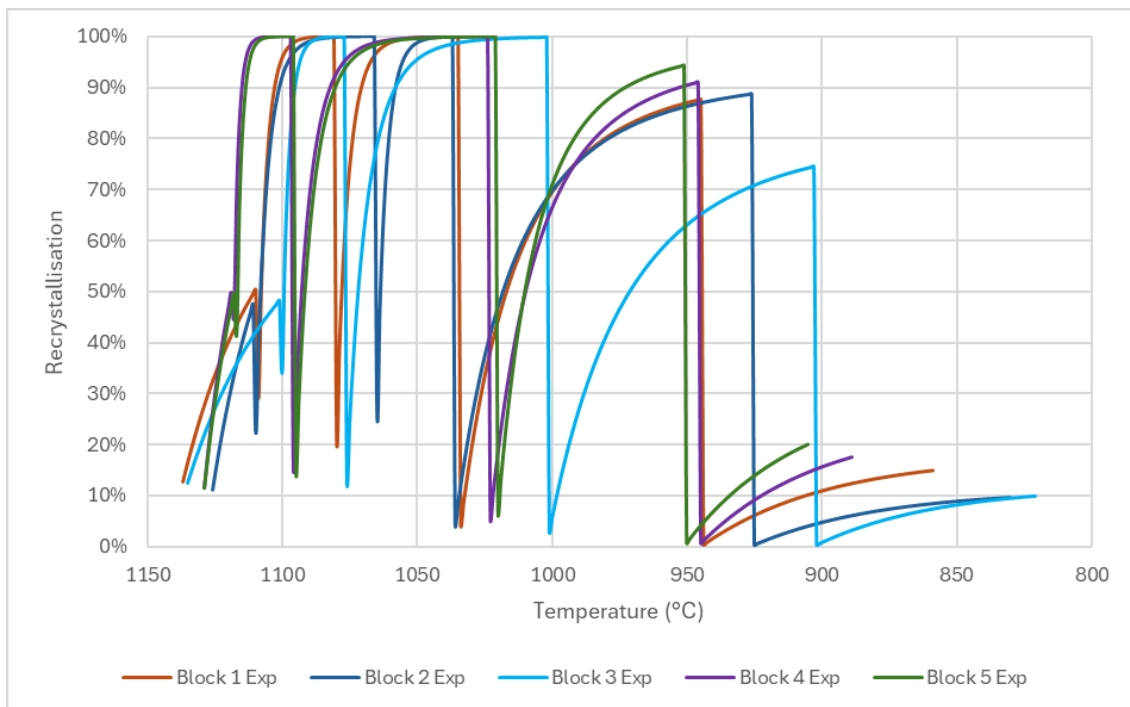
Figure 155- Jmat Pro simulation of fraction recrystallisation for Experimental chemistry blocks 1-5, as a function of temperature.

The average percentage of the recrystalised fraction for the DP800 chemistry was found to be less than that of the lower carbon experimental composition. This is to be expected since chemical additions such as Nb are known to retard recrystallisation, refining the grain size, as well as forming precipitates at lower temperatures.

It was found for both chemistries, between blocks 1-5 there was very little variation in the simulated austenite grain size for each of the inter-pass time variations. For this reason the grain sizes have been plotted as a function of chemistry rather than block number.
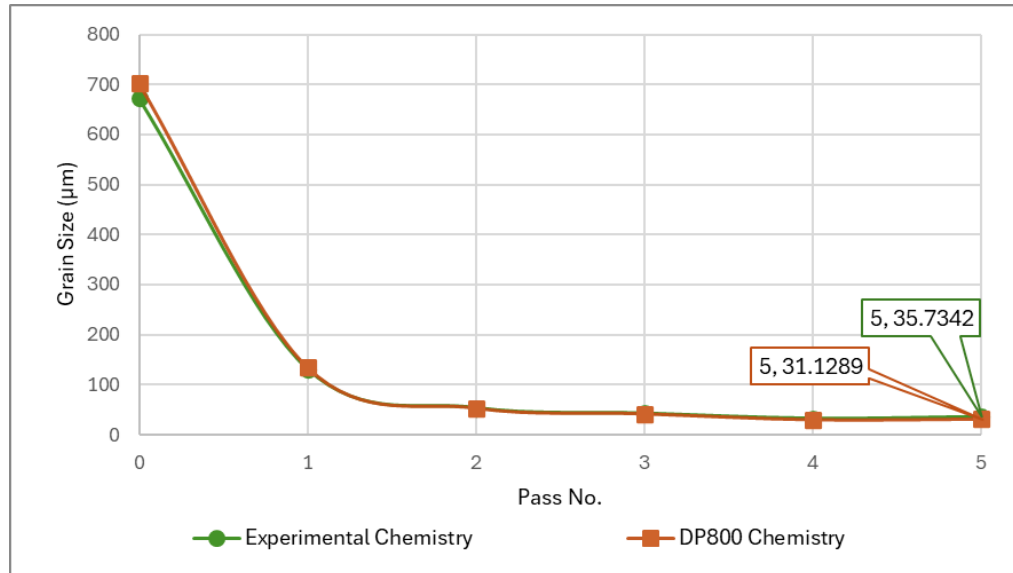
Figure 156- Simulated grain size as a function of roll pass for Experimental Chemistry and DP800 chemistry.

It is clear that the grain size is also constant between chemistries, despite there being some difference in the recrystallisation per pass for the two chemistries. This result is unusual since the microalloying elements present in DP800 are likely to refine the grain structure, this brings into question the accuracy of the grain size measurement of the multi-pass hot rolling model in Jmat Pro for this particular chemistry.

From the results shown above it is clear that introducing a pause between rolling passes, in order to vary the FRT, was not a successful approach in varying the transformation characteristics on the ROT, in the case of the lower carbon experimental chemistry used. The intention in using Jmat Pro to produce a parallel simulation of the DP800 parameter was to investigate the likely effects of a more complicated microalloyed composition on the process outcomes, however due to the similarity of the grain size results despite the different chemistries this approach may also be unreliable.

5.5. Conclusion

In conclusion it seems that varying the rolling schedule in the laboratory setting, in order produce varying final rolling temperatures is not a viable approach to creating a varied effect on the transformation of the steel on the ROT. Jmat pro also was not convincing in reproducing the simulation with a DP800 chemistry due to the questionable grain size

results, despite a sensible comparison of percentage recrystallisation being produced between the two chemistries. Therefore this experiment should be repeated using the DP800 chemistry in order to determine the promise of this experimental approach.

6. RAP Scale-Up

6.1. Study Justification

This research has focussed on the study of Tata Steel's DP800 grade in laboratory production of hot band steel strip at the 2.5kg scale. However, many of the optimisations that have been undertaken for the laboratory mill and ROT are applicable to other grades also. For this reason, the optimised process route was trialled on a modified variant of one of Tata Steel's IF (Interstitial Free) steel grades, of VIM cast origin. Prior to this, this IF grade had been produced through the RAP route. The exact chemistry cannot be provided in this thesis, however an interstitial free steel is typically one that is highly formable and low is percentage weight of carbon, and a low tensile strength especially by comparison to DP800, see section 1.1.4. It is commonplace however to add other microalloying elements to 'tune' the mechanical properties or probability of the steel to suite the needs of the customer of manufacturer. Some examples of these include phosphorus, manganese and silicone in the case of solid solution strengthening[142].

Based on the findings of section 4.1, the 'Old' rolling schedule was utilised, since in the case of DP800 a more representative rolling schedule of the Port Talbot hot mill, did not result in a more representative hot band microstructure, but rather a less representative one. This also removes the compilation of the manufacture of a chamfered sample, instead a standard block was used. However the ability to reduce the number of passes in achieving the same net reduction, whilst maintaining a high FRT remains of value to SAMI and their continued research.

The optimised ROT settings determined from section 4.2 were used for one block, which was subsequently placed in the coiling furnace. Whereas another block was quenched to reveal the austenite grain size upon entry to the ROT, using the same method described in section 4.1.8.

This section also aims to compare process route with the 40g RAP process route shown in section 1.5.2, for both the modified IF grade and the DP800 grade. And therefore compare the results of the 'hot-band' material at two different scales of manufacture, for two contrasting grades, and discuss the possible differences between them both.

6.2. Modified IF Results

The below image is a stitched micrograph of the section of the quenched plate perpendicular to the rolling direction. Etched using Marshall's reagent showing the prior austenite grains. A variation in grain structure through thickness, likely as a result of an increased cooling rate at the strip surface prior to quenching, resulting in less grain growth and recrystallisation at the strip surface during hot rolling. Remnants of as cast microstructure can also be seen by the vertically elongated grains, perpendicular to the plate surface, showing a very different microstructure to the DP800 quenched samples discussed previously. Some banding is also present nearer the top surface of the plate.
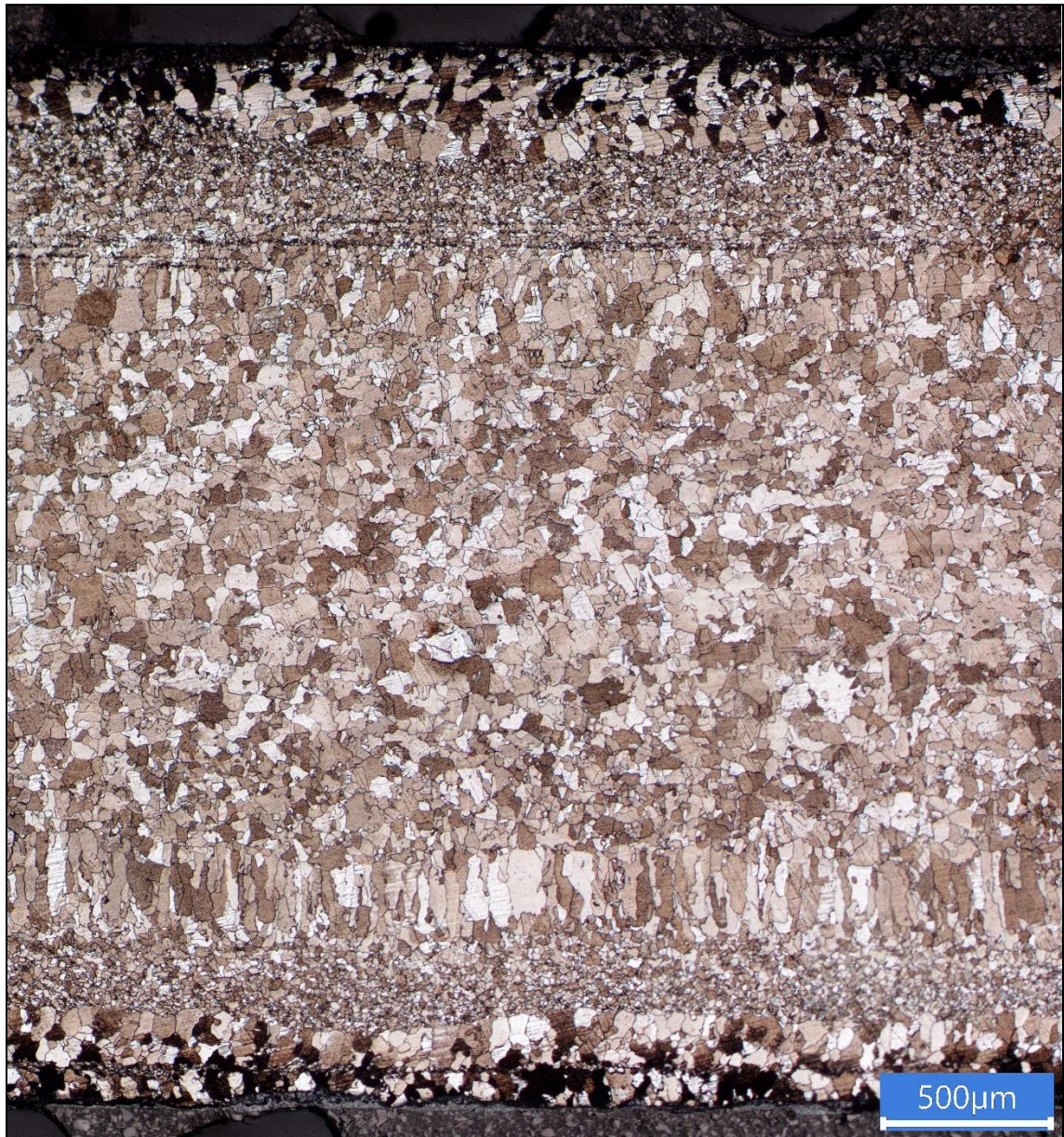
Figure 157- Stitched composite image hot rolled, quenched IF grade steel, showing parent austenite grains.

Average grain size analysis was performed in the middle section of the sample, to measure the prior austenite grain size in the bulk of the strip, in order to avoid remnants of the as-cast microstructure as well as the excessively small grains near the strip surface. The average austenite grain size was found to be was found to be 36μm. Again a Jmat Pro simulation was used to simulate the hot rolling procedure, and the starting grain size was calculated using the 'Reaustenisation' tool, using the experimentally determined furnace heating profile. This yielded a final grain size of 33.4μm, which is within 8% of the experimentally determined value, showing good agreement with the simulation.
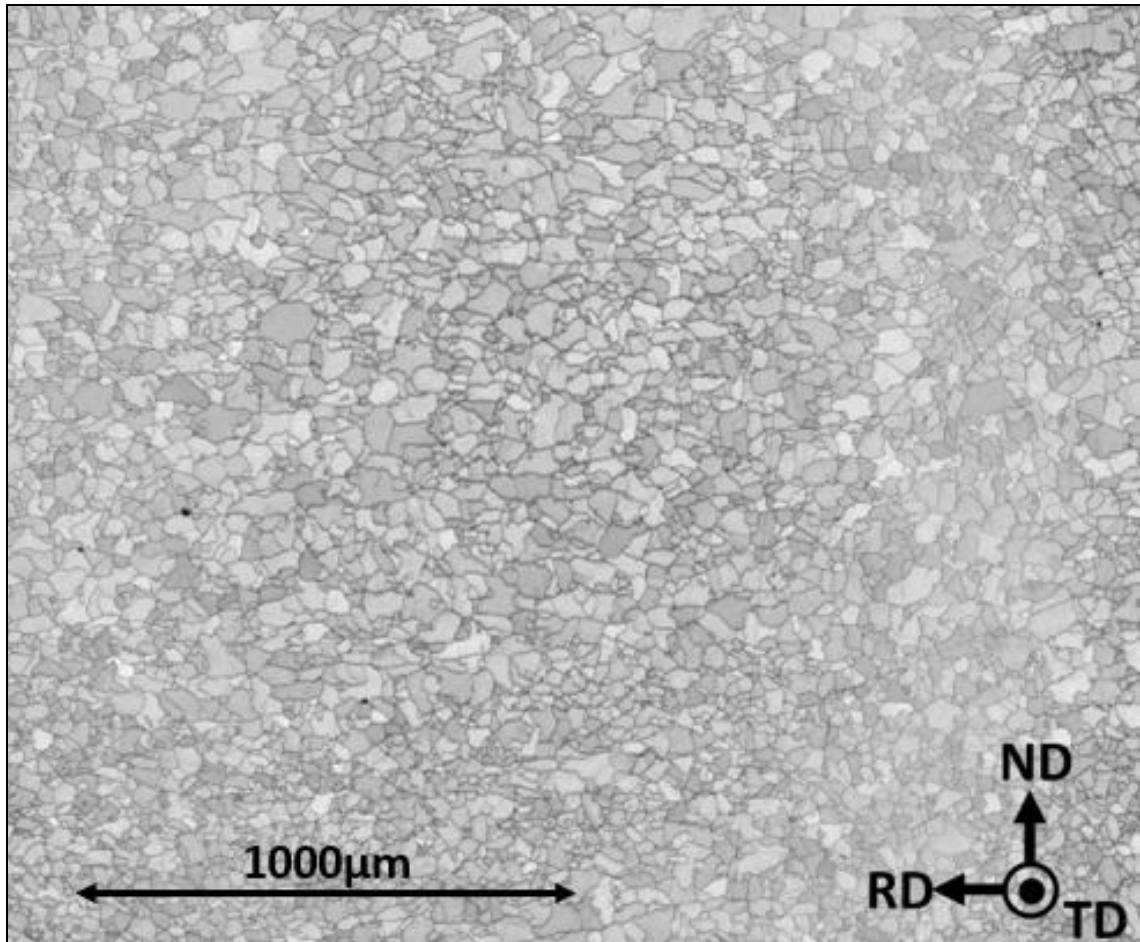
Figure 158- Electron microscope micrograph of a RAP produced IF grade, at the 'hot-band' stage.

The above sample was produced and prepared by the Mach1 research institute at Swansea University. The average grain size, at the strip centre was found to be 25.4µm. Note this is the hot band microstructure and not the quenched microstructure so is not comparable with Figure 157. The aim of this body of work is to compare it with the sample shown below which was produced using the VIM and subsequently the 7-pass rolling schedule, used previously in this research.
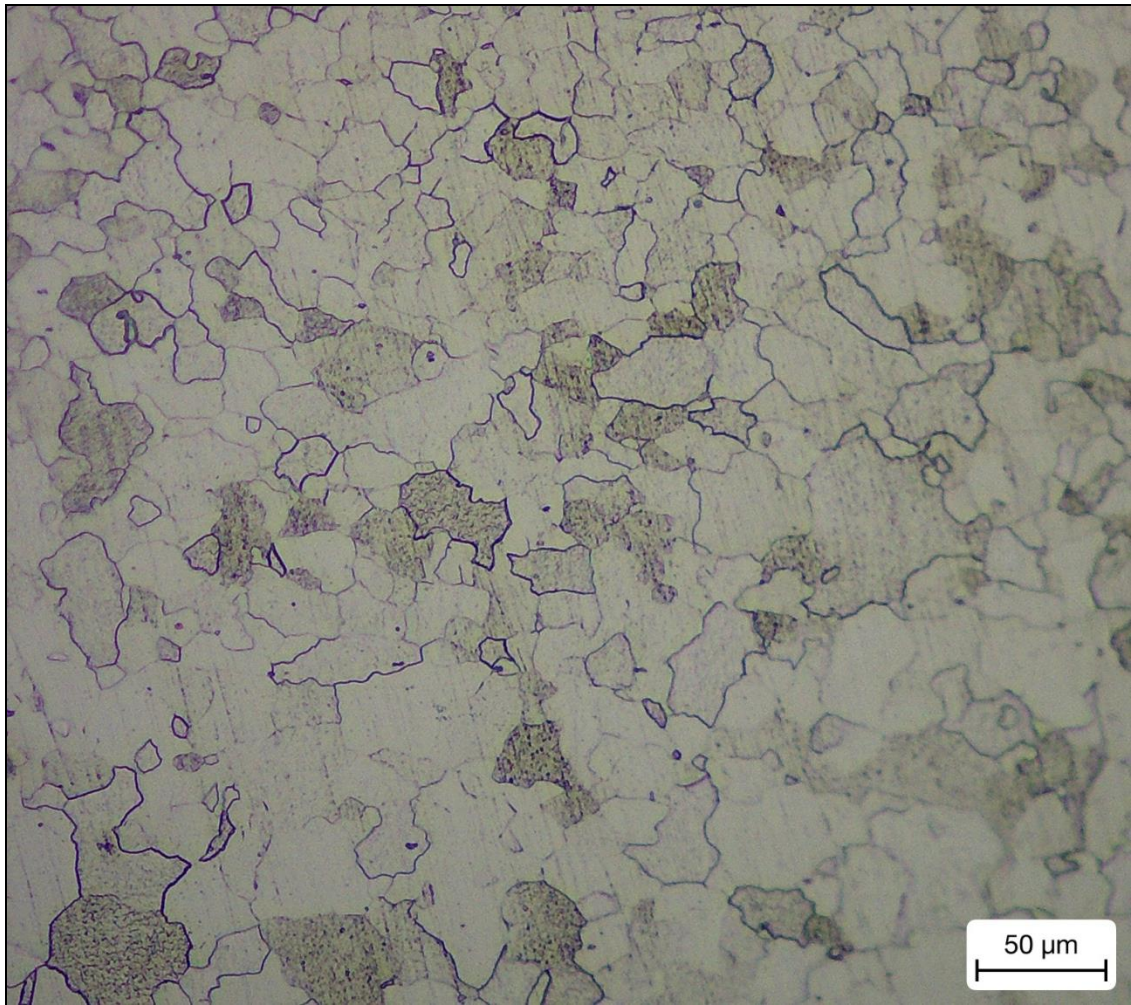
Figure 159- Optical micrograph of a VIM produced modified IF grade, at the 'hot-band' stage.

The above figure shows the ferritic grain structure, of the sample, perpendicular to the rolling direction. Similarly to the RAP produced sample there is no evidence of banding, unlike some DP grades, but rather a uniform equiaxed grain structure. The average grain size of the VIM produced IF grade was found to be 16.7μm.

6.3. DP800 Results

The below micrograph is of a 40g RAP sample, produced by Mach1:
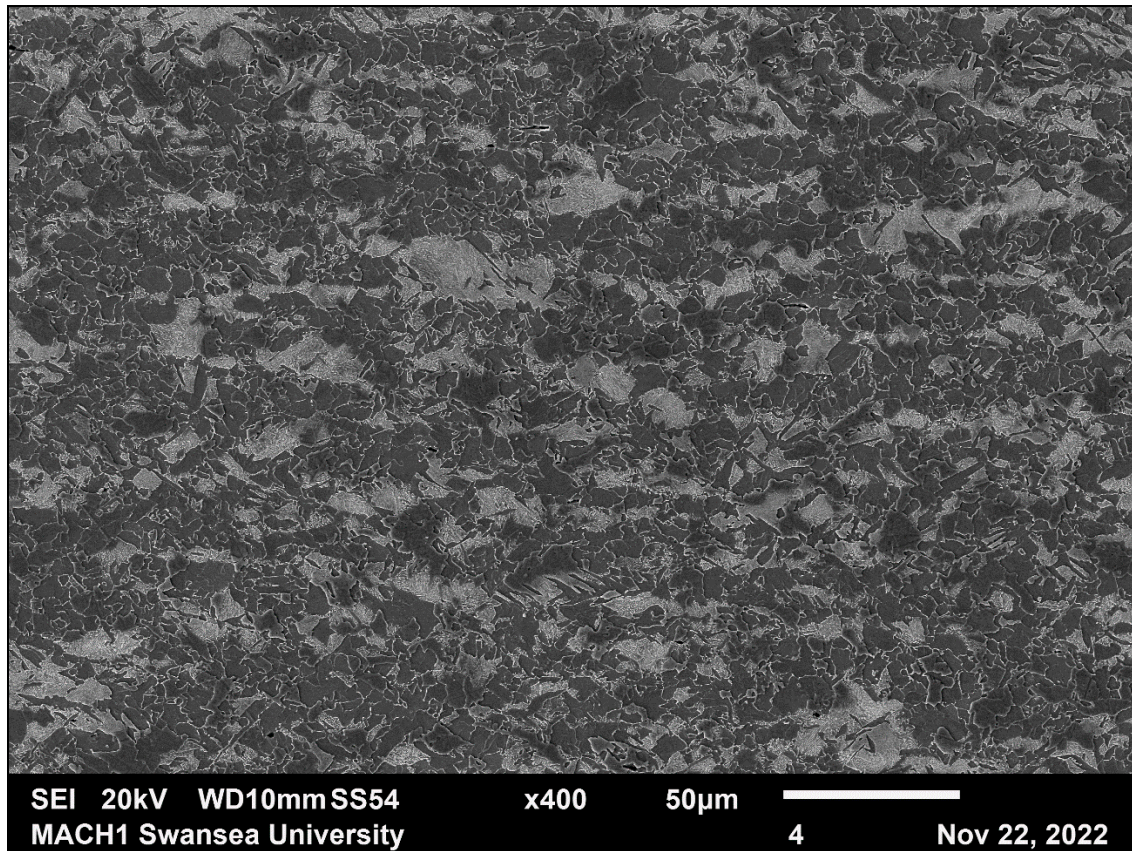
Figure 160-- Electron microscope micrograph of a RAP produced DP800, at the 'hot-band' stage.

Similarly to the VIM produced DP800 'hot-band' samples, longitudinal pearlitic structures are present, somewhat similar to banding. The average grain size of the RAP produced samples was found to be 4.58μm. The VIM produced samples discussed previously in this research have had their mechanical properties determined by Plastometry, as discussed in section 2.3. However due to the limited sample thickness of the RAP method, this did not produce reliable results. In order to determine the mechanical properties of these RAP produced samples Zhang, W. Harrison, T. Abdullah and colleagues have developed a novel miniature tensile specimen [143]. An example of this mini tensile is shown below:
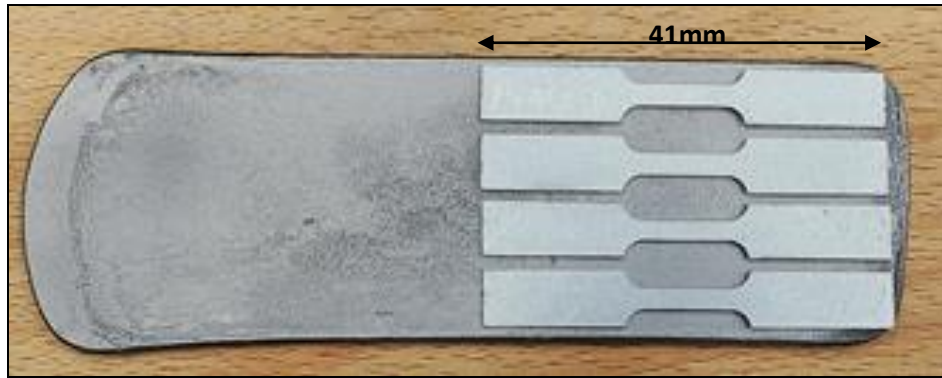
Figure 161- Mini tensile shown against a 40g RAP produced hot rolled plate, produced by the Mach1 team at Swansea University.

Using this novel method, the UTS of the RAP produced DP800 'hot-band' material was found to be 581MPa.

The VIM produced sample of DP800 has already been analysed and discussed in section 4.1.7, since this was the most promising variant of the laboratory mill rolled samples, by comparison to the plant produced material. The micrograph is shown below:
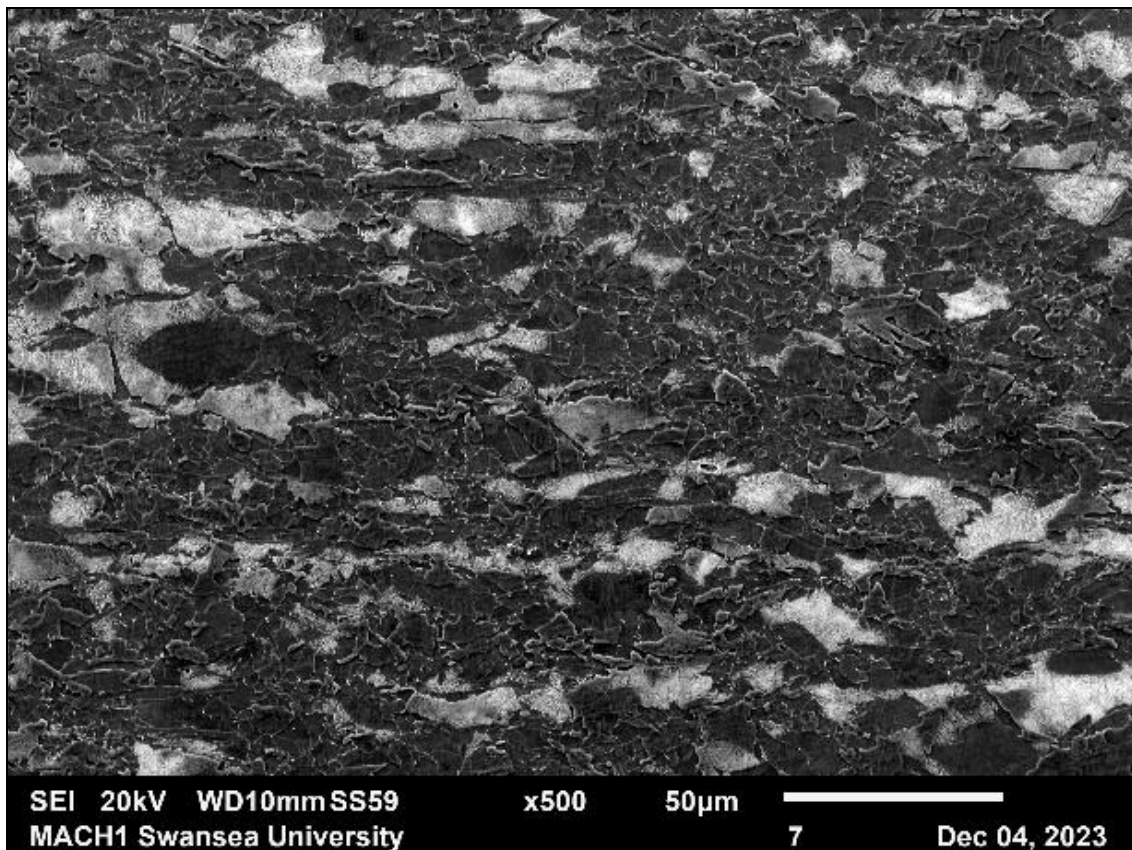
Figure 162- VIM produced, laboratory hot rolled SEM micrograph of DP800.

As discussed previously this specimen showed some evidence of longitudinal pearlitic formations, which could not be considered continuous banding, but more indicative of a

hot rolled microstructure. As discussed previously the average grain size was found to be 3.83μm and the UTS was found to be 735MPa.

6.4. Discussion

The below figures shown the grain size for the relative production methods, for both chemistries as well as the comparative UTS results for the DP800. UTS measurements for the modified IF grade have not yet been determined, since miniature tensile specimens have not yet been manufactured for this novel grade.
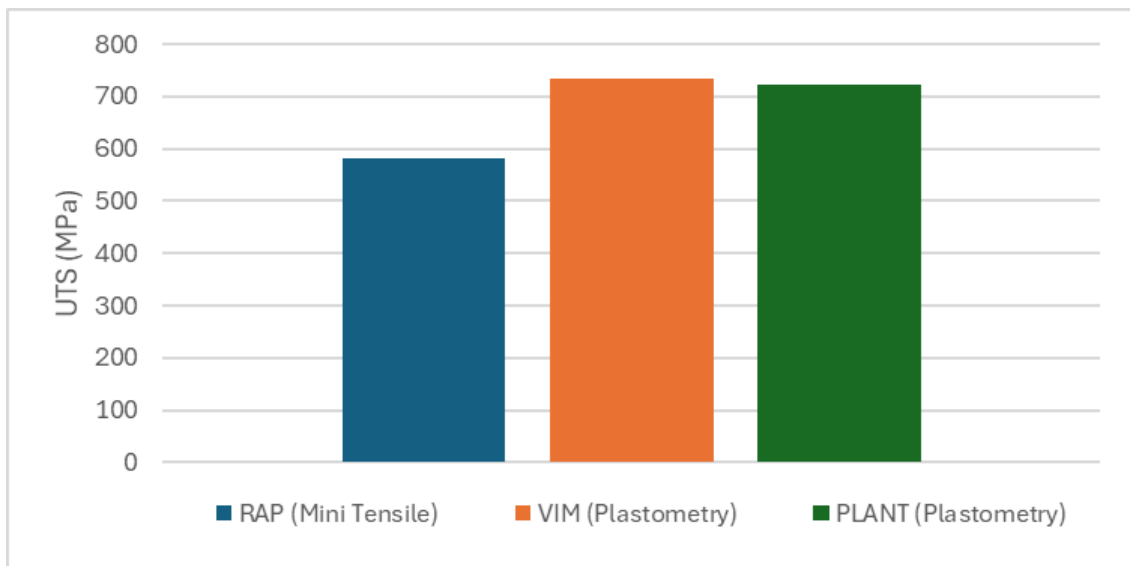
Figure 163- UTS results for each production method for DP800 samples, with measurement methods for determining the UTS listed in legend.

The larger VIM produced sample yielded a closer adherence to the UTS of the plant produced sample being within approximately 2% of the plant produced value, opposed to 22% for the RAP produced sample. Note UTS is used for comparison because plastometry, for the samples studies in this thesis, did not yield reliable results for elongation, so instead UTS was chosen as a comparison metric. The reason for the better adherence regarding the mechanical properties is likely due to the average grain size of the samples, shown below:
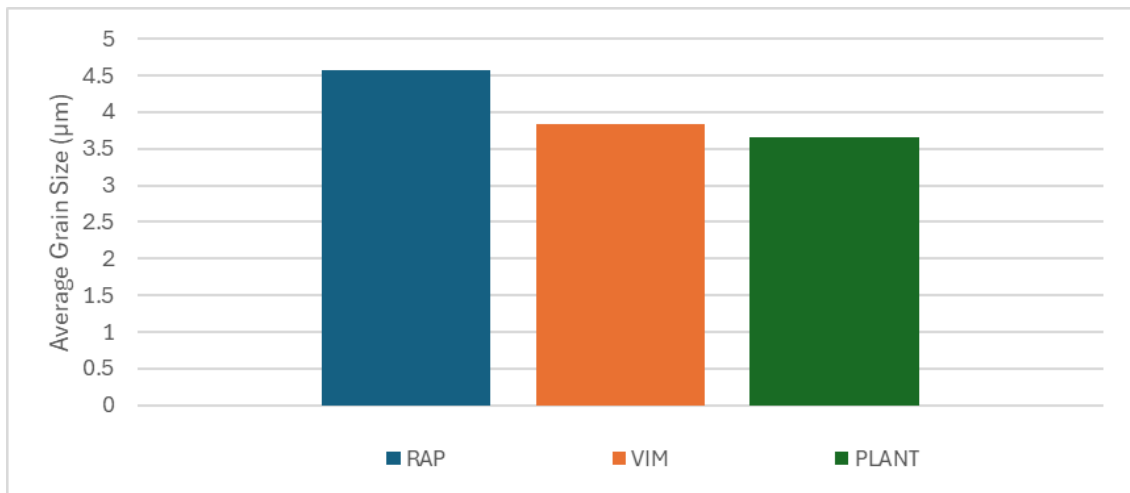
Figure 164- Average grain size for each of the production methods of DP800.

The larger average grain size exhibited by the RAP produces sample is likely responsible for the lower UTS. The VIM produced sample was within 5% of the plant value, whereas the RAP method was within 22% of the plant value. Showing for the case of PD800 multi-pass reverse hot rolling, at a larger scale produced a more representative grain structure, over a smaller RAP method in the pursuit of the recreation of 'hot-band' material.

As mentioned previously the UTS of the modified IF grade is not included in this analysis, so will instead focus on the microstructural observations of the two samples.
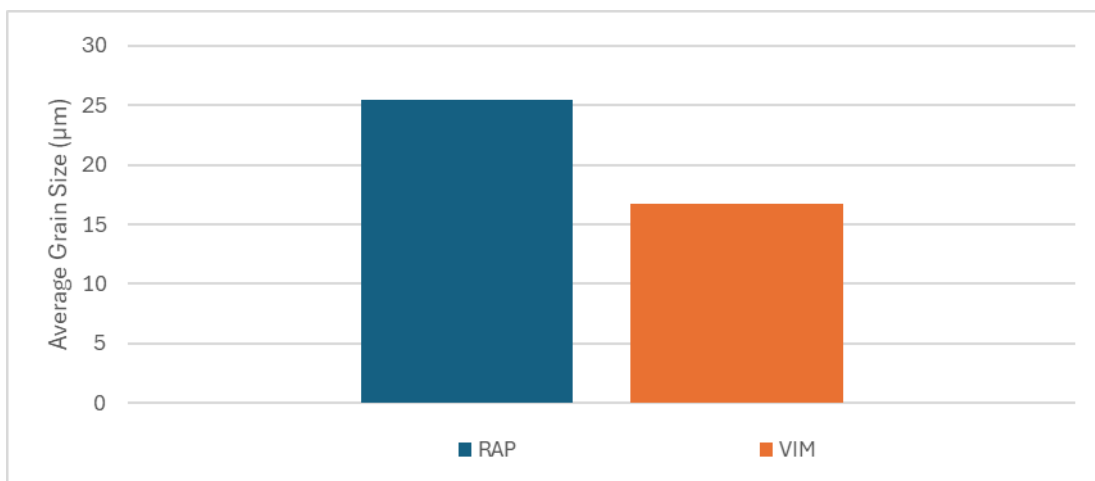
Figure 165-Average grain size for each of the production methods of the modified IF Grade.

Similarly the results of the DP800 average grain size, the RAP method produced a significantly more coarse grain structure, had the mechanical properties been assessed it is likely that this too would have resulted in a lower UTS for the RAP produced samples. Since this is an experimental grade there is not a plant produced microstructure to compare against, however by comparison to the DP800 results it may be that that in this case the VIM produced sample results in a more representative microstructure. With refence to

section 1.5.2 the manufacturing process of RAP produces samples only allows the opportunity for single pass reduction, with a relative reduction of 40% in the hot rolling stage, due to the small sample size and rapid heat loss associated. Any attempt to roll consecutive passes would likely result in microstructural deformation below the TNR and introduce pancaking into the grain structure, destroying the desired equiaxed structure. Another limiting factor is the total amount of reduction that can be imparted into the sample in a single pass, because the total reduction is limited, the amount of grain refinement is therefore limited, which explains the results seen in Figure 164 and Figure 165.
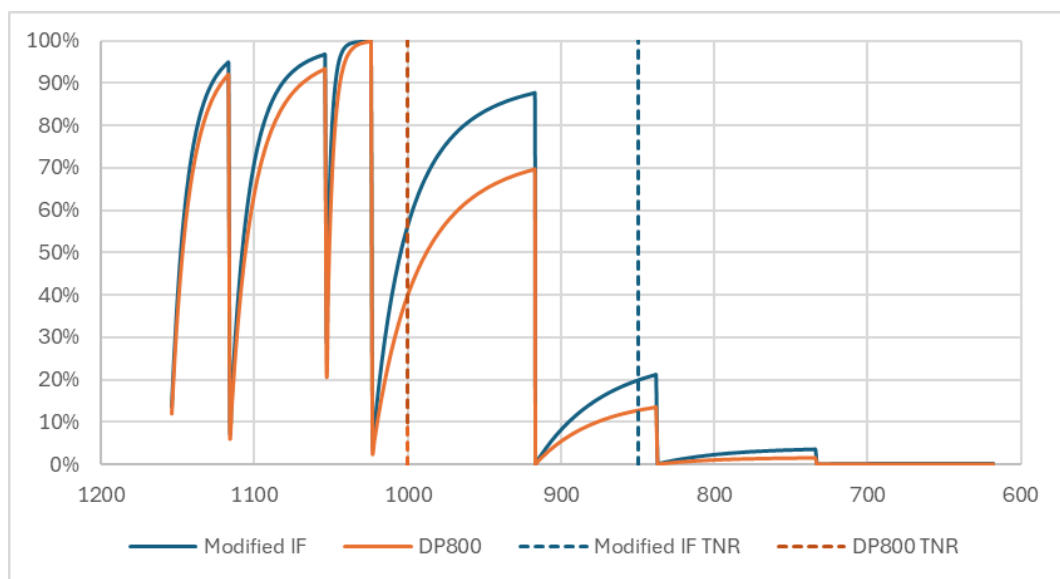
Figure 166- JMat Pro Simulations of fraction recrystallisation as a function of temperature for the modified IF grade and DP800.

Comparing the chemistries back-to-back, the DP800 exhibited a finer grain size. This is to be expected due to the presence of grain refining elements such as NB which present as barriers to grain growth by pinning the grain boundaries. Figure 166 shows the simulated fraction recrystallisation as a function of temperature, from Jmat Pro. The T_{NR}s for both chemistries were calculated using the Bai[66] equation, outlined in section 1.7.1.1.1, and overlayed onto the graph. As expected the T_{NR} for the IF grade is lower than that of DP800. This would likely allow for more recrystallisation in the latter roller passes and therefore result in more grain growth, which also explains the more coarse grain structure seen. Furthermore the IF grade also exhibits greater volume fractions of recrystallisation for each and every roller pass.

For the above simulation the starting grain size was also modelled, using Jmat Pro, via the process outlined in section 4.1.7. Despite the difference in chemistry the starting austenite

grain size was found to be fairly close; 702µm for DP800 and 678µm for the modified IF grade. Despite this convergence of grain size, likely due to the long reheat times the resultant final microstructure was found to be varied for each grade, with the DP grade exhibiting a finer average grain size.

This study has shown the varied behaviour of two contrasting microalloyed steel grades. The different resultant microstructures have been characterised along with accompanying simulations of the transformation kinetics have shown why these varied microstructures have arisen. Since the IF grade is an experimental composition, it cannot be compared against plant produced sample to evaluate the validity of the process route.

7.   Conclusions

This project aimed to increase knowledge regarding the problem of poor hot-band coil formability through both physical experimentation and simulation methods, recommendations to this end were not produced.

However the knowledge gained regarding the physical experimentation of hot rolling, through the SAMI process route, has be extensive. A new sample design has been identified which allows greater design freedom for future research in creating novel rolling schedules, with load prediction to protect the Lewis Mill. These limitations and benefits of this design over older design have been identified and quantified microstructurally for the DP800 product.

Furthermore, the two process routes; the 40g RAP route, pioneered by Mach1 and the SAMI process route utilising 2.5kg VIM casts, have been compared in the setting of the manufacture of DP00 hot-band manufacture. It was found that the multi-pass hot rolling resulted in a better representation over the single pass rolling RAP route. The increased degree of gain refinement, made possible by the increased sample size was found to be responsible for the more representative grain structure and mechanical properties, since better heat retention allowed for multiple rolling passes and therefore more grain refinement. However the SAMI/VIM route requires more time and material.

Plastometry was also identified as a helpful tool in the classification of steel samples, that had undergone hot rolling and cooling treatments. It was tested against a number of steel samples that had undergone subtly different cooling paths, and the simulated UTS was compared against 'real' UTS results determined through A80 tensile specimens. Good agreement between the two methods was found in determining the UTS of hot band material, and where there was not good agreement it was found this was due to local fluctuations in material properties. This has been identified as a good option for the rapid evaluation of mechanical properties, which is of particular benefit in the setting of RAP where a large number of samples are generated quickly. This asset at Swansea University has been used regularly following the results presented in this research for a number of steel grades, produced via both the SAMI and the RAP route. Using the data gained from

this project, optimisation to the 'general steel' model has been made, improving the simulation of stress strain curved from indentation and profile data.

It was hoped that at the outset of the project the Titan model could be optimised and subsequently used to change the cooling parameters to increase the volume fraction of ferrite transformation on the strip, reducing the formation of bainite and the coil head and tail, increasing product yield. Despite this not being achieved, the limitations of the Titan model were identified, regarding optimisation from plant data. In addition to the this a greater understanding of the Mitron transformation model within Titan has been gained, this knowledge has been identified as being industrially valuable for work on the hot strip mill at Tata Steel Port Talbot.

8. Future Work

8.1. Future Mitron/ Titan Optimisation

As discussed previously the limited transformation data for the given journals made optimisation of the ROT model a challenge. At the time of writing transformation monitors have been fitted to the ROT and initial data sets are being created for a variety of steel grades. These transformation monitors are will be placed down the length of the ROT, in the same locations as IP1, IP2, IP3 and the CT pyro and measure the magnetic permeability of the strip, this signal is used to determine the degree of ferritic transformation in the strip along its length[144].

As a result another PhD has been funded which focusses on using machine learning techniques to vary the setting within the Mitron model such that the best combination of settings is sought for all steel grades. This has only recently been made possible due to the large amount of transformation data being created. This project was key in realising the complexity of the optimisation task.

Once this optimisation is complete, the Titan model can then be used to model theoretical process changes and therefore predict the resultant transformation. This will prove to be highly useful in eliminating production issues such as coil end effects.

8.2. Suggested modification to Laboratory Rolling Setup

Throughout this research project it has been made clear that u number of upgrades to the SAMI processing route would be desirable in better replication of the Port Talbot hot strip mill as well as increasing design freedom of the thermomechanical treatment. Many of the following upgrades have been discussed with SAMI staff who agree these would be beneficial.

- Possibility of a single transformation detector to determine real time transformation measurement of material on the ROT. Currently transformation has to be inferred from the final grain structure after the coiling furnace. This would remove the need of the researcher to mount, grind, polish and each sample to measure the resultant transformation.

- A heated mill bed. The mill bed is the material the samples rest upon between each rolling pass. These are currently constructed of solid brass. As such they remove a large amount of heat through the conduction of the plate. A heated bed would eliminate this a increase the number of rolling passes that could be implemented before becomes lower than the desired final rolling temperature.

- IR heaters. These would also assist is retaining heat better into the samples during hot rolling. These could prove to be particularly effective due to the large surface area to volume ratio of the hot rolled plates.

- Increased cooling capacity. It was determined that the experimental setup in the SAMI process cannot match the temperature gradients that the Port Talbot ROT can generate through its laminar flow headers, this has microstructural implications on the degree of ferrite transformation that can be achieved. A water chiller could be added to decrease the water temperature to increase the temperature gradient possible.

- Metered water flow. Other laboratory ROT setups discussed in this paper utilise pressure regulated water headers. One drawback of the SAMI process is that a header tank is used to generate sufficient water pressure. As s result when the water level is low, the pressure decreases also. This can decrease the predictability of the cooling of samples. This is particularly problematic when multiple plates are being processed in one session.

9. Appendix
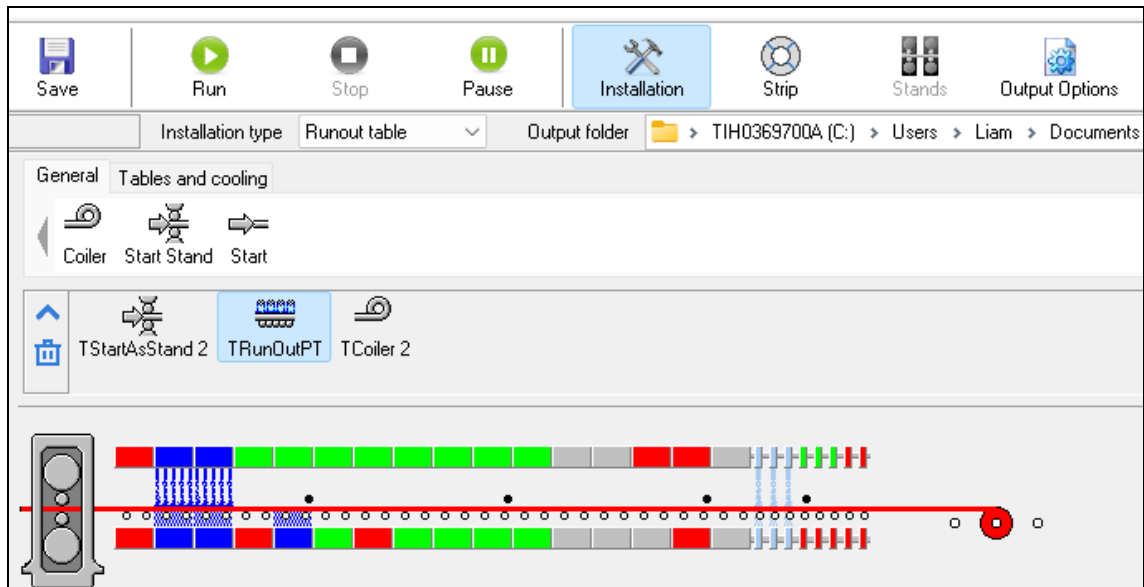
Figure 167- Port Talbot ROT setup within Titan.
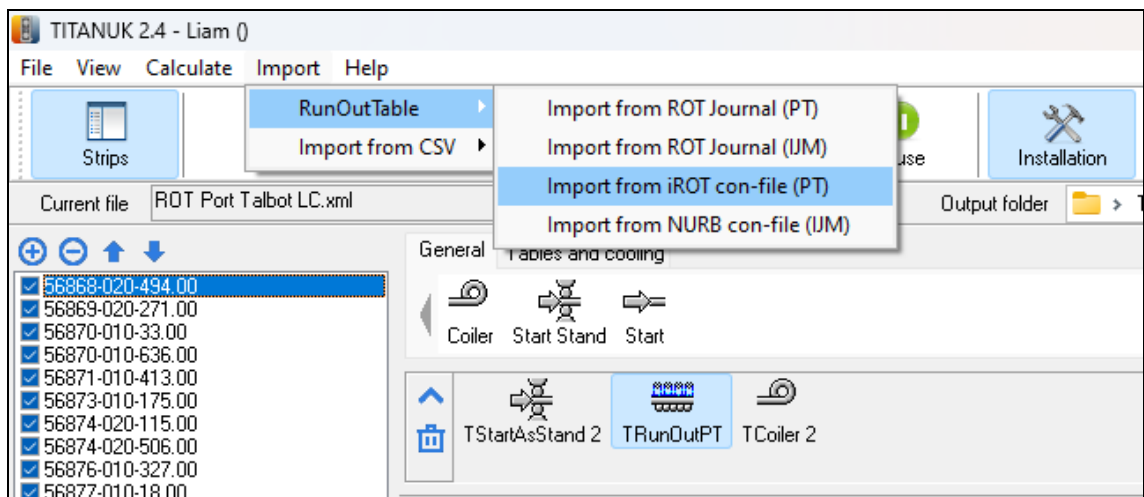
Figure 168- Journal files being uploaded to Titan.
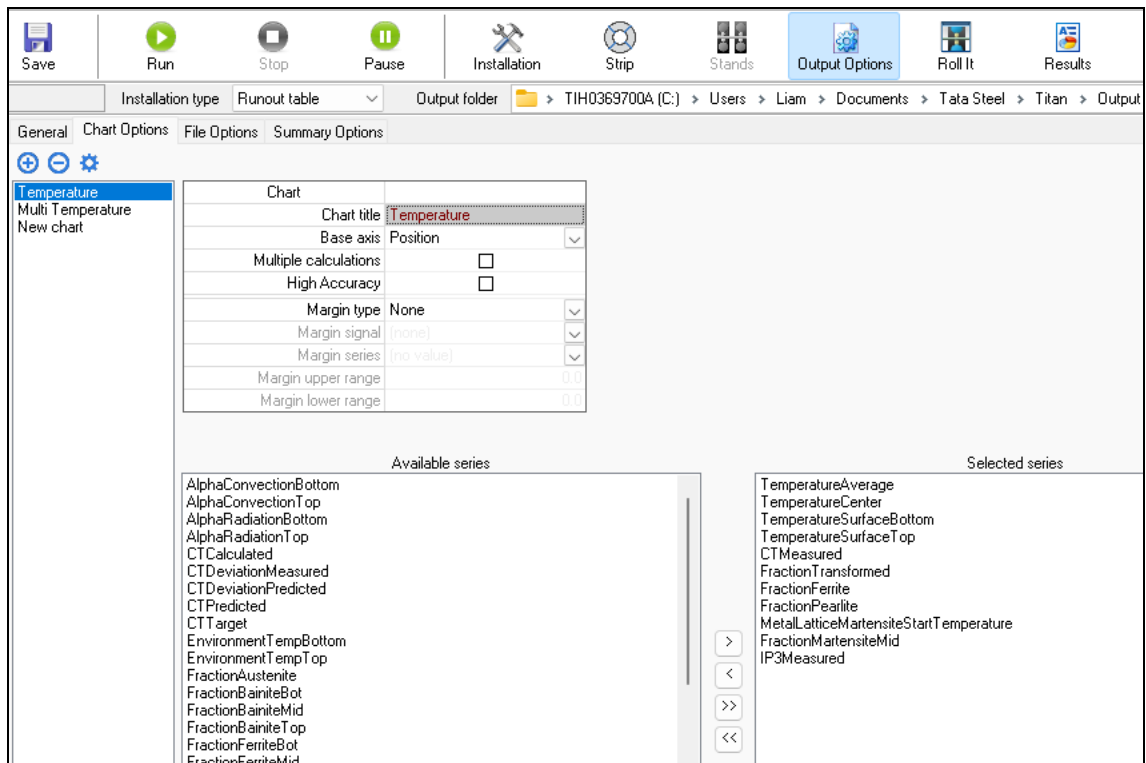
Figure 169- Chart creation in Titan.
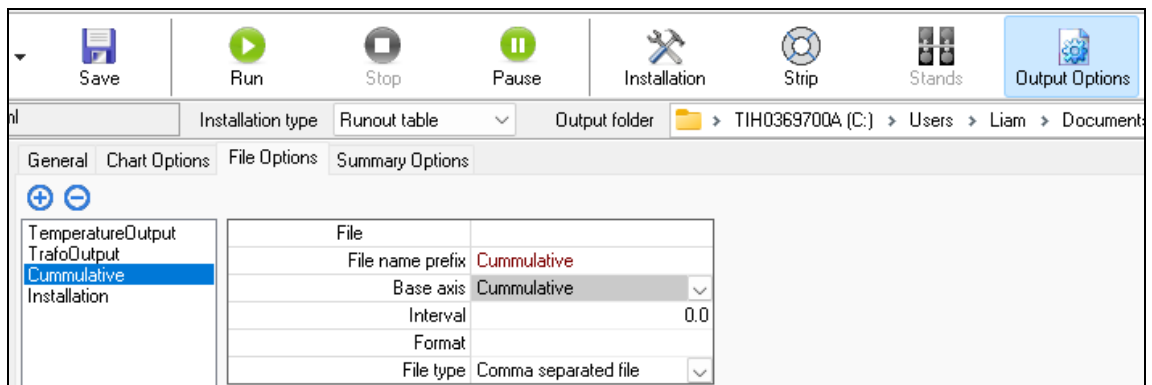
Figure 170- Creation of cumulative file for Titan ROT outputs.
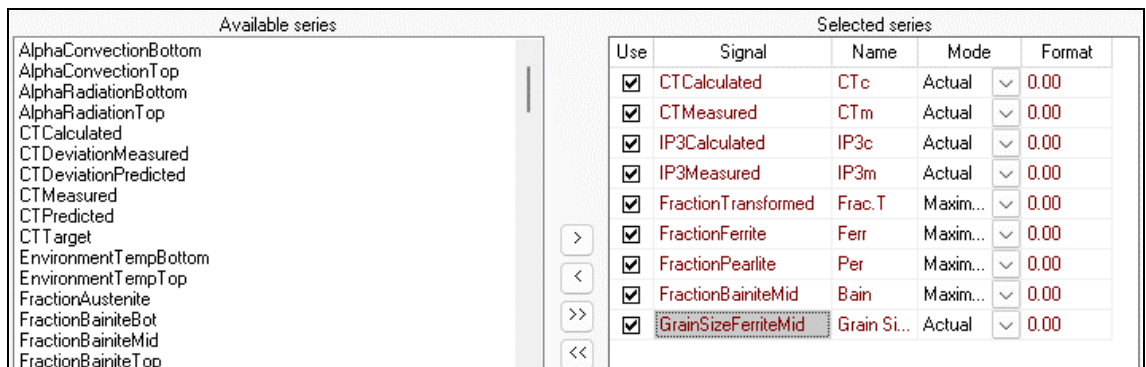
Figure 171- Selecting the data series to be included in the cumulative file.

Table 35- laboratory ROT speed for a given dial position.

Dial Setting	Time (s)			Average Deviation (s)	Average Time (s)	Velocity (m/s)
	1	2	3			
1	31.0	30.0	31.0	0.4	30.7	0.13
2	16.0	17.0	16.0	0.4	16.3	0.25
3	10.0	11.0	11.0	0.4	10.7	0.36
4	9.0	8.5	9.0	0.2	8.8	0.44
5	7.6	7.7	7.7	0.0	7.7	0.52
6	7.1	6.9	7.1	0.1	7.03	0.56
7	6.2	6.5	6.4	0.1	6.4	0.63
8	6.0	6.1	6.1	0.0	6.	0.66

Table 36-Modelled Load and Experimentally measured load for six DP600 samples, previously hot rolled.

Roller Pass No.	Peak Load per Roller Pass No. (kN)													
	1		2		3		4		5		6		7	
	Model	Exp	Model	Exp	Model	Exp	Model	Exp	Model	Exp	Model	Exp	Model	Exp
DP600 1	18.3	26.3	24.1	37.5	32.9	41.8	38.2	37.7	40.0	45.1	44.4	46.0	52.1	36.9
DP600 2	20.6	26.2	24.5	33.7	33.0	41.5	35.5	34.3	38.7	40.7	43.4	46.9	46.7	37.5
DP600 3	18.6	27.6	24.8	38.9	38.4	47.2	44.1	39.9	47.0	49.9	53.2	57.4	52.8	46.0
DP600 4	19.4	35.2	25.0	45.1	34.8	52.0	36.7	45.6	40.4	56.7	44.5	69.1	48.2	55.3
DP600 5	20.2	30.7	24.9	39.3	35.6	42.6	37.1	46.2	41.0	48.2	48.2	57.2	47.3	54.6
DP600 6	19.2	25.4	24.6	38.5	31.2	37.2	40.7	47.1	40.2	49.5	45.1	55.4	49.5	56.8
Average Diff (kN)	9.2		14.2		9.4		5.1		7.1		8.9		8.8	

10. Bibliography

1. Tasan, C.C., et al., *An Overview of Dual-Phase Steels: Advances in Microstructure-Oriented Processing and Micromechanically Guided Design.* Annual Review of Materials Research, 2015. **45**(1): p. 391-431.
2. Ishikawa, T., *1 - Understanding and controlling microstructural evolution in metal forming: an overview*, in *Microstructure Evolution in Metal Forming Processes*, J. Lin, D. Balint, and M. Pietrzyk, Editors. 2012, Woodhead Publishing. p. 3-16.
3. Transport, D.o. *Government takes historic step towards net-zero with end of sale of new petrol and diesel cars by 2030.* Low emission and electric vehicles, 2020.
4. Association, W.S. *FutureSteelVehicle.* 2018 [cited 2020 20 April 2020]; Available from: https://www.worldautosteel.org/projects/future-steel-vehicle/.
5. Contributions, Y.o.A.S. *20 Years of Automotive Steel Contributions.* General News 2016 18 April 2016 [cited 2020 20 April 2020]; Available from: https://www.worldautosteel.org/20-years-of-automotive-steel-contributions/.
6. *RAPID ALLOY PROTOTYPING PROSPERITY PARTNERSHIP.* [Web Page] [cited 2023 07 Match 2023]; Description of the Prosperity Partnership's activities and various work packages.]. Available from: https://www.rapidalloyprototyping.co.uk/.
7. International, A., *Alloying: Understanding the Basics*, ed. J.R. Davis. 2001: ASM International. 647.
8. WorldAutoSteel. *Advanced High-Strength Steel (AHSS) Definitions.* Steel Basics [Article] 2021 [cited 2023 14 March 2023]; Available from: https://www.worldautosteel.org/steel-basics/automotive-advanced-high-strength-steel-ahss-definitions/.
9. Callister, W.D., *Materials Science and Engineering - An Introduction.* 7 ed. 2007: Wiley.
10. Fonstein, N., *7 - Dual-phase steels*, in *Automotive Steels*, R. Rana and S.B. Singh, Editors. 2017, Woodhead Publishing. p. 169-216.
11. Basu, S., et al., *Study of microstructure-property correlations in dual phase steels for achieving enhanced strength and reduced strain partitioning.* Materialia, 2022. **25**: p. 101522.
12. Honeycombe, R. and H.K.D.H. Bhadeshia, *Steels: Microstructure and Properties.* 1996: Wiley.
13. WorldAutoSteel. *Dual Phase.* [cited 2023 March 16 2023]; AHSS Application Guidelines]. Available from: https://ahssinsights.org/metallurgy/steel-grades/ahss/dual-phase/.
14. Poliak, E.I., et al. *THERMOMECHANICAL PROCESSING OF ADVANCED HIGH STRENGTH STEELS IN PRODUCTION HOT STRIP ROLLING.* 2009.
15. Santos, A.P.d.R., et al., *Texture, microstructure and anisotropic properties of IF-steels with different additions of titanium, niobium and phosphorus.* Journal of Materials Research and Technology, 2018. **7**(3): p. 331-336.
16. Manna, R., *Heat Treatment, Tata Steel- TRAERF Faculty Fellowship Visiting Scholar*, in *Presentation on theme: "Heat Treatment R. Manna Banaras Hindu University".* 2018: University of Cambridge.
17. Terao, H., *Structure and mechanical properties of high-manganese dual-phase steels.* Journal of Materials Science, 1986. **21**(5): p. 1715-1720.
18. Dulucheanu, C., et al., *Structures and Mechanical Properties of Some Dual-Phase Steels with Low Manganese Content.* Metals, 2022. **12**(2): p. 189.
19. Karmakar, D., et al., *Niobium-Silicon Microalloyed High Strength Structural Steel.* International Journal of Metallurgical Engineering, 2014. **3**: p. 1-5.
20. Deva, A., B.K. Jha, and N.S. Mishra, *Silicon as grain refiner in niobium microalloyed hot rolled steel.* Materials Science and Technology, 2011. **27**(3): p. 710-712.

21. Preston, R.R., *The Solid Solution Hardening of Steel by Silicon*, in *Strength of Metals and Alloys*, P. Haasen, V. Gerold, and G. Kostorz, Editors. 1979, Pergamon. p. 1025-1030.

22. Setia, P., et al., *Influence of Si content on the microstructure and mechanical properties of silicon stainless steel.* Materials Science and Engineering: A, 2022. **829**: p. 142141.

23. Beeghly, H.F., *Determination of Aluminum Nitride Nitrogen in Steel.* Analytical Chemistry, 1949. **21**(12): p. 1513-1519.

24. Clarke, K.D., *12.10 - Austenite Formation and Microstructural Control in Low-Alloy Steels*, in *Comprehensive Materials Processing*, S. Hashmi, et al., Editors. 2014, Elsevier: Oxford. p. 345-361.

25. Lee, K.-H., et al., *Characterization of transition behavior in SA508 Gr.4N Ni–Cr–Mo low alloy steels with microstructural alteration by Ni and Cr contents.* Materials Science and Engineering A-structural Materials Properties Microstructure and Processing - MATER SCI ENG A-STRUCT MATER, 2011. **529**: p. 156-163.

26. Fahim, K. and M.M.A.R. Hossain, *Phase Transformation in Micro-Alloyed Steels*, in *Engineering Steels and High Entropy-Alloys*, S. Ashutosh, D. Zoia, and K. Sanjeev, Editors. 2020, IntechOpen: Rijeka. p. Ch. 3.

27. Dan, W., Z. Shujian, and Z. Qingdong, *The influence of Cr on the microstructure and electrochemical behavior of high strength low-alloy steel.* Materials Research Express, 2020. **7**(6): p. 066522.

28. Hall, E.O., *The Deformation and Ageing of Mild Steel: II Characteristics of the Lüders Deformation.* Proceedings of the Physical Society. Section B, 1951. **64**(9): p. 742.

29. Rancel, L., M. Gómez, and S.F. Medina, *Influence of Microalloying Elements (Nb, V, Ti) on Yield Strength in Bainitic Steels.* steel research international, 2008. **79**(12): p. 947-953.

30. Bleck, W., A. Frehn, and J. Ohlert, *Niobium in dual phase and trip steels.* Niobium, Science and Technology, 2001.

31. Mohrbacher, H., et al., *Metallurgical Effects of Niobium in Dual Phase Steel.* Metals, 2020. **10**(4): p. 504.

32. Abad, R., et al., *Interaction between Recrystallization and Precipitation during Multipass Rolling in a Low Carbon Niobium Microalloyed Steel.* Isij International - ISIJ INT, 2001. **41**: p. 1373-1382.

33. Alsalamah, H., *The Effect of Prior Austenite Grain Size on Transformation Behaviour as a Function of Cooling Rate in Nuclear Pressure Vessel Steel SA508 G4N*, in *Department of Material Science and Engineering*. 2020, The University of Sheffield: Sheffield. p. 149.

34. Baker, T.N., *Processes, microstructure and properties of vanadium microalloyed steels.* Materials Science and Technology, 2009. **25**(9): p. 1083-1107.

35. Hernandez, D., B. López, and J.M. Rodriguez-Ibabe, *Ferrite Grain Size Refinement in Vanadium Microalloyed Structural Steels.* Materials Science Forum, 2005. **500-501**: p. 411-418.

36. Hu, H., et al., *The effects of Nb and Mo addition on transformation and properties in low carbon bainitic steels.* Materials & Design, 2015. **84**: p. 95-99.

37. Mao, Z., A. Farkoosh, and D. Seidman, *Effects of Alloying Elements on Carbon Diffusion in the Austenite (f.c.c.)- and Ferrite (b.c.c.)-Phases*. 2024.

38. Baker, T.N., *Titanium microalloyed steels.* Ironmaking & Steelmaking, 2019. **46**(1): p. 1-55.

39. Wang, S., et al., *Titanium microalloying of steel: A review of its effects on processing, microstructure and mechanical properties.* International Journal of Minerals Metallurgy and Materials, 2022. **29**: p. 645-661.

40. Rees, G.I., et al., *The effect of niobium in solid solution on the transformation kinetics of bainite.* Materials Science and Engineering: A, 1995. **194**(2): p. 179-186.

41. Sunil, B. and S. Rajanna, *Evaluation of mechanical properties of ferrite-martensite DP steels produced through intermediate quenching technique.* SN Applied Sciences, 2020. **2**(8): p. 1461.

42. najafi birgani, E. and M. Pouranvari, *EFFECT OF MARTENSITE VOLUME FRACTION ON THE WORK HARDENING BEHAVIOR OF DUAL PHASE STEELS.* 2023.

43. Todorov, R.P. and K.G. Khristov, *Widmanstatten Structure of Carbon Steels.* Metal Science and Heat Treatment, 2004. **46**(1): p. 49-53.

44. TataSteelEurope, *Cold-rolled DP800-UC.* 2016, Tata Steel Europe Limited.

45. Parker, S.V., *Modelling of Phase Transformations in Hot-Rolled Steels*, in *Department of Materials Science and Metallurgy*. 1998, University of Cambridge: Cambridge, UK. p. 223.

46. Koval'chuk, G.Z., et al., *Effect of Widmanstatten ferrite on some properties of hypoeutectoid steel.* Metal Science and Heat Treatment, 1979. **21**(2): p. 114-117.

47. Bodnar, R.L. and S.S. Hansen, *Effects of Widmanstätten ferrite on the mechanical properties of a 0.2 pct C-0.7 pct Mn steel.* Metallurgical and Materials Transactions A, 1994. **25**: p. 763-773.

48. Hussain Dawki, A.G., Omar El-Kolaly, *A Review Paper on the Development of Dual Phase Steel.* Journal of Heavy Metal Toxicity and Diseases 2020. **5**(1): p. 1-18.

49. Bhadeshia, H. and R. Honeycombe, *Chapter 13 - Weld Microstructures*, in *Steels: Microstructure and Properties (Fourth Edition)*, H. Bhadeshia and R. Honeycombe, Editors. 2017, Butterworth-Heinemann. p. 377-400.

50. Bhadeshia, H.K.D.H., *Diffusional formation of ferrite in iron and its alloys.* Progress in Materials Science, 1985. **29**(4): p. 321-386.

51. Hulme, C., *The thermal stability of bulk nanocrystalline steels*. 2016.

52. Xiong, Z.P., et al., *Strain-induced ferrite formation and its effect on mechanical properties of a dual phase steel produced using laboratory simulated strip casting.* Journal of Alloys and Compounds, 2017. **721**: p. 291-306.

53. Hong, S.C. and K.S. Lee, *Influence of deformation induced ferrite transformation on grain refinement of dual phase steel.* Materials Science and Engineering: A, 2002. **323**(1): p. 148-159.

54. Karmakar, A., et al., *Development of Ultrafine-Grained Dual-Phase Steels: Mechanism of Grain Refinement During Intercritical Deformation.* Metallurgical and Materials Transactions A, 2013. **44**(9): p. 4106-4118.

55. Mukherjee, K., S.S. Hazra, and M. Militzer, *Grain Refinement in Dual-Phase Steels.* Metallurgical and Materials Transactions A, 2009. **40**(9): p. 2145-2159.

56. Yada, H., C.-M. Li, and H. Yamagata, *Dynamic γ→α Transformation during Hot Deformation in Iron–Nickel–Carbon Alloys.* ISIJ International, 2000. **40**(2): p. 200-206.

57. Celada-Casero, C., J. Sietsma and M.J. Santofimia, *The role of the austenite grain size in the martensitic transformation in low carbon steels.* Materials & Design, 2019. **167**: p. 107625.

58. López, B. and J.M. Rodriguez-Ibabe, *4 - Recrystallisation and grain growth in hot working of steels*, in *Microstructure Evolution in Metal Forming Processes*, J. Lin, D. Balint, and M. Pietrzyk, Editors. 2012, Woodhead Publishing. p. 67-113.

59. Ballard, T.J., et al., *Double twist torsion testing to determine the non recrystallization temperature.* Scientific Reports, 2021. **11**(1): p. 1495.

60. Homsher, C.N., *Determination of the non-recrystallization temperature (TNR) in multiple microalloyed steels*. 2013.

61. Akhtar, M.N., et al., *Determination of Non-Recrystallization Temperature for Niobium Microalloyed Steel.* Materials, 2021. **14**(10): p. 2639.

62. Li, Z., D. Wu, and H.-s. LÜ, *Effect of Thermomechanical Processing on Mechanical Properties of Hot Rolled Multiphase Steel.* Journal of Iron and Steel Research, International, 2008. **15**(1): p. 55-60.

63. Tian, Y., et al., *Effect of rolling reduction below γ non-recrystallization temperature on pancaked γ, microstructure, texture and low-temperature toughness for hot rolled steel.* Materials Science and Engineering: A, 2020. **794**: p. 139640.

64. Roucoules, C., et al., *Softening and microstructural change following the dynamic recrystallization of austenite.* Metallurgical and Materials transactions A, 1994. **25**: p. 389-400.

65. Ray, P.K., R.I. Ganguly, and A.K. Panda, *Determination of recrystallization stop temperature (TR) of an HSLA steel*. 2004.

66. Bai, D., et al., *Effect of deformation parameters on the*. Metallurgical Transactions A, 1993. **24**: p. 2151-2159.

67. Fletcher, F. *Meta-analysis of Tnr measurements: Determining new empirical models based on composition and strain*. in *Austenite Processing Symposium (Internal company presentation)*. 2008.

68. TataSteelEurope, *MITRON Functional Specification and Initial Model Settings Port Talbot*. 2011`, Tata Steel Europe. p. 37.

69. Ma, L.-q., et al., *Effect of Niobium and Titanium on Dynamic Recrystallization Behavior of Low Carbon Steels*. Journal of Iron and Steel Research International, 2008. **15**(3): p. 31-36.

70. Zhang, Z.-h., et al., *The effect of Nb on recrystallization behavior of a Nb micro-alloyed steel*. Materials Science and Engineering: A, 2008. **474**(1): p. 254-260.

71. TataSteelEurope, *User Manual for Titan 2.5*. 2023. p. Titan Rolling Process Model

72. Staalman, D., et al., *Improving the Through-Furnace Accuracy of Slab Temperature Prediction and Optimizing Pacing in Reheating Furnaces of a Hot Strip Mill*. 2015.

73. Lenard, J.G., *1 - Introduction*, in *Primer on Flat Rolling (Second Edition)*, J.G. Lenard, Editor. 2014, Elsevier: Oxford. p. 1-15.

74. WALES, M.N. *Tata Steel Now Home to the First Digitally Fired Furnaces in the World Using Laser Technology*. Business News Wales 2022.

75. Khosla, A.G., *A fundamental understanding of clinking during the cooling and reheating of as-cast steel slabs*, in *Mechanical Engineering*. 2020, Imperial College London: London. p. 236.

76. Kundu, A., *Grain Structure Development During Casting, Reheating and Deformation of Nb-Microalloyed Steel* in *School of Metallurgy and Materials College of Engineering and Physical Sciences*. 2011, University of Birmingham: Birmingham. p. 354.

77. Theyssier, M.C., *3 - Manufacturing of advanced high-strength steels (AHSS)*, in *Welding and Joining of Advanced High Strength Steels (AHSS)*, M. Shome and M. Tumuluru, Editors. 2015, Woodhead Publishing. p. 29-53.

78. Okita, C.O.T., *Austenitic Grain Refinement through Static Recrystallization Immediately after Hot Rolling*. Transactions of the Iron and Steel Institute of Japan, 1984. **24**(9): p. 726-733.

79. Bright, G.W., et al., *Variability in the mechanical properties and processing conditions of a High Strength Low Alloy steel*. Procedia Engineering, 2011. **10**: p. 106–111.

80. Lawson, A., *Tata Steel to begin Port Talbot job cuts within months, say unions*, in *The Guardian* 2023, Guardian News & Media Limited Online.

81. C.Dasarathy, *Examples of fractures, failures and rejections in engineering materials and components*. 2011. p. 61.

82. Mostert, R., B. Ennis, and D. Hanlon, *Adapting AHSS concepts to industrial practice*. 2013.

83. Malinowski, Z., et al., *Implementation of the Axially Symmetrical and Three Dimensional Finite Element Models to the Determination of the Heat Transfer Coefficient Distribution on the Hot Plate Surface Cooled by the Water Spray Nozzle*. Key Engineering Materials, 2012. **504-506**: p. 1055-1060.

84. Wolf, D.H., F.P. Incropera, and R. Viskanta, *Jet Impingement Boiling*, in *Advances in Heat Transfer*, J.P. Hartnett and T.F. Irvine, Editors. 1993, Elsevier. p. 1-132.

85. Kalinin, E.K., I.I. Berlin, and V.V. Kostiouk, *Transition Boiling Heat Transfer*, in *Advances in Heat Transfer*, J.P. Hartnett and T.F. Irvine, Editors. 1987, Elsevier. p. 241-323.

86. Kalinin, E.K., I.I. Berlin, and V.V. Kostyuk, *Film-Boiling Heat Transfer*, in *Advances in Heat Transfer*, T.F. Irvine and J.P. Hartnett, Editors. 1975, Elsevier. p. 51-197.

87. Brutin, D., *7.1 Introduction*, in *Droplet Wetting and Evaporation - From Pure to Complex Fluids*. Elsevier. p. 85.

88. Resl, O., et al., *Influence of Porous Oxide Layer on Water Spray Cooling*. 2022.

89. Technologies, P. *STECKEL & PLATE STECKEL MILLS*. 2023 [cited 2023 14 July 2023]; Available from: https://www.primetals.com/portfolio/hot-rolling-flat/steckel-plate-steckel-mills.

90. Legrand, N., et al., *Thermo-mechanical Coil Cooling Model to Tackle Shape and Mechanical Properties Issues after Hot Rolling of Steel Sheets*. 2022.

91. Bui, A.-H. and A. Le, *Strength and microstructure of cold-rolled if steel.* Acta Metallurgica Slovaca, 2016. **22**: p. 35.

92. Saunders, P., *Examination of the factors affecting quality on continuous annealing processing lines*. 2008.

93. FROHLING, D. *SPECIALTY Rolling Mills*. [Webpage] 2022 [cited 2022 24 October]; Available from: https://www.danieli-froehling.de/rolling-mills/specialty-mills.

94. Corporation, M. *Automatic Hot Rolling Machine (Single Sample) for Research of Alloy Deformation - MSK-HRP-MG3*. 2022 [cited 2022 24 October]; Available from: https://www.mtixtl.com/MSK-HRP-MG3.aspx.

95. OCAS. *Lab scale heavy gauge hot rolling, now fully automated*. 2022 [cited 2022 24 October]; Available from: https://www.ocas.be/cases/lab-scale-heavy-gauge-hot-rolling-now-fully-automated/.

96. Mohammed, F., *Initial Lewis Mill Run-Out-Table (ROT) Calibration Trials*. 2012, Tata Steel: Tata Steel, Swindon Technology Centre. p. 4.

97. Taylor, T., et al., *Evaluation method for hot rolling & run out table cooling parameters.* Materials Science and Technology, 2021. **37**(17): p. 1386-1403.

98. Okada, H., et al., *Prevention of Red Scale Formation during Hot Rolling of Steels.* ISIJ International, 1995. **35**.

99. Farrugia, D., et al., *Rapid Alloy Prototyping for a range of strip related advanced steel grades.* Procedia Manufacturing, 2020. **50**: p. 784-790.

100. CONSARC. *Consarc Products*. 2023 [cited 2023 23 June 2023]; Web page displaying Consarc Various Induction Furnaces]. Available from: https://consarc.com/products/small-rd-vim-furnaces/.

101. Brimacombe, J.K.S., I. V.; Hawbolt, E. B.; Meadowcroft, T. R.; Militzer, M.; Pool, W. J. et al., *Microstructure Engineering in Hot Strip Mills, Part 1 of 2: Integrated mathematical Model*, in *Microstructure Engineering in Hot Strip Mills*. 1998, American Iron and Steel Institute: United States. p. 90.

102. Patil, M., et al. *Effect of Deformation in Roughing Mill on Mechanical Properties of Microalloyed API Steel Grades*. in *HSLA Steels 2015, Microalloying 2015 & Offshore Engineering Steels 2015*. 2016. Cham: Springer International Publishing.

103. Kraner, J., et al., *The INFLUENCE OF THE HOT-ROLLING TECHNIQUE FOR EN AW-8021B ALUMINIUM ALLOY ON THE MICROSTRUCTURAL PROPERTIES OF A COLD-ROLLED FOIL.* Materiali in tehnologije, 2021. **55**.

104. Wang, W.-t., et al., *A comparison of deformation, microstructure, mechanical properties and formability of SUS436L stainless steel in tandem and reversible cold rolling processes.* Journal of Iron and Steel Research International, 2019. **26**(5): p. 442-451.

105. Barbosa, R.B., F.; Yue, S.; Jonas, J.J, *The influence of chemical composition on the recrystallisation behaviour of microalloyed steels*, in *Proceedings of the International Conference on Physical Metallurgy of Thermomechanical Processing of Steels and Other Metals THERMEC-88*. 1988: Tokyo. p. 55-61.

106. Hodgson, P., *Rapid method for determining the effect of process variables on recrystallisation.* Materials science and technology, 1996. **12**(9): p. 788-790.

107. Roucoules, C., S. Yue, and J. Jones. *Effect of dynamic and metadynamic recrystallization on rolling load and microstructure*. in *1 st International Conference on Modelling of Metal Rolling Processes*. 1993.

108. Sellars, C.M., *Modelling microstructural development during hot rolling.* Materials Science and Technology, 1990. **6**(11): p. 1072-1081.

109. Siciliano, F. and J.J. Jonas, *Mathematical modeling of the hot strip rolling of microalloyed Nb, multiply-alloyed Cr-Mo, and plain C-Mn steels.* Metallurgical and Materials Transactions A, 2000. **31**(2): p. 511-530.

110. Sulzbach, G., et al., *Optimization of Thermomechanical Processing under Double-Pass Hot Compression Tests of a High Nb and N-Bearing Austenitic Stainless-Steel Biomaterial Using Artificial Neural Networks.* Metals - Open Access Metallurgy Journal, 2022. **12**: p. 1783.

111. McMahon, C.J. and C.D. Graham, *Introduction to Engineering Materials: The Bicycle and the Walkman*. 1992: Merion Books.

112. Dimatteo, A., M. Vannucci, and V. Colla, *Prediction of Mean Flow Stress during Hot Strip Rolling Using Genetic Algorithms.* ISIJ International, 2014. **54**(1): p. 171-178.

113. MISAKA Y, Y.T., *Formulation of mean resistance of deformation of plain carbon steel at elevated temperature.* Journal of the Japan Society for Technology of Plasticity, 1967. **8**: p. 414-422.

114. Bruna, R.F.S., *Super High Strength Steels*, in *Super High Strength Steel Conference*. 2005: Rome, Italy

115. Siciliano, J.F., et al., *Mathematical Modeling of the Mean Flow Stress, Fractional Softening and Grain Size during the Hot Strip Rolling of C-Mn Steels.* ISIJ International, 1996. **36**(12): p. 1500-1506.

116. Kim, S.I., Y. Lee, and S.M. Byon, *Study on constitutive relation of AISI 4140 steel subject to large strain at elevated temperatures.* Journal of Materials Processing Technology, 2003. **140**(1): p. 84-89.

117. Orowan, E., *The Calculation of Roll Pressure in Hot and Cold Flat Rolling.* Proceedings of the Institution of Mechanical Engineers, 1943. **150**(1): p. 140-167.

118. Sims, R.B., *The Calculation of Roll Force and Torque in Hot Rolling Mills.* Proceedings of the Institution of Mechanical Engineers, 1954. **168**(1): p. 191-200.

119. Karman, T.V., *On the Theory of Rolling.* Zeitschrift für Angewandte Mathematik und Mechanik, 1925. **5**: p. 130-141.

120. Vazquez-Fernandez, N.I., et al., *Adiabatic Heating of Austenitic Stainless Steels at Different Strain Rates.* Journal of Dynamic Behavior of Materials, 2019. **5**(3): p. 221-229.

121. Langi, V., et al., *Effects of strain rate and adiabatic heating on mechanical behavior of medium manganese Q&P steels.* Materials Science and Engineering: A, 2023. **865**: p. 144659.

122. Harding, R.A., *Temperature and structural changes during hot rolling.*, in *Department of Metallurgy*. 1977, Univeristy of Sheffield: Sheffield. p. 429.

123. Cheng, Y.W., et al., *Constitutive Behavior Modeling of Steels Under Hot-Rolling Conditions*, U.S.D.o. Commerce, Editor. 1999, Technology Administration National Institute of Standards and Technology: USA, Boulder, Colorado 80303-3328. p. 116.

124. Tsiloufas, S., *Ductile Fracture Characterization for Medium Carbon Steel Using Continuum Damage Mechanics.* Materials Sciences and Applications, 2012. **03**: p. 745-755.

125. Sekimoto, Y., et al., *Effects of Rolling Condition on the Surface Temperature of Work Roll in Hot Strip Mill.* Transactions of the Iron and Steel Institute of Japan, 1976. **16**(10): p. 551-560.

126. Voort, G.V. *Indentifying Isothermally-Transformed Steel Microstructural Constituents*. Tech Notes, 2015. **5**, 5.

127. LePera, F.S., *Improved etching technique for the determination of percent martensite in high-strength dual-phase steels.* Metallography, 1979. **12**(3): p. 263-268.

128. M. Y. Hasbi1, M.R.W.a., F. Citrawati1, S. A. Chandra1 and L. Suhaemi, *Identification of Bainite in a Multi-phase Microstructure of an Austempered Steel Alloy: A Metallography Approach.* JURNAL SAINS MATERI INDONESIA, 2021. **23**(1): p. 7.

129. ASTM, *Standard Test Methods for Determining Average Grain Size*. 2021, ASTM International: Pennsylvania, USA. p. 11.

130. ISO, *ISO 6892-1:2016*, in *Metallic materials — Tensile testing — Part 1: Method of test at room temperature*. 2016, ISO. p. 79.

131. Trevor William Clyne, J.E.C., Max Burley, James Dean, *Profilometry-Based Inverse Finite Element Method Indentation Plastometry.* Advanced Engineering Materials, 2021. **23**(9).

132. Plastometrex, *Indentation Plastometer - User Manual*. 2023, Plastometrex UK: Cambridge UK. p. 56.

133. SenteSoftware, *JMatPro, Practical Software for Materials Engineers*. 2021.

134. METEK, S. *SPECTROLAB S – Leading the Revolution in High-End Metal Analysis*. [Website] 2024 [cited 2024 29 April 2024]; SPECTROLAB website desciding spark OES]. Available from: https://www.spectro.com/products/optical-emission-spectroscopy/spectrolab-s-metal-analysis#.

135. Davies, C., *Prosperity Quarterly Review*. 2022, Prosperity Partnership.

136. Kumar, S., *Prosperity Work Package III. Quarterly Review, Technical Update*. 2019, Swansea Univeristy

137. Li, H., et al. *Friction in the roll bite under various hot rolling conditions*. 2005.

138. Rodriguez-Galeano, K.F., et al., *A new approach to etching low-carbon microalloyed steels to reveal prior austenite grain boundaries and the dual-phase microstructure.* Journal of Microscopy, 2023. **289**(2): p. 73-79.

139. Benscoter, A. and M. Perricone, *Marshall's Reagent: Origins, Modifications, and New Applications.* Microscopy and Microanalysis, 2005. **11**(S02): p. 76-77.

140. Niessen, F., et al., *Parent grain reconstruction from partially or fully transformed microstructures in MTEX.* Journal of Applied Crystallography %@ 1600-5767, 2022. **55**(1): p. 180-194.

141. Spivak, L.V. and N.E. Shchepina, *Calorimetric Effects in the Structural and Phase Transitions of Metals and Alloys.* The Physics of Metals and Metallography, 2020. **121**: p. 968+.

142. WorldAutoSteel. *Interstitial-Free High Strength*. 2024 [cited 2024 July 22 2024]; Available from: https://ahssinsights.org/metallurgy/steel-grades/interstitial-free-high-strength/.

143. Zhang, L., et al., *Formability prediction of interstitial-free steel via miniaturized tensile specimen for Rapid Alloy Prototyping.* Applied Mathematical Modelling, 2023. **124**: p. 713-733.

144. PrimetalsTechnologiesLtd. *TRANSFORMATION MONITOR ON-LINE MEASUREMENT OF STEEL TRANSFORMATION*. 2023 [cited 2025 29 May 2025]; Available from: https://www.primetals.com/fileadmin/user_upload/content/01_portfolio/5_hot-rolling-flat/plate-mill/brochures/TRANSFORMATION_MONITOR.pdf.